BRNO UNIVERSITY OF TECHNOLOGY
VYSOKÉ UČENÍ TECHNICKÉ V BRNĚ

FACULTY OF MECHANICAL ENGINEERING
FAKULTA STROJNÍHO INŽENÝRSTVÍ

INSTITUTE OF MATERIALS SCIENCE AND ENGINEERING
ÚSTAV MATERIÁLOVÝCH VĚD A INŽENÝRSTVÍ

HIGH TEMPERATURE DEFORMATION MECHANISMS
MECHANISMY POŠKOZENÍ ZA VYSOKÝCH TEPLOT

DOCTORAL THESIS
DIZERTAČNÍ PRÁCE

AUTHOR   Mgr. Milan Heczko
AUTOR PRÁCE

SUPERVISOR   Prof. Mgr. Tomáš Kruml, CSc.
ŠKOLITEL

BRNO 2018

Abstract: Two advanced highly-alloyed austenitic steels based on the Fe-Ni-Cr matrix were studied in conditions of low cycle fatigue both at room and elevated temperature. Extensive set of experimental and characterization tools was used for the investigation of inter-related effects of alloys composition, microstructure, deformation mechanisms and overall material response under load. Key mechanisms and factors determining mechanical properties and performance in the service were analysed and discussed in the relation to the materials design.

- Standard fatigue experiments were performed at room temperature and at 700°C. Cyclic hardening/softening curves, cyclic deformation stress-strain curves, Coffin-Manson and Wöhler fatigue life curves were determined.

- Various characterization techniques of electron microscopy were used to study changes of the microstructural state of the alloys due to the cyclic loading at room and elevated temperatures.

- Fatigue behaviour, strength and cyclic plastic response of studied materials were explained in relation to the microstructure and microstructural aspects of deformation mechanisms both at room and elevated temperatures.

- It was found that Sanicro 25 exhibits the highest high temperature strength of all alloys from the same class. Its extraordinary properties are related to the two nanoparticle populations, Cu-rich coherent precipitates and dispersoid-like MX nanoparticles, which play fundamental role in the determination of strength and overall cyclic response. As a result of pinning effects and associated obstacles, dislocation motion in this alloy is significantly retarded preventing formation of substructures with lower stored internal energy. With recovery heavily suppressed, forest dislocation strengthening supported by precipitation and solid solution hardening, leads to the remarkable increase of cyclic strength at elevated temperatures.

Key words: low cycle fatigue, cyclic strengthening, nanoparticles, MX, NbC, Cu, austenitic steel, cast dendritic structure, deformation mechanisms, fatigue life, cyclic response, electron microscopy, HAADF, STEM, diffraction

Abstrakt: Dvě pokročilé vysoce legované austenitické oceli s Fe-Ni-Cr matricí byly studovány za podmínek nízkocyklové únavy jak za pokojové tak vysoké teploty. Široká škála experimentálních a charakterizačních nástrojů byla použita ke studiu vzájemně souvisejících aspektů zahrnujících chemické složení slitin, mikrostrukturu, deformační mechanismy a celkovou odezvu materiálů na externě působící zatížení. Klíčové mechanismy a faktory definující mechanické vlastnosti a výkonnost v reálném provozu byly analyzovány a diskutovány v souvislosti s materiálovým designem.

- Standardní únavové experimenty byly provedeny za pokojové teploty a teploty 700°C. Byly získány křivky cyklického zpevnění/změkčení, cyklické deformační křivky, Coffin-Manson a Wöhlerovy křivky.

- Ke studiu změn mikrostrukturního stavu slitin v důsledku cyklického zatěžování za pokojové a zvýšené teploty byla použita široká škála technik charakterizace pomocí elektronové mikroskopie.

- Únavové chování, pevnost a cyklická plastická odezva studovaných materiálů byla vysvětlena v souvislosti s mikrostrukturními změnami a mikrostrukturními aspekty deformačních mechanismů jak za pokojové tak za zvýšených teplot.

- Bylo zjištěno, že Sanicro 25 vykazuje nejvyšší pevnostní charakteristiky ze všech materiálů stejné třídy. Výjimečné vlastnosti této slitiny jsou spojeny s populacemi dvou typů nanočástic, koherentními precipitáty bohatými na měď a nanočásticemi typu MX s charakteristikou disperzoidu. Tyto nanočástice mají klíčový vliv na pevnost a celkovou cyklickou odezvu. V důsledku interakcí s precipitáty způsobujících zachytávání je pohyb dislokací v Sanicro 25 významně zpomalen, což vede k potlačení normálních procesů zotavení obvykle vedoucích ke změně uspořádání dislokační struktury tak, aby byla celková vnitřní energie systému co nejnižší. Takové uspořádání je tvořeno například dislokačními buňkami. Jelikož jsou procesy zotavení potlačeny, dislokační struktura za vysokých teplot je charakteristická homogenní distribucí dislokací o vysoké hustotě s velkou mírou vzájemných interakcí. V kombinaci s dalšími mechanismy zpevnění jako jsou precipitáty a substituční prvky v tuhém roztoku, tyto deformační mechanismy vedou k významnému zvýšení cyklické pevnosti za vysokých teplot.

Klíčová slova: nízkocyklová únava, cyklické zpevnění, nanočástice, MX, NbC, Cu, austenitická ocel, litá dendritická struktura, deformační mechanismy, únavový život, cyklická odezva, elektronová mikroskopie, HAADF, STEM, difrakce

Bibliography of the Thesis

HECZKO, M. *High Temperature Deformation Mechanisms.* Brno: Brno University of Technology, Faculty of Mechanical Engineering, 2019. 189 p. Supervisor: Prof. Mgr. Tomáš Kruml, CSc.

Declaration

I declare that my doctoral thesis "High Temperature Deformation Mechanisms" was written by my own under the supervision of Prof. Mgr. Tomáš Kruml, CSc. All information sources are given in the References section at the end of the thesis.

Brno, 31. 10. 2018: ………………………….
                                                           signature

Acknowledgements

First and foremost, I would like to thank my advisor, Professor Tomáš Kruml, not only for his professional guidance and tireless support throughout my doctoral study and academic career but also for being literally an Iron Man role model both in sportsmanship and research. Also, I would like to thank for support and help in the process of Fulbright fellowship application. Further thanks then belong to Professor Jaroslav Polák for the stimulating and fruitful discussions and for many advices given to me not only in the field of fatigue crack initiation.

Special thanks belong to Professor Michael J. Mills, who gave me an opportunity to be a part of the best electron microscopy characterization facility in the world and one of the best materials science research groups. I can honestly say that it has been my privilege to work in the Mike Mills group and that it was an enriching experience which changed the perspective how I look at the science now. Also, I would like to thank Fulbright committee for giving me an opportunity to be a part of such a prestigious program which literally changed my life not only professionally, but also personally.

I would like to thank everyone from the groups at the Ohio State University and also at the Paul Scherrer Institute who helped me during my stays abroad.

I would like to thank my colleagues from the Institute of Physics of Materials for many successful collaborations, and also for many valuable advices not only connected with my thesis. I also would like to thank for their help with experiments, especially Jiří Tobiáš and other technicians maintaining machines in perfectly operational state. Thank you to Professor Antonín Dlouhý for help and for many great discussions and meetings related to the electron microscopy. Also I would like to thank Martin Petrenec, who gave me the opportunity to come to the Institute of Physics of Materials and who convinced me to pursue the doctoral study program.

Most importantly, I would like to thank my family; Veronika, my life partner and also a great colleague in research, who has always been supportive and understanding and who stood by me in difficult times throughout my academic career; my parents Jana and Milan, my brother Marek and my grandparents Aurelie and Milan and Ludmila and Petr; all deserve special thanks for unwavering support, love and patience. I would not be where I am today without them. I respectfully dedicate this document to them with much gratitude and thanks.

Thank you all.

Contents

I. Introduction

Nowadays, increasing energetic and economic efficiency represents a necessary condition for a sustainable development of the modern civilization and human society. The required efficiency level can only be reached through a development of new materials with a permanently improving performance.

Numerous components used in the automotive, aerospace as well as in the power generation industry are challenged by coupling of severe conditions such as repeated cyclic loading, high temperatures and environmental effects that can significantly limit their useful life in the service. Improving the temperature capability of materials used for construction of these components could translate into significant increase in jet-engine or power generation process efficiency, resulting in substantial cost savings over their service life, and also beneficial environmental impact by reducing emissions amount.

The properties of existing materials are significantly below physical limits and it is just a question of material and processing design, to which extent the real materials can approach these limits. In one of the most important properties, the material strength domain, the fundamental limits are given by theoretical strength, and by the melting point. A vast untapped potential exists in design and processing allowing extension of materials performance further beyond. It is almost general rule that increasing strength of bulk materials is coupled with decreasing ductility. Thus, besides of improving strength, a second aim of the new design of materials should be preserving or even improving their ductility.

Substantial effort focused on the high temperature regime performance improvement led to development of several new types of complex materials. Creep resistant nickel based superalloys strengthened by coherent ordered intermetallic γ´-precipitates present proven and stable candidates for state-of-the-art high temperature applications, where benefits of their performance overcome their very high cost [1].

When compared to Ni-based superalloys, oxide dispersion strengthened (ODS) ferritic steels exhibit a considerably improved microstructural stability in the high temperature regime. Their microstructure consists of the steel matrix strengthened by dispersion of stable yttrium-based oxides of typical size between 2-30 nm and of volume fraction of about 0.5%. Excellent creep strength of the ODS steels is associated with an attractive interaction between dislocations and incoherent oxide particles as was successfully modelled by Rösler and Arzt [2, 3].

Recent representative of novel class of scientifically and technologically interesting materials are high-entropy alloys (HEAs). These single-phase solid solution alloys (called also as multicomponent or compositionally complex alloys) consisting of five or more elements in equiatomic proportions, are intriguing, because they exhibit a potential for solid solution hardening (high strength) combined with a good ductility in case of face-centered cubic lattice with a lagre number of slip systems. This is one of the reasons why HEAs are the subject of a rapidly increasing research [4–8] since Yeh et al. [4] defined this new class of alloys in 2004.

Their promising properties imply many applications, which require high strength and thermal stability up to 800°C as well as wear and oxidation resistance.

Knowledge obtained in relation with discovery of new alloy classes and as a result of advancement in materials research significantly helped with improvement of known conventional systems such as austenitic steels. Adjusted design, alloying and processing path modification led to the material class of the highly-alloyed face-centered cubic (FCC) solid solution based alloys, also called as super-austenitic stainless steels. Providing sufficient high temperature performance they became highly-cost-effective alternative in applications where only expensive Ni-based superalloys are applicable. [9, 10]

Two different structural materials belonging to the class of highly-alloyed FCC solid solution based alloys are studied in this work. Extensive set of experimental and characterization tools is used for the investigation of inter-related effects of alloys composition, microstructure, deformation mechanisms and overall material response under load. Key mechanisms and factors determining mechanical properties and performance in the service are analysed and discussed in the relation to the materials design.

II. Aims of the work

The primary goal of the research study to be presented in this thesis was to investigate two highly-alloyed FCC solid solution based alloys used in high temperature applications, in particular power generation industry and ethylene cracking furnaces. Special emphasis is put on investigation, identification and characterization of deformation mechanisms determining cyclic plastic response, strength and ductility of both materials at high temperatures. Mutual correlation between alloys composition, microstructure and macroscopic response are discussed along with the materials design. Several minor goals were specified to be accomplished within the study as listed below:

- Characterization of initial state of materials, discussion of differences in alloys design.

- Determination of basic fatigue life curves, Manson – Coffin and derived Wöhler curves at room and elevated temperatures.

- Study of cyclic stress-strain response of materials and determination of cyclic hardening/softening curves at room and elevated temperatures.

- Advanced characterization of deformation microstructure produced by testing both at room and elevated temperatures. Correlation of observations to the cyclic stress-strain response of materials.

- Explanation of fatigue behaviour of studied materials in relation to the microstructure and microstructural aspects of deformation mechanisms both at room and elevated temperatures.

- Identification of key factors in alloys design affecting their performance in the service. Discussion.

III. Current state of the knowledge

1. FCC-based structural materials for high-temperature applications

Within group of structural materials based on FCC matrix, austenitic stainless steels are the most widely used type of alloys. Having outstanding corrosion resistance, high oxidation resistance and superior creep-fatigue properties they present perfect cost-effective candidate for industrial applications at high temperatures.

In the last two decades, most studied representative of this class of materials was conventional austenitic stainless steel of 316-type used in service up to temperatures of 650°C. Creep performance was investigated in detail [11, 12] as well as microstructural stability after long-term thermal exposures [13]. Gerland et al. [14, 15] delivered comprehensive study of cyclic stress-strain response and fatigue behaviour in relation to the dislocation structure changes in range of different temperatures. The work on dislocation structures was then further extended by Kruml et al. [16, 17]. In more recent publications, evolution of deformation microstructure as a result of cyclic loading of 316-type of steel was reported by Pham et al. [18]. Other papers were focused on more complex mechanical testing, such as fatigue-dwell testing [19] or thermo-mechanical testing [20].

Efforts to increase alloy performance and strength at high temperatures led to development of steels modified by alloying. Some variants were produced with changed ratio and amount of Cr/Ni content as 304-type [10, 21, 22], some other were alloyed with additional elements to increase precipitation of secondary phases, enhance solid solution strengthening or even modify stacking fault energy [23]. Two alloys studied in this work belong to recent representatives of advanced engineering. Highly-alloyed austenitic stainless steel Sanicro 25 is considered as a crucial material for use in the power generation industry, while Manaurite XTM is a centrifugally casted alloy developed as a structural material for pipe coils in ethylene cracking furnaces. In following chapters, background of both studied materials is introduced and discussed in detail.

1.1 Sanicro 25

Although combustion processes generate carbon dioxide, coal-fired thermal power generation is still one of the most important ways for the long-term future to satisfy the world-wide demand for electric power. This has increased pressure on the coal fired power industry to raise the operating efficiency of the plants thereby reducing the emissions.

One of the ways how to accomplish this task is to increase the maximum steam temperature and the steam pressure. Nowadays, modern power plants operate at temperatures around 600°C and pressures of 30 MPa with maximum efficiency reached from 45 to 47%. By increasing the steam temperature up to 700°C and pressure up to 35 MPa, advanced ultra-super critical (A-USC) conditions are reached. As a consequence, a power plant heat

efficiency of higher than 50% can be obtained and CO_2 emission can be reduced by about 45% when compared to the standard super critical (SC) conditions [9, 10, 24].

Satisfying requested advancement in power plant performance requires design of new heat-resistant materials with improved high-temperature strength, enhanced creep properties and sufficient high-temperature corrosion resistance when compared to conventional alloys used in standard SC conditions. Excluding possible candidate materials in the field of Ni-based superalloys, attention was put towards notably more cost-effective heat resistant super-austenitic steels. One of the alloys newly developed primarily for use in superheaters and reheaters in the next generation A-USC coal-fired boilers at material temperatures up to 700°C (1292°F) is the Sandvik Sanicro 25 [9, 10, 24].

When compared to widely used conventional steel of 316-type or even other similar heat-resistant alloys (e.g. NF709, Super304H, HR3C, etc.[10]), Sanicro 25 has unique composition in terms of type and amount of chemical elements used together as can be seen in Tab. 1.1. It is based on the Fe-Ni-Cr alloy system with a high amount of Ni and Cr combined with variety of other alloying elements. While 22.5 wt% Cr should secure good steam oxidation resistance and hot corrosion resistance, a high Ni content of approximately 25.0 wt% and high amount of N are used for the stabilization of the FCC austenite phase. For solid solution and precipitation strengthening, a combination of a high content of W, Co, Nb, Cu and other elements have been added.

	Fe	Ni	Cr	W	Cu	Co	Nb	Mn	Si	N	C	Mo	
Sanicro 25	Bal.	25.0	22.5	3.6	3.0	1.5	0.5	0.5	0.2	0.23	0.1	-	-
316 (L/H)	Bal.	10.0-14.0	16.0-18.0	-	-	-	-	2.0 max	1.0 max	0.1 max	0.03-0.1	2.0-3.0	+P,S, B
NF709	Bal.	23.0-27.0	19.0-22.0	-	-	-	0.1-0.4	1.5 max	0.75 max	0.1-0.2	-	1.0-2.0	+B, Ti,
HR3C	Bal.	17.0-23.0	24.0-26.0	-	-	-	0.2-0.6	2.0 max	0.75 max	0.15-0.3	0.04-0.1	-	-
304	Bal.	8.0-12.0	18.0-20.0	-	-	-	-	2.0 max	1.0 max	-	0.08 max	-	-
Super 304H	Bal.	7.5-10.5	17.0-19.0	-	2.5-3.5	-	-	1.0 max	0.3 max	0.05-0.12	0.07-0.13	-	+B, Al
347 /HFG	Bal.	9.0-13.0	17.0-20.0	-	-	-	8-10 × %C	2.0 max	1.00 max	-	0.04-0.1	-	-

Table 1.1: Comparison of chemical composition of Sanicro 25 super-austenitic stainless steel with conventional steel of 316-type and other Fe-Ni-Cr based alloys (in wt.%). [10]

First research studies of Sanicro 25 focused on creep performance and strength [9, 24], microstructural stability after long-term thermal exposure [25] and also on corrosion and oxidation resistance [26]. In recently published work, it has been reported that the highly-alloyed steel Sanicro 25 exhibits excellent corrosion resistance combined with the highest creep strength at 700°C among all heat-resistant austenitic steels commercially available today [9]. In Fig. 1.1, comparison of the creep rupture stress after 100000 hours at 700°C (the values were extrapolated) is shown for several different austenitic and nickel-based alloys. Except Alloy 617, Sanicro 25 exhibits highest creep strength. Also, when comparison is made on the relative creep rupture strength map showing ferritic steels, austenitic alloys and nickel-

based alloys and superalloys as shown in Fig. 1.2, it is clear that the performance of Sanicro 25 is well above conventional austenitic steels or even other similar highly-alloyed steels like NF709. Having high temperature strength at 700°C close to much more expensive Ni-based alloys suggests very promising potential of this material for further applications.
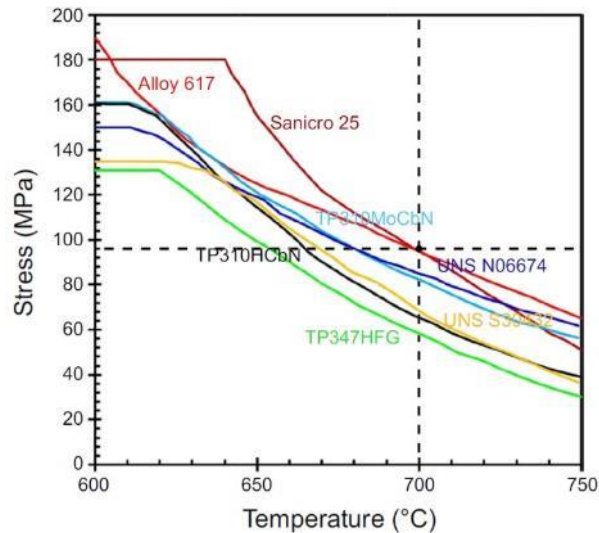
Figure 1.1: Comparison of the creep strength of different austenitic and nickel-based alloys based on data of European Pressure Directive. The values have been extrapolated to 100000 hours. Data are from European VdTÜV datasheets; TP347HFG 547; UNS S30432 550; UNS No S31042/TP310HCbN, 546; TP310MoCbN (NF709) 563; UNS N06674 (HR6W) 559; and Alloy 617 485 (Taken from [9]).
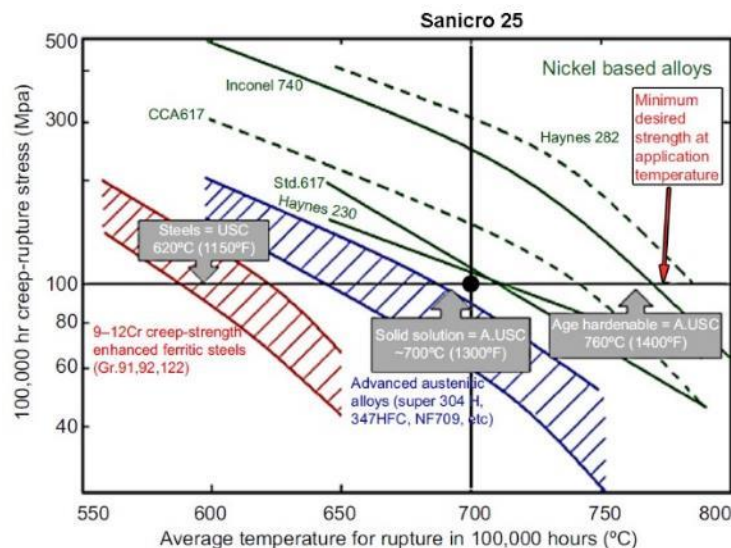
Figure 1.2: Comparison of relative stress rupture strength of steels and nickel based alloys as potential candidate materials for ultra-supercritical and A-USC plant operation at 700°C. Creep rupture strength of Sanicro 25 is highlighted in the micrograph (Taken from [27]).

In real service, structural components are not loaded only monotonically. They undergo complex loading conditions, in most cases cyclically repeated, which can be characterized in terms of the low cycle fatigue, dwell-fatigue and thermo-mechanical fatigue. Since the material can behave completely differently when cyclic loading is present, there is a strong

need for detailed investigation of mechanisms governing cyclic response and cyclic strength both during room and elevated temperature testing. This is fundamental to an improved understanding of the overall microstructural changes and corresponding mechanisms leading to the exceptional high temperature behavior of this alloy.

1.2 Manaurite XTM

Highly-alloyed refractory steels are used as centrifugally cast tubes and sand cast junctions in the hot part of cracking and reforming furnaces for the petrochemical industry [28–30]. Ethylene furnaces, cracking liquid or gas hydrocarbon molecules in the presence of steam, operate at high cracking temperatures and sometimes also at high pressures. Several processing conditions challenge furnace design and materials for the furnace. Recently, many coil suppliers have put a lot of effort into the research of such a construction material that can withstand higher operating conditions and operate under the extreme environment of an ethylene furnace (high temperatures, aggressive environments and high internal pressures) for long periods of time (8 to 12 years). As a result, a special class of cast, heat-resistant refractory steels has been developed [31, 32].

These alloys have high chromium content necessary to maintain high corrosion resistance while high nickel content allows stability of the austenitic structure what is crucial to ensure good creep properties. The microstructure usually consists of an austenitic matrix and eutectic primary carbides precipitated in the interdendritic regions. Combined with additional secondary precipitates formed during aging this further secures good mechanical properties at high temperatures [31, 33].

Mostly used alloys of this material class are HP-NbTi alloy [31], Alloy 800, wrought alloy Sandvik 353 MA and also Manaurite XM or Manaurite XTM, which is studied in this work [29]. Manaurite XTM produced by Manoir Industries in Pitres, France is a structural material of main parts of ethylene furnaces (see Fig. 1.3), which are used for hydrocarbon processing and cracking. One of the particular procedures is so-called steam cracking - a petrochemical process in which saturated hydrocarbons are broken down into smaller, often unsaturated, hydrocarbons by breaking carbon-carbon bonds. It is the principal industrial method for producing olefins, including ethylene and propylene.

The cracking process results in slow deposition of coke, a form of carbon, on reactor walls leading to significant degradation of the reactor efficiency. Reaction conditions are designed to minimize this effect as much as possible. Nonetheless, a steam cracking furnace can usually only run for a few months at a time between de-cokings. De-coking procedure requires the furnace to be isolated from the process and then a flow of steam or a steam/air mixture is passed through the furnace coils. This converts the hard solid carbon layer to carbon monoxide and carbon dioxide. Once this reaction is complete, the furnace can be returned to service. [34, 35]
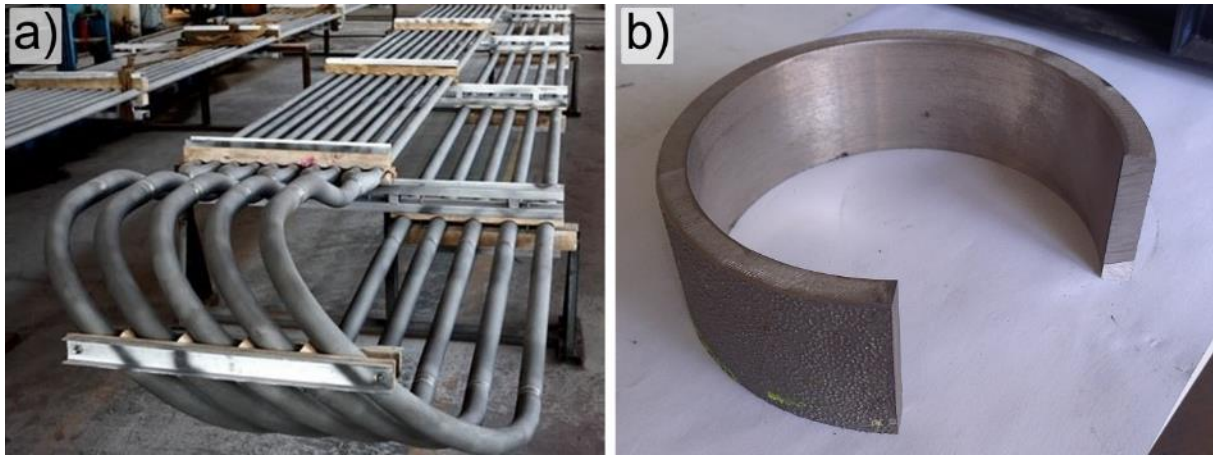
Figure 1.3: (a) Example of multi-pass configuration-type coils of Manaurite XTM used in ethylene furnaces. (b) Cut from the cast tube with tube wall thickness of 8 mm.

Ethylene furnaces usually consist of a multi-pass type arrangement of coils. Feedstock composed of gas and fluid at the room temperature enters coil system of tubes, which is schematically visualized in Fig. 1.4.
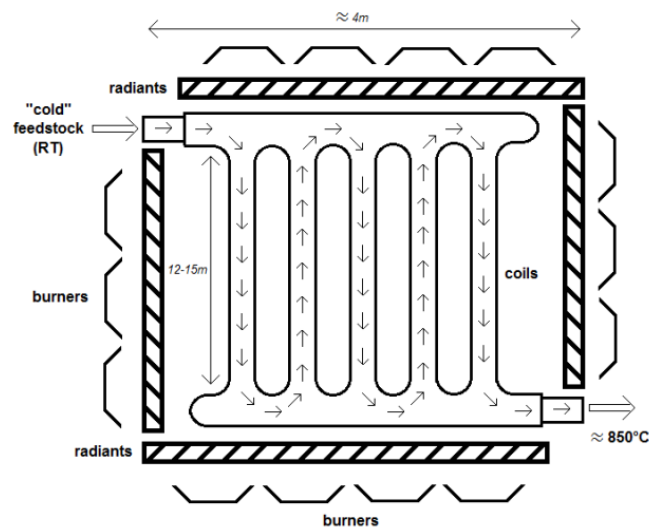
Figure 1.4: Scheme of the ethylene furnace arrangement.

Ethylene furnace operation starts when the radiants are heated up by the burners. The radiants are made from a high temperature resistant material with a high coefficient of thermal conductivity. Manaurite XTM tubes are then heated up by the heat transfer from radiants maintained at high temperature of about 2000°C.

For proper cracking operation, feedstock temperature has to be at least 850°C during the whole procedure. However, to satisfy this condition, coil exterior has to be heated up by the burner system to higher temperature of approx. 950°C. That is mainly due to the tube wall thickness and also the material coefficient of thermal conductivity. As a result, thermal gradients are present in the tube material. It is usually possible to measure only temperature on the surface of the tube and temperature of the feedstock leaving the furnace system.

Heating up and cooling down rates recommended by cracking furnace producer are shown in Fig. 1.5a. Starting procedure usually takes approx. 10 hours but it could differ depending on customer. The schematic micrograph showing time dependence of tube surface temperature in regard to service conditions is drawn in Fig. 1.5b.
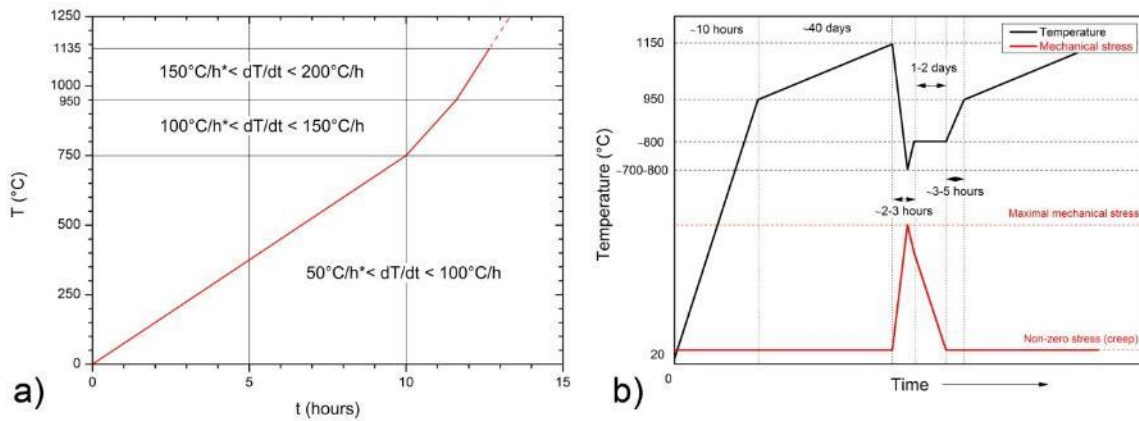
Figure 1.5: (a) Recommended heating/cooling rates. (b) Schematic showing evolution of the material temperature and stresses acting on the material during one cycle of cracking operation.

Cracking operation induces formation of the coke layer on the inner surface of the tubes immediately after the start - coke deposit takes place as the feedstock is processed through the coils (see schematic picture in Fig. 1.6a). Since the coke layer acts as a thermal barrier, the furnace operator has to increase the temperature on tube surface. This allows the cracking temperature inside the tube to remain the same despite the coke thickness.
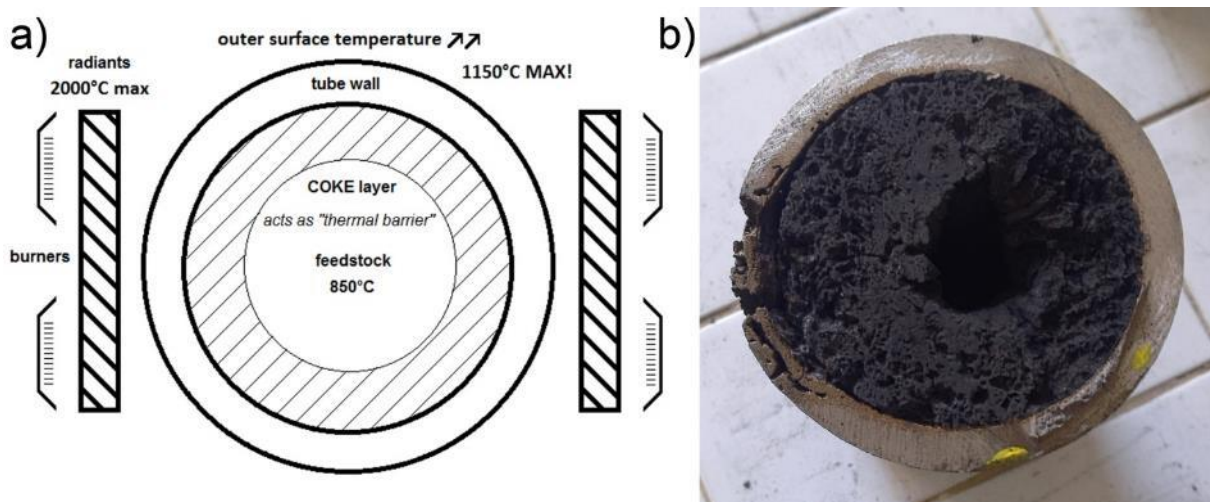
Figure 1.6: (a) Schematic of coke layer deposition process on the inner surface of the tubes. (b) Picture of coil tube completely filled with deposited coke layer.

On average, cracking operation lasts approximately 40 days. In most cases the furnace is shut down because of two main reasons. When the temperature on the surface of the coils increases up to the material operating limit (i.e. 1150°C) or when the pressure drop due to the constriction of surface is too small (coke can fill almost the whole diameter of the tube – see Fig. 1.6b).

With the coil system filled up with the coke the cracking process cannot continue and de-coking procedure has to be performed. Tube surface is cooled down to the temperature of approximately 700°C to 800°C in 2 or 3 hours. Immediately after cool down, the temperature rises a little bit due to exothermal effects and release of particular amount of heat. Then, after temperature stabilization, mix of steam and air is sent through the coils to destroy the coke layer. According to Manoir Industries, de-coking procedure usually takes about 1 to 2 days. After that, the ethylene furnace is prepared for the next service cycle. Sometimes the whole system is shut down completely after de-coking (see Fig. 1.7a). Here, it is important to note that the de-coking procedure has to be performed first, otherwise coke filled inside the tubes can cause significant damage in the tube walls as the whole arrangement is cooled down to the room temperature (see Fig. 1.7b). As will be discussed further, the coke has much lower coefficient of thermal expansion than the tube wall material. When cooling down the coke shrinks lesser than the tube wall generating significant stress fields in the material possibly causing plastic deformation at high temperatures. Considering that, the de-coking procedures can present key events determining service operation life time of the material.

Since there is a lack of any systematic study of cyclic behaviour of Manaurite XTM or any other similar refractory FCC based alloy, delivering detailed investigation of mechanisms governing cyclic plastic response of this class of alloys both at room and elevated temperature can further contribute to the enhancement of the Manaurite XTM alloy design and subsequently improvement of operational life time.
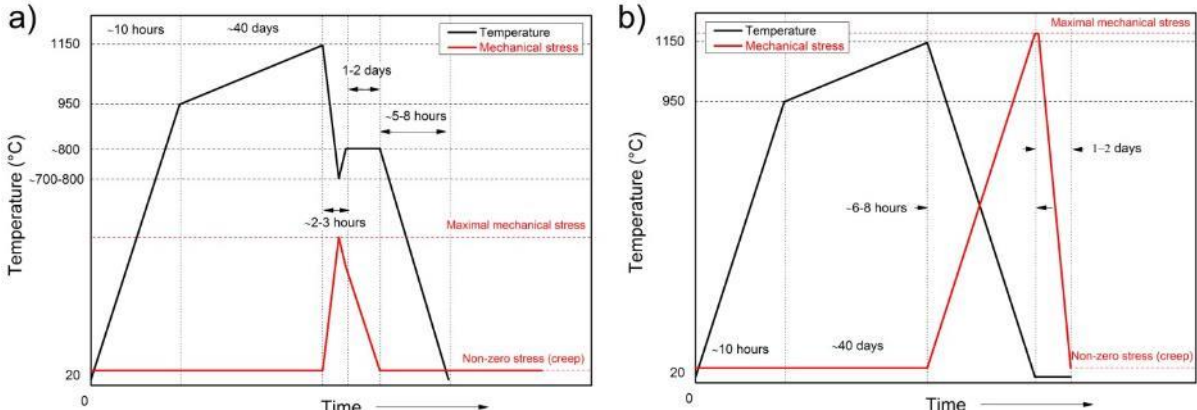

Figure 1.7: (a) Schematic micrograph of one cycle of cracking operation followed by the de-coking procedure and furnace shut down. (b) If the cooling to room temperature is performed prior to the de-coking procedure, tube walls are subjected to larger damage.

2. Microstructure of metals

This section gives a brief overview of the basic materials science concepts and the physically based principles defining fundamental properties of material. When trying to explain two of the most important material properties – strength and ductility – it is important to start with definition of crystal structure and lattice defects. The plastic deformation of solid matter is ultimately related to the mobility of crystal defects in the lattice, while the microstructural obstacles acting against can define strength of the material.

In the first part of this section, concepts describing atomic arrangements in a crystal lattice are summarized. Then, the overview of lattice defect types is presented and different mechanisms enabling plastic deformation are discussed. Rest of the text is then focused on microstructural features affecting plastic response and strength of material as well as mutual correlation of microstructural and macroscopic response in metals. If not referred to otherwise, this section uses general information of the following references: [36–41].

2.1 Crystal structure

At the atomic length scale, most solids feature crystalline structure that can be described as regular arrangement of atoms. The constituent atoms are arranged in a symmetric pattern that repeats itself periodically in three dimensions. The group of atoms in the material having the full symmetry of the crystal that constitutes repeating pattern is called the *unit cell*. By placing a motif unit of one or more atoms at every lattice site the regular structure of a perfect crystal is obtained.
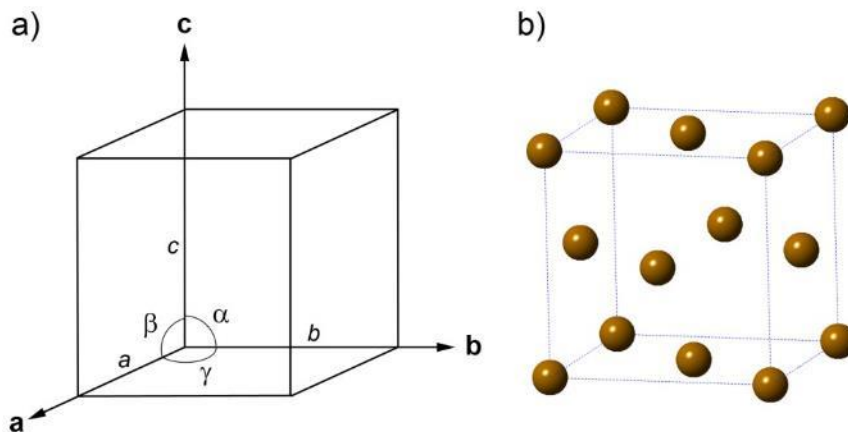
*Figure 2.1: (a) Geometrical illustration of unit cell of face-centered cubic crystal lattice with parameters a = b = c, and α = β = γ = 90 degrees. Basis vectors are **a**, **b**, **c**. (b) Visualisation of unit cell including atom positions.*

In crystallography, the atom positions in a unit cell or a crystal can be described by translation (or lattice) vector **t** in a direct crystallographic space as

$$\mathbf{t} = u\mathbf{a} + v\mathbf{b} + w\mathbf{c}, \qquad (2.1)$$

where **a**, **b**, **c** are three non-coplanar vectors (*primitive vectors*) denoting the crystallographic basis along the three sides of the unit cell, and (*u*, *v*, *w*) are integers. Integer linear combinations of three basis vectors demark the atomic coordinates. In general, crystal lattice unit cell can be fully described by stating the lengths of the three basis vectors and their mutual angles. Lattice parameters are then *a*, *b*, *c*, *α*, *β*, *γ*. (see schematic visualisation in Fig. 2.1). [37]

While the crystal structures of most pure metals are body-centered cubic (BCC), face-centered cubic (FCC) and close-packed hexagonal (HCP) lattices, the structures of alloys and non-metallic compounds are often more complex.

For the analytical studies of crystal structures, particularly in the theory of diffraction, the concept of *reciprocal space* and *reciprocal lattice* plays a fundamental role. While the direct lattice is usually a periodic spatial function in real-space, the reciprocal lattice represents the Fourier transformation of that function represented in reciprocal space.

The reciprocal lattice vector **g** can be described as

$$\mathbf{g} = h\mathbf{a}^* + k\mathbf{b}^* + l\mathbf{c}^*,$$
(2.2)

where **a***, **b***, **c*** are the basis vectors in reciprocal space and (*h*, *k*, *l*) integers. The basis vectors are connected to the real-space by the following relationships:

$$\mathbf{a}^* = \frac{\mathbf{b} \times \mathbf{c}}{V} \quad \mathbf{b}^* = \frac{\mathbf{c} \times \mathbf{a}}{V} \quad \mathbf{c}^* = \frac{\mathbf{a} \times \mathbf{b}}{V},$$
(2.3)

where *V* is the unit cell volume in real-space.

The reciprocal space is orthogonal to the real-space. The reciprocal lattice vector **g**, with components (*h*, *k*, *l*), is perpendicular to the plane with Miller indices (*hkl*). For this reason, a reciprocal lattice vector is often denoted with the Miller indices as subscripts, e.g. $\mathbf{g}_{hkl}$. [36, 37, 39]

Each point (*hkl*) in the reciprocal lattice corresponds to a set of lattice planes (*hkl*) in the real space lattice. The direction of the reciprocal lattice vector $\mathbf{g}_{hkl}$ is parallel to the normal vector **n** of the real-space planes. The magnitude of the reciprocal lattice vector is given in reciprocal length and is equal to the reciprocal of the *interplanar spacing* d_{hkl} of the real space planes [39]:

$$|\mathbf{g}_{hkl}| = \frac{1}{d_{hkl}}.$$
(2.4)

2.2 Lattice defects

All real crystals contain lattice defects locally disturbing the regular arrangement of the atoms. Based on their characteristics, they are divided into four categories: *point defects* (vacancies and interstitials), *line defects* (dislocations), *planar defects* (stacking faults, grain boundaries) and *bulk defects* (voids). Selected lattice defect types are further discussed in detail.

If we ignore thermal vibrations, all the atoms in a perfect crystal are located at specific atomic sites. Then, two types of point defects can be characterized, a *vacant atomic site* or *vacancy*,

and a *self-interstitial atom* as is schematically illustrated in Fig. 2.2. Vacancies and interstitials are considered as intrinsic lattice point defects. On contrary, the extrinsic point defects are for example impurity atoms in a crystal. Impurity atoms can take up two different types of atomic sites, (a) *substitutional*, in which an atom of the parent lattice is replaced by the impurity atom (of different type), and (b) *interstitial*, in which the impurity atom is at a non-lattice site. All the point defects produce a local distortion in the normally perfect crystal also related to the amount of additional energy in the crystal.[36]
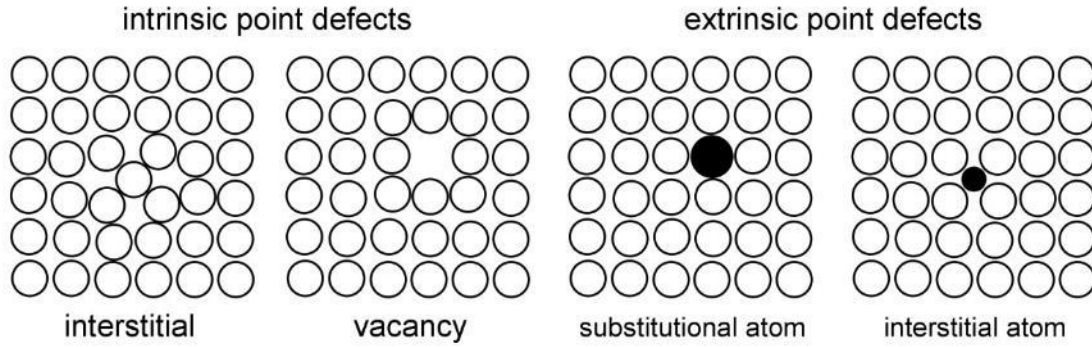
Figure 2.2: Schematic illustration showing intrinsic lattice point defects, i.e. interstitials and vacancies, and extrinsic point defects, i.e. substitutional and interstitial impurity atoms.

Strong evidence for the existence of *dislocations* as a line defects arose from attempts to explain discrepancy between calculated theoretical critical shear stress and experimental values of the applied shear stress required to plastically deform a single crystal. In a perfect crystal where dislocations are absent, this deformation occurs by sliding of neighbouring atomic planes over each other. As first calculated by Frenkel in 1926, there is a periodic shearing force required as given by simplified relation [36]:

$$\tau = \frac{Gb}{2\pi a} \sin \frac{2\pi x}{b},$$
(2.5)

where τ is the applied shear stress, G is the shear modulus, b the spacing between atoms in the direction of the shear stress, a the spacing of the rows of atoms and x is the shear translation of the two rows away from the low-energy position of stable equilibrium (x = 0). In case of small strains x/a, and considering $b \approx a$, the maximum value of τ can be defined as the *theoretical critical shear stress*

$$\tau_{th} \approx \frac{G}{2\pi},$$
(2.6)

being sizeable fraction of the shear modulus. Despite the fact these are approximate calculations, it is shown that τ_{th} is many orders of magnitude greater than the observed values of the resolved shear stress for slip measured in real, well-annealed crystals. In 1934, E. Orowan, M. Polanyi and G.I. Taylor stated independently, that the difference between theoretical prediction and experiment can be explained in terms of the theory of dislocations. Instead of the simultaneous movement of one whole atomic array, the atoms from one of the surrounding planes break their bonds and re-bond with the atoms at the terminating edge so the half plane of atoms is moved, one at a time. The energy required to break a single bond is far less than that required to break all the bonds on an entire plane of atoms at once. Most

crystalline materials contain dislocations so their strength is lower than the theoretically expected τ_{th} (an exception are the Whiskers with a high degree of crystal perfection).[36, 39]

Two main types of dislocations can be defined – *edge* and *screw* dislocations. Schematic illustration of both is shown in Figure 2.3. Edge dislocation is a defect where an extra half-plane of atoms is inserted into a perfect lattice (see Fig. 2.3a). On the other hand, the arrangement of atoms around a screw dislocation can be simulated by displacing the crystal on one side of ABCD rectangle relative to the other side in the direction AB as shown in Figure 2.3b.
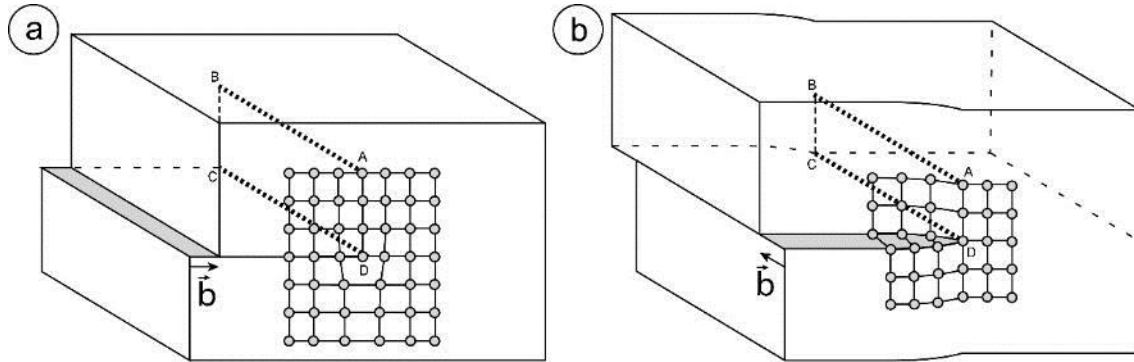
Figure 2.3: Schematic visualisation of (a) edge dislocation segment where Burgers vector is perpendicular relative to the dislocation line (dashed line CD) and (b) screw dislocation segment where dislocation line is parallel with Burgers vector.

Dislocations are described by two vectors. A unit vector tangent **l** represents the *dislocation line* while the magnitude and direction of the lattice distortion resulting from a presence of dislocation in a crystal lattice is represented by the *Burgers vector* **b**. The Burgers vector of an edge dislocation is perpendicular to the line of the dislocation while the Burgers vector of a screw dislocation is parallel (see schematic visualisations in Fig. 2.3 and Fig. 2.4). *Dislocation character* is determined by angle between dislocation line vector **l** and Burgers vector **b**. It can have values from 0° to 90°. Dislocation lines must either form closed loops or branch into other dislocations. They can end at the crystal surface and at grain boundaries, but never inside a crystal. In real materials, generally the dislocations are *mixed*, i.e. they exhibit both edge and screw character as shown in Fig 2.4b.[36, 39]

The *dislocation density ρ* is defined as the total length of dislocation line per unit volume of crystal (stated in units of m^{-2}). Thus for a volume *V* containing line length *l*,

$$\rho = \frac{l}{V}.$$
(2.7)

In well-annealed metal crystals ρ is usually between 10^{10} and 10^{12} m^{-2}, while in crystals after heavy plastic deformation it can be about 10^{14} to 10^{15} m^{-2}. An increase in the dislocation density can be the result of: (a) elongation of existing dislocations, (b) nucleation processes at stress concentrators, (c) activation of Frank-Read sources initiated by a bowing out of dislocations pinned by obstacles such as precipitates, jogs, etc., (d) cross-slip activity, and (e) the dislocation emission from the grain boundaries [36, 39] .
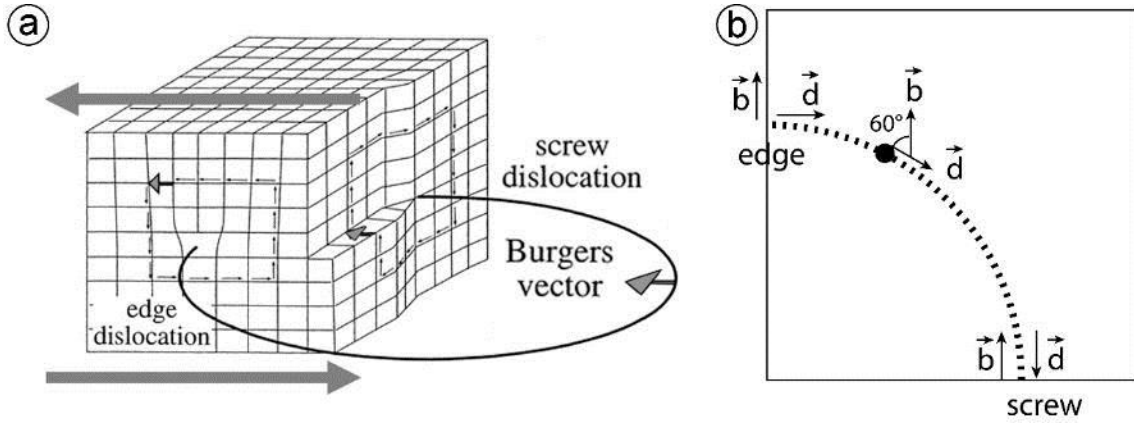
Figure 2.4: (a) Schematic visualisation of dislocation loop in the crystal lattice. Dislocation has edge, screw and mixed segments. (b) View perpendicular to the dislocation loop plane. In case of edge segment, Burgers vector is perpendicular to the dislocation line while for screw segment, it is parallel. If angle between Burgers vector and dislocation line is from 0 to 90 degrees, dislocation has mixed character. Image modified after [40].

The dislocations are source of internal stresses in the crystal. The atoms in a crystal containing a dislocation are displaced from their perfect lattice sites, and the resulting distortion produces a *stress field* around the dislocation. The stresses and strains can be obtained by conventional elasticity theory. However, when the center of a dislocation in a crystal is approached, elasticity theory is not valid anymore and non-linear, atomistic models have to be used. This region is called the *core* of the dislocation and in most cases its radius lies in the range from *b* to 4*b*.

Having stress and strain fields, the dislocations carry a *strain energy* which increases the internal energy of a faulted crystal. The total energy of a dislocation per unit length is given as:

$$E_{total} = E_{core} + E_{elastic\ strain}, \qquad (2.8)$$

The elastic strain energy of the dislocation, stored outside of the core, may be determined by integration of the energy of each small element of volume.

$$E_{el}(edge) = \frac{Gb^2}{4\pi(1-\nu)} \ln\left(\frac{R}{r_0}\right) \qquad (2.9)$$

$$E_{el}(screw) = \frac{Gb^2}{4\pi} \ln\left(\frac{R}{r_0}\right) \qquad (2.10)$$

Equations (2.9) and (2.10) demonstrate that E_{el} depends on the core radius r_0 and the crystal radius R. If realistic values for R and r_0 are taken, the approximate equation for the elastic strain energy per unit length of dislocations can be written as:

$$E_{el} = \alpha G b^2, \qquad (2.11)$$

where $\alpha \approx 0.5 - 1$. In contrast to the elastic energy, the energy of the dislocation core E_{core} will vary as the dislocation moves through the crystal lattice with the periodic atomic potential. This gives rise to the lattice resistance to dislocation motion called as the *Peierls-Nabarro stress*. [36, 39]

Single crystal or *monocrystalline* solid is a material in which the crystal lattice of the entire sample is continuous and unbroken to the edges of the sample, with no grain boundaries and defects associated with them. On contrary, *polycrystalline materials* consist of several grains with mutually different orientations. These materials are normally mechanically isotropic on a macroscopic level, unless a texture exists with particular grain orientations that occur with a higher probability than others [39]. Important microstructural features associated with polycrystalline materials are planar defects, interfaces between two crystallites called *grain boundaries*. Their standard characterization is based on the *misorientation angle* between the grains or crystallites. It is defined as the smallest angle needed to rotate one neighbouring crystallite of the boundary onto the other one. While for *low-angle grain boundaries (LAGB)* the misorientation angle is below 5°, for *high-angle grain boundaries (HAGB)* it is above 10-15°.

In most cases LAGBs are represented by uniform array of one, two, three or more sets of dislocations, also called as low energy dislocation configurations, where the superimposed long-range elastic fields are cancelled so the energy per dislocation is reduced. These dislocation arrangements then separate regions of the crystal which differ in orientation by less than 5°. In case of simplest type of LAGB, symmetrical tilt boundary, the misorientation angle is approximately $\vartheta \approx b/h$, where b is magnitude of Burgers vector of the dislocations contained in the boundary and h is the distance between boundary dislocations. The energy per dislocation stored in a LAGB decreases with increasing misorientation (see Fig. 2.5).
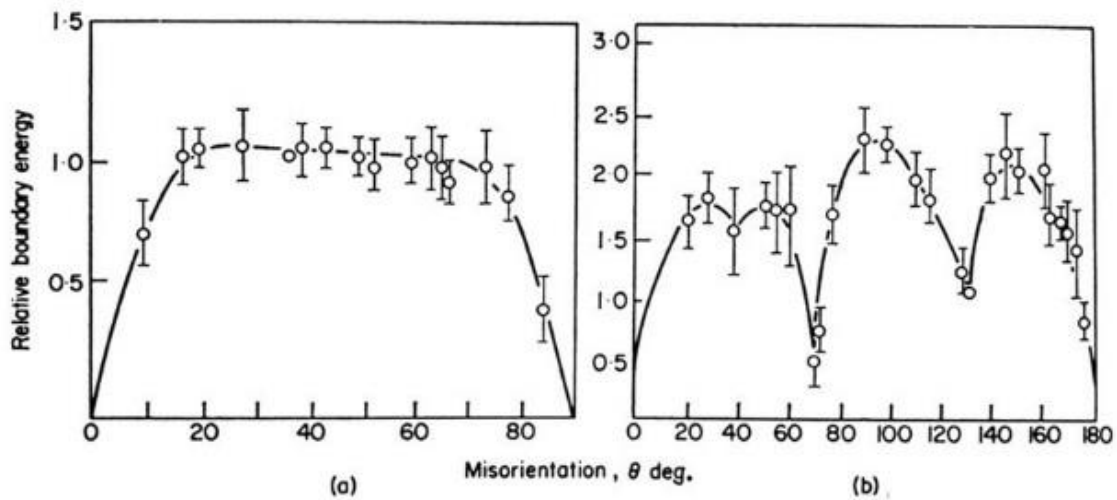
Figure 2.5: Measured grain boundary energies for symmetric tilt boundaries in Al (a) when the rotation axis is parallel to <100>, (b) when the rotation axis is parallel to <110>. (Taken from [42]).

In comparison with LAGBs, HAGBs are considerably more disordered, with large areas of poor fit of two crystallite lattices. The boundary consists of structural units depending on both the misorientation of two grains and the character of their interface. In the concept of the coincidence site lattice (CSL), the degree of fit (Σ) between the structures of two crystallites is described by the reciprocal of the ratio of coincidence sites to the total number of sites. In this framework, it is possible to draw the lattice for the 2 grains and count the number of atoms that are shared (coincidence sites), and the total number of atoms on the boundary (total number of sites). For example in case of coherent twin boundary (Σ3), there is one atom of

each three that is shared between the two lattices. Low-angle boundaries (Σ1) will have lower interfacial energy than e.g. high-mobility boundaries in fcc materials (Σ7). Deviations from the ideal CSL orientation can be accommodated by local atomic relaxation or by presence of grain boundary dislocations.[36, 39, 40]

At some conditions, in particular depending on the boundary structure, character of interface, temperature, external load as well as solute and vacancy concentrations, the grain boundaries can migrate due to the atomistic processes occurring in the vicinity of the boundaries (climb, glide, diffusion, etc.). Here, it is important to note that the mobility of grain boundaries can be affected by either primary or secondary precipitates which can develop pinning effect and prevent migration.

2.3 Mechanisms of plastic deformation

Deformation mechanisms governing plastic deformation in metals are significantly temperature dependent. In the regime of low temperatures, i.e. $T \leq 0.5T_m$, the most common manifestation of plastic deformation in crystalline solids is conservative movement of dislocations, so-called dislocation slip or glide. In crystals where deformation due to dislocation glide is complicated, also commonly at low temperatures and/or at high strain rates, deformation twinning can be present. At high temperatures facilitated diffusion enables dislocation climb resulting in a non-conservative movement of dislocations out of the glide plane. In this chapter, the role of different deformation mechanisms is briefly summarized.
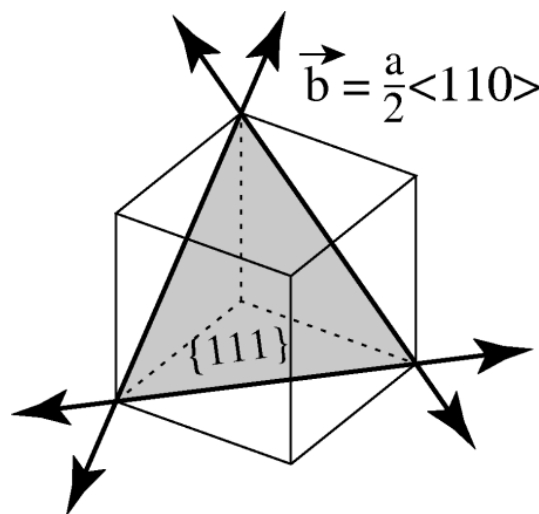
Figure 2.6: Slip systems in face-centered cubic crystal lattice. Slip planes are of {111} type and slip directions of <110> type with corresponding Burgers vectors a/2<110>. *There are four equivalent slip planes each with three possible slip directions forming twelve slip systems in total (image taken with permission from T. Kruml [41]).*

Dislocation slip occurs when the dislocation moves in the surface containing both its dislocation line and Burgers vector. It depends on the direction of the applied load and is strongly related to specific planes and crystallographic directions. First of all, it is restricted to particular planes containing the Burgers vector, i.e. *slip planes*. Commonly these are the planes with the highest density of atoms, i.e. those which are most widely spaced. The *slip direction* is then the direction on the slip plane corresponding to one of the shortest lattice

translation vectors. Often, this direction is one in which the atoms are most closely spaced. Together, slip plane and slip direction forms *slip system*. Some of the slip systems in face-centered cubic crystal lattice are schematically visualised in Fig. 2.6.[36, 39]

Illustration in Fig. 2.7 shows single crystal being deformed in tension by an applied force F along the cylindrical axis. If the cross-sectional area is A_0 the *tensile stress σ* parallel to F can be defined as

$$\sigma = \frac{F}{A_0} \tag{2.12}$$

The force has a component $F \cos \lambda$ in the slip direction, where the λ is the angle between F and the slip direction **b**. This force acts over the slip surface which has an area

$$A = A_0 \cos \phi, \tag{2.13}$$

where ϕ is the angle between F and the normal **n** to the slip plane. Thus the *shear stress τ*, resolved on the slip plane in the slip direction can be defined as

$$\tau = \frac{F}{A_0} \cos \phi \cos \lambda \tag{2.14}$$

If F_c is the tensile force required to start slip of the dislocation, the corresponding value of the shear stress τ_c is called the *critical resolved shear stress (CRSS)* for slip.
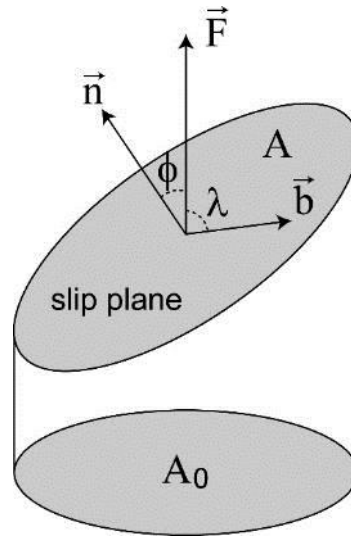
Figure 2.7: Illustration of the geometry of slip in a cylindrical single crystal. (Image taken with permission from T. Kruml [41]).

The quantity $\cos \phi \cos \lambda$ is known as the *Schmid factor m*. According to *Schmid's law*, irreversible plastic deformation takes place only if the shear stress acting within the slip plane and in the slip direction exceeds a critical value, i.e. CRSS τ_c. The directional dependence of the crystal with respect to the applied load is the origin of the plastic anisotropy in single crystal materials.

In face-centered cubic metals the screw dislocations move in {111} type planes. However, they can change their slip plane from one {111} plane to another if it contains the direction of Burgers vector **b** by process known as *cross-slip* as is schematically shown in Fig. 2.8.

The shortest lattice vectors, and therefore the most likely Burgers vectors for dislocations in the face-centered cubic structure, are of type ½<110>. As they are translation vectors for the lattice, glide of a dislocation with this Burgers vector leaves behind a perfect crystal and the dislocation is a *perfect dislocation*. Fig. 2.9a represents a ½<110> edge dislocation in a face-centered cubic metal. The (110) planes perpendicular to **b** have a two-fold stacking sequence αβαβ…as well as the "extra half-plane" which is represented by two (110) half-planes. Besides glide of the perfect dislocations, it is possible that the dislocation movement is split into two *partial dislocations*, if the energy required for the same deformation to occur is lower. Partial dislocations belong to the *imperfect dislocations* which shift the atoms only by a fraction of lattice parameter *a*.[36, 39, 41]
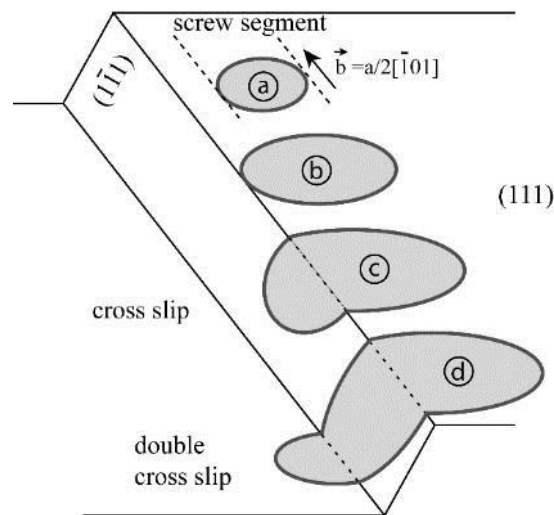
Figure 2.8: Sequence of events (a), (b), (c) in cross slip in a face-centered cubic metal. The [$\bar{1}01$] *direction is common for* (111) *and* (1$\bar{1}$1) *close-packed planes. A screw dislocation is free to glide in either of these planes. Cross slip produces a non-planar slip surface. Double cross slip is shown in (d) (Image taken from T. Kruml* [41] *with permission).*

Most important partial dislocations recognized in face-centered cubic metals are the Shockley partial dislocations associated with slip. The perfect dislocation with Burgers vector $\frac{1}{2}\langle 110 \rangle$ dissociates into two Shockley partial dislocations $\frac{1}{6}\langle 211 \rangle$ and $\frac{1}{6}\langle 12\bar{1} \rangle$. As one part of a crystal slides over another across a {111} plane to form a stacking fault, the energy varies from minima at translations corresponding to perfect stacking to maxima when atoms across the fault are directly over each other. The extra crystal energy per unit area of stacking fault is the *stacking fault energy (SFE)* γ_{SFE}. When a SFE is plotted as a function of fault translation vector a *gamma surface* is obtained.[36, 39, 41]

The stacking fault energy can be determined from the equilibrium distance d_{SFE} between the two partial dislocations, as:

$$\gamma_{SFE} = \frac{Gb^2}{4\pi d_{SFE}}, \qquad (2.15)$$

Where **b** is the Burgers vector of perfect dislocation and *G* is the shear modulus. Since individual Shockley partial dislocations cannot cross-slip, their recombination has to take a place. This is easier in case of materials with high stacking fault energies γ_{SFE} where the separation distance of the Shockley partials d_{SFE} is smaller. As a result, the materials with high stacking fault energies, e.g. aluminium ($\approx$ 140 mJm^{-2}) or copper ($\approx$ 78 mJm^{-2}), exhibit more spatial dislocation arrangements then low stacking fault energy metals and alloys, e.g. silver ($\approx$ 20 mJm^{-2}).[36, 39, 41]
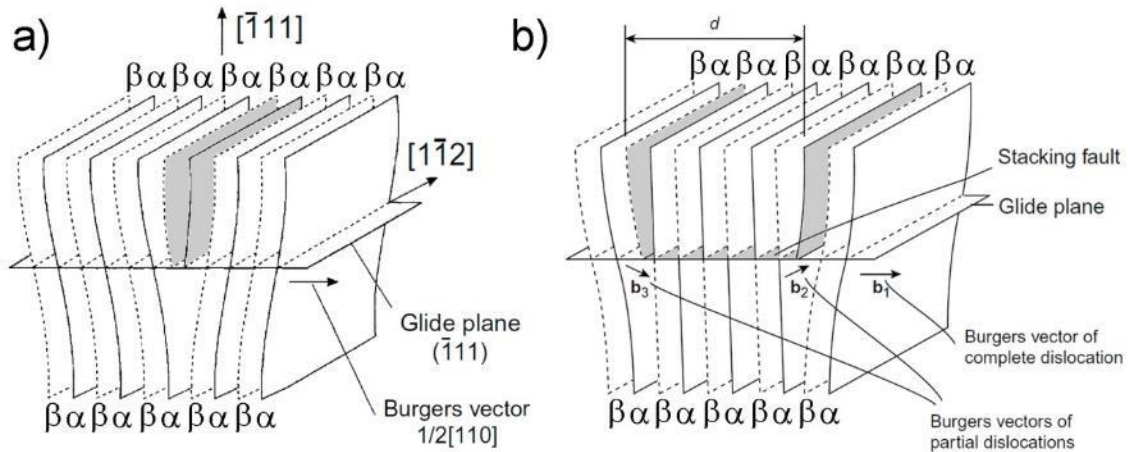
Figure 2.9: (a) Two extra half-planes (highlighted by grey colour) represent unit edge dislocation 1/2[110] *in a face-centered cubic crystal. (b) Formation of an extended dislocation by dissociation of a unit edge dislocation into two Shockley partials of Burgers vectors* **b₂** *and* **b₃** *separated by a stacking fault (after* [36]*).*

Deformation twinning is an important deformation mode in many materials and alloys with a deficiency in independent slip systems. Also, it is common mechanism of plastic deformation at lower temperatures. It is a process in which a region of a crystal undergoes a homogeneous shear that produces the original crystal structure in a new orientation. The twinning is associated with dislocation motion on a coordinated scale, in contrast to dislocation slip, which takes a place independently at several locations in the crystal. Therefore, the shear stress required to initiate twinning is larger than the one needed to activate dislocation slip.

In Fig. 2.10, the example of the deformation twin in the face-centered cubic crystal is shown. It was formed by coordinated movement of Shockley partial dislocations $\frac{1}{6}[1\bar{1}2]$ Generally, the presence of twinning as a deformation mode is significantly dependent on type of the crystal structure, the temperature, strain rate, applied stress level as well as grain size and precipitates presence.

At high temperatures ($T \geq 0.5T_m$) the diffusion processes become more important as the atoms can be relocated through the crystal lattice. This leads to the diffusion controlled mechanism where edge dislocations can move out of their slip plane by *dislocation climb*. When atoms diffuse away from or to the dislocation core, it is possible for edge dislocations to propagate perpendicular to their slip plane. Compressive stresses increase the possibility of an atom of the dislocation core to diffuse to a vacancy in the lattice and tensile stresses enhance the diffusion from the lattice into the dislocation core (as shown in Fig. 2.11a where dislocation is in the tensile stress field along *x* direction). The dislocation which moves by climb has

characteristic zig-zag step-like features of the dislocation line perpendicular to the slip plane called *jogs*. If the step-like feature is formed so it lies in the slip plane, it is called *kink* as shown in illustration in Fig. 2.11b. As climb requires thermal activation, it is non-conservative except for the case where conservative *pipe diffusion* of atoms along the dislocation core is active.[36, 39]
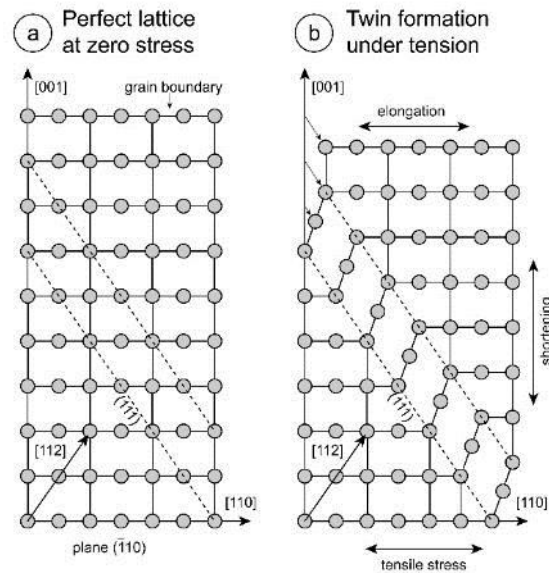
Figure 2.10: *Deformation twinning in face-centered cubic crystal lattice. Image plane is* $(\bar{1}10)$*. Twinning plane* (111) *is observed edge-on. The twinning direction is* $\frac{1}{6}[1\bar{1}2]$*, i.e. the same as the Burgers vector of Shockley partial dislocations. Twinning plane presents special type of grain boundary marked as* Σ3*. (Taken from* [43]*).*
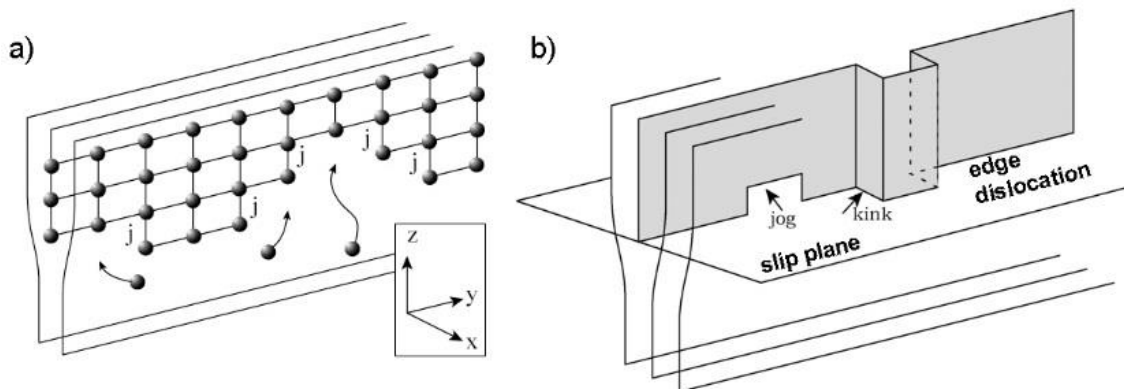
Figure 2.11: (a) Edge dislocation located in tensile stress field along x-direction. Atoms diffuse from the lattice to the dislocation core causing edge dislocation to climb in negative z-direction. Jogs are marked with letter "j". (b) Schematic visualisation of jogs and kinks (image taken from T. Kruml [41] *with permission).*

34

3. Strength of crystalline solids

The resistance of a material against the plastic deformation is closely linked to the mobility of dislocations and their interactions with obstacles they encounter on their path. There are different types of obstacles and factors on different length-scales that strongly affect the strength of the material, including crystal structure and the chemical composition itself, dislocation arrangements and subgrains, grain boundaries and grain sizes in general, the presence of secondary phases and precipitates and also additional alloying by substitutional or interstitial atoms. [36, 39, 44]

Apart from the effects associated with the diffusion at high temperature, plastic deformation occurs by the glide of dislocation and hence the *critical shear stress* for the onset of plastic deformation is the stress required to move dislocations. Therefore, as soon as an external load locally reaches the critically resolved shear stress the plastic deformation takes a place. The level of stress required to maintain plastic flow is called *flow stress* and has to be the same or higher than the critical resolved shear stress. The dislocation glide is normally self-sustaining, i.e. dislocations multiply in a way that the imposed deformation can be accommodated. When there are sufficient mobile dislocations, the local flow stress is controlled by the dislocation propagation through the crystal with all its obstacles.[36, 39, 44]

In the following overview, the different obstacles influencing the propagation of dislocations through the crystal and therefore affecting the macroscopic strength of the material are summarized.

3.1 Flow stress and the theory of thermal activation

Generally, the motion of a dislocation is opposed by short-range barriers, which can be overcome by thermal activation, and long-range forces proportional to the shear modulus G and producing barriers too large for thermal activation to be significant.

If dislocation is gliding in the x-direction under an applied resolved shear stress τ^*, which produces a force $\tau^* b$ per unit length on the line, the obstacles to slip of this dislocation will produce resisting force K, as is shown in Fig. 3.1. Spacing of the obstacles along the line will be l, so the applied forward force on the line per obstacle will be $\tau^* bl$. At the temperature 0 K, the slip will stop at position x_1 if $\tau^* bl$ is less than K_{max}. To overcome the barrier, the line must move to x_2. The isothermal energy change required is the area under the K versus x curve between x_1 and x_2. It can be written as

$$\Delta F^* = \int_{x_1}^{x_2} K dx, \tag{3.1}$$

where ΔF^* stands for the *Helmholtz free energy change*. Part of this energy can be provided in the form of *mechanical work* done by the applied load and is $\tau^* bl(x_2 - x_1)$. This can be rewritten as $\tau^* V^*$, where V^* is known as the *activation volume* for the process. Then, the remainder required energy can be written as

$$\Delta G^* = \Delta F^* - \tau^* V^*. \tag{3.2}$$

The term ΔG^* states for the *free energy of activation*. It is the Gibbs free energy change between the two states x_1 and x_2 at the same temperature and applied stress and it presents the *thermal component*. The probability of energy ΔG^* occurring by thermal fluctuations at temperature T is given by the Boltzmann factor

$$\exp\left(\frac{-\Delta G^*}{kT}\right).$$ (3.3)

If the dislocation is effectively vibrating at a frequency ν, it successfully overcomes barriers at a rate of $\nu \exp\left(\frac{-\Delta G^*}{kT}\right)$.[36]
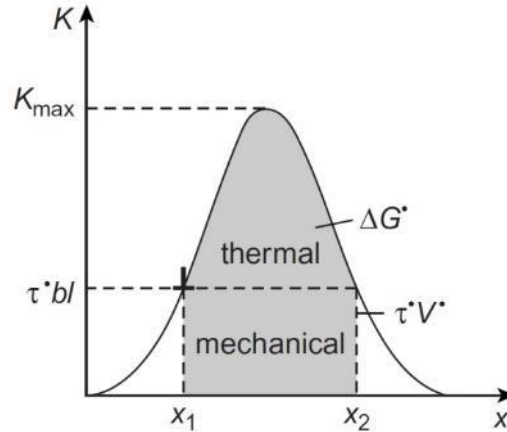
Figure 3.1: Profile of resistance force K plotted as a function of distance x for barrier opposing dislocation motion (image taken from [36]).

The flow stress consists of two contributions. The *thermal component*, also called as *effective stress*, is the driving force for plastic flow. It includes the resistance of dislocation motion against short-range obstacles that can be overcome by additional thermal activation, in particular the probabilistic overcoming of barriers due to thermal vibrations of dislocations as was described above. An increase in temperature or a decrease in applied strain rate provides an increase in the probability of thermal activation and therefore results in a reduction in total flow stress. Obstacles leading to thermal stress are the Peierls-Nabarro stress, solute atoms, repulsive and (conditionally) attractive dislocation trees in a dislocation forest and fine coherent precipitates.

The *athermal component* includes the internal stress and is interpreted as the resistance to dislocation motion due to elastic long-range interactions. Since the barriers are too large for thermal activation to be significant, it is almost independent on the temperature apart from the small variation of the shear elastic modulus. Obstacles of athermal character are mainly long-range internal stress fields caused by complex dislocation arrangements and large semi-coherent or incoherent precipitates and secondary phases.

It is important to note, that during deformation of crystalline materials, dislocation substructures develop that can be characterized by a heterogeneous arrangement of dislocations in the matrix. Formation of dislocation multi-pole configurations as walls, cells or subgrains leads to long-range internal elastic stress fields. These then interfere with the stress fields of the mobile dislocations and thereby cause an anisotropic increase of the flow stress, i.e. *backstress*. Interacting with dislocation substructures, moving dislocations can

experience both short-range (thermal component) and long-range interactions (athermal component).[36, 39, 45–48]

3.2 Peierls-Nabarro stress (lattice friction)

The applied resolved shear stress required to make a dislocation glide in an otherwise perfect crystal without the assistance of thermal activation, i.e. at $T = 0$ K, is called the *Peierls-Nabarro stress*. The Peierls-Nabarro stress arises as a direct consequence of the periodic structure of the crystal lattice and depends significantly on the form of the force-distance relation between individual atoms, i.e. on the nature of the interatomic bonding. Sometimes, it is called as the basic lattice resistance or the *lattice friction* stress. The term lattice friction is used not only at 0 K, but generally at any testing temperature.[36, 39]

Periodic potential is associated with the periodic arrangement of atoms in the lattice. Dislocations then tend to lie along the close-packed directions of a slip plane where the potential energy of the lattice is minimal (see schematic in Figure 3.2). To move the dislocation from one equilibrium position to another, the extra energy has to be provided in the form of an applied stress to overcome the potential barrier.[39, 41]
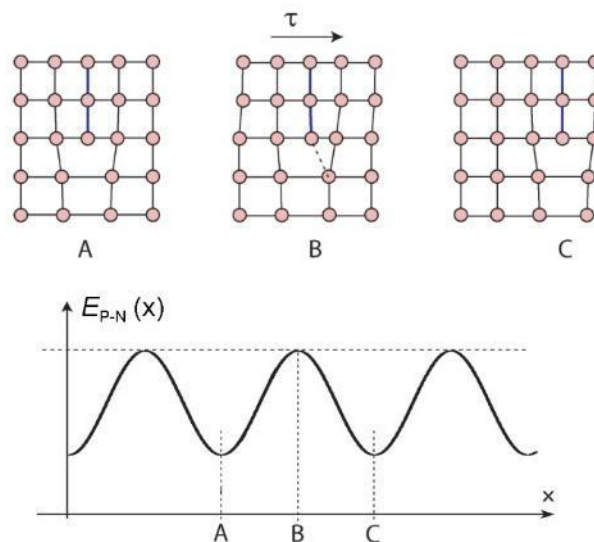
Figure 3.2: Glide of dislocation without presence of obstacles. In A, dislocation is in equilibrium position in so-called Peierls valley. To move to another equilibrium position B, the extra energy has to be added so the Peierls-Nabarro potential energy E_{P-N} can be overcome (image taken from [41]*).*

Since the Peierls-Nabarro stress strongly depends on the type of interatomic bonding, it is the highest in covalent crystals, intermediate in ionic crystals, low in body-centered cubic crystals and negligible in face-centered cubic crystals.

At temperatures above 0 K, the thermal fluctuations enhance the overcoming of the periodic crystal potential by reducing the Peierls-Nabarro stress, so it is considered as the thermal flow stress component.

3.3 Solid solution strengthening

The interaction of dislocations with point defects such as vacancies, interstitials and substitutional atoms is the basis of *solid solution strengthening*. Point defects cause a very local distortion of the crystal lattice (see schematic in Fig. 3.3) which then interacts with the stress-field of dislocations. This interaction can be attractive or repulsive, depending on the misfit of the point defect and the matrix and also on the relative position of the point defect to the slip plane of the interacting dislocation. Generally, oversized defects are repulsive if they are above the slip plane of dislocation, i.e. interacting with the compressive strain field, and attractive if they are below, i.e. interacting with the tensile stress field of dislocation. The reverse is true for undersized defects. [39]
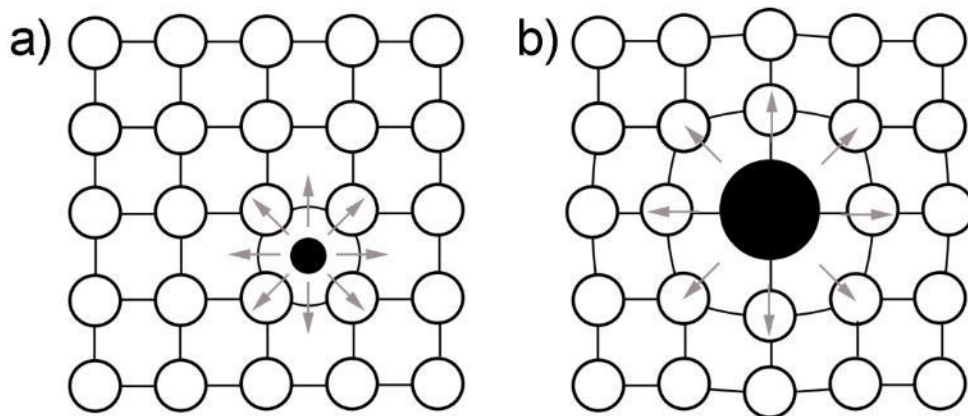
Figure 3.3: Schematic image of (a) interstitial and (b) substitutional solute atoms causing local distortion of the crystal lattice accompanied by elastic stress fields.

At elevated temperature, the point defects can be sufficiently mobile to diffuse through the lattice as they are attracted by dislocations. Then, within the dislocation core itself, the arrival of defects can have several effects. Vacancies and interstitial atoms can cause dislocation climb. In alloys, solute atoms may segregate and form a dense solid *solution atmospheres*. Commonly in face-centered cubic solid solution based alloys, carbon and nitrogen as fast interstitial elements form so-called *Cottrell atmospheres* (see schematic in Fig. 3.4). If a perfect dislocation dissociates into partial dislocations, the stacking fault formed changes locally the crystal structure. As a result, the solute solubility in the fault region may be different from that in the surrounding matrix. Consequent change in chemical potential will then cause solute atoms to diffuse to the fault leading to the formation of *Suzuki atmosphere*. This chemical effect may then present a barrier to the dissociated dislocations mobility. On the other hand, if solutes are present locally in high concentrations, they may interact to form precipitates along the dislocation cores thereby pinning the dislocation. Both effects then can eliminate the long-range stress field of the dislocation so the solute flow is terminated.

The importance of solute segregation in or near the dislocation core is that an extra stress (or thermal activation) is required to overcome the attractive dislocation-defect interactions and move the dislocation away from the concentrated solute region. In such a case, the dislocation is *locked* by the solutes. A high external stress is needed to remobilise the pinned dislocation but once it is freed, the mobile dislocation is not affected anymore. Subsequent heat treatment,

however, allows the solutes to diffuse back to dislocations again what can re-establish the locking effect. This is the basis of *strain aging*. [36, 39, 49]
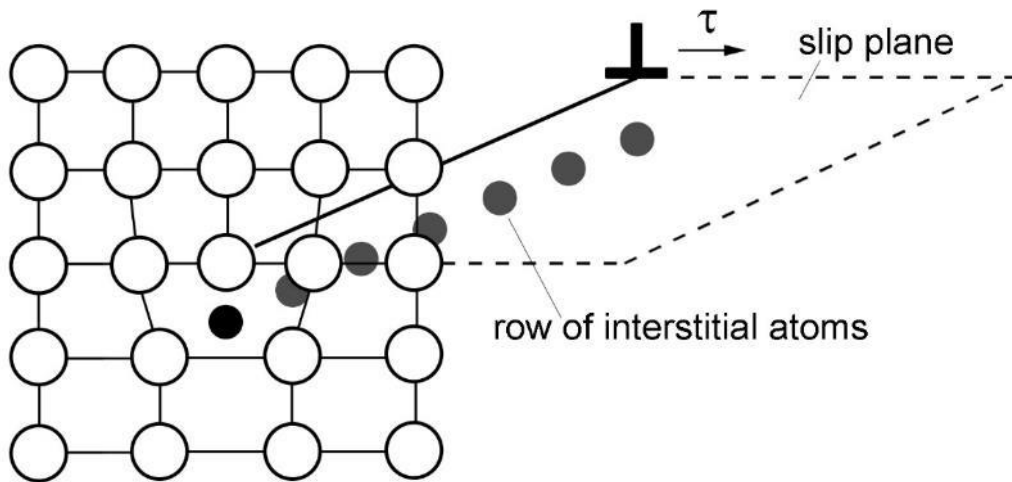
Figure 3.4: Schematic image of Cottrell atmosphere. Row of interstitial solute atoms (black) is located in the core of edge dislocation in cubic crystal lattice. A sufficiently high applied shear stress will cause the dislocation to separate from the solute atoms by gliding on the slip plane.

Here, it is worthy of note that especially in case of cyclic loading, when the deformation temperatures are high and the strain rates are low enough, the enhanced point defect mobility may enable repeated pinning and unpinning of dislocations by the solutes during dislocation motion. This produces a repeated yielding process known as *dynamic strain aging* (*or Portevin-Le Chatelier effect*), characterized by a serrated stress-strain curve.[36, 39]

3.4 Precipitation strengthening

Complex structural materials usually contain one or more alloying elements that are dissolved in a base matrix. There is a maximum concentration, i.e. the *solubility limit*, to which the atoms of alloying element can be dissolved in solution in their parent crystal. For concentration of solute above the solubility limit, the excess atoms of alloying element tend to precipitate and form secondary phases in the matrix. Some elements such as interstitial N or C and substitutional Nb, W, Mn act as solid solution strengtheners when present at low concentrations, but at high concentrations they tend to form precipitates. The solubility limit varies with *temperature*. At elevated temperatures, the dissolved alloying elements are relatively mobile, they diffuse within the matrix possibly segregating and forming clusters and nucleation cores. On the other hand, if the solution-treated alloy is rapidly cooled (e.g. quenched) to room temperature, insufficient time is allowed for precipitation and a *super-saturated solid solution* is obtained. Subsequent increase of temperature then can lead to the secondary phase precipitation as sufficient thermal energy is available to overcome the nucleation barrier. In most cases, precipitates start to nucleate in fine homogeneous dispersion. As the aging time increases, some particles coarsen and become larger at the expense of others, which can even dissolve. The spacing between the precipitates decreases

with their decreasing number. Eventually, after very long times, the equilibrium structure is established.

The structure of the *interface* between two phases, i.e. the nucleating precipitate and the parent matrix, governs the kinetics of the secondary phase formation and growth. Moreover, the character of the interface and the structural and crystallographic *orientation relationship* of two phases determine the mechanisms at which the dislocations will be interacting with nucleated precipitates and therefore the resistance to their motion.

In most cases, at the onset of precipitates nucleation, first structural features are small and *coherent*. Coherent precipitates usually have none or very small lattice misfit with the parent crystal. Lattice parameters *misfit δ* is defined as

$$\delta = \frac{a_\beta - a_\alpha}{a_\alpha} \tag{3.4}$$

where a_α and a_β are lattice parameters of crystal structures α and β, respectively (see schematics in Figs. 3.5 and 3.6). Two mutually coherent phases can be oriented as cube-on-cube or can have different orientation if the interatomic distances along the direction parallel with the interface are the same (see Fig. 3.5). The orientation relationship can be specified in terms of a pair of parallel planes and directions, i.e., {*hkl*}$_\alpha$//{*hkl*}$_\beta$ and <*uvw*>$_\alpha$//<*uvw*>$_\beta$. In case of coherent interfaces, the lattice misfit is accommodated just by the lattice distortion so coherency elastic strain fields are usually present at these interfaces. It is important to note that while the structure of coherent interface can be perfect, there still will be an interfacial energy due to the bonding between atoms from different phases, i.e. *chemical contribution*. According to Howe [50], such an interface can have energy $\gamma_{chem} \approx 1 - 200$ mJm^{-2}.
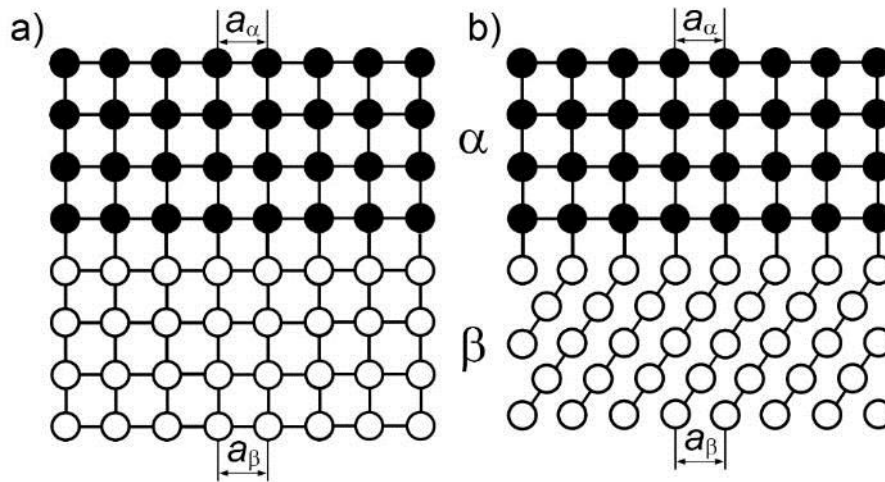
Figure 3.5: Example of strain-free fully coherent interfaces. (a) Each crystal has a different chemical composition but the same crystal structure. (b) The two phases have different lattices. Coherent interfaces are possible e.g. between FCC and HCP lattices if the interatomic distances along close packed directions are the same.
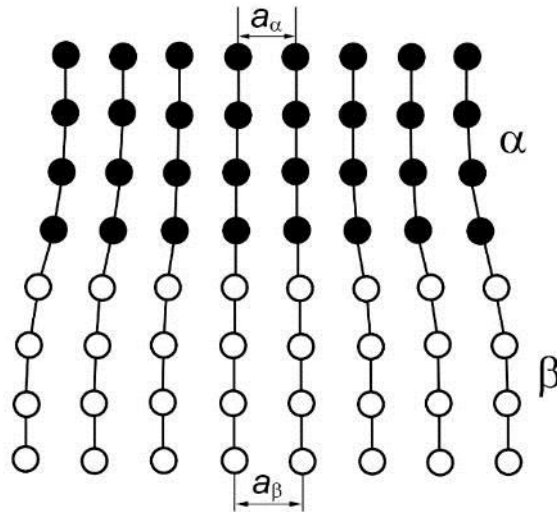
Figure 3.6: A coherent interface with slight mismatch leads to coherency strains in the adjoining lattices.

If the lattice misfit is too large, the elastic energy associated with the coherency strains can be relieved by the introduction of a periodic array of dislocations at the interface, so-called *misfit dislocations*. Such an interface is then called as the *semi-coherent*. The misfit dislocations have spacing D which is determined by lattice misfit as follows [36, 50]:

$$D = \frac{a_\beta + a_\alpha}{2\delta} \tag{3.5}$$

The secondary phases and precipitates which have semi-coherent interface do not necessarily have to share cube-on-cube relationship and coherent interface on all facets with the matrix.
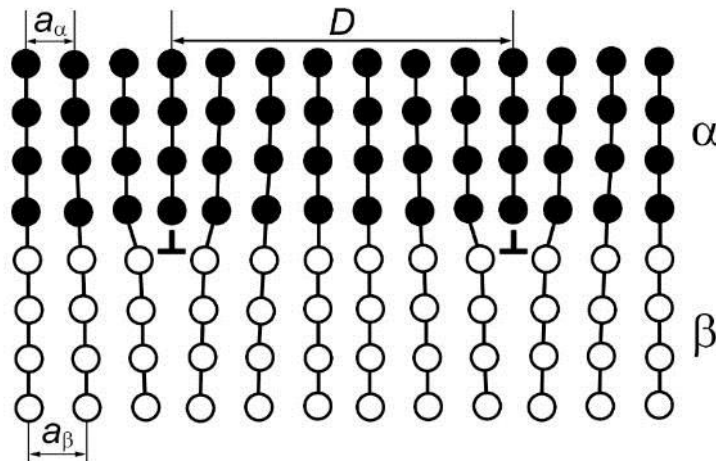
Figure 3.7: A semi-coherent interface. The misfit parallel to the interface is accommodated by a periodic array of misfit edge dislocations. Spacing between misfit dislocations is marked as D.

Energies of semi-coherent interfaces have both chemical and structural contributions. Structural part can be estimated by dividing the energy per unit length of the dislocation by the dislocation spacing. Therefore:

$$\gamma_{structural} \approx \frac{Gb\delta}{2} \qquad (3.6)$$

According to Howe the energy of the semi-coherent interface can vary around $\gamma_{semicoh} = \gamma_{structural} + \gamma_{chemical} \approx 200 - 800$ mJm^{-2}. For large spacing D, the structural contribution of the interfacial energy would be proportional to the density of misfit dislocations. However as D decreases, the energy follows a logarithmic dependence and saturates. The limit to dislocation-based structures is then approximately at $\delta \sim 0.25$ where D will be close to $4b$ and cores of misfit dislocations will start to overlap [50].

In case of large lattice misfits, coherency can be completely lost. Precipitates are usually oriented randomly and lattice columns of matrix and secondary phase do not fit each other to form the *incoherent* interface (see schematic in Fig. 3.8) with disordered structure, similar to random large-angle grain boundaries. Incoherent interfaces have large interfacial energy significantly dominated by the structural contribution $\gamma_{incoh} \approx 800 - 2500$ mJm^{-2} [50]. Usually, fully incoherent are large coarsened precipitates after long aging times. However, there can be also some special cases. As reported by Rösler and Arzt [2, 3], nanometer-sized particles of incoherent nature can exist in the case of oxide-dispersion-strengthened alloys.
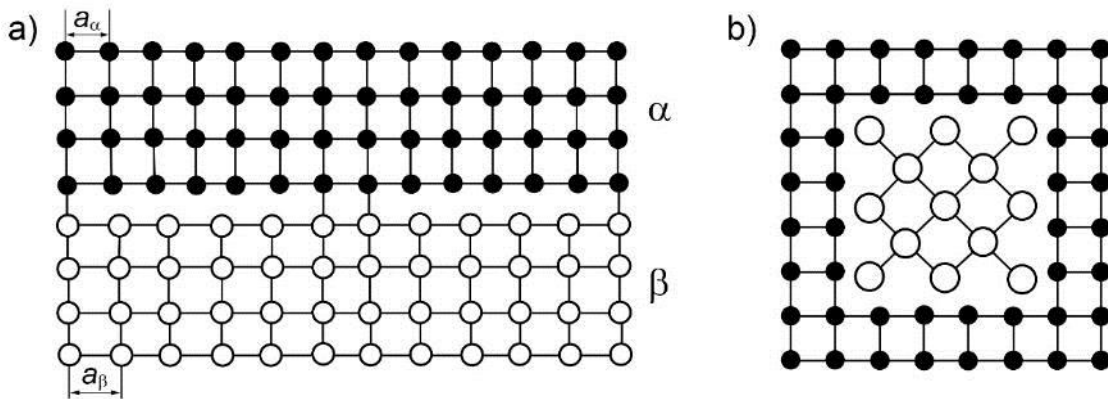
Figure 3.8: An incoherent interface. (a) Two crystal lattices are oriented as cube-on-cube but lattice misfit is so large that misfit dislocations cannot accommodate it. Arrays of several atomic columns of two phases which do not fit together are separated by planes fitting perfectly. (b) Schematic example of case observed more commonly. Two phases have incoherent interface and are oriented randomly.

The behaviour of a dislocation under applied stress is different in case of the interaction with dispersion of small coherent particles, larger semi-coherent precipitates or coarse distribution of large incoherent phases. Some of the key mechanisms determining the interaction of dislocation with precipitates are summarized below. The text is based on detailed overview presented by D.J. Lloyd [51].

When precipitates nucleate and grow, they intersect slip planes in random fashion. A gliding non-screw dislocation without diffusion must either *cut through the precipitates* or penetrate the array by *bowing between the obstacles*. It will adopt the mechanism offering the *lowest*

resistance. The stress corresponding to this short-range mechanism must be compared with that required to overcome the internal stress τ_i produced by coherent precipitates in the surrounding lattice.

When a gliding dislocation encounters an array of obstacles it bows out between them, as shown in Fig. 3.9.
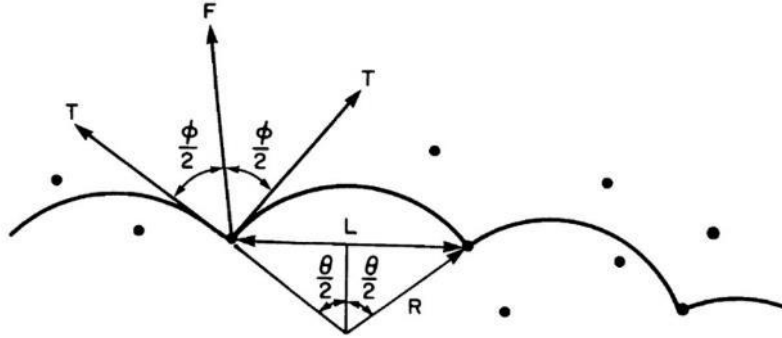
Figure 3.9: Schematic visualisation of a dislocation on a slip plane in which each obstacle exerts a localized glide resistance force F, balanced in equilibrium by line tension forces T. Taken from D.J. Lloyd [51].

At some curvature, when the included angle ϕ between adjacent arms of the dislocation reaches a critical value the obstacle is overcome and the dislocation moves forward. The obstacle strength F can be expressed in terms of the breakaway angle ϕ_c, since the force balance in Fig. 3.9 gives

$$F = 2T\cos\left(\frac{\phi_c}{2}\right) \tag{3.7}$$

where T is the dislocation line tension. Clearly the maximum strength obstacle will have for a $\phi_c = 0$, where the particle behaves as an impenetrable obstacle. On the other hand for $\phi_c > 0$, the particle can be sheared under the shearing force F. It is important to note that in reality the obstacles on the glide plane will have a spectrum of strengths.

The applied shear stress τ causes the dislocation of Burgers vector b to bow into a loop of radius of curvature R, where

$$\tau b = \frac{T}{R} \tag{3.8}$$

This assumes that the line tension is independent of the dislocation character.

Based on the geometry in Fig. 3.9, it can be stated that

$$2R\sin\left(\frac{\theta}{2}\right) = L \tag{3.9}$$

so that

$$\tau b = \frac{2T\sin\left(\frac{\theta}{2}\right)}{L} \tag{3.10}$$

Since $\frac{\theta}{2} = \left(90 - \frac{\phi}{2}\right)$, by combining equations (3.7) and (3.10) we get

$$\tau = \frac{2T\cos\left(\frac{\phi}{2}\right)}{bL} = \frac{F}{bL} \tag{3.11}$$

To predict the overall strengthening effect of the precipitates the expressions for F for the different strengthening mechanisms have to be developed and correct obstacle spacing L has to be chosen.

In random arrays of weak obstacles a dislocation advances by breaking from a few widely-spaced obstacles before unpinning along the entire length. It retains a roughly straight shape. The effective obstacle spacing L_F along an almost straight line is given by the *Friedel relation*. In steady state at the flow stress, when a dislocation unpins from one obstacle it moves forward to encounter one other (see schematic in Fig. 3.10). The area swept in so doing is therefore the area of glide plane per obstacle A, where $\sqrt{A} = L_s$ is the average spacing of obstacles in the plane. If there are N_s obstacles per unit area in the glide plane, according to Friedel [52] following equation can be written as

$$AN_s = 1 \tag{3.12}$$
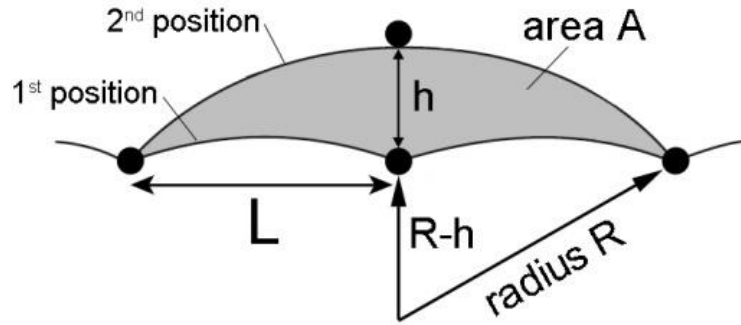
Figure 3.10: Dislocation unpinning from one obstacle (1ˢᵗ position) moves forward and encounters other obstacle (2ⁿᵈ position). During that motion the area of glide plane per obstacle A is swept.

For a regular square array of obstacles, the average spacing L_s between them is defined as

$$L_s = \frac{1}{\sqrt{N_s}} \tag{3.13}$$

And hence

$$A = L_s^{\,2} \tag{3.14}$$

From the geometry in Fig. 3.10,

$$A \approx hL \approx L_s^{\,2} \tag{3.15}$$

And

$$R^2 = L^2 + (R - h)^2 \tag{3.16}$$

Which for $h << R$ becomes

$$L^2 = 2hR \tag{3.17}$$

Substituting for h from equation (3.15) and for R from equation (3.9), the *effective* or *Friedel obstacle spacing* L_F is stated as

$$L = L_F = \frac{L_S}{\sqrt{\cos\left(\frac{\phi}{2}\right)}} \tag{3.18}$$

Therefore the effective obstacle spacing is a function of square lattice spacing and the obstacle strength. The stronger the obstacle the smaller is the effective obstacle spacing.

Substituting into equation (3.11) we obtain

$$\tau = \frac{2T\left[\cos\left(\frac{\phi}{2}\right)\right]^{3/2}}{bL_S} \tag{3.19}$$

It is important to note that equation (3.19) was derived assuming an essentially straight dislocation, i.e. *weak* obstacles ($\phi \geqq 140$ degrees), and a square array of obstacles. In case of *strong* obstacles ($\phi \rightarrow 0$) when Orowan looping occurs rather than particle shearing, equation (3.19) is invalid. For strong obstacles with $\phi < 100$ degrees Brown and Ham [53] have suggested the expression

$$\tau = \frac{0.84}{bL_S} 2T \left[\cos\left(\frac{\phi}{2}\right)\right]^{3/2} \tag{3.20}$$

Line tension forces T can be related to the value for the dislocation line tension. If a constant line tension is assumed, ignoring dislocation character, according to Friedel [52] following equation can be written

$$T = \frac{Gb^2}{2} \tag{3.21}$$

There are different mechanisms which can determine the strength of the obstacle. In many alloy systems two or more of these mechanisms may operate simultaneously but often one will dominate.

(I) *Coherency strengthening* is as a result of the elastic coherency stresses surrounding a precipitate. Due to the misfit of lattice parameters of matrix and precipitate elastic strain field is introduced in the matrix around a particle.

In general, the models describing coherency strengthening consider the case of an infinite straight edge dislocation interacting elastically with a spherical coherent precipitate of radius r and misfit parameter ε, given by

$$\varepsilon = \frac{1}{3}\frac{(1+v)}{(1-v)}\frac{\Delta a}{a} \approx \frac{2}{3}\delta \tag{3.22}$$

where δ is the fractional difference in lattice parameter between the particle and the matrix.

According to Brown and Ham [22, 53] the misfit parameter ε can be given also by using Young modulus of elasticity E of matrix and bulk modulus of precipitate B:

$$\varepsilon = \frac{3B}{3B + \frac{2E}{(1+v)}} \delta \tag{3.23}$$

Using isotropic elasticity theory Gerold and Haberkorn [54] found the interaction force between a straight edge dislocation and the precipitate to be

$$F_{\mathrm{M}} = \left(\frac{3}{2}\right)^{3/2} \frac{Gb|\varepsilon|r^3}{z^2} \text{ for } \frac{z^2}{r^2} > \frac{3}{4}$$

And   (3.24)

$$F_{\mathrm{M}} = 8Gb|\varepsilon|z \left(1 - \frac{z^2}{r^2}\right)^{1/2} \text{ for } \frac{z^2}{r^2} < \frac{3}{4}$$

where z is the distance of the glide plane from the central plane of the precipitate. The problem of this approach is to find an appropriate average value of F_{M} to substitute into equation (3.7) since the glide dislocation interacts with the strain fields of both precipitates that intersect the glide plane and those that are some distance away. However, all models result into an expression for small precipitates, interaction with straight dislocation and small breaking angle ϕ, as follows [51]:

$$\tau_{\mathrm{CS}} = k(\varepsilon G)^{3/2} \left(\frac{rfb}{T}\right)^{1/2} \tag{3.25}$$

where k is a numerical factor dependent on the averaging procedure chosen. In the Gerold and Haberkorn theory $k = 3$ for edge dislocations and $k = 1$ for screw dislocations. In the Gleiter theory $k = 11.8$. Here, it is important to note that the expression is very approximate, partially due to the fact that it considers only straight edge dislocations and also because of averaging procedure leading to appropriate k value. Parameter f is the *volume fraction of the particles* which can be defined as the volume fraction of N_s spheres in unit volume of $2r$ m^3:

$$f = \frac{\frac{4}{3}\pi r^3 N_s}{2r} = \frac{2\pi r^2 N_s}{3} \tag{3.26}$$

(II) *Chemical strengthening* is coming from the atomic bond switching when a dislocation shears a precipitate. In other words, it arises from the energy required to create an additional particle/matrix interface of specific energy γ_S when the particle is sheared by glide dislocation. The maximum force on the dislocation due to the new interface is $F = 2\gamma_S b$. Substituting into equations (3.7), (3.19) and using the square lattice spacing L_s, following equation is obtained:

$$\tau_{\mathrm{CHS}} = \left(\frac{6\gamma_S{}^3 bf}{\pi T}\right)^{1/2} \frac{1}{r} \tag{3.27}$$

(III) *Stacking fault strengthening* is due to the difference in stacking fault energies in the precipitate and the matrix. As a result, the separation of the partial dislocations will also be different when the dislocations move from the matrix into the particle. The maximum force experienced by the split dislocation is given by

$$F_{\mathrm{M}} = \Delta\sigma r_S B \tag{3.28}$$

where $\Delta\sigma$ is the difference in stacking-fault energies, B is a function of $\Delta\sigma$, the line tension T and r_S, the planar particle radius. If r_S is smaller than the partial dislocation separation in the matrix, the equation for stacking-fault strengthening can be written as

$$\tau_{SF} = \Delta\sigma^{3/2}\left(\frac{3\pi^2 fr}{32Tb^2}\right)^{1/2} \tag{3.29}$$

For large particles the stacking fault strengthening decreases with increasing particle size.

(IV) *Modulus strengthening* arises from differences between the elastic moduli of the precipitate and the matrix. The energy of a dislocation is a function of the shear modulus of the lattice within which it resides. As a dislocation moves from the matrix into a particle of different shear modulus there is a change in dislocation energy and hence an interaction force between the dislocation and the particle. Majority of the models describing modulus strengthening involve the difference in shear modulus, ΔG, between the matrix and the particle. Unfortunately, the shear moduli of most of the precipitate particles are unknown.

In one of the more recent approaches, Russel and Brown model the situation where the dislocation energy changes abruptly at the particle-matrix interface. By considering the local dislocation equilibrium at the point of breakaway they show that, for attractive obstacles (i.e. $G_P < G_M$), the equivalent expressions to equations (3.19) and (3.20) are

$$\tau_M = \frac{2T}{bL_S}\left(1 - \frac{E_1^2}{E_2^2}\right)^{3/4} \tag{3.30}$$

$$\tau_M = \frac{2T}{bL_S}\left(1 - \frac{E_1^2}{E_2^2}\right)^{1/2} \tag{3.31}$$

where E_1 is the dislocation line energy in the particle and E_2 is the line energy in the matrix.

(V) *Atomic-order strengthening* is caused by the increase in energy associated with a dislocation that shears through an ordered coherent precipitate creating an antiphase boundary (APB). When APB is formed, it has an energy σ_{APB} per unit area. This energy is then the force opposing dislocation motion. The maximum interaction force for a single dislocation shearing an ordered particle is

$$F_M = 2\sigma_{APB}r_S \tag{3.32}$$

which when substituted into equations (3.7) and (3.19) gives

$$\tau_0 = \frac{\sigma_{APB}}{b}\left(\frac{4\sigma_{APB}fr}{\pi T}\right)^{1/2} \tag{3.33}$$

This equation however would be relevant only in case if the dislocations travelled singly through the lattice. Since they travel in pairs where the second dislocation usually removes the disorder, the equation has to be modified. Brown and Ham have considered the situation where the leading dislocation is bowed out to the critical configuration and the trailing dislocation is essentially straight. The net result is an increase in stress on the leading dislocation. Two expressions for order strengthening are then obtained as follows:

$$\tau_0 = \frac{\sigma_{\text{APB}}}{2b}\left[\left(\frac{4\sigma_{\text{APB}}fr}{\pi T}\right)^{1/2} - f\right] \text{ for } r < \frac{T}{\sigma_{\text{APB}}} \tag{3.34}$$

$$\tau_0 = \frac{\sigma_{\text{APB}}}{2b}\left[\left(\frac{4f}{\pi}\right)^{1/2} - f\right] \text{ for } r > \frac{T}{\sigma_{\text{APB}}} \tag{3.35}$$

(VI) *Orowan strengthening*, arises from the resistance exerted by impenetrable obstacles on glide dislocations (see schematic in Fig. 3.11). When particles cannot be sheared, $\phi = 0$ and the obstacle strength equation (3.7) becomes

$$F = 2T \tag{3.36}$$

By substituting into equation (3.11) and using the simple dislocation line tension equation (3.21) we obtain

$$\tau_{Orowan} = \frac{2T}{bL} = \frac{Gb}{L} \tag{3.37}$$

which is the basis of the Orowan equation. For an accurate assessment the line tension and obstacle spacing has to be considered in detail. Taking in account the interaction between the two arms of the bowing dislocation on opposite sides of the particle, the effective line tension of the dislocation has to be taken as

$$T = \frac{Gb^2}{4\pi}\left(\frac{1+\nu-3\nu\sin^2\xi}{1-\nu}\right)\ln\left(\frac{2r}{r_0}\right) \tag{3.38}$$

where ν is Poisson´s ratio, r_0 is the inner cut-off radius $\approx b$. For a pure edge segment $\xi = \pi/2$, while for a pure screw segment $\xi = 0$.

The line tension of a dislocation is different for edge and screw segment. However, the Orowan stress is independent of the nature of the dislocation because the curvature of a screw dislocation will be less than that of an edge resulting in larger average obstacle spacing for the screw segment. The difference in obstacle spacing will compensate for the difference in dislocation line tension. The appropriate line tension will then be the geometric mean for edge and screw components. Taking account of these factors the final expression for the Orowan stress is

$$\tau_{Orowan} = \frac{0.84Gb}{2\pi(1-\nu)^{1/2}L}\ln\left(\frac{2r}{r_0}\right) \tag{3.39}$$

Since impenetrable obstacles are usually relatively large their size cannot be ignored. As a result, L should be considered as the clear interparticle spacing based on the equation:

$$L_S = N_S^{-1/2} - 2r_S \tag{3.40}$$

Where r_s is *the average planar particle radius* related to *the average particle radius r*, and *the volume fraction of particles f* by following equations [51]:

$$f = \frac{\pi r_S^2}{L_S^2} \tag{3.41}$$

$$r_S = \frac{\pi r}{4} \tag{3.42}$$

That is

$$L_S = \left(\frac{2\pi}{3f}\right)^{1/2} r \qquad\qquad (3.43)$$

In Fig. 3.12, increase of flow stress as a result of coherency strengthening (Eq. 3.25) and Orowan looping (Eq. 3.39) is plotted versus precipitate radius. It is shown that the precipitation hardening mechanism generally depends on the size of the precipitate particles. At small r, cutting will dominate, while at large r, bowing will prevail. The plot of both equations shows that there is a critical radius at which max strengthening occurs. With further coarsening of particles, strengthening effect diminishes.
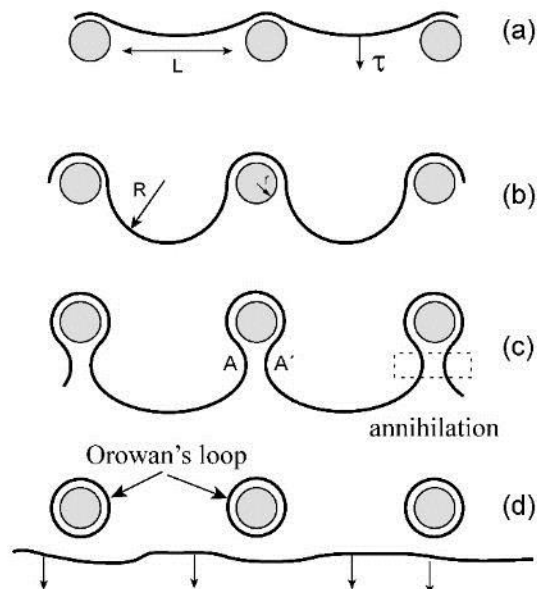
Figure 3.11: Schematic visualisation of the Orowan mechanism. (a) Edge dislocation encounters array of particles of diameter r. (b)(c) The line bows between the obstacles until the segments at A and A′ are parallel ($\phi = 0$). They then attract and annihilate. (d) The line moves forward leaving Orowan loops around the obstacles. Taken from T. Kruml [41].
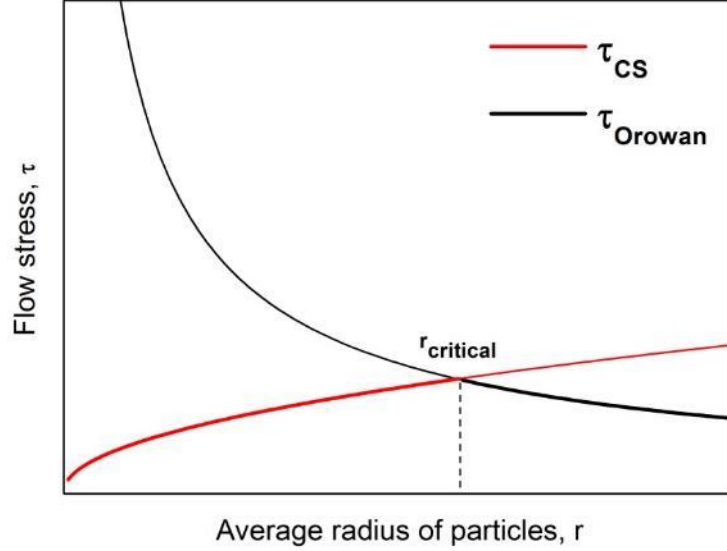
Figure 3.12: Increase of flow stress as a result of coherency (Eq. 3.25) and Orowan strengthening (Eq. 3.39) mechanisms. In general, the strengthening mechanism depends on the size of the precipitates. Small particles will be sheared while large particles will be overcome by Orowan mechanism.

In some cases, Orowan stress is also the flow stress for dispersion strengthening, a process in which incoherent obstacles such as oxide particles are deliberately added to a softer metal matrix. However, at high temperatures, cutting and Orowan bowing can be replaced by diffusional climb-controlled mechanisms: a dislocation stopped at a particle can bulge out of the slip plane and surmount the particle. This introduces a temperature and strain rate dependent component to this threshold [39]. Rösler and Arzt [2, 3] developed a model based on the key idea that dislocations more commonly reside in attractive traps because the dislocation line reduces its energy by lying at the interface between the matrix and an incoherent dispersoid. The attractive interaction causes a threshold stress τ_d, which must be exceeded in order to detach the dislocation from the particle after climb is completed [2]:

$$\tau_d = \frac{Gb}{2\lambda}\sqrt{1 - k^2},\tag{3.44}$$

where the mean spacing between neighboring precipitates λ is defined as:

$$\lambda = r\sqrt{\frac{2\pi}{3f}}.\tag{3.45}$$

The attractive interaction between particle and dislocation is modeled by assuming that the line energy of the dislocation is relaxed at the incoherent interface. The parameter k is then considered as a relaxation parameter with values between 0 (maximum of attractive interaction with the particle) and 1 (no attractive interaction). According to Arzt and Wilkinson [2], only a very modest attractive interaction between dislocations and particles is required in order for dislocation detachment to become the strength-controlling process.

3.5 Dislocation forest strengthening

Dislocations have a characteristic stress/strain fields which are mainly responsible for their interactions with different obstacles. In general, dislocations move on various intersecting slip planes and interact with each other. Dislocations, which act as obstacles to the movement of dislocations from other slip system are called *forest dislocations*. As the strain is increased the dislocation density raises and in addition to primary also other slip systems are activated. The number of mutual dislocation-dislocation interactions increases rapidly leading subsequently to the increase of the flow stress. This process is called *strain* or *work hardening*.

There are several different types of dislocation-dislocation interactions possible. To move two dislocations located on parallel slip planes of certain spacing past each other requires the application of an external stress to act against their interaction force, called as *Peach-Köhler force* (see schematic visualisation in Fig. 3.13). This force can be characterized by the long-range stress fields of two dislocations. Depending on their relative position and sign, the force will lead to repulsion or attraction of the dislocations. Dislocations of different signs lying on the same slip plane attract each other and annihilate, whereas dislocations on different planes can arrange in a dipole configuration drawing an angle of 45° between each other. As the thermal activation is ineffective in case of these interactions, only an athermal contribution to the flow stress is introduced by this interaction. [36].
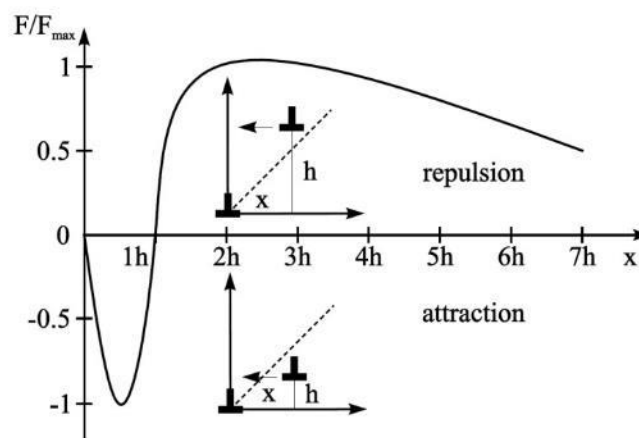
Figure 3.13: Schematic of the Peach-Köhler force for two edge dislocations of same sign. The bisecting line constitutes the equilibrium position, dislocation dipole. Behaviour is inverse for edge dislocations of different sign. Taken from [39].

The intersection of gliding dislocations with forest dislocations is related to both thermal and athermal flow stress. If the result of interaction is jog creation, the movement of such structure is independent of internal stress. It has short-range character and is therefore related to the thermal flow stress component. On the other hand, interaction of the long-range stress fields of forest dislocations with the stress field of incoming dislocation contributes to the athermal flow stress component. While interaction of two edge dislocations with perpendicular Burgers vectors can result in a jog formation, the two edge dislocations with anti-parallel Burgers vectors can form a kink. Since the length of the dislocation is increased by these processes, they are associated with thermal activation providing necessary extra energy. Jogs created by interactions of edge and screw or two screw segments of dislocations can move out of slip

plane with the help of thermally activated processes, including the production of vacancies or the take-up of interstitials. [39]

The athermal component of the flow stress imposed by the interaction of glide and forest dislocations arises from their long-range internal stresses. Dislocations can either form *attractive* or *repulsive junctions* what constitutes the major part of *dislocation strengthening*. Assuming that the dislocations are completely randomly distributed within the grains, the interaction of glide and forest dislocations should be well-approximated by the Taylor work-hardening relationship between dislocation density ρ and flow stress τ_{Taylor} in a single crystal [55]:

$$\tau_{\text{Taylor}} = \alpha G b \sqrt{\rho}, \tag{3.46}$$

where α is constant $0.2 - 0.4$ for polycrystals [56], G is the shear modulus of the matrix, b is magnitude of Burgers vector and ρ is dislocation density.

Upon repeated activation of a dislocation source, dislocations of the same sign and mainly edge segments moving on the same slip plane form dislocation arrangement called as *pile-up*, mostly in front of obstacles such as grain boundaries. The obstacles cause a locally higher yield stress than the surrounding matrix. Due to the elastic interactions between the dislocations of a pile-up, the leading dislocation experiences a forward stress pushing against the obstacle. This can cause the activation of dislocation sources in neighboring grains or initiate cross-slip. On the other hand, the following dislocations in the pile-up are prevented in their further movement by a *long-range backstress*. The forward stress equals the applied stress amplified by the number of the piled-up dislocations. As the backstress opposes the applied stress at the dislocation source, additional external load has to be applied to maintain the plastic deformation. Pile-ups can therefore be responsible for large long-range stresses.[39]

In materials that exhibit easy cross-slip the formation of dislocation pile-ups is rather unlikely. However, long-range internal stresses in these materials arise from the presence of different phases or from *heterogeneous dislocation substructures*. Determination of the flow stress coming from the dislocation arrangements such as walls, channels or cellular structures was thoroughly studied by [57, 58]. As reported by [59], during cyclic deformation of metal structures characteristic by walls of high dislocation density surrounding areas free of dislocations are formed. These heterogeneous, locally very different dislocation structures feature locally different flow stresses so the plastic deformation of two different regions is mainly localized into the soft dislocation cell interiors. Based on the composite approach presented by [60], the macroscopic flow stress is the result of the local flow stresses of the soft and hard regions weighted by their respective volume fractions.[39]

In case of two- or multi-phase alloys or precipitation hardened materials, plastically deformed grains consist of uniformly and locally non-uniformly deformed areas [39, 61]. The uniform deformation is accommodated by the accumulation of *statistically stored dislocations* which are then responsible for work-hardening. Deformation of a heterogeneous microstructure containing different phases, grains of different orientations or precipitates requires the maintenance of the deformation compatibility between the regions of different strength. The internal strain gradients are accommodated by so-called geometrically necessary dislocations (GNDs) near the grain boundaries or precipitates [39]. These GNDs are then related to long-range internal stresses that vary over a distance that is associated with the spacing between the

phases, precipitates and other hard structural features. Mughrabi [62] has reported that the contribution of GNDs to the macroscopic flow stress is marginal in the case of heterogeneously distributed dislocations, while they role is more significant in the case of two-phase or precipitation hardened materials, where GNDs are present in higher density.[39]

3.6 Grain boundary strengthening

There are important differences between plastic deformation in single-crystal and polycrystalline materials, where the grain boundaries act as strong barriers to dislocation motion. From experimental measurement of the yield stress σ_y of polycrystalline aggregates in which grain size d is the only material variable, it has been found that the empirical relationship is satisfied as follows:

$$\sigma_y = \sigma_0 + \frac{k_y}{\sqrt{d}}. \tag{3.47}$$

The stress σ_0 is a material constant for the starting stress for dislocation movement (or the resistance of the lattice to dislocation motion), k_y is the strengthening coefficient (a constant specific to each material). This empirical relation between yield stress and grain size is called the *Hall-Petch equation* [36, 63, 64].
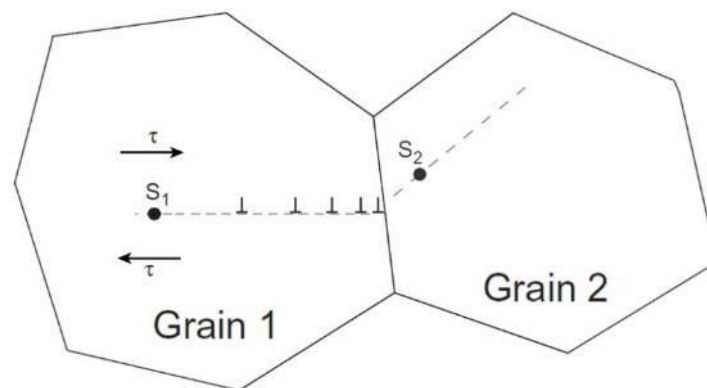
Figure 3.14: Schematic illustration of a pile-up formed of dislocations from source S_1 in grain 1 under an applied resolved shear stress τ. S_2 is a dislocations source in grain 2. The trace of the preferred slip plane in each grain is marked by a dashed line (after [36]).

One explanation of Hall-Petch relationship is that under an applied stress, existing dislocations and dislocations generated by Frank-Read sources in one grain will move through a crystalline lattice until reaching a grain boundary where repulsive stress field will present obstacle to further dislocation motion. As more dislocations propagate to this boundary, dislocation *pile-up* occurs composed of dislocations which are unable to overcome the boundary. Within the pile-up, dislocations will generate repulsive stress fields leading to the repulsive force on the dislocation incident with the grain boundary. If stress fields are large enough, the energetic barrier for the dislocation diffusion across the boundary will be reduced allowing further deformation in the neighbouring grain (see schematic in Fig. 3.14). In other words, the dislocation sources in an adjacent grain will operate at the yield stress. Decreasing

the grain size decreases the amount of possible pile-up dislocations at the grain boundary so the higher applied stress is then necessary to move a dislocation across.

Although such a pile-up model was first used to explain the Hall-Petch relationship, other interpretations are possible as well. Overview of alternative, non-pileup theories and interpretation models such as *source theory* or *work hardening theory* was summarized by [39].

3.7 Combination of strengthening mechanisms

In majority of structural alloys used in real service a combination of several strengthening mechanisms operate. Some alloys contain more than one precipitate type where each will make its own contribution to the strength of the alloy. In other cases additional strengthening mechanisms, not necessarily associated with the particles, may be operating, e.g. solid solution or grain boundary strengthening. The question than arises how these mechanisms interact together and how to estimate their overall effect on flow stress increase. Some authors suggest to find the most important strengthening mechanism and neglect remaining, others propose to simply summarize all contributions $\Delta\tau_i$ as [65]:

$$\Delta\tau_{tot} = \sum_{i=0}^{n} \Delta\tau_i \tag{3.48}$$

Makin and Foreman [66, 67] performed one of the first computer modelling experiments in which a dislocation passed through random array of point obstacles. The strength of obstacles was defined by critical angle ϕ_c (see Eq. 3.7). They determined the shear stress $\Delta\tau$ for dislocation passing through an array of obstacles of various strengths and combination of various obstacle types. The result was following:

- for combination of two populations of weak obstacles, the resulting flow stress increase is given by a Pythagorean superposition law, i.e. root mean square of stresses related to the two obstacle arrays taken separately:

$$\Delta\tau_{tot} = \sqrt{\Delta\tau_A^2 + \Delta\tau_B^2}; \tag{3.49}$$

- for combination of two different strong obstacles, the result is close to arithmetic sum;
- small number of strong obstacles added to dense array of weak obstacles has significant strengthening effect;
- small number of weak obstacles in dense array of strong obstacles has almost no effect on the resulting strengthening.

Conclusion based on thorough work of Makin and Foreman [66, 67] suggests that the problem of combining several strengthening mechanisms cannot be simply generalised and needs careful modelling and simulations based approach dealing with every mechanism in detail.[68]

At the end of chapter, it is worthy of note that the presented mathematical equations can be used in a simplified analytical approach when trying to describe acting fundamental mechanisms. However, to deliver proper quantified description of the problem, extensive set of experimental data has to be used as an input into the physically-based models properly dealing with the phenomena ongoing on atomistic level. Mobility of dislocations, their mutual interactions or interaction with obstacles and subsequent effects on macroscopic response,

thermodynamics and precipitation of secondary phases, etc. all of these can be studied using various modelling and simulations based approaches such as ab-initio calculations, molecular dynamics, three-dimensional discrete dislocation dynamics modelling, phase-field modelling, and others. The multi-scale modelling approach then can combine several of these tools, using a results from one type of simulations as a necessary input for another one [69–73].

4. Low cycle fatigue damage

In materials science the term fatigue could be defined as a sequence of processes which occur in material loaded by the time variable external forces and lead to initiation of fatigue crack, its propagation and consequential final fatigue fracture. When a machine part or a whole structure is loaded by cyclic external forces, a complete fracture may occur, although no obvious damage can be observed throughout the majority of the loading cycles. Moreover, the magnitude of the external forces may be so small that their single application does not result in any noticeable damage.

Cyclic loading of material leads to cumulative and irreversible complex microstructural changes on both atomistic and microscopic scale-level. As a result, fatigue cracks initiate and propagate through the material leading consequentially to the final fatigue fracture [74–76].

4.1 Stages of fatigue life

The process of fatigue damage could be separated into several individual stages as is shown in Fig. 4.1. However, despite the fact that each stage could occur in a different period of the fatigue life, no clear boundary between them exists and usually each stage merges into one another.
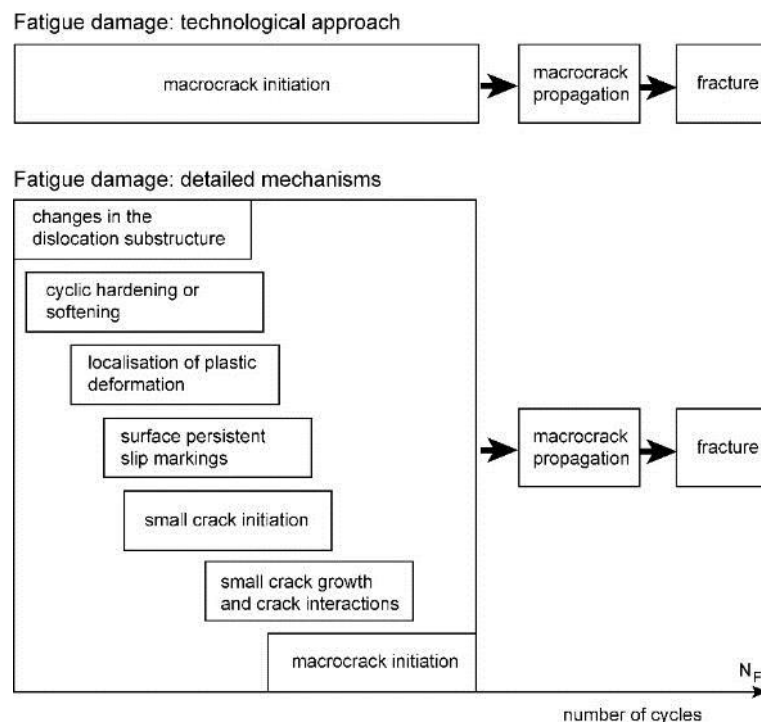
Figure 4.1: Stages of fatigue damage leading to failure of material (adapted from [75]*).*

From the technological point of view, there are two important phases of fatigue life: (I) initiation of a macrocrack and then (II) the crack growth and propagation until the fracture. While the latter could be sufficiently described by the fracture mechanics, adequate understanding of processes leading to the initiation of crack has to be reached by fully microscopic approach at micro- and nano-scale levels.

56

As the cyclic loading starts, due to the presence and accumulation of cyclic plastic deformation, internal dislocation structure develops. Dislocation density increases as the dislocations are generated and annihilated and their mutual interactions lead to the change of macroscopic cyclic response of material what is characterised by initial cyclic hardening and/or cyclic softening.

With further cyclic loading and evolution of the dislocation structure, cyclic plastic strain localizes into persistent slip bands (PSB). Along with PSBs formation in the bulk of the material, as a consequence, persistent slip markings (PSMs) emerge on the surface. As the surface relief develops and PSMs are well established, fatigue cracks are initiated often within them, as they act as a stress concentrators. With additional cycling, short fatigue cracks grow, affect each other and coalesce until one of the cracks becomes major crack leading then to the macrocrack initiation.

In following sections, the individual stages of fatigue damage are discussed in detail based on [74–76].

4.2 Cyclic stress-strain response of material

Mutual correlation between stress and strain during the cyclic loading characterizes cyclic plastic response of material. As mentioned previously, change in response to cyclic loading is mainly due to the evolution of density and configuration of internal microstructural defects.

The standard symmetrical uniaxial cyclic loading tests could be performed in three basic regimes depending on which variable is controlled and kept constant during the experiment. The most common are strain-controlled fatigue tests, where the total strain amplitude (ε_a) is pre-set as a constant and the other parameters are measured. The other two regimes are then plastic strain amplitude (ε_{ap}) and stress amplitude (σ_a) controlled tests.

In strain controlled cycling with constant strain amplitude, the growth in stress amplitude and the drop in plastic strain amplitude represents cyclic hardening of the material. Cyclic softening is then opposite effect, where stress amplitude decreases with each additional cycle.

The primary hardening or softening period can be followed by steady-state cyclic deformation in which the stress-strain response remains unchanged. The hysteresis loop is closed and does not change significantly with number of cycles. Example of such hysteresis loop is shown in Fig. 4.2. The loop is characterised mainly by saturated stress amplitude σ_a and plastic strain amplitude ε_{ap} and also by the loop shape parameter V_H [75] defined as

$$V_H = \frac{W}{4\varepsilon_{ap}\sigma_a},$$

(4.1)

where the hysteresis loop area W represents the specific energy dissipated in a material within one cycle.

The hardening/softening behaviour of the material within the fatigue life is often characterised by plots called cyclic hardening/softening curves. In strain cycling with constant total or plastic strain amplitude, these curves are represented by the dependence of the stress amplitude on the number of cycles [75, 76].
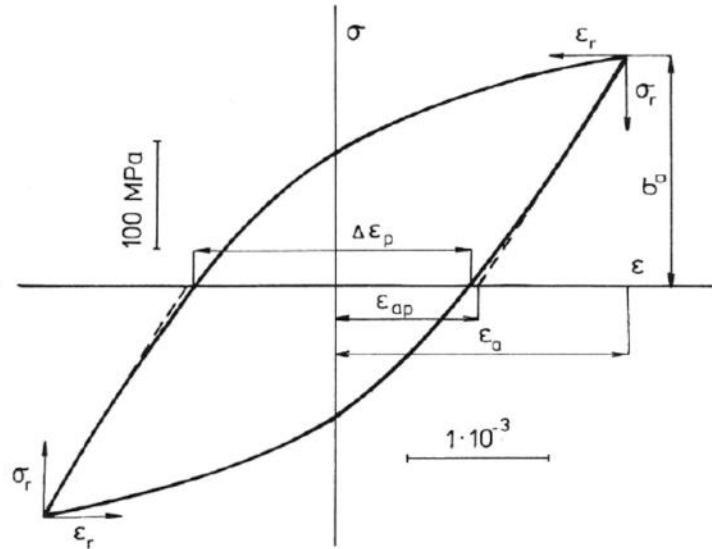
Figure 4.2: The saturated hysteresis loop. Taken from [75].

4.3 Microstructure evolution

The original microstructure of metals subjected to cyclic loading can differ substantially and depends on composition, thermal and mechanical treatment, previous history, etc. However, the evolution of the initial microstructure has some features common for various metals and alloys. These are closely connected with the alternating character of cyclic plastic straining and other specific features characteristic to lattice structure and the properties of dislocations and other lattice defects in the material.

Cyclic plasticity and its relation to the dislocation structure has been studied thoroughly in both face-centered cubic single crystals and polycrystals. Most intensive works were done on polycrystalline metals and single-phase alloys, namely in copper [59, 77–84], copper alloys [85–87], aluminium and its alloys [88, 89], nickel and its alloys [90], and stainless steels [91–94]. Despite the fact that the grain size is an important parameter in cyclic straining of polycrystals, considerable similarity between the behaviour of single crystals and polycrystals has been noted as discussed in [75].

Solute additions can affect both the cyclic stress-strain response and the dislocation structures considerably. As discussed in Chapter 3, the stacking fault energy of the structural alloy is usually lower than that of the pure metal and, therefore, the slip character changes. Studies of Feltner and Laird [78] on Cu-Al alloys and Lukáš and Klesnil [79] on Cu-Zn alloys have shown strong tendency to planar slip character and homogeneous dislocation distribution in alloyed materials. As the content of alloying elements increased, the stacking fault energy decreased notably resulting into large separation distance between the Shockley partial dislocations therefore preventing easy recombination.

In case of structural materials, probably the most detailed and thorough studies have been performed on 316-type austenitic stainless steel. The majority of works have been focused on investigating the microstructures developed during cycling with different strain amplitudes at

the failure [14, 16, 17, 95, 96]. A few detailed works on deformation structure evolution during the fatigue life have been presented as well [14, 18].

As noted previously, the stacking fault energy in austenitic stainless steels is quite low (in case of 316-type, it is reported to be lower than 20 mJm^{-2} [16, 97]). Under cyclic loading, the dislocation density increases significantly and since low stacking fault energy and possible short-range ordering effects restricts cross-slip of dislocations, their movement is usually limited to planar slip within one slip system only. As a result, dislocation interaction becomes more complicated and more tangled structures are formed usually leading to the initial hardening cyclic response of loaded material.

With further cyclic loading, dislocations move and can interact together, i.e. annihilate or make a dipole configuration. As a consequence, the total dislocation density tends to reach its equilibrium state and remains almost constant after achieving a maximum. Depending on type of material, general structural state (stacking fault energy, alloying, thermo-mechanical treatment, etc.) and depending also on the orientation of particular grain relative to the loading axis, secondary slip systems can be activated further facilitating interactions between dislocations. More complex dislocation structures are formed as the system tends to reach minimum of internal energy. In this stage of cyclic loading, along with progressive change of dislocation microstructure, cyclic plastic deformation localizes into PSBs. These structural features can accommodate cyclic plastic deformation and in simple metals like copper [59, 80–83] and nickel [84] and also in 316-type of steels [16, 17, 59], they are usually observed in the form of ladder-like structures consisting of dislocation-rich walls separated by dislocation-free channels. As reported by Polák et al. [83], in polycrystalline copper localization of cyclic plastic deformation occurs in the early stage of loading, in particular after 10 to 1000 cycles depending on applied plastic strain amplitude and temperature. Cyclic softening response of material is usually observed in relation to localization of cyclic plastic deformation.

As a result of continuous cyclic loading, different materials can exhibit different nature of internal structure changes. For example, at sufficiently high loading levels, where several slip systems are active, vein, labyrinth and wall/channel structures can transform into spatial cellular dislocation structures. However, from the perspective of fatigue, the PSBs are the most important structural features not only for cyclic slip localization but mainly in regard to fatigue crack initiation. That is discussed in the next section.

4.4 Surface relief formation and fatigue crack initiation

The fundamental source of information allowing for an understanding of the mechanisms leading to the initiation of fatigue cracks is the dislocation structure of the bands of localized cyclic slip, i.e. PSBs. Numerous theoretical models describing the mechanism leading to cyclic slip localization, formation of the surface relief and stage I fatigue crack initiation were proposed. Following text is based on detailed overview recently presented by Polák et al. [98].

The first treatment of dislocation interactions in PSBs appeared in the work of Essmann and Mughrabi [99]. They considered the expansion of dislocation loops from the walls across the channels, interactions with dislocations in neighbouring walls, and their annihilation (see Fig. 4.3). Simultaneous formation and annihilation of dislocations lead to the achievement of a saturated dislocation density in cyclic straining. Moreover, the production and annihilation of

dislocations result in point defect production in the walls and their annihilation by sweeping dislocations. Relatively high saturated point defect density was estimated [98, 99].
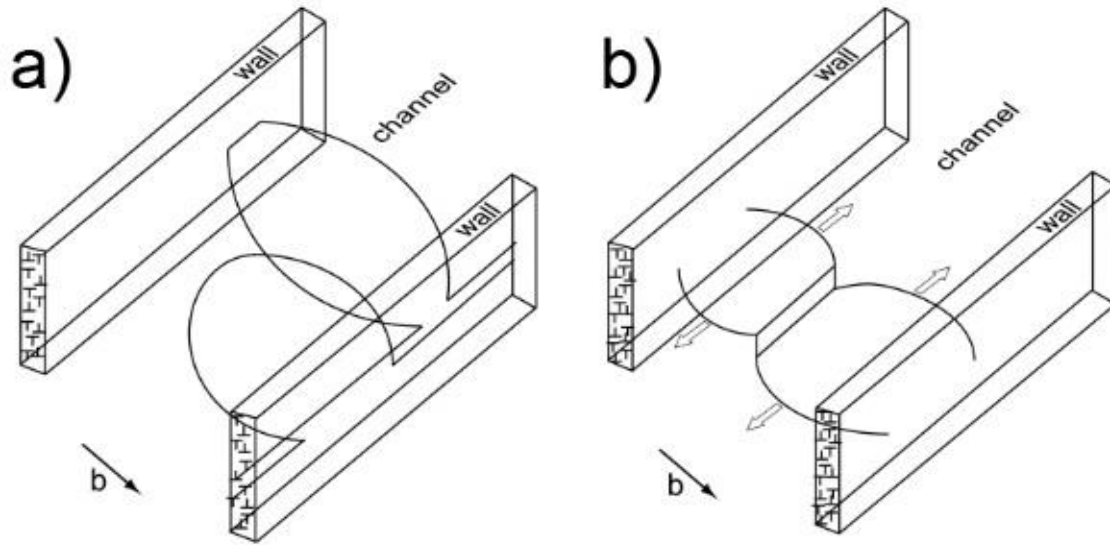
Figure 4.3: Schematics of loop emission from the dislocation rich wall in a ladder-like structure of PSB (a) expansion of the loops from one wall (b) expansion of two loops from the neighbouring walls on neighbouring slip planes and formation of unit dipole in the channel (taken from Polák and Man [100]).

The production of point defects in cyclic straining motivated Essmann et al. [101] to propose the first physically-based model (EGM model) which was able to explain the formation of extrusions and intrusions in fatigued metals. The EGM model is based on the production of vacancies due to dislocation interactions in the walls of PSBs. Vacancies represent extra volume and cause internal compressive stresses within PSBs. These stresses are relaxed in the direction of active Burgers vector and an extrusion starts to grow where the PSB emerges on the surface. Mughrabi [102] considers the source of crack initiation to be the stress concentration from extrusion and notch effects due to random slip within PSBs. Stage I shear fatigue crack forms as a result of previously formed extrusion and stress accumulation in the roughened extrusion surface (acute angle between Burgers vector and specimen surface).

Coinciding with the work by Essmann et al. [101], Tanaka and Mura [103] modelled PSBs by the line of dislocation dipoles impinging on the grain boundary. They proposed the formation of embryonic cracks in dislocation pile-ups accumulated under cyclic stress. The layers of dislocation dipoles can be transformed into a free surface (crack) when the stored energy accumulated after *N* cycles becomes equal to the surface energy. They derived a simple equation relating the number of cycles to crack initiation with the specific fracture energy of the material and applied strain or stress amplitude. The Tanaka and Mura model has been revised and modified many times (see e.g. [104, 105]) and used for the prediction of the fatigue life curves for a number of materials. In spite of some success in fatigue life prediction, the modelling of PSBs by the line of dislocation dipoles is not in a good agreement with real dislocation structures of PSBs in simple face-centered cubic and body-centered cubic metals. A more realistic dislocation structure of PSBs has recently been considered by Sauzay et al. [105, 106] in calculation of the internal stresses produced at PSB impinging

grain boundaries. Due to the finite thickness of PSBs and observed dislocation arrangement, these stresses are substantially lower than calculated by the pile-up model.[98]
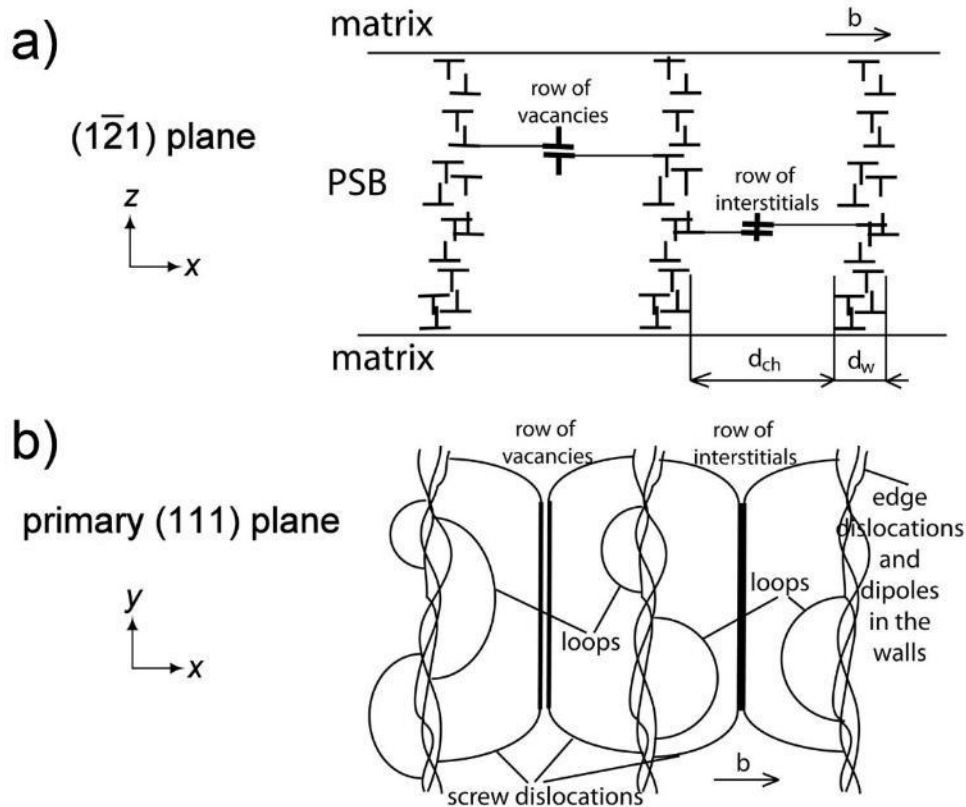

Figure 4.4: Schematics of dislocation interactions and formation of point defects in a PSB, (a) projection in $(1\bar{2}1)$ plane, (b) projection in primary (111) slip plane (taken from Polák and Man [100]*).*

The EGM model was further developed by Polák [107]. Since point defects in copper are highly mobile at room temperature [108–110], they readily anneal out during cyclic loading and static extrusions considered in the EGM model [101] cannot accumulate in room temperature cyclic loading. Consequently, the mechanism of extrusion formation proposed in the EGM model has been substantially modified [107]. Polák´s model considers the production of point defects not only in the dislocation walls but also in channels of the PSBs (see Fig. 4.4). Moreover, point defects, predominantly vacancies which are steadily produced in the channels, migrate (during cycling) to the dislocation walls and to the matrix where they are absorbed at edge dislocations. Migration of vacancies from PSBs to the matrix (see Fig. 4.5) results in systematic transfer of atoms in the opposite direction (i.e. toward PSBs). The matter is thus readily accumulated at PSBs and internal compressive stresses arise within. Compressive stress is relaxed plastically in the direction of the primary Burgers vector and the steady growth of an extrusion is envisaged. The growth of extrusions has been described quantitatively, provided vacancies are absorbed at PSB/matrix interface, by Polák and Sauzay [111]. Due to the matter conservation law, intrusions arise on the PSB/matrix boundary. The kinetics and the shape of the intrusions have been calculated using the data on vacancy production and migration corresponding to polycrystalline copper [112, 113]. The intrusions represent crack-like defects with high stress concentration and fatigue cracks start to grow from the tips of intrusions parallel with the Burgers vector by slip-unslip mechanism.

It is important to note, that in spite of numerous models of fatigue crack initiation accompanied by numerous recent high resolution observations [114–118], different opinions still exist on the sources of crack initiation in cyclic straining and the real initiation mechanism has not yet been recognised.[98]
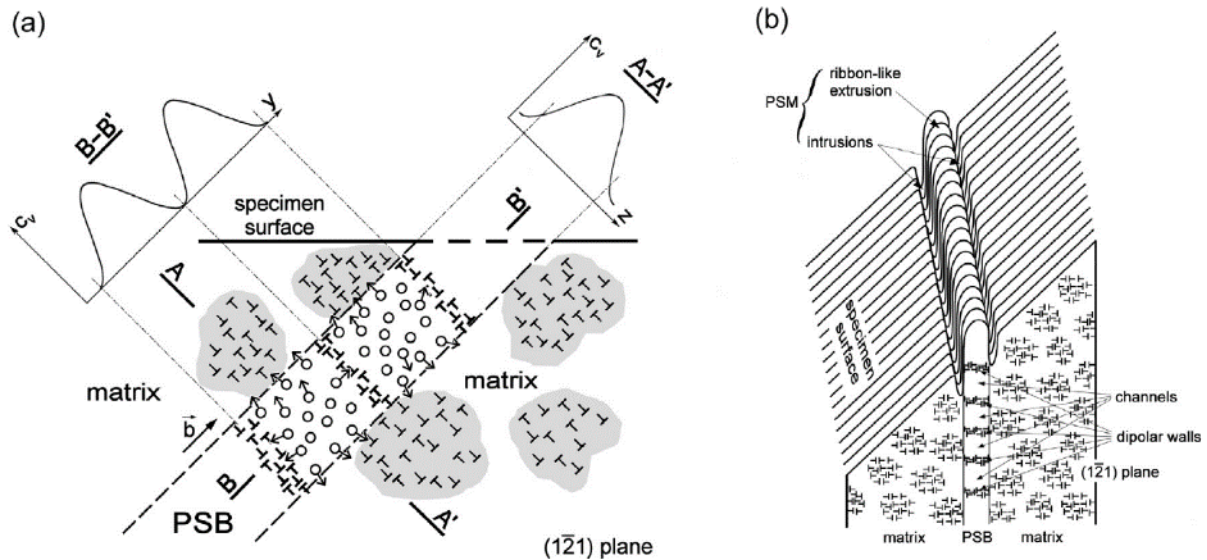
Figure 4.5: Schematics of the relation of the internal ladder-like dislocation structure of a PSB and resulting surface relief, (a) point defect production in PSB and their migration to the matrix, (b) resulting surface profile consisting of central extrusion and two parallel intrusions. Taken from Polák and Man [100].

4.5 Fatigue crack growth

Fatigue cracks could be divided into several different categories, as follows [119].

- Cracks of length smaller than approx. 1 mm are considered as **small cracks**. Three types of these cracks can be distinguished according to their dimensions:

  1. Physically small cracks of length up to 1 mm. Here the difference between long and small crack is determined by a different closure stresses.

  2. Mechanically small cracks. These cracks have the same or smaller proportions than the size of the plastic zone at the crack tip. Stress and strain fields around this crack cannot be described by elastic fracture mechanics.

  3. Microstructurally small cracks, which have the same of smaller proportions when compared to characteristic structural unit (e.g. grain size).

- **Short cracks** defined and described in regard to the fracture mechanics. Here, the range of stress intensity factor (ΔK) at the tip of the short crack is lower than the threshold value (ΔK_{th}).

- **Long cracks** where ΔK is larger than ΔK_{th}. In the certain interval of long crack length, their propagation is described by Paris-Erdogan law.

Crack propagation stage represents an important period which often determines the fatigue life of the specimen, component or structure. In cyclic loading of smooth homogeneous bodies above the fatigue limit, many fatigue cracks can be initiated and initially the simultaneous growth of several cracks is observed. However, most cracks stop and generally only one dominant crack propagates until final fracture [75].

4.6 Effects of high temperature

The fatigue behaviour of materials is influenced by temperature and additional effects must be taken into account if complete characterization is desired. Thermally activated processes play an important role, and diffusion and recovery are accelerated. From microstructural point of view, the elevated temperature facilitates dislocation motion in cyclic straining. Various thermally activated mechanisms, such as cross-slip and climb help to overcome obstacles to dislocation motion, so the resulting dislocation structures can be notably different from that at room temperature. The mobility of point defects produced in cyclic straining increases and thermal fluctuations contribute to separating the row of point defects that arise through mutual annihilation of edge dislocations or non-conservative motion of jogs on screw dislocations. Dislocation climb is enhanced and recovery processes start easier than at room temperature.[75, 120]

At high temperatures, the diffusion rates of interstitial and substitutional solutes are enhanced what can lead to rapid precipitation and growth of secondary phases notably affecting mechanical properties. As discussed in Chapter 3, dense dispersion of nano-scale precipitates can significantly enhance strength of the alloy. On the other hand, secondary phases nucleated on the grain boundaries can detrimentally affect corrosion and oxidation resistance of the material. Formation of solute atom atmospheres can appear (Cottrell, Suzuki atmospheres, etc.). The dislocations can be pinned by the interstitial atoms whose diffusion rate is high enough to catch the moving dislocations. As a consequence of these microstructural changes, cyclic stress-strain response of material could be significantly modified.

The microstructural features that lead to the cyclic strain localization and the initiation of fatigue cracks at room temperature and at elevated service temperatures differ significantly [121]. At high temperatures, the early fatigue damage is not only affected by the type of loading [122, 123], but also by the environmental effects causing grain boundary oxidation and cracking [124, 125]. Brittle oxides grown at the grain boundaries induce rapid crack initiation due to their fracture during cycling. Coffin [120, 124] presented a repeated oxide layer rupture model, where further oxidation of freshly exposed metal can be accelerated by the oxidation of carbides, formation of corrosion pits or oxide intrusions along the grain boundaries and within the grains. The cracks propagate preferentially intergranularly. High impact on crack propagation has stress corrosion cracking when the brittle oxide layer cracks under the tensile loading stress. During the period the crack is open oxygen can penetrate into the metal and new oxides can rise [120, 124].

High temperature in participation with the environmental conditions has then a significant detrimental effect on the degradation of the near-surface material properties. This leads subsequently to the earlier crack initiation and growth under the conditions affected by oxidation [123]. Material resistance to the near-surface high temperature degradation in terms

of the oxide formation, especially along the interfaces, is closely connected with the chemical composition and the initial microstructural state.

It is worth of noting that very important is also the effect of the time factor, i.e. the role of strain-time and the stress-time history. Strain rate plays fundamental role. In high temperature cyclic straining with low strain rate or in cycling with dwell/hold periods applied during the cycle, in addition to fatigue, also creep damage mechanisms has to be considered.

IV. EXPERIMENT

5. Mechanical testing

5.1 Specimens

From both materials, Sanicro 25 and Manaurite XTM, the specimens for the mechanical testing were machined parallel to the rod/tube axis. Cylindrical specimens with the diameter 8 mm and the gauge length 14 mm for room temperature testing and 6 mm in diameter and 15 mm gauge length with button ends for elevated temperature testing were produced (see Fig. 5.1). To eliminate the effect of the surface roughness on the fatigue life the area within the gauge length was mechanically grinded. In case of Sanicro 25 the specimens were solution annealed at 1200°C for one hour and cooled in the air after the production of their crude shape.
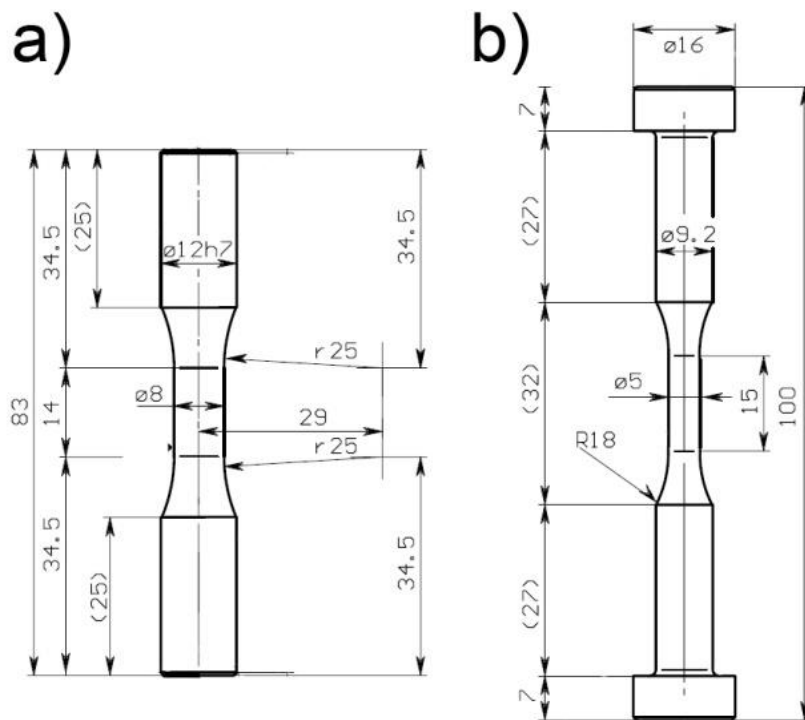
Figure 5.1: Geometries of (a) standard cylindrical specimen used for room temperature tests and (b) cylindrical specimen with button ends used for isothermal cycling at elevated temperatures.

In case of centrifugally casted alloy Manaurite XTM, anisotropy of mechanical properties for monotonic and cyclic loading of material at room temperature has been investigated. For that purpose, special small specimens perpendicular to the tube axis were designed and prepared as shown in Figure 5.2a.

The first type of the small sample was selected as perpendicular to the tube axis and parallel to the direction of dendrites, i.e. the direction of melt solidification. This direction was marked as "radial" and the geometry of the specimen is shown in detail in Fig. 5.2b. The total length of the sample was 27 mm, while gauge length was 8 mm. Second type of small specimen was produced from the tube wall as perpendicular to the tube axis and perpendicular to the direction of dendrite solidification. This direction was marked as "tangential" and the specimen geometry is shown in Fig. 5.2c. It had total length of 35 mm and gauge length of 9 mm. For both samples, diameter of gauge length part was 2.3 mm, while the diameter of grip part was 5 mm. For mounting into the grips of the testing machines, adapters were used.
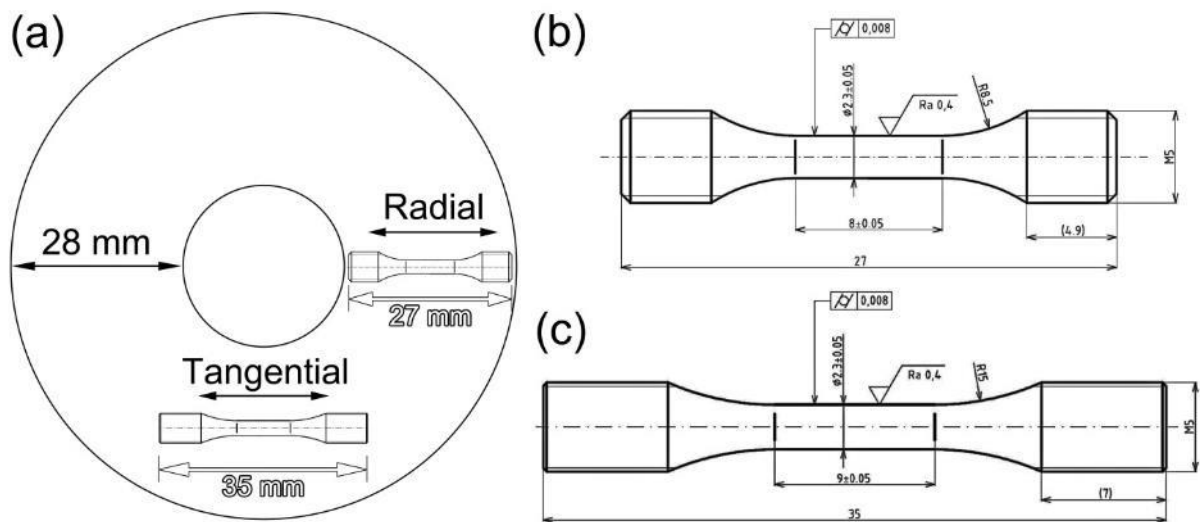
Figure 5.2: (a) Schematic drawing showing the orientation at which the two types of small samples were produced from the tube wall. (b) Geometry of small sample marked as "radial" produced parallel with the solidification direction. (c) Geometry of small sample marked as "tangential" produced perpendicular to the solidification direction.

5.2 Methodology

All tests were performed using computer controlled electrohydraulic MTS system. At room temperature mechanical grips held at constant temperature were used and strain was measured and controlled with an extensometer having the 8 mm base. High temperature tests were performed with hydraulic grips, split resistance furnace and high temperature axial extensometer with 12 mm base. Tensile tests at room and at elevated temperatures were performed using identical specimens and extensometer as used for high temperature fatigue testing. The constant strain rate 2×10^{-3} s^{-1} was used in tensile loading. At the onset of the tensile test both the displacement and the strain using the extensometer were measured. When the maximum strain range of the extensometer was reached (approx. 8%) the extensometer was removed and tensile test continued with control of the displacement and the displacement rate corresponding to the selected constant strain rate. Engineering strain was later calculated from the displacement.

In cyclic loading at room temperature specimens were cyclically strained in symmetrical cycle with total strain control and constant total strain rate 5×10^{-3} s^{-1} in symmetric cycle. Constant strain amplitudes ε_a cycling was applied to individual specimens at each temperature using standard MTS low cycle fatigue (LCF) program. Number of cycles to fracture N_f corresponds to the drop of the ratio of the mean stress to the stress amplitude below -0.1. Hysteresis loops were recorded during cycling and stress amplitudes and plastic strain amplitudes were evaluated. Plastic strain amplitude was defined as equal to the half-width of the hysteresis loop at mean stress.

Continuous isothermal high temperature tests were carried out in a computer controlled electro-hydraulic MTS 810 test machine at a temperature of 700°C in air. High temperature hydraulic grips and a split three-zone resistance furnace were used to keep the desired temperature with minimum temperature gradient across the gauge length. Specimen temperature was controlled and monitored by three thermocouples. During the experiment, temperature is maintained at the set temperature with precision of +-2 °C. Grips were cooled by water. Fully reversed total strain controlled cyclic loading (R_ε = -1) with constant strain rate 2×10^{-3} s^{-1} was applied. Force was measured by a load cell and strain was measured and controlled using high temperature extensometer with long ceramic rods and 12 mm base, touching directly the specimen. Specimen was heated up to high temperature (about 30 min) and after full stabilization (about 1 h) cyclic straining was started.

6. Microstructural characterization

6.1 Scanning electron microscopy

Surface of the specimens considered for further characterization by scanning electron microscope (SEM) or for extraction of thin TEM lamella were mechanically polished by SiC grinding papers up to Grit Rating 4000. For finer finish, oxide polishing suspension (OPS), in particular colloidal silica of 40 nm in size, was used. As a last step, specimen was put for one or two days into the vibratory polishing machine. Cleaning was done using ultrasound cleaning system.

The surface observations of the specimens were done by use of Tescan Lyra3 XMU SEM operating with field emission gun (FEG). Microscope is equipped with focused ion beam (FIB), X-Max80 energy dispersive X-ray spectroscopy (EDS) detector for compositional microanalysis and also with electron backscatter diffraction (EBSD) detector, all produced by Oxford Instruments and operated with Aztec software.

In case of Manaurite XTM, technique of FIB nanofabrication was used to produce site-specific and crystallographic orientation-specific lamellae for subsequent high resolution characterization using transmission electron microscopy. For that purpose, FEI Helios Nanolab 660 dualbeam (SEM + FIB) microscope was used. First, the area of interest was found and documented using standard secondary electrons (SE) imaging mode in SEM. Then, a platinum layer of the thickness of about 1.5 to 2 μm was deposited using focused ion beam. Afterwards, FIB was used to trench rectangular craters from both sides of the future thin foil (see Fig. 6.1a). Lamella was further bonded to the extraction needle (nanomanipulator),

completely separated from the grain (see Fig. 6.1b), mounted to the supporting copper grid and subjected to further thinning. Both surfaces of the lamella were finally thinned with ions using low acceleration voltage (5 kV) in order to remove or minimize the damage caused by previous steps. Final thin lamella thickness was about 100 nm.
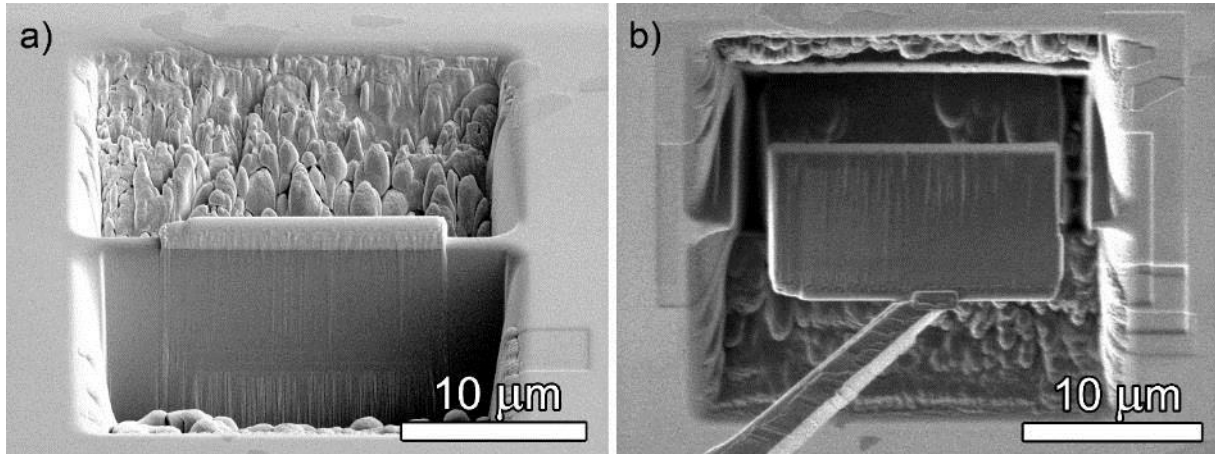
Figure 6.1: SEM secondary electrons mode image showing examples of steps from the procedure of thin TEM lamella preparation. (a) Rectangular craters were trenched from both sides of future thin TEM lamella. (b) Foil is undercut, mounted to nanomanipulator and extracted from the grain. Later, it is bonded to the supporting copper or molybdenum grid and subjected to further thinning.

6.2 Transmission electron microscopy

The microstructure was investigated using both transmission electron microscopy (TEM) and scanning transmission electron microscopy (STEM). The spatial arrangement of dislocations in grains was determined using the technique of oriented foils. Thin plates were cut from the gauge length of the bulk specimens by electric-discharge machine perpendicular, parallel and at the angle of 45° to the loading axis. The samples were mechanically grinded to prepare thin plates of a thickness of approximately 0.08 mm, which were then punched out to produce discs having a diameter of 3 mm. These were marked to indicate the loading direction. The discs were then electrolytically polished using a double jet device TenuPol2. For Sanicro 25, the electrolyte was composed of 95% of acetic acid and 5% of perchloric acid. The polishing conditions were 80V-90V, 0.2 mA and temperature of 13°C to 16°C. Owing to its cast dendritic microstructure, only site-specific FIB foil extraction was used for samples preparation in case of Manaurite XTM.

The samples were investigated by standard bright field (BF) diffraction contrast imaging (DCI) technique on the Philips CM12 TEM working at 120 kV equipped with a double tilt holder. Later, for both diffraction contrast and high resolution phase contrast imaging (high resolution TEM (HRTEM)), the JEOL JEM-2100F TEM working at 200 kV and equipped with STEM and EDS detectors was used. Both TEM microscopes are located at the Institute of Physics of Materials, Czech Academy of Sciences.

The foils were fixed in the TEM holder with the mark of the loading direction aligned with respect to the holder axis in order to know the loading axis during observations. Dislocation

structure was analysed using different diffraction vectors. The Burgers vectors and the types of dislocations were determined using zero contrast conditions. Diffraction patterns and Kikuchi lines were used to determine the crystallographic orientation of the stress axis in individual grains. If not stated otherwise, the Miller´s indexes were permutated so that the strain axis vector lay in or on the border of the basic stereographic triangle defined by the apexes [001], [011], [$\bar{1}$11].

For atomic resolution observations of inspected grains, the foils were tilted in order to perform high-angle annular dark-field (HAADF) zone axis imaging using a probe aberration-corrected FEI Titan3 80-300 kV STEM. Defects contrast was also imaged by using low-angle annular dark-field (LAADF) STEM. By simply adjusting the microscope camera length, and thus the acceptance angle of the annular detector, it is possible to transition from HAADF Z-contrast imaging mode performed by exclusively collecting electrons which have been scattered to high angles to the small-angle scattered electrons sensitive on defect contrast. High spatial resolution energy dispersive X-ray spectroscopy was conducted at 300 kV using an image-corrected FEI Titan3 60-300 kV with a Super-X EDS detector, and utilizing the Bruker Esprit software. The detection system uses four silicon drift detectors that are located radially around the objective pole piece and specimen stage for improved collection performance. The presence of carbon and nitrogen was verified using electron energy-loss spectroscopy (EELS). Two aberration-corrected FEI Titan3 microscopes were used during the Fulbright fellowship supported stay at the Center of Electron Microscopy and Analysis at The Ohio State University. Later, work was finished using an image-corrected FEI Titan-Themis 60-300 kV S/TEM within the research infrastructure of Central European Institute of Technology. For analysis of data, VELOX software was used as delivered by ThermoFisher Scientific/FEI. Atomic resolution STEM images were corrected for possible drift and scanning beam distortions using drift corrected frame integration (DCFI) function integrated in VELOX software.

V. RESULTS

7. Initial state of the material

7.1 Sanicro 25

The experimental material, highly-alloyed austenitic stainless steel Sanicro 25 of grade UNS S31035, was supplied by Sandvik Sweden in bars of 150 mm in diameter. The nominal composition (in wt%) of the material reported in datasheet delivered with rods is given in Tab. 7.1. After machining of the crude shape of the specimens for mechanical testing, they were annealed at 1200 °C for one hour and cooled in air. This state of the material is referred to as "initial" in the text.

	Fe	Ni	Cr	W	Cu	Co	Nb	Mn	N	Si	C
This work	42.9	25.0	22.5	3.6	3.0	1.5	0.5	0.5	0.23	0.2	0.1
Producer Min/Max	Rest	23.5 – 26.6	21.5 – 23.5	2.0 – 4.0	2.0 – 3.5	1.0 – 2.0	0.3 – 0.6	0.6 Max	0.15 – 0.30	0.4 Max	0.04 – 0.1

Table 7.1: The nominal composition of studied Sanicro 25 highly-alloyed austenitic stainless steel (in wt%). Composition of steel studied in this work is compared with the composition guaranteed by the producer [9].

Representative low magnification view of the overall microstructure in the initial state is shown as EBSD scan in Fig. 7.1. Area containing 256 grains was analysed with the scanning resolution of 1 micrometer. Grains are oriented randomly with no texture.
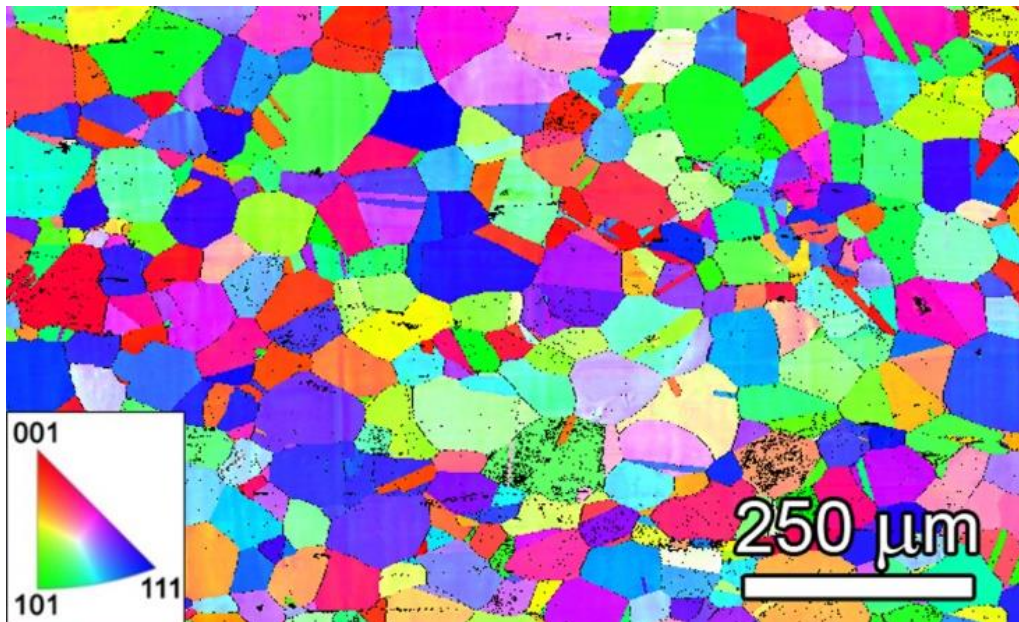

Figure 7.1: EBSD scan showing overall microstructure in the initial state. Grains are oriented randomly with no texture present.

The average grain size, determined by the intercept method, was 60 μm; but, large grains of size up to 500 μm were found as well. After annealing at 1200 °C for 1 h, only one predominant primary precipitate is present in the microstructure, the complex nitride designated as Z-phase with a composition of (Cr,Nb)N as will be discussed further below. Depending on their size they could be subdivided into three categories. Particles of the size up to approx. 100 nm are the smallest and also the most numerous. They are present mainly in the interior of larger grains (30 μm and more in diameter) (see Figs. 7.2a and 7.2b). Second type of precipitates, mostly of spherical shape and notably larger (approx. 400 nm) when compared to those in the interior, were observed at the grain boundaries (see Fig. 7.2b). The third group formed chain-like arrangements of the largest rod-like particles, around 1 μm in diameter, oriented parallel to the hot-rolling direction. They are imaged and highlighted by arrow in the upper right corner of Fig. 7.2a.
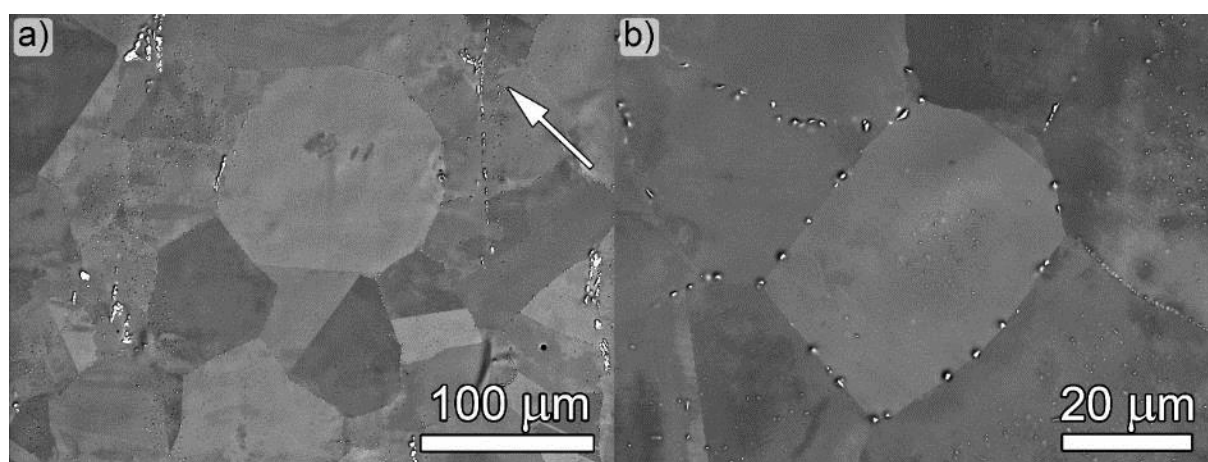
Figure 7.2: SEM micrographs (backscattered electrons mode) of electrolytically polished surface of the Sanicro 25 after annealing for 1 hour at 1200°C and cooling in air. (a) Primary Z-phase precipitates are clearly distinguishable present as chain-like arrangements of large rod-like particles parallel with rolling direction (highlighted by arrow in the image). (b) They are also located within the grains and at the grain boundaries.

In STEM mode, energy X-ray dispersive spectroscopy was used on particles located at the edge of electropolished TEM foil to analyze the chemical composition. In Fig. 7.3, colored chemical maps of detected elements are shown. It is evident that the particle is rich mainly in Nb, Cr and N, while Fe, Ni, Co and Cu are significantly depleted. Rapid change of the composition at the particle/matrix interface is clearly documented by linescan performed on precipitate located at the grain boundary as shown in Fig. 7.4. The composition of the particle is similar to that previously reported for a complex nitride, i.e. (Cr, Nb)N designated as Z-phase [25, 126, 127]. Particles of Z-phase have been observed frequently in Nb stabilised austenitic steels containing a high level of nitrogen [16, 83]. Since they precipitate relatively fast and form a fine distribution of small particles, they are referred as beneficial for strengthening effects [25, 126, 127].
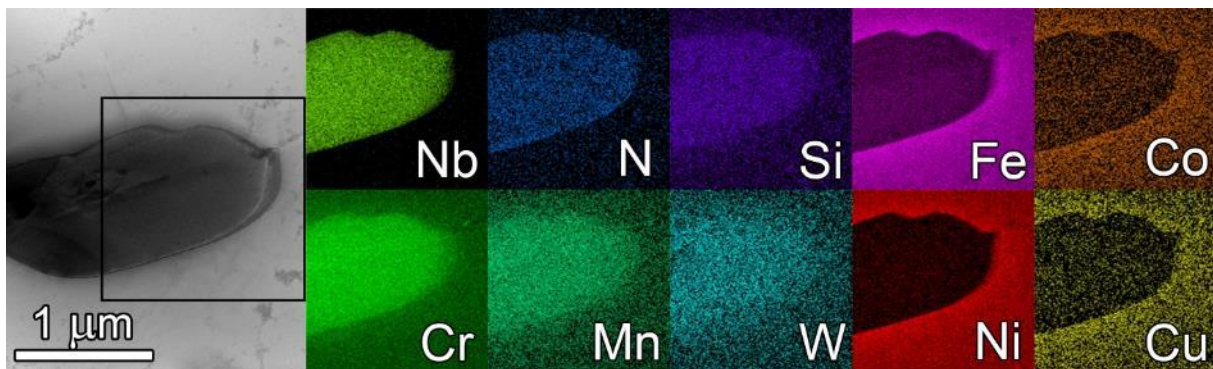
Figure 7.3: STEM EDS map analysis of Z-phase particle in initial state of the material. Colored map shows that particle is rich mainly on Nb, Cr, N. Also Mn, W and Si are present preferentially in particle rather than in matrix. On the contrary, Fe, Ni, Co and Cu are depleted or even absent within the particle volume.

Crystal structure of the Z-phase for the stoichiometry CrNbN has been proposed as a distorted body-centered tetragonal (unit cell with space group P4/nmm) with lattice parameters a = 3.04 Å and c = 7.39 Å [126, 127]. Small concentrations of a few substitutional elements (e.g. Fe, Mo) can be dissolved in Z-phase [126, 127]. In austenitic steels, the empirical formula is approximately $(Cr_{0.8}Fe_{0.2})(Nb_{0.9}Mo_{0.1})N$ [127], however the composition varies with the composition of the steel. According to Sourmail [126], the Z-phase exhibits very good stability at high temperatures since its dissolution starts between 1300°C and 1450°C, depending on the composition of the steel. At high temperatures, it is usually the predominant precipitate.
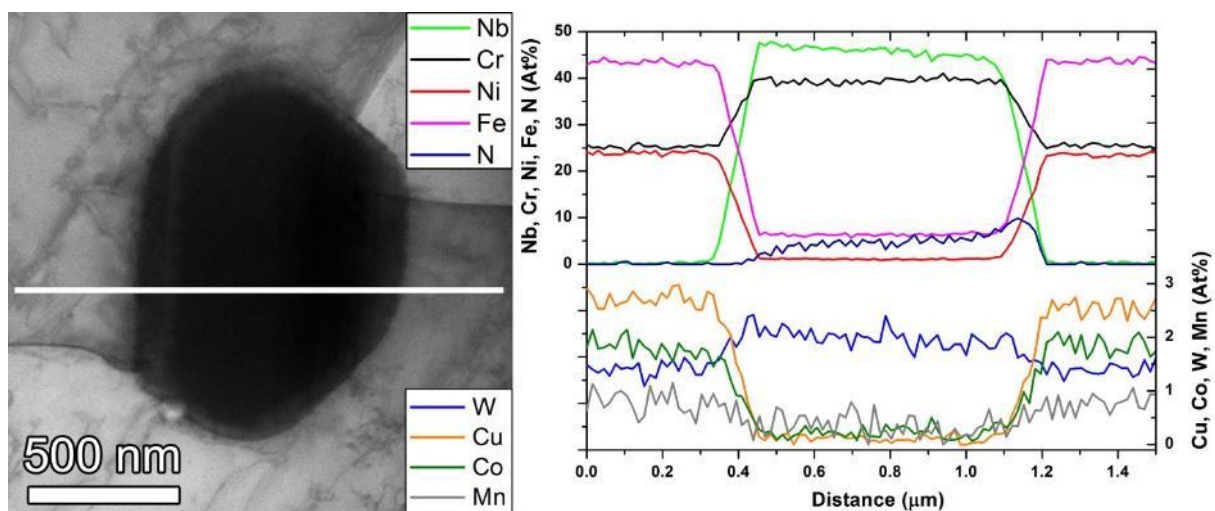
Figure 7.4: STEM-EDS linescan obtained across the particle of Z-phase present at the boundary of three neighbouring grains in initial state. Mainly Nb, Cr and N are rich within the particle, while Fe, Ni, Cu and Co are significantly depleted or absent.

The microstructure of Sanicro 25 in the as-received condition was studied thoroughly by Zurek et al. [25]. They have found only Z-phase particles present, what is in a good agreement with our study. In addition to Z-phase, the presence of a very small amount of $M_{23}C_6$ chromium carbides has been reported in the initial state. However, according to Sourmail

[126], the dissolution temperature of these carbides should be below 1100°C, suggesting their presence after annealing is arguable.

In Fig. 7.5, a bright field STEM diffraction contrast image shows the microstructure of the initial state of the material. Annealing at 1200°C for 1 h significantly decreases dislocation density. Only individual dislocations and pile-ups are observed, mostly tangled close to the incoherent Z-phase precipitates. Based on foil thickness measurement (t/λ) determined using EELS, the average dislocation density has been roughly estimated to be $\sim 9 \times 10^{12}$ m^{-2} in the initial state.
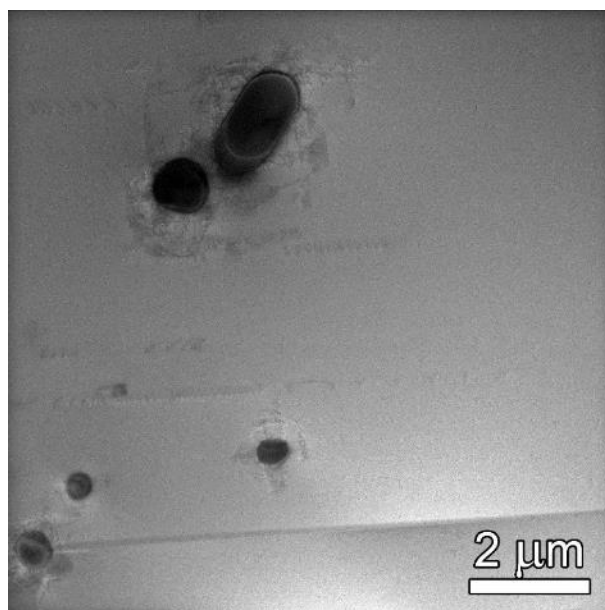
Figure 7.5: BF-STEM image of the microstructure in the initial state taken close to [001] zone axis. As a result of annealing, dislocation density is low ($\sim 9 \times 10^{12}$ m^{-2}). The only precipitates present are Z-phase complex nitrides.

7.2 Manaurite XTM

The experimental material with the trade name Manaurite XTM belongs to the class of highly-alloyed Ni-based refractory steels with austenitic matrix. The nominal composition (in wt%) of the alloy reported in datasheets delivered with the material is given in Tab. 7.2.

	Fe	Ni	Cr	Cu	Nb	Mn	Si	C	Mo	P	S	Pb	Sn	Ti	Zr
Producer Min/Max	Rest	43.0 – 48.0	35.0 – 37.0	0 – 0.25	0.5 – 1.0	0 – 1.5	1.20 – 2.00	0.40 – 0.45	0 – 0.5	0 – 0.025	0 – 0.015	20 ppm	50 ppm	Add.	Add.

Table 7.2: The nominal composition of highly-alloyed Manaurite XTM alloy (in wt%) as guaranteed by producer.

The material was supplied in the form of centrifugally cast tube. In centrifugal casting, a permanent mold is rotated continuously about its axis at relatively high speeds (usually from 300 to 3000 rpm). The molten metal is poured inside and as a result of centrifugal rotation it is thrown towards the inside surface of the outer mold wall where it solidifies after cooling. The

metal solidifies from the outside toward the center (axis) of rotation. Centrifugal casting is usually characteristic by fine-grained structure near the outer diameter as is discussed further below. On the other hand impurities and inclusions are driven to the surface of the inner diameter (to the center of rotation) and therefore in the most cases the inner and outer layers of the tube are machined away.

Based on the customer´s requirements, there is a broad range of tube types produced by Manoir Industries. However, straight pipes of 4 m in length and tube wall thickness varying from 6 to 10 mm are the most common standard. Standard type of tubes can be further manufactured, bent and welded together to produce more complex piping arrangements used in the ethylene cracking furnaces. For the purpose of research works, special tubes with the wall thickness of 28 mm were produced as shown in Fig. 7.6a. With walls being thick enough, it was possible to prepare specimens for the mechanical testing.
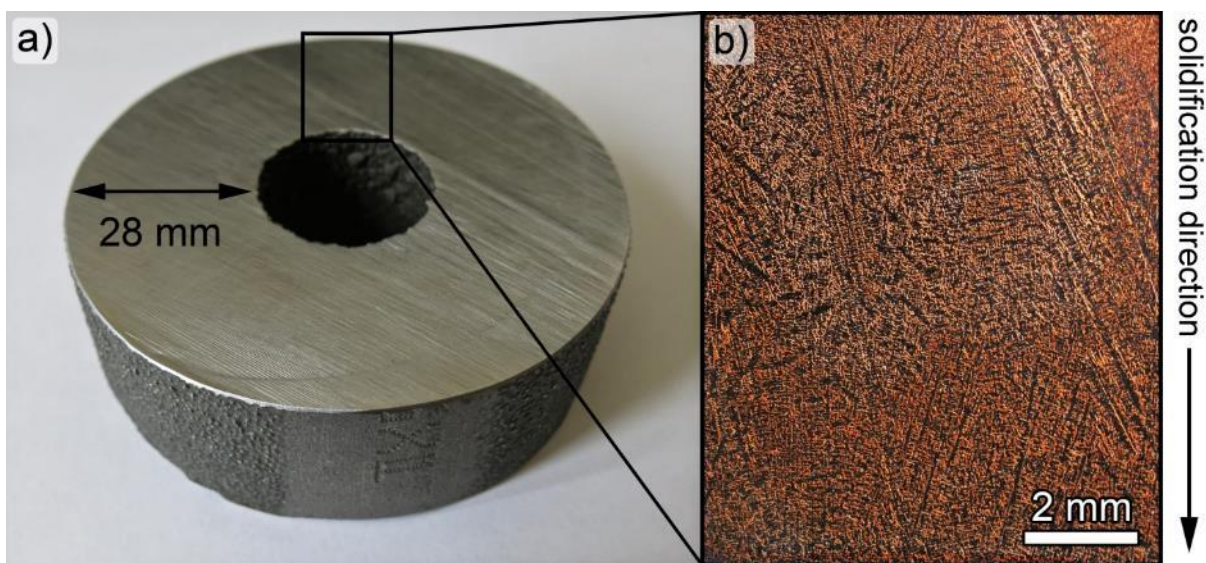
Figure 7.6: (a) Centrifugally casted pipe prepared with wall thickness of 28 mm. Outer diameter and inner diameter of the pipe is 82 mm and 26 mm, respectively. (b) Detail of polished surface visualized by light microscope reveals dendritic microstructure. Central axes of the dendrites are aligned in the.

Centrifugal casting as a method of production leads to the specific microstructure of the alloy characteristic by dendritic morphology. With the high degree of thermal undercooling in the molten metal, nucleated crystals grow preferentially along energetically favourable crystallographic directions during the solidification. As a result, each growing crystal has a distinctive, non-faceted tree-like form, known as a dendrite. As each dendritic spike grows, latent heat is transferred into the surrounding liquid restraining the formation of other spikes in its nearest vicinity. Usually, the spacing of primary dendrites and secondary dendritic arms is regular.

Two types of grains can be observed. Fine equiaxed grains are found in the areas where solidification of the melt originated while large columnar elongated grains aligned parallel with the casting direction form the major part of the tube wall. During post-manufacturing, outer layer of the tube wall containing equiaxed grains is usually machined away.

Overview image of the characteristic microstructure with the dendritic morphology in initial state obtained on the polished surface by light microscope is shown in Fig. 7.6b. Clearly, the central axes of the dendrites are aligned along the solidification direction.

Dendritic morphology of the alloy was studied further in detail by use of scanning electron microscopy techniques. Electron backscattered diffraction was used on the polished surface to reveal individual grains, bring further information about their misorientation and the character of the grain boundaries between them. In Fig. 7.7a, the dendritic structure is visualized by secondary electrons imaging mode. Corresponding EBSD scan in Fig. 7.7b then reveals individual dendritic grains, which have columnar character and are aligned along the casting direction. Average misorientation of the grains determined from the EBSD scan is about 31 degrees, the boundaries between the dendritic grains are therefore the large angle boundaries. Detail of a few columnar grains and their grain boundaries is shown in Fig. 7.8a and Fig. 7.8b in secondary electrons imaging mode and corresponding EBSD scan, respectively. It is well resolved that the grain boundaries have serrated character. Moreover, they are decorated with numerous primary precipitates formed during solidification. The precipitates are located not only at the grain boundaries, but also within the columnar grains where they are aligned along the axes of dendritic spikes.
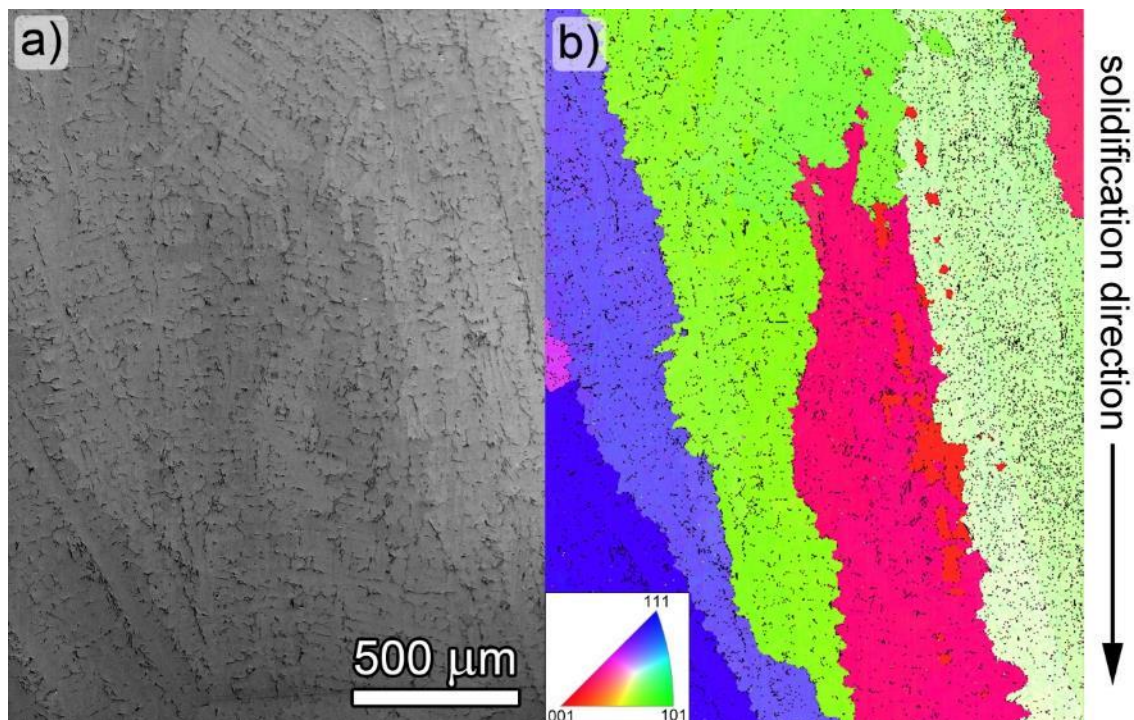
Figure 7.7: (a) SEM image taken in secondary electrons imaging mode shows typical microstructure in the as-received condition of the material. (b) Corresponding EBSD scan reveals individual dendritic grains, which have columnar character and are aligned along the casting direction. Average misorientation of the grains determined from EBSD scan is about 31 degrees.
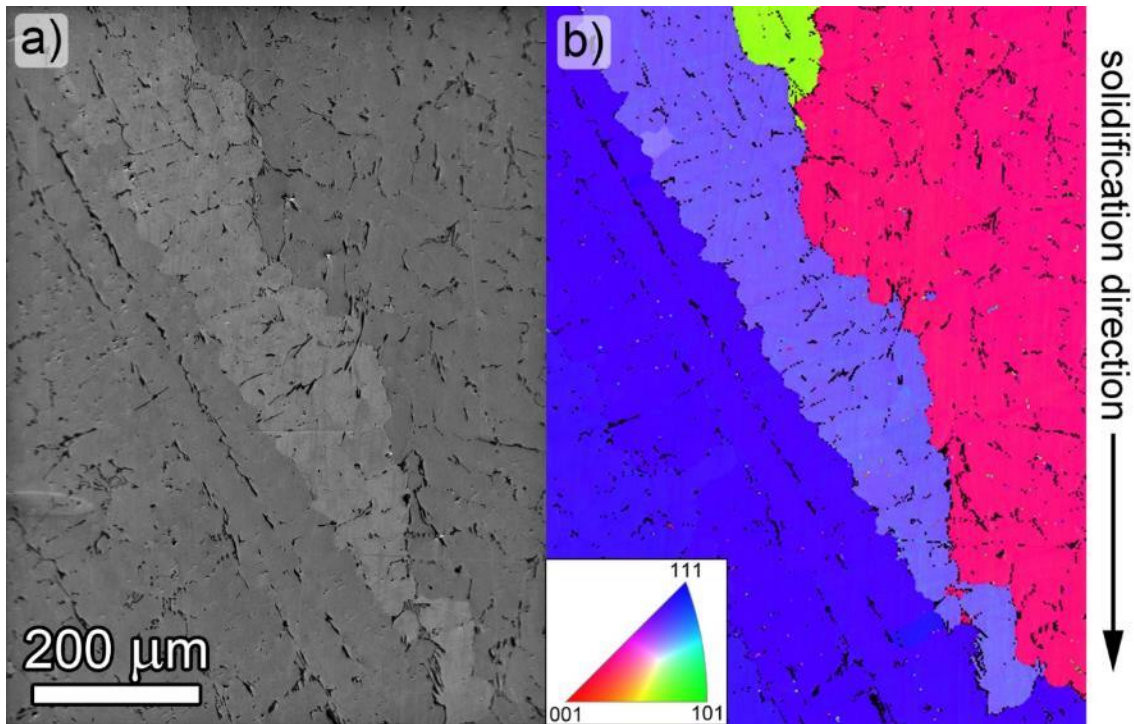
Figure 7.8: (a) SEM image showing dendritic structure of grains in detail accompanied by corresponding EBSD scan (b).
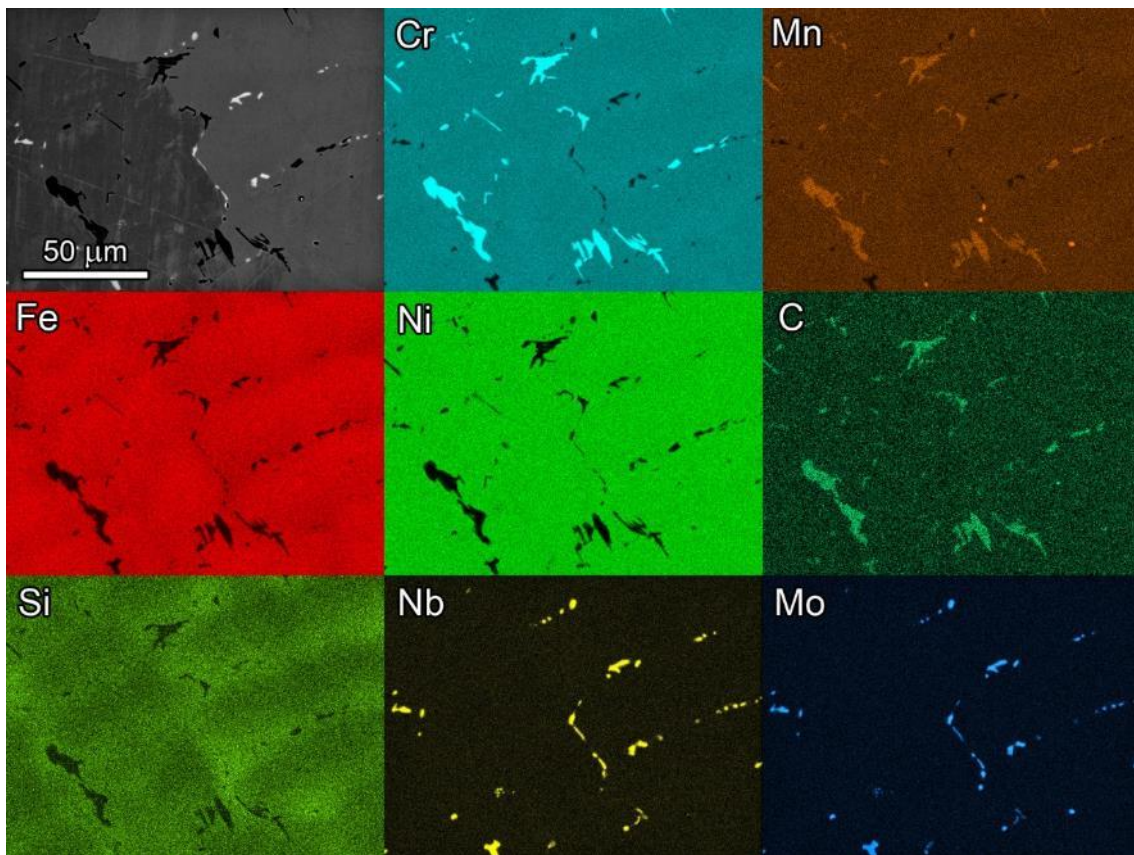
Figure 7.9: SEM-EDS mapping performed at the grain boundary. Numerous $M_7C_3/M_{23}C_6$ precipitates rich in Cr are found in the areas in between of dendritic spikes and also at the grain boundaries. Smaller carbides of MC type rich in Nb are found there as well.

In Fig. 7.9, SEM-EDS analysis of the area at the grain boundary maps distribution of the chemical elements. Two populations of precipitates are observed. Notably larger and more numerous are precipitates rich in Cr, Mn and C. As will be discussed later, they are mostly M_7C_3 or $M_{23}C_6$ Cr-rich carbides. Smaller are then carbides of MC type rich in Nb and Mo. In addition, a few spherical particles rich in Ti were found as well (see Fig. 7.10).
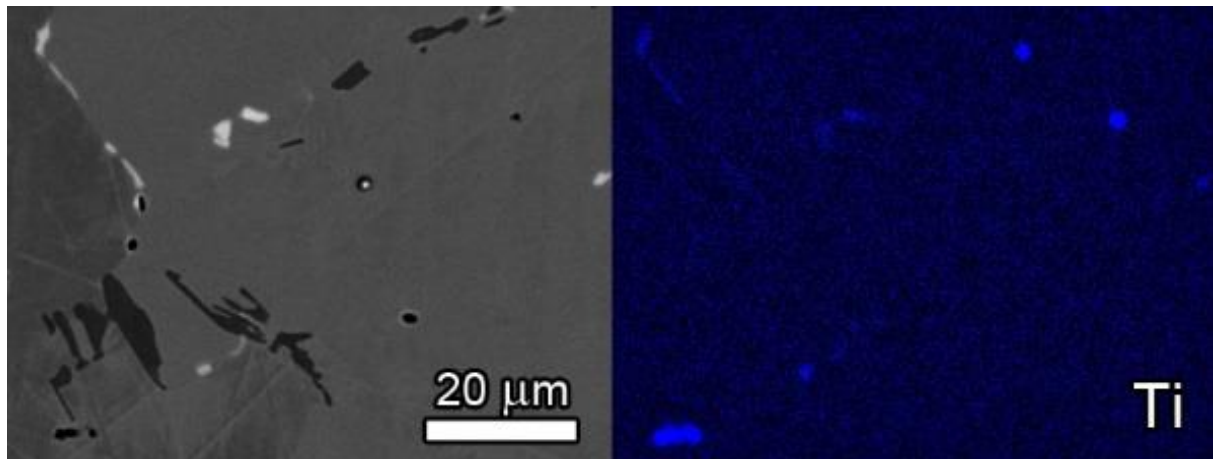
Figure 7.10: Along with two populations of $M_7C_3/M_{23}C_6$ Cr-rich and MC Nb-rich carbides also particles rich in Ti were detected by SEM-EDS mapping.

Cast dendritic structure can be characteristic by inhomogeneous distribution of matrix elements within the dendritic grains. This is well documented by SEM-EDS linescan which was performed across several dendritic spikes perpendicular to their growth axis as shown in Fig. 7.11a. It is clear that the content of Fe is decreased in areas between the dendritic spikes, while content of Si and Cr is notably increased. Both content of Fe and Cr in matrix varies within 5 wt.% as shown in Fig. 7.11b.
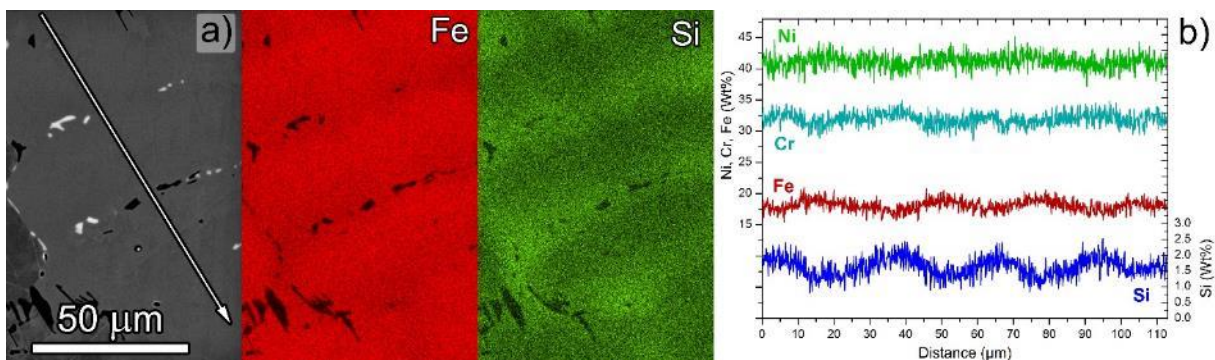
Figure 7.11: SEM-EDS linescan was performed across several dendritic spikes perpendicular to their growth axis to reveal content variation as highlighted by white arrow. (a) SEM image is accompanied by EDS maps showing Fe and Si content in the area. (b) SEM-EDS linescan demonstrates, that Fe is depleted in the regions between the dendritic spikes while Si content is notably increased there.

Joubert et al. [29] used the method called computer coupling of phase diagrams and thermochemistry (CALPHAD) based on different thermodynamic databases to determine phase equilibrium of Manaurite XM alloy. As was already noted in Chapter 1.2, Manaurite

XM is grade very similar to the Manaurite XTM. They have found out that in the as-cast material, primary precipitates are mostly eutectic binary carbides M_7C_3 and $M_{23}C_6$ rich in Cr and MC carbides rich in Nb and also Ti. For some thermodynamic databases, also a Nb(Ti)-Ni silicide called G-phase is reported, however it has not been confirmed experimentally.

As a result of thermal exposure at high temperatures above 700°C, along with secondary intra-granular precipitation of $M_{23}C_6$ Cr-rich carbides, eutectic primary carbides of M_7C_3 type were observed to decompose and transform into $M_{23}C_6$ type.

8. Mechanical behavior of Sanicro 25

8.1 Tensile tests

Two sets of monotonic loading experiments were performed. First, the effect of temperature on the performance of material during tensile test was studied. Tensile tests at room and at an elevated temperature of 700°C were done using MTS servo-hydraulic machine, hydraulic collet grips and split resistance furnace. Loading was performed under total strain control at strain rate 2×10^{-3} s^{-1}. Strain was measured using an axial extensometer with 12 mm base.

At the onset of the tensile test both the displacement and the strain were measured using the extensometer. When the maximum strain range of the extensometer (approx. 8%) was reached the extensometer was removed and tensile test continued with control of the displacement and the displacement rate corresponding to the selected constant strain rate. Engineering strain was later calculated from the displacement.
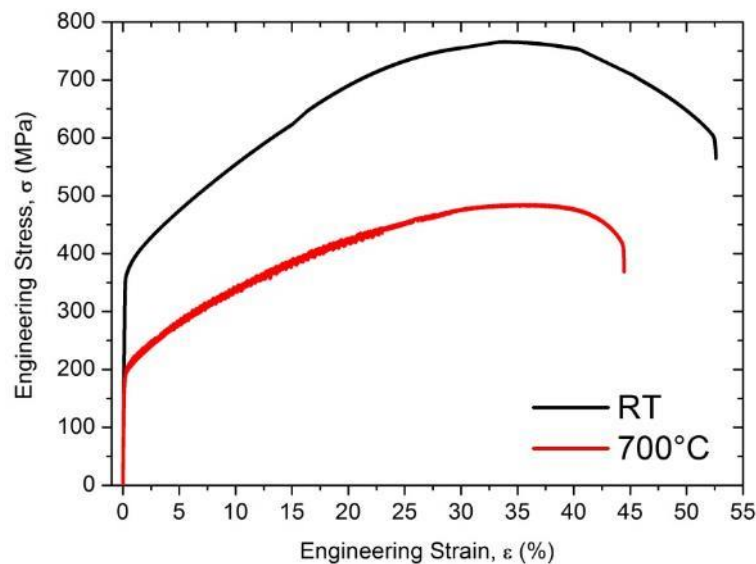
Figure 8.1: Tensile stress-strain curves of Sanicro 25 at room temperature and at 700°C.

Tensile stress-strain curves of the Sanicro 25 steel obtained at room and at elevated temperature are shown in Fig. 8.1. Tensile stresses and yield strength at a temperature of 700°C are substantially lower than those at room temperature. Characteristic tensile parameters are displayed in Tab. 8.1a.

Additional tensile experiments were performed to study difference between as received and solution annealed (initial) state and also to study the effect of aging at 700°C on the mechanical properties of the material. Four different samples were selected for the room temperature tensile test – two specimens representing as received and initial state of the material and two specimens after 6 h and 153 h of thermal exposure at 700°C in air (cooling to room temperature was done in air). Comparison of tensile stress-strain curves of these specimens is shown in Fig. 8.2 and characteristic tensile parameters are summarized in Table 8.1b.
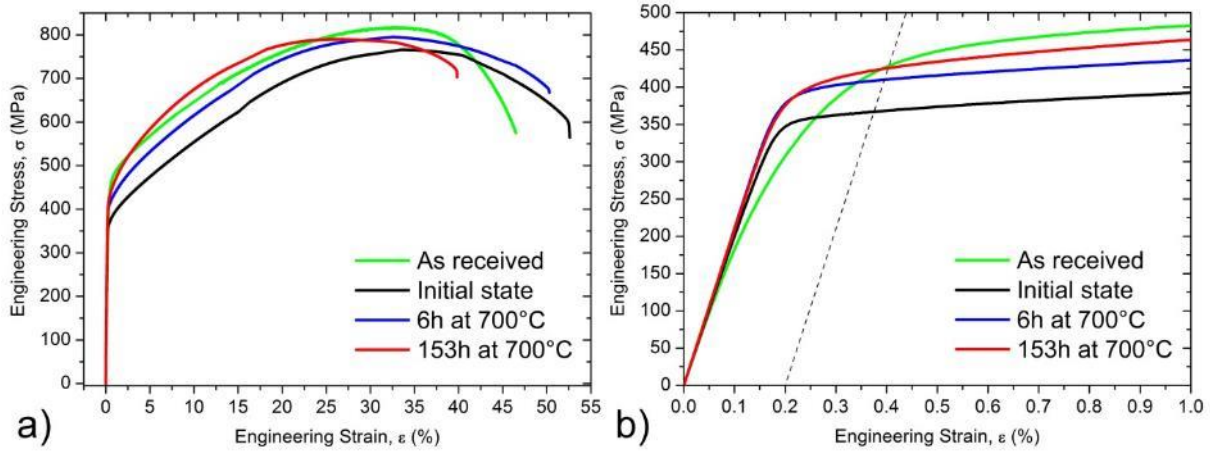
Figure 8.2: (a) Comparison of room temperature tensile stress-strain curves of specimen representing initial state of the material and specimens aged at a temperature of 700°C for 6 and 153 h. (b) Detail of elastic part of stress-strain curves emphasizing increase of yield strength as a result of thermal exposure.

Specimen	E [GPa]	Y.S. at 0.2% [MPa]	U.T.S. [MPa]	Total fracture strain [%]
(a) Effect of testing temperature				
RT	198	368	765	52
700°C	150	198	485	44
b) Effect of thermal exposure at 700°C				
As received, RT	197	433	816	47
Initial state, RT	198	368	765	52
Aged 6h, RT	209	410	795	50
Aged 153h, RT	208	426	790	40

Table 8.1: Tensile properties of Sanicro 25. (a) Characteristic tensile parameters are compared for material tested at room and elevated temperature and (b) for material in as received and initial state and after thermal exposure to 700°C in air tested at room temperature.

Mechanical data clearly indicate that the exposure of the material in initial state to a temperature of 700°C leads to notable increase of yield stress, ultimate tensile strength while the total fracture strain slightly decreases. Already after 6 h spent at 700°C, yield stress and ultimate tensile strength increases by 42 MPa (+11 %) and 30 MPa (+4 %), respectively. With further thermal exposure leading to total 153 h spent at a temperature of 700°C, additional increase by 16 MPa (+5 %) is observed for yield stress while ultimate tensile strength slightly decreases to 790 MPa. Microstructural origins of this mechanical behaviour and consequences having governing role in the increased cyclic strength of this alloy are discussed later in the text.

8.2 Cyclic response of the material

Cyclic hardening/softening curves of specimens loaded over a wide interval of total strain amplitudes at room and elevated temperature are plotted in Figs. 8.3a and 8.3b, respectively. Stress amplitude σ_a is plotted vs. number of cycles N. Corresponding plots of plastic strain amplitude ε_{ap} versus number of cycles N are shown in Fig. 8.4.
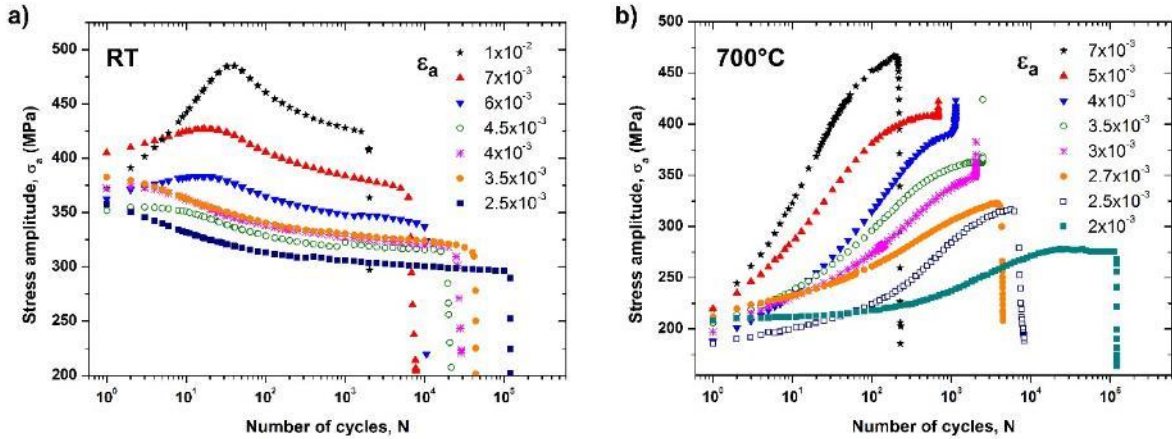
Figure 8.3: Cyclic hardening/softening curves of Sanicro 25 at (a) room temperature and at (b) temperature of 700°C. Stress amplitude σ_a is plotted vs. number of cycles N. Strain amplitudes are given in the Figures.
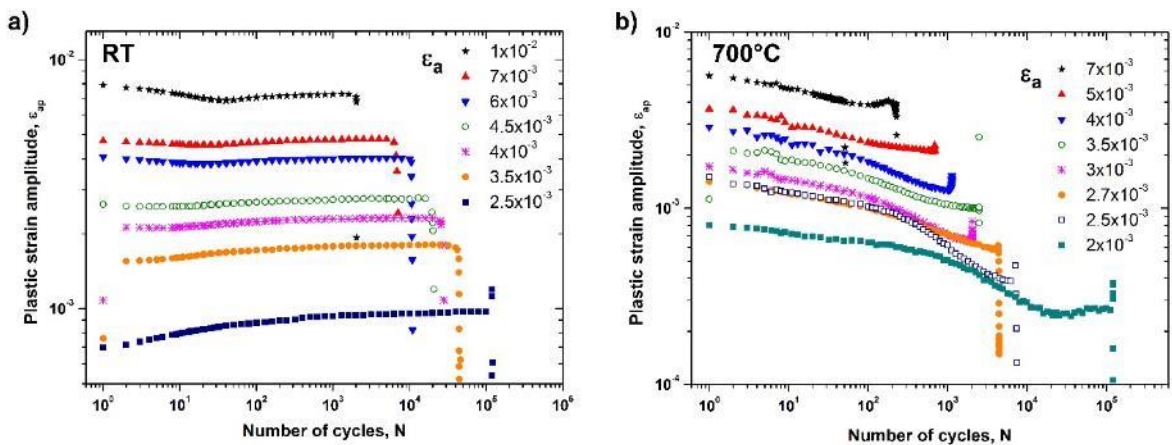
Figure 8.4: Cyclic hardening/softening curves of Sanicro 25 at (a) room temperature and at (b) temperature of 700°C. Plastic strain amplitude ε_{ap} is plotted versus number of cycles N.

At room temperature cycling with total strain amplitudes lower than 5×10^{-3} material exhibits cyclic softening which starts from the beginning of loading and persists until failure. In cycling with strain amplitudes higher than 5×10^{-3} significant cyclic hardening is present during the initial period of loading (about 20-30 cycles) followed afterwards by cyclic softening stage for the rest of the fatigue life. The stress amplitude and plastic strain amplitude has a tendency to saturation during the fatigue life for all strain amplitudes.

Substantially different behaviour is observed in cyclic loading at temperature 700°C. Plot in Fig. 8.3b shows appreciable cyclic strengthening for all strain amplitudes. The initial increase of the stress amplitude with each cycle indicates a notable work-hardening effect. The higher

the applied strain amplitude, the more significant the increase of the cyclic stress is observed during the initial period of cycling. With further cyclic loading, the hardening rate decreases and the tendency to reach saturation of the cyclic stress is noticed, especially in the case of lower strain amplitude tested samples, i.e. samples tested for the highest number of cycles. Duration of fatigue test, i.e. the time of thermal exposure of specimens, ranged from 153 to 6 h for the lowest and highest strain amplitude, respectively.

8.3 Cyclic stress-strain curves

The fraction of fatigue life during which the stress and plastic strain amplitudes are close to the saturated values is higher in room temperature cycling than in cycling at 700°C. In both cases, however, the major part of the fatigue life can be characterized by the stress and plastic strain amplitudes at half-life. These values were thus used for the construction of the cyclic stress-strain curves (CSSCs), which are shown in Fig. 8.5.
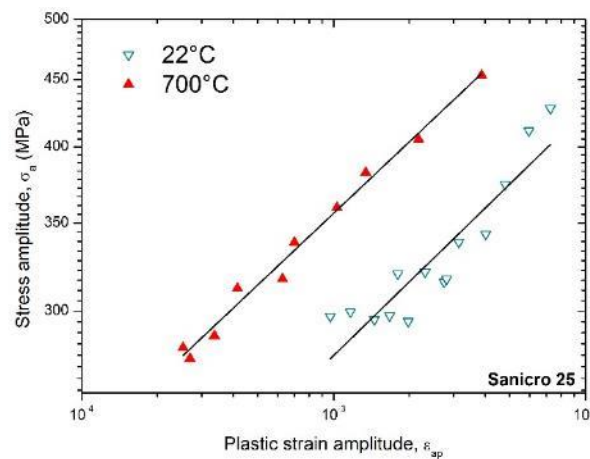
Figure 8.5: Cyclic stress-strain curves of Sanicro 25 at two temperatures.

Unlike conventional austenitic steels, the CSSC of Sanicro 25 at a temperature of 700°C is substantially above the curve plotted at room temperature. For selected stress amplitude, reached amplitude of plastic strain is lower at a temperature of 700°C than at room temperature. Curves were fitted by the power law

$$\sigma_{\mathrm{a}} = K'(\varepsilon_{ap})^{n'}. \tag{8.1}$$

The fatigue hardening coefficient K' and fatigue hardening exponent n' were evaluated using least square fitting. They are shown in Tab. 8.2.

8.4 Fatigue life curves

Fatigue life curves were plotted in Coffin-Manson plot in Figure 8.6a and in derived Wöhler plot in Figure 8.6b. It is evident that both plots in cycling at room temperature shows longer fatigue life than in cycling at a temperature of 700°C. The Coffin-Manson plot expresses the resistance of material to the cyclic plastic strain. Experimental data were fitted by the Coffin-Manson law

$$\varepsilon_{\mathrm{ap}} = \varepsilon'_f (2N_f)^c. \tag{8.2}$$

Parameters ε'_f and c were evaluated by least square fitting and are shown in Tab. 8.2. Fig. 8.6a shows that when compared to room temperature the cycling of Sanicro 25 at a temperature of 700°C results in approximately 50 times reduction of the fatigue life for equal saturated plastic strain amplitudes.
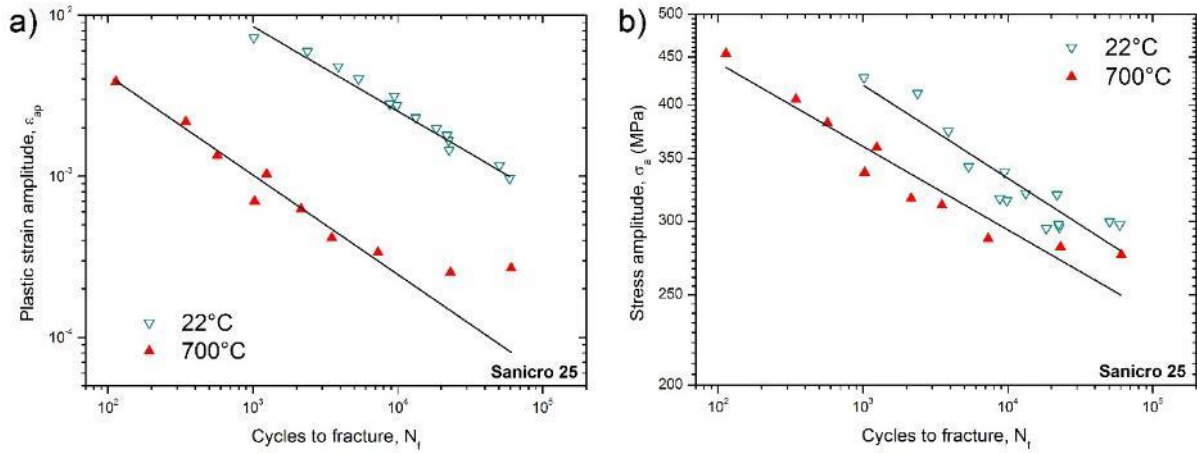
Figure 8.6: Sanicro 25. (a) Coffin-Manson fatigue life curves and (b) Derived Wöhler fatigue life curves at two temperatures.

Derived Wöhler plots shown in Fig. 8.6b were fitted with the Basquin relation

$$\sigma_{\mathrm{a}} = \sigma'_f (2N_f)^b \tag{8.3}$$

Parameters σ'_f and b determined by least square fitting are again listed in summarizing Tab. 8.2 along with the rest of the low cycle fatigue parameters of Sanicro 25 at two temperatures.

T [°C]	K' [MPa]	n'	ε_f'	c	σ_f' [MPa]	b [MPa]
22	1006	0.186	0.700	-0.526	962	-0.100
700	1243	0.181	0.090	-0.539	797	-0.090

Table 8.2: Low cycle fatigue parameters of Sanicro 25 at two temperatures.

9. Mechanical behavior of Manaurite XTM

9.1 Tensile tests

Four tensile tests were performed at different temperatures using MTS servo-hydraulic machine and hydraulic collet grips. Loading was done under total strain control at strain rate 1×10^{-3} s^{-1}. Strain was measured using an extensometer. Heating of the sample was maintained by a heating induction coil and the temperature was measured by thermocouples on three different places of the sample. Tensile stress-strain curves of Manaurite XTM steel obtained at room temperature and at elevated temperatures of 600°C, 900°C and 1050°C are shown in Fig. 9.1a.
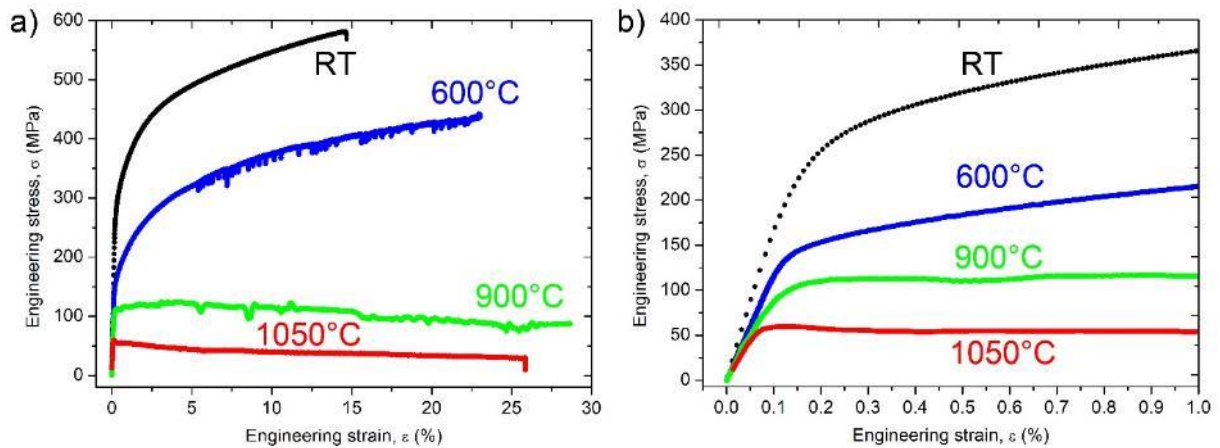
Figure 9.1: (a) Comparison of tensile stress-strain curves of Manaurite XTM obtained at RT, 600°C, 900°C and 1050°C. (b) Detail of stress-strain diagrams highlighting notable decrease of yield strength at elevated temperatures.

Temperature dependence of characteristic tensile parameters was studied. Young modulus of elasticity E, yield stress $R_{p0.2}$ and $R_{p0.02}$, ultimate tensile strength σ_f and total fracture strain ε_f are given in Tab. 9.1.

Temperature	RT	600°C	900°C	1050°C
Young Modulus E (GPa)	172	122	107	89
Yield Strength at 0.2% (MPa)	302	170	118	56
Yield Strength at 0.02% (MPa)	224	136	96	58
Ultimate Tensile Strength (MPa)	581	442	124	59
Total Fracture Strain (%)	14.5	>23	>28	>25

Table 9.1: Summary of tensile properties of Manaurite XTM at four different temperatures.

It is clear that the elevated temperature affects all the characteristic tensile parameters. Modulus of elasticity, yield and ultimate tensile strength decreases notably as the material becomes very ductile close to the operation temperature of 1050°C.

With elastic part of the stress-strain curve being negligibly small at service temperature the deformation is driven mostly in the plastic region. The transition from the elastic zone through

a yield point to the plastic zone is rapid and followed by a strong immediate relaxation. With force remaining constant large strains are reached by relaxation of the material.

Since the high temperature stress-strain curves have sharp yield point, both the yield strength at 0.2% and at 0.02% of total strain was determined. Temperature dependence of both parameters is plotted in Fig. 9.2b.
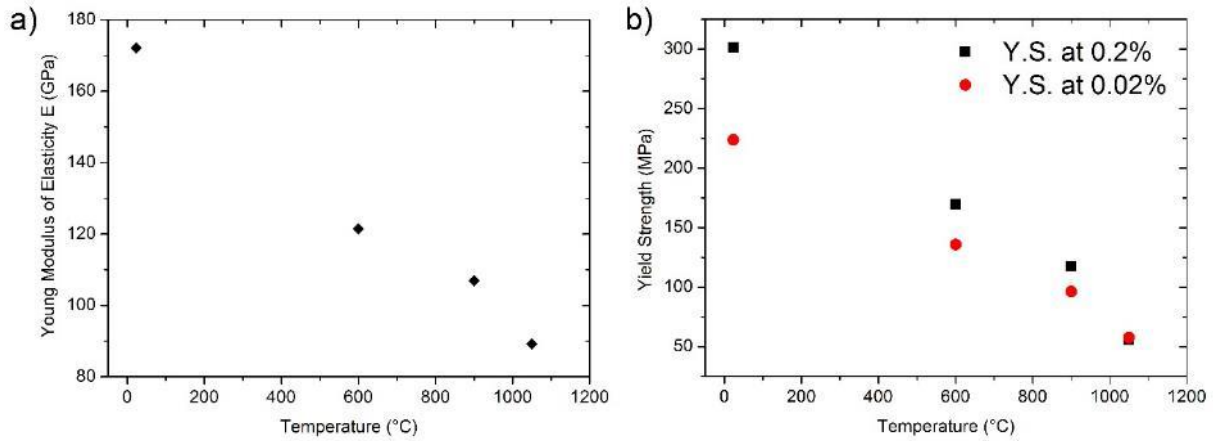
Figure 9.2: Temperature dependence of Young modulus (a) and yield strength (b).

Tensile stresses and yield strength of material at elevated temperatures are substantially lower than those at room temperature (see Fig. 9.1). At temperature of 900°C and 1050°C, Manaurite XTM shows easy plastic flow and no work hardening.

9.2 Tensile tests – investigation of material anisotropy

Anisotropy of mechanical properties of Manaurite XTM at room temperature monotonic loading was studied using small samples prepared from the tube wall. They were extracted with two different orientations - radial and tangential - with respect to the tube axis, as was discussed in detail previously in chapter 5.1.
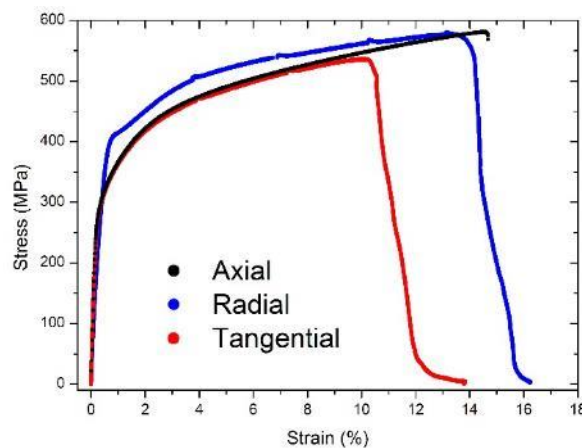
Figure 9.3: Comparison of tensile stress-strain curves obtained at room temperature with three different types of samples prepared from the tube wall parallel with axial, radial and tangential direction.

Tensile tests were performed at room temperature and with same strain rate as in case of standard cylindrical specimens parallel with the tube (axial specimens). To mount small samples to standard grip system, adapters had to be fabricated and used. Comparison of tensile stress-strain curves corresponding to samples tested in axial, radial and tangential direction is shown in Fig. 9.3.

Orientation of sample	Axial	Radial	Tangential
Yield Strength at 0.2% (MPa)	302	349	298
Yield Strength at 0.02% (MPa)	224	148	196
Ultimate Tensile Strength (MPa)	581	577	536
Total Fracture Strain (%)	14.5	14-16	11-14

Table 9.2: Summary and comparison of parameters obtained from room temperature tensile experiments performed on three different types of samples prepared from the tube wall parallel with axial, radial and tangential direction.

Tab. 9.2 shows comparison of obtained characteristic tensile parameters in axial, radial and tangential direction. It is clear that in axial and tangential directions, i.e. directions perpendicular to the central axes of dendrites, tensile parameters differ notably from the radial direction. Yield strength at 0.2% of total strain is higher by approximately 16%. Also the shape of tensile stress-strain curve obtained for radial direction is slightly different from that in axial and tangential directions. The conclusion is that Manaurite XTM should be considered as close to anisotropic material, in spite of its aligned dendritic microstructure.

9.3 Cyclic response of the material

Cyclic hardening/softening curves of specimens loaded over a wide interval of total strain amplitudes at room and elevated temperature are plotted in Fig. 9.4a and Fig. 9.4b, respectively. Stress amplitude σ_a is plotted vs. number of cycles N. Corresponding plots of plastic strain amplitude ε_{ap} versus number of cycles N are shown in Fig. 9.5.
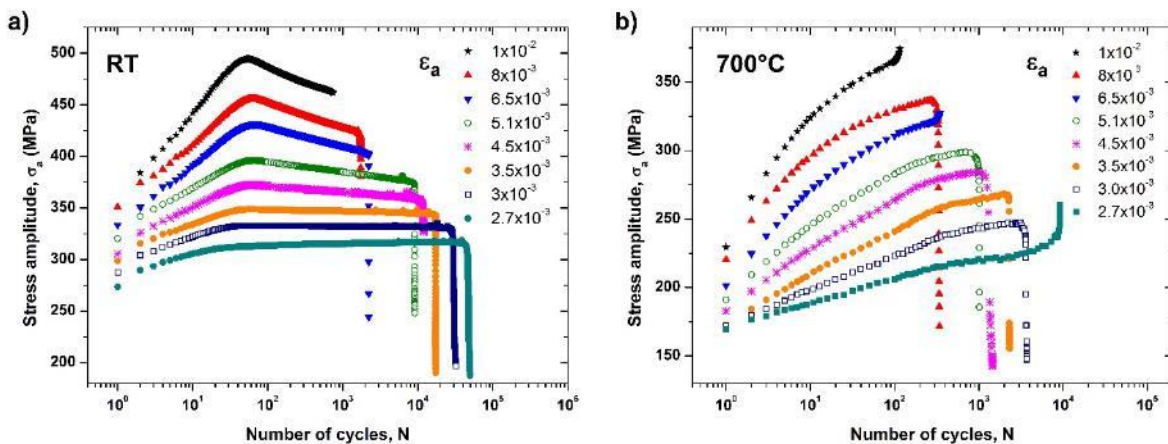

Figure 9.4: Cyclic hardening/softening curves of Manaurite XTM at (a) room temperature and at (b) temperature of 700°C. Stress amplitude σ_a is plotted vs. number of cycles N.
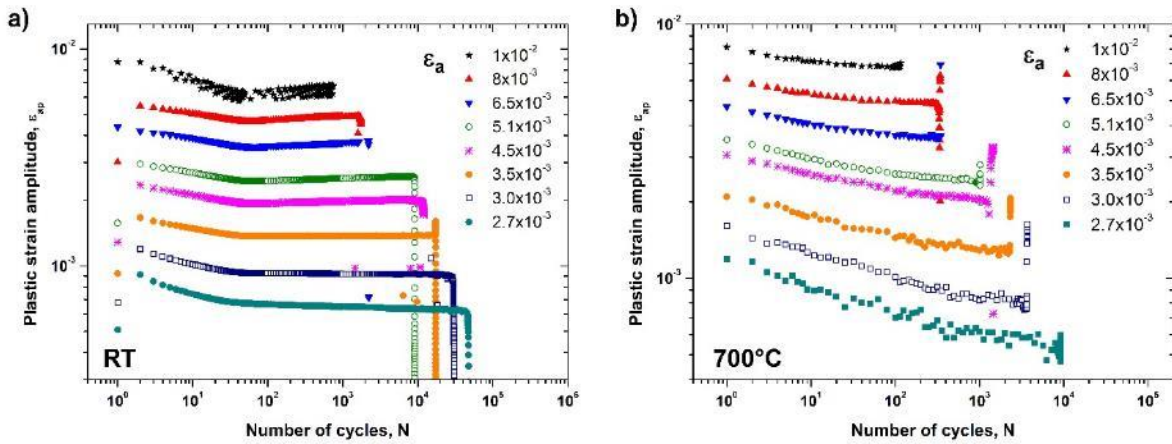
Figure 9.5: Cyclic hardening/softening curves of Manaurite XTM at (a) room temperature and at (b) temperature of 700°C. Plastic strain amplitude ε_{ap} is plotted versus number of cycles N.

In case of room temperature cyclic loading, Manaurite XTM exhibits initial hardening for all strain amplitudes (Fig. 9.5a). The higher the applied strain amplitude, the more significant the increase of the cyclic stress is observed during the initial period of cycling. Specimens tested with strain amplitude lower than 3.5×10^{-3} have a tendency to saturation shortly after about 40-60 loading cycles. On contrary, in loading with higher strain amplitudes, appreciable cyclic softening follows immediately after initial hardening period. Again, the higher the applied strain amplitude, the higher the rate of cyclic softening is after inflection point. The plastic strain amplitude has a tendency to saturation during the fatigue life for all strain amplitudes.

At a temperature of 700°C, material exhibits cyclic strengthening for all strain amplitudes. The rate of hardening, i.e. the increment of stress amplitude per cycle, decreases immediately from the beginning after first cycle. With further cycling, tendency to saturation of the stress amplitude is clearly visible for all strain amplitudes (see Fig. 9.5b).

9.4 Cyclic stress-strain curves

The fraction of fatigue life during which the stress and plastic strain amplitudes are close to the saturated values is higher in room temperature cycling than in cycling at 700°C. In both cases, however, the major part of the fatigue life can be characterized by the stress and plastic strain amplitudes at half-life. These values were thus used for the construction of the cyclic stress-strain curves, which are shown in Fig. 9.6.

The CSSC of Manaurite XTM at a temperature of 700°C is below the curve plotted at room temperature. For selected stress amplitude, reached amplitude of plastic strain is much higher at a temperature of 700°C than at room temperature. Curves were fitted by the power law stated previously by Eq. (8.1). The fatigue hardening coefficient K' and fatigue hardening exponent n' were evaluated using least square fitting. They are shown in Tab. 9.3.
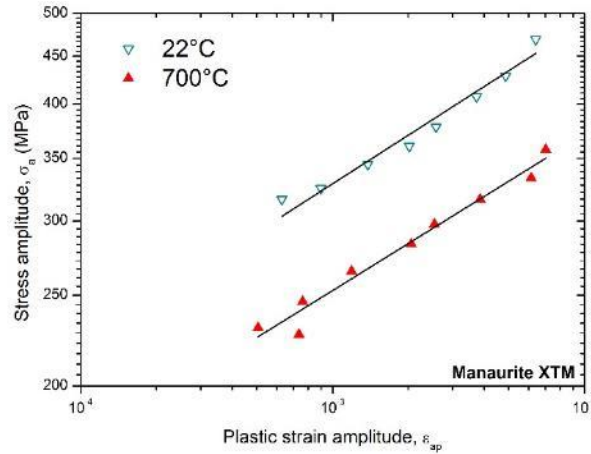
Figure 9.6: Cyclic stress-strain curves of Manaurite XTM at two temperatures.

9.5 Fatigue life curves

Fatigue life curves were plotted in Coffin-Manson plot in Fig. 9.7a and in derived Wöhler plot in Fig. 9.7b. It is evident that both plots in cycling at room temperature shows longer fatigue life than in cycling at a temperature of 700°C. The Coffin-Manson plot expresses the resistance of material to the cyclic plastic strain. Experimental data were fitted by the Coffin-Manson law defined by Eq. (8.2). Parameters ε'_f and c were evaluated by least square fitting and are shown in Tab. 9.3. Fig. 9.7a shows that when compared to room temperature the cycling of Manaurite XTM at a temperature of 700°C results in reduction of fatigue life by factor of 7.
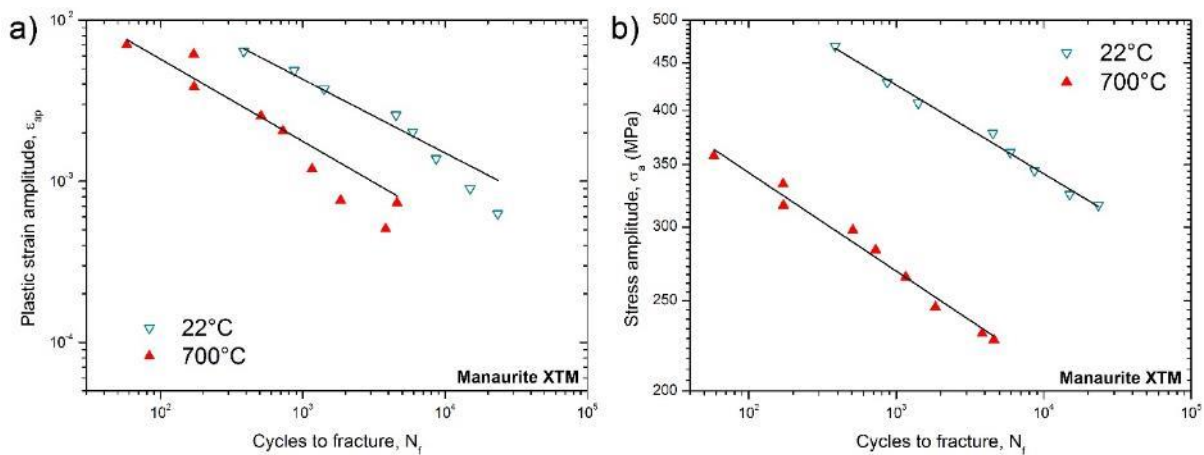
Figure 9.7: Manaurite XTM. (a) Coffin-Manson fatigue life curves and (b) Derived Wöhler fatigue life curves at two temperatures.

Derived Wöhler plots shown in Fig. 9.7b were fitted with the Basquin relation (Eq. 8.3). Parameters σ'_f and b determined by least square fitting are listed in summarizing Tab. 9.3 along with the rest of the low cycle fatigue parameters of Manaurite XTM at two temperatures.

T [°C]	K' [MPa]	n'	ε_f'	c	σ_f' [MPa]	b [MPa]
22	1084	0.173	0.138	-0.457	877	-0.095
700	802	0.167	0.085	-0.510	600	-0.106

Table 9.3: Low cycle fatigue parameters of Manaurite XTM at two temperatures.

9.6 Cyclic response – investigation of material anisotropy

Cyclic experiments were performed at room temperature and with same strain rate as in case of standard cylindrical specimens prepared for testing in axial direction. Again, adapters were used for mounting small samples into the grip system of mechanical testing system. Tests were performed at room temperature with three different total strain amplitudes, in particular 3×10^{-3}, 5×10^{-3} and 1×10^{-2}. Hardening/softening curves are plotted in Fig. 9.8a while graph showing corresponding plastic strain amplitudes as a function of number of cycles is plotted in Fig. 9.8b. It is clear that the cyclic response of material is almost the same in case of axial and tangential directions for total strain amplitudes $5\times10^{-3}$ and 1×10^{-2}. In case of amplitude 3×10^{-3} reached level of plastic strain amplitude is slightly lower for tangential direction. Regarding cyclic response of Manaurite XTM in radial direction, stress amplitude is slightly lower for amplitude 1×10^{-2}, while for total strain amplitudes 5×10^{-3} and 3×10^{-3} it is similar as in case of axial testing. Largest difference has been found for testing at strain amplitude 3×10^{-3} where reached plastic strain amplitude for radial direction is notably lower than in axial and tangential directions.
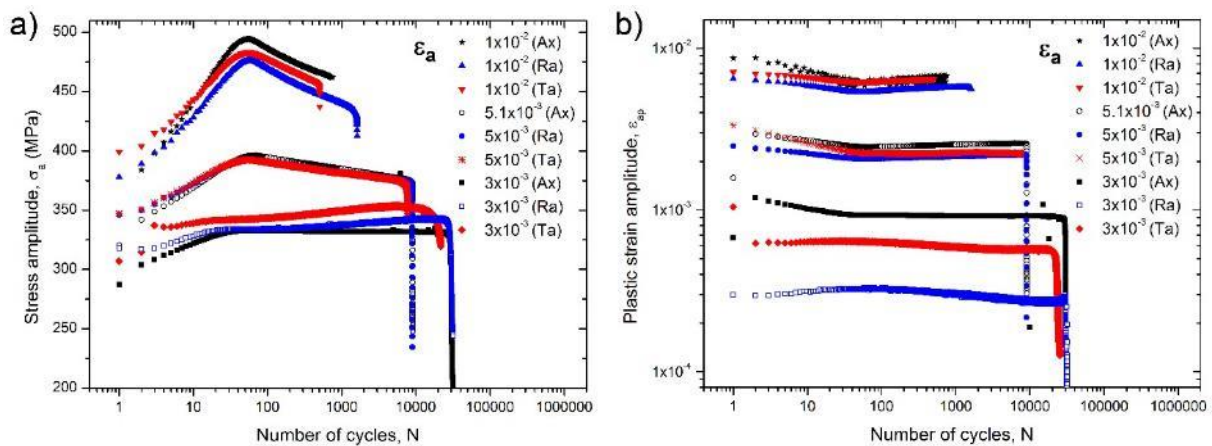
Figure 9.8: (a) Comparison of cyclic hardening/softening curves of fatigued samples produced with "axial", "radial" and "tangential" orientation for three total strain amplitudes. (b) Corresponding plot showing plastic strain amplitude as a function of number of cycles.

9.7 CSSC and fatigue life curves – investigation of material anisotropy

Fatigue life curves were determined for anisotropy tests in radial and tangential. Despite the fact that sets of only three fatigued samples were used for radial and tangential direction, results were compared to get at least approximate insight into the differences in behavior and properties of material with respect to the type of direction used.
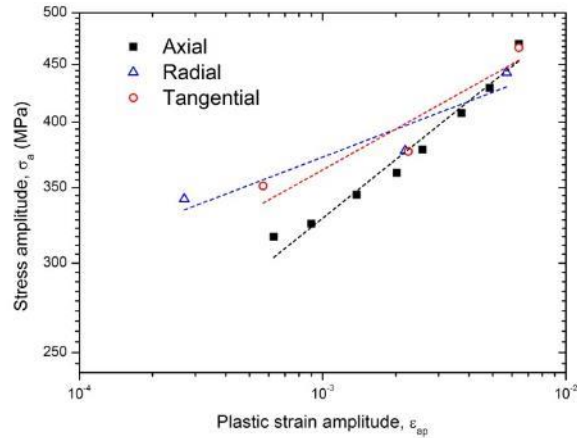
Figure 9.9: Comparison of cyclic stress-strain curves of fatigued samples produced in "axial", "radial" and "tangential" direction.

Comparison of cyclic stress-strain curves of fatigued samples produced in axial, radial and tangential direction is shown in Fig. 9.9. It seems that the lower the stress amplitude the higher the difference between the reached plastic strain amplitude is. For example in radial direction, for stress amplitude slightly below 350 MPa, reached plastic strain amplitude is almost by one magnitude lower than in axial direction. When considering the distribution of measured points in cyclic stress-strain curves, there is a slight indication that two different mechanisms of deformation could be present – one at high stress amplitudes and one at low stress amplitudes.

Comparison of Coffin-Manson fatigue life curves of fatigued samples produced in axial, radial and tangential direction is shown in Fig. 9.10a. Again, it is evident that for lower reached plastic strain amplitudes, fatigue life is shorter in radial direction, while in axial and in tangential direction it is comparable.
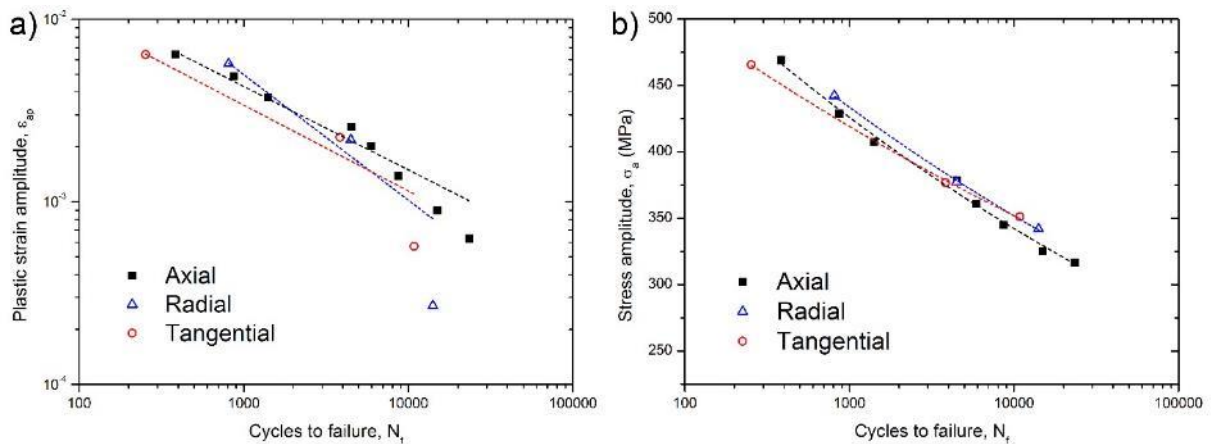
Figure 9.10: (a) Comparison of Coffin-Manson fatigue life curves of fatigued samples produced in "axial", "radial" and "tangential" direction. (b) Derived Wöhler fatigue life curves.

In Fig. 9.10b, Derived Wöhler fatigue life curves are shown for samples tested in axial, radial and tangential direction. All three curves are consistent and reached cycles to failure for selected stress amplitudes are almost the same for all three directions.

10. Microstructural evolution – Sanicro 25

10.1 Microstructural changes as a result of cyclic loading at room temperature

10.1.1 Low strain amplitudes

Microstructural changes in the material as a result of cyclic loading at room temperature were investigated by use of conventional transmission electron microscopy (CTEM) methods. TEM foils of three different types were produced for each studied sample as was mentioned in Chapter 6. Tens of grains were investigated on each foil and selected grains were then subjected to a detailed analysis in terms of crystallography. Sample loaded with total strain amplitude $\varepsilon_a = 3.5 \times 10^{-3}$ (saturated plastic strain amplitude $\varepsilon_{aps} = 1.8 \times 10^{-3}$) was selected as a representative for the study of the dislocation arrangements at conditions of low strain amplitude.
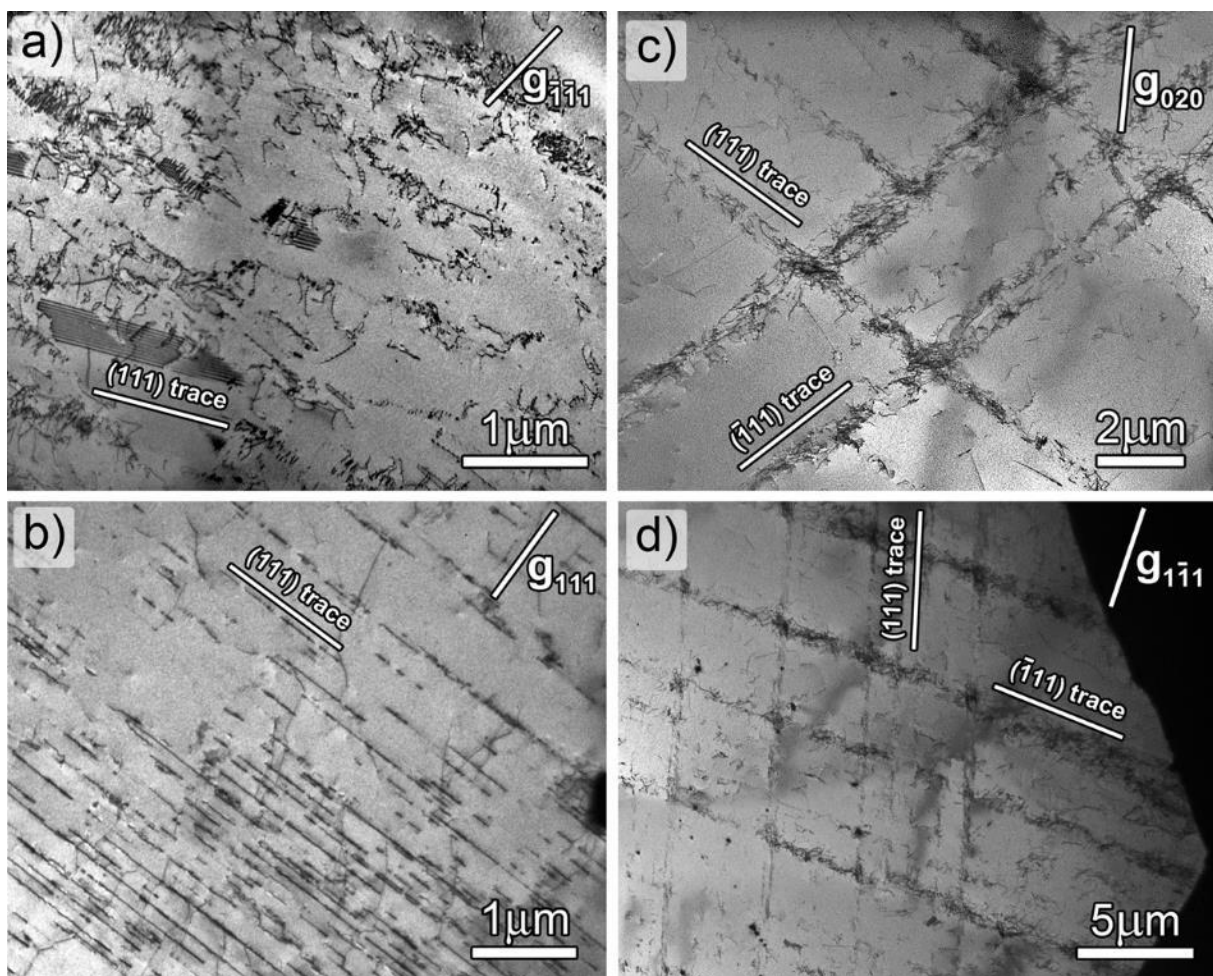
Figure 10.1: Overview of typical dislocation structures observed at low strain amplitudes after failure. (a) Planar arrangement with individual dislocations, pile-ups, stacking faults etc. similar to the as received condition. (b) Planar structure with onset of localization of slip to primary slip plane. (c) (d) Two intersecting systems of high dislocation density bands separated by dislocation-poor regions.

In the case of planar structures in typical representative of conventional Fe-Ni-Cr based austenitic steels, alloy of 316L type, dislocations gliding on primary planes {111} are

distributed relatively randomly within the volume of grains [14, 16–18, 128]. This type of planar microstructure was observed in Sanicro 25 as well, but the general character is different. Fig. 10.2 presents typical deformation microstructure at the end of fatigue life and it could be seen that in majority of grains there is a tendency to dislocation generation and their arrangement in thin parallel bands with high dislocation density which are separated by areas almost free of dislocations. Beam direction was perpendicular to the normal vector of active primary slip plane (111) and dislocation structure is imaged in the plane ($1\bar{2}1$) (see the schematic drawing in Fig 10.2). Most of the observed dislocations belong to the primary slip system (111)[$\bar{1}01$] with Schmid factor (SF) 0.490. The trace of the primary slip plane is marked in the image as well as the projection of the primary Burgers vector.
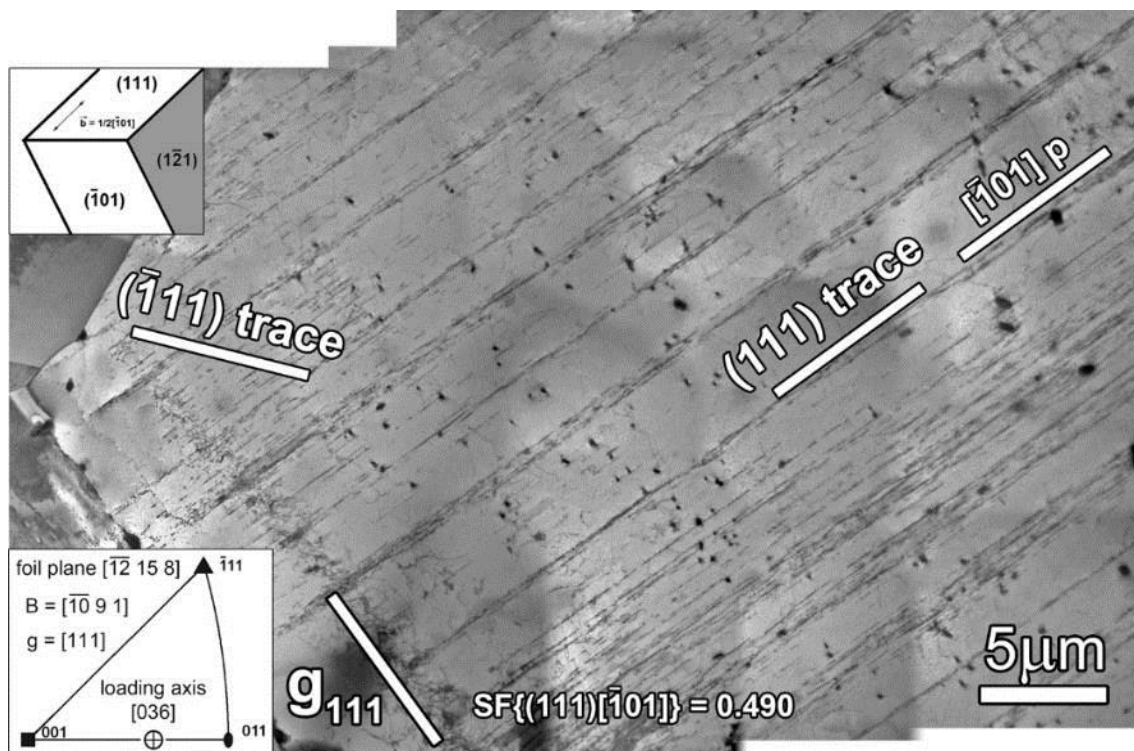
Figure 10.2: Characteristic planar dislocation structure with dislocation rich bands separated by areas free of dislocations. B = [$\overline{10}$ 9 1], g = [111], *foil plane* [$\overline{12}$ 15 8] *and loading axis* [036]. *Trace of the primary slip plane* (111) *and the direction projection of the primary Burgers vector* [$\bar{1}01$] *to the plane of the image are marked.*

Detail of parallel dislocation rich bands in a different grain oriented for single slip is shown in Fig. 10.3. TEM foil was cut perpendicular to the loading axis and when compared to previous grain, the same type of dislocation arrangement is shown but from the different crystallographic direction (see schematic drawing in Fig. 10.3). By tilting of the sample and by comparing several diffraction conditions the thickness of the bands was found to be 380 nm and the average distance between the bands was estimated to be 1.6 μm. Tilt of the bands with respect to the beam direction was taken in consideration in this estimation.

For diffraction condition **g** = [$\bar{1}\bar{1}1$], the primary slip plane (111) is tilted by 69° with respect to the beam direction and therefore it is possible to distinguish individual dislocation segments in Fig 10.3. Both Burgers vector and character of dislocations were determined.

Mostly edge segments of ordinary dislocations from primary slip system (111)[$\bar{1}$01] having SF 0.486 are observed.

More extensive TEM study revealed that the dislocation density within the bands is not always homogeneous and areas with lower dislocation density can be observed even within these arrangements. Here, it is worthy to note that along with the high dislocation density bands, also ladder-like dislocation structure characteristic by alternations of dislocation rich walls and dislocation poor channels like in copper [59, 80, 81, 83] was found. However, such structures were observed very rarely as will be discussed further in the next sections.
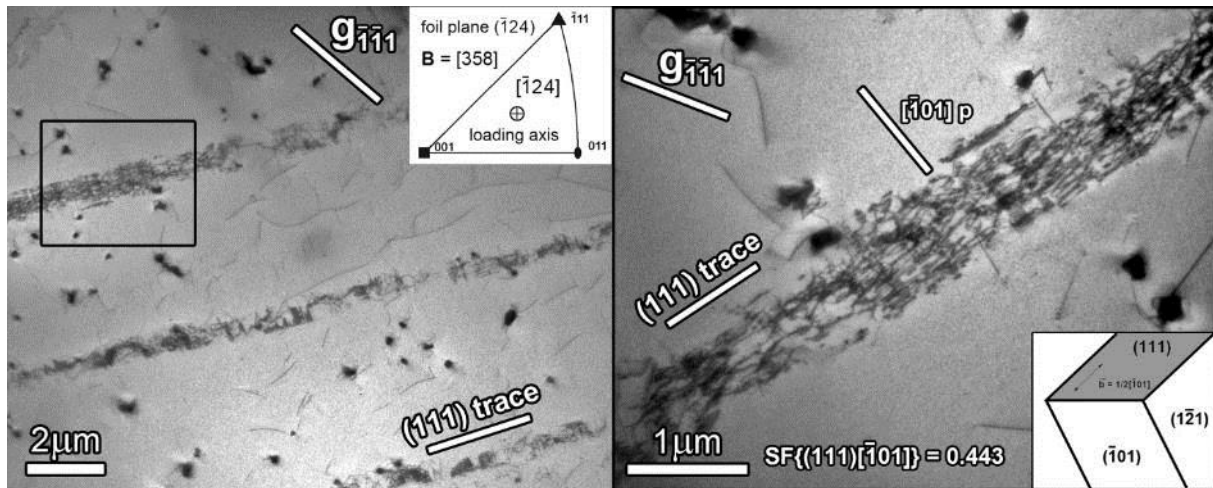
Figure 10.3: Overview picture of characteristic planar dislocation structure consisting of dislocation rich bands. Detail of high dislocation density band is shown in black inset. Mostly edge segments of primary dislocations with **b** *= 1/2[$\bar{1}$01] are visible.* **B** *= [358],* **g** *= [$\bar{1}\bar{1}$1], foil plane and loading axis [$\bar{1}$24].*
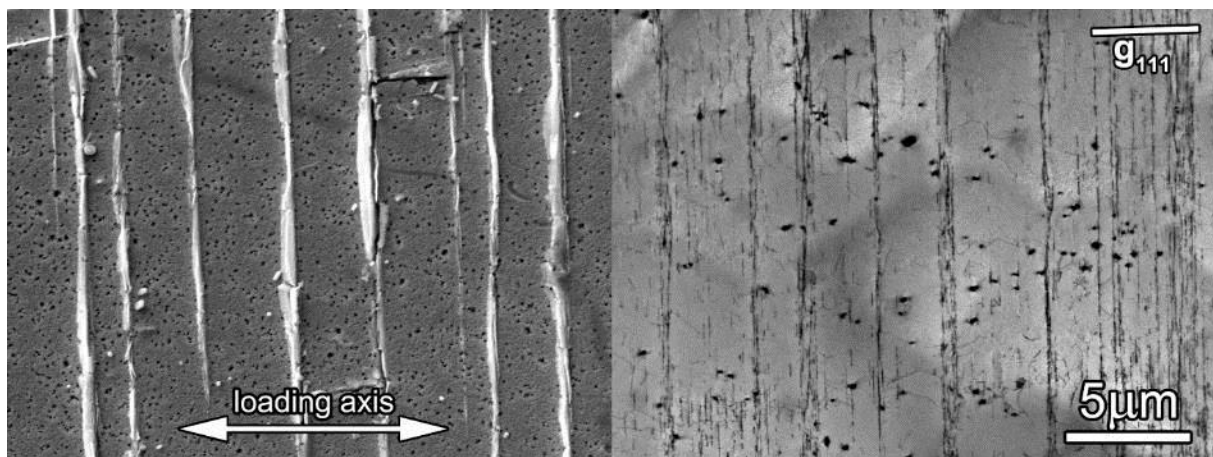
Figure 10.4: Comparison of SEM micrograph of grain surface showing persistent slip markings (PSMs) and TEM micrograph (a different grain; the one which is shown in Fig. 10.2) of internal dislocation microstructure showing dislocation rich bands. Loading direction for surface grain is marked in the SEM image.

Based on the observation of tens of grains from three different types of TEM foils, it could be stated that the strong planarity of dislocation slip prevails. In the majority of the grains only

one slip system is active, however also grains with two developed intersecting slip systems were found (e.g. see Fig. 10.1d).

The dislocation arrangement of the high dislocation density bands can also carry localized high plastic strain and produce persistent slip markings on the surface. That is in a good agreement with the high resolution surface observations. Comparison of SEM micrograph of grain surface with distinctive PSMs and TEM micrograph of internal deformation microstructure with dislocation rich bands is shown in Fig. 10.4. It is obvious that the distance between dislocation rich bands and also their thickness corresponds well to the PSMs observed on the surface.

10.1.2 High strain amplitudes

Sample loaded with total strain amplitude $\varepsilon_a = 7 \times 10^{-3}$ (saturated plastic strain amplitude $\varepsilon_{aps} = 4.8 \times 10^{-3}$) was selected as a representative for the study of the dislocation arrangements at conditions of high strain amplitude. The most observations were performed on foils cut at the angle of 45° to the loading axis. Planarity of slip strongly prevailed in majority of observed grains. However, much more grains oriented for double or even triple slip were found in comparison with low strain amplitude.
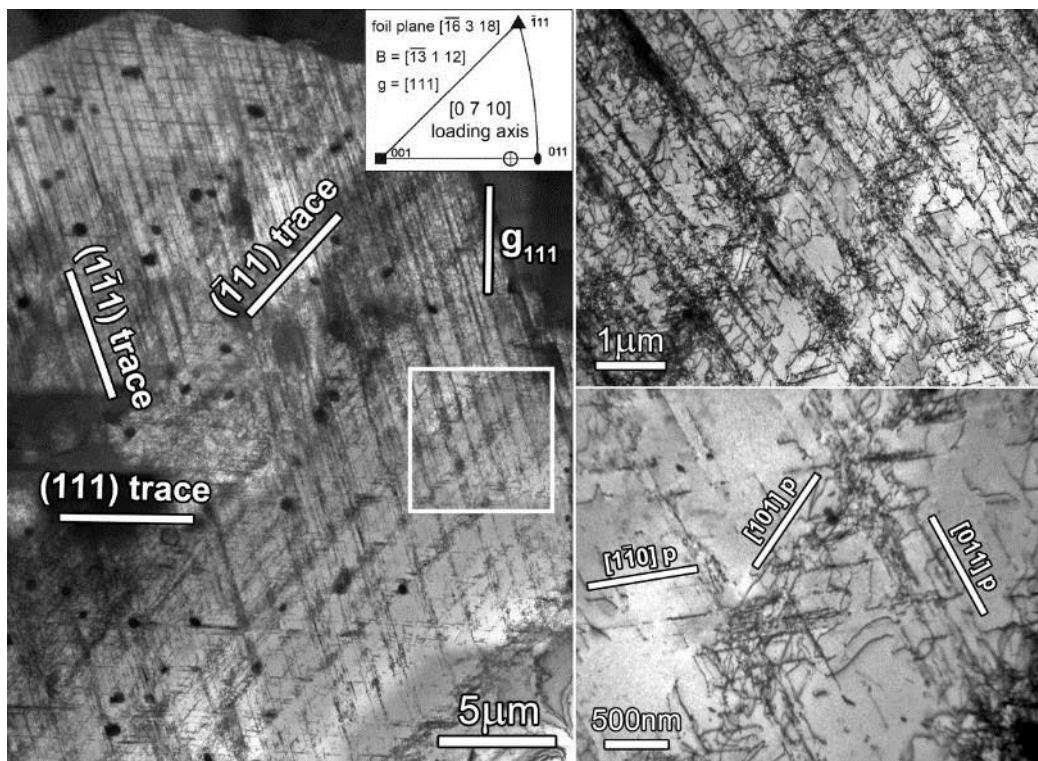
*Figure 10.5: Overview picture of grain oriented for triple slip. In inset highlighted by a white square the details of slip band intersections are shown. Traces of activated slip planes are marked as well as projections of important Burgers vectors. Foil plane is [$\overline{16}$ 3 18], **B** = [$\overline{13}$ 1 12], **g** = [111] and loading axis is [0 7 10].*

Typical deformation microstructure for selected loading conditions is shown in Fig. 10.5. On the left side of the micrograph, overview of grain with three activated slip systems is

presented. Magnified detail of slip planes intersection (highlighted by a white square) is visualised within two insets. Observations in different diffraction conditions revealed that the majority of dislocations belong to the slip systems $(\bar{1}11)[101]$, $(111)[1\bar{1}0]$ and $(1\bar{1}1)[011]$ with corresponding Schmid factors 0.466, 0.326 and 0.140.

The distance of dislocation rich bands is approximately the same as in arrangements observed at low strain amplitude. Nevertheless, since there are more slip systems activated, dislocation density is generally higher than in the case of loading with low strain amplitudes.
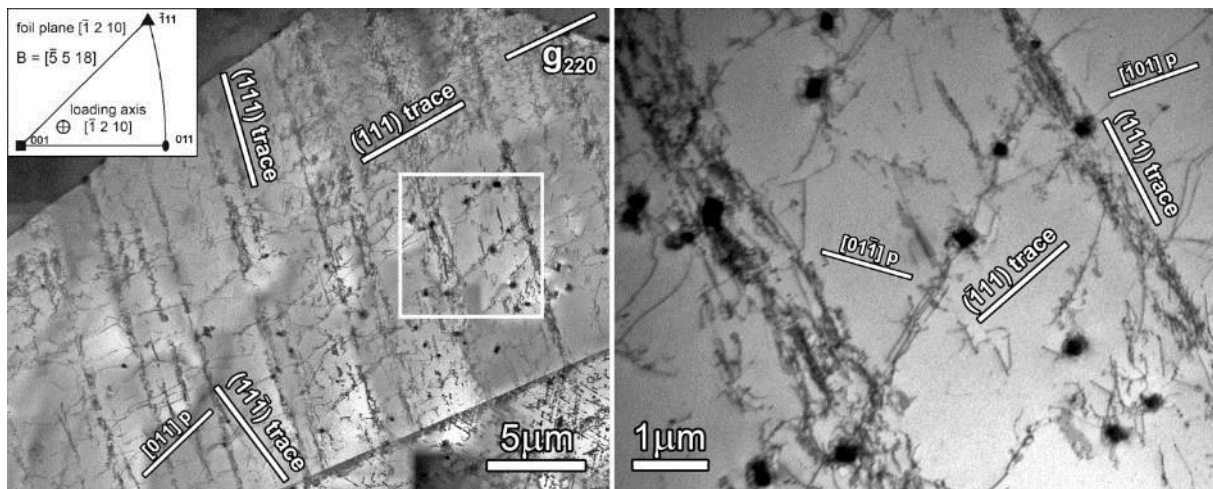
Figure 10.6: Inspected grain from the foil cut perpendicularly to the loading axis. The inset shows the details of interaction of edge dislocations from secondary slip system with Z-phase precipitates of size approx. 200 nm. **B** $= [\bar{5}\ 5\ 18]$, **g** $= [220]$, *foil plane and loading axis had same vector* $[\bar{1}\ 2\ 10]$.

The high amount of Z-phase precipitates of size about 400 nm or smaller was observed within the grain interior and at the grain boundary. However, only a few grains were found with the clear evidence of interaction of dislocations with these particles. Example of such a grain is shown in Fig. 10.6.

Overview picture on the left reveals that the majority of observed dislocations (edge segments) belongs to the primary slip system $(111)[\bar{1}01]$ with the highest SF = 0.470. Near the grain boundary (see the lower left corner of the picture) a few edge segments of dislocations from secondary slip system $(11\bar{1})[011]$ with SF = 0.420 were found. Further from the grain boundary, in the area within the grain volume (marked by a white square) the interaction of edge dislocations from the secondary slip system $(\bar{1}11)[01\bar{1}]$ with SF = 0.404 with precipitates of the size of approx. 200 nm was detected. Based on these observations it can be concluded that at certain conditions, Z-phase particles of size about 200 nm or smaller could act as obstacles to dislocation as will be discussed later.

Although, the planar configuration of dislocations is prevailing and represents characteristic deformation microstructure observed in the majority of grains, few exceptions were found as well. In Fig. 10.7, a grain oriented for single slip is shown. The dislocation arrangement reminiscent of ladder-like structure is found. The analysis reveals that high dislocation density walls are perpendicular to the primary Burgers vector $[\bar{1}01]$ (SF of primary slip system is 0.443). These walls alternate with areas of low dislocation density, so called channels. In case

of simple metals like copper and nickel and also in case of some structural alloys like conventional 316L steel, cyclic plastic strain localization is connected with the formation of ladder-like dislocation structures [59].
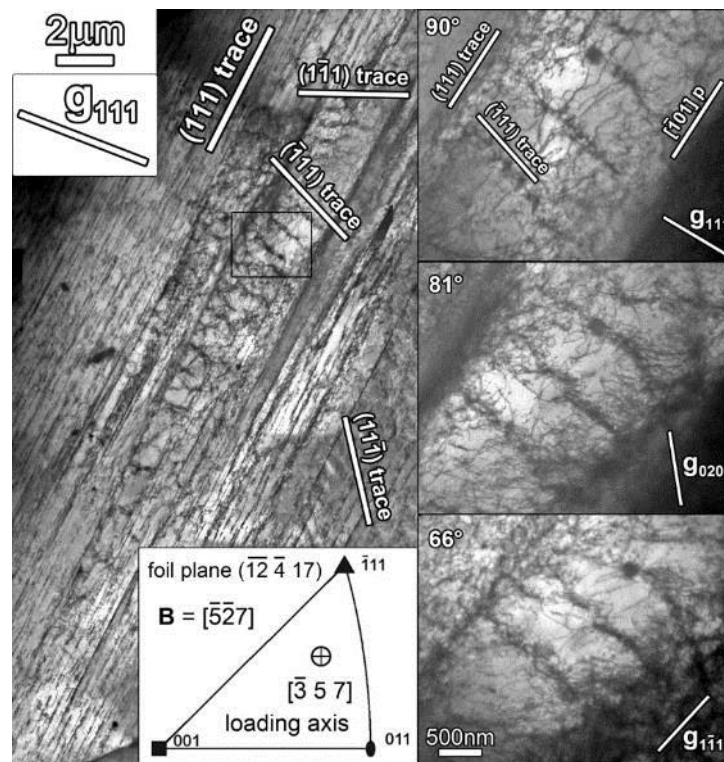
*Figure 10.7: Grain oriented for single slip. Dislocation structure reminiscent of ladder-like structure is formed in between areas with planar dislocation arrangements. Details show characteristic walls and channels in three different diffraction conditions. Angle between normal vector of primary slip plane (111) and beam direction is noted for each **g**.*

In the case of Sanicro 25, it is important to note that the spatial dislocation configuration resembling walls/channels or ladder-like structure is rare. Strong tendency towards planar slip is preserved in the majority of grains.

It was documented earlier [14, 16–18] that at high strain amplitudes, planar dislocation structures in 316L rearrange into spatial formations after activation of cross-slip and slip on additional slip systems. Complex, multi-pole configurations, so-called vein-like dislocation arrangements form and decrease the internal stored energy of the system. The onset of such phenomena was observed also in Sanicro 25 and is shown in Fig. 10.8.

Overview micrograph visualises part of relatively large grain oriented for double slip. On the left side of image, within the interior of grain and further from the boundary, dislocations are arranged into planar structure while on the right side of the picture, near the grain boundary, dislocation structure resembling well known veins or vein-like spatial arrangements is present.

The area of the grain marked by symbol A is shown in detail in two diffraction conditions in Fig. 10.9. High density of slip bands is observed, i.e. when compared to low strain amplitude images, much higher density of dislocations is present but general nature of the arrangement

is similar. TEM analysis of this region revealed that screw segments of dislocations from slip system $(11\bar{1})[1\bar{1}0]$ with SF = 0.263 form the majority of dislocations arranged into planar-like structure.
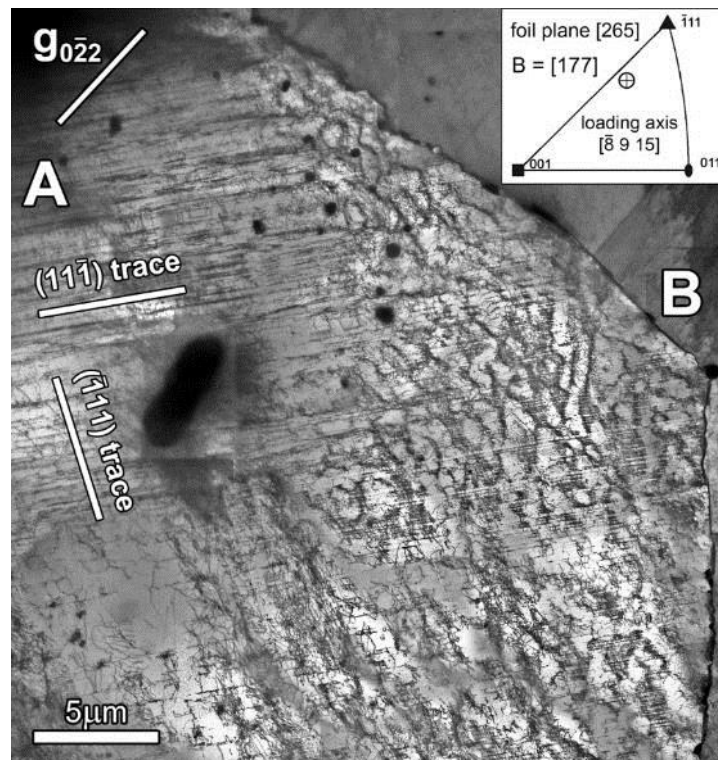
Figure 10.8: Overview picture of a grain oriented for double slip. Within the bulk of the grain, planar dislocation arrangement with high dislocation density is present. Close to the grain boundary rearrangement into spatial vein-like dislocation structure could be observed.
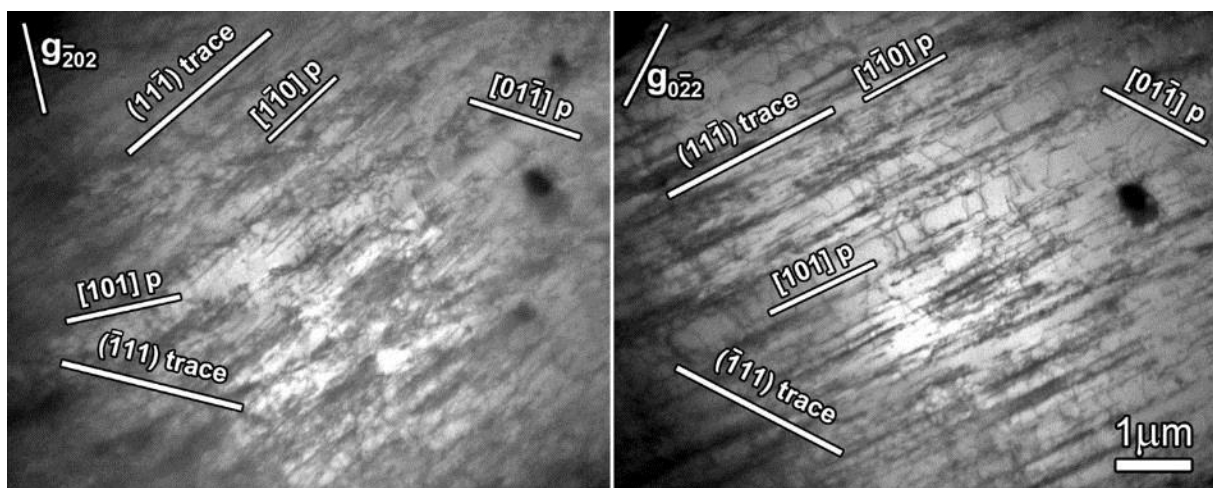
Figure 10.9: Detail of planar high density dislocation arrangement from the place marked by symbol A in Fig. 10.8. Dislocations from three different slip systems are visible.

The cross-slip mechanisms have been probably already activated in this grain and also dislocations from other slip systems were present. Few edge segments of dislocations from the secondary slip system $(\bar{1}11)[101]$ with SF = 0.247 as well as from the system $(11\bar{1})[01\bar{1}]$

with SF = 0.212 are visible in an image with $\mathbf{g}$ = [0$\bar{2}$2]. These secondary dislocations play a significant role in the formation of spatial vein-like dislocation configuration in the region near the grain boundary where their density has increased. This area marked by symbol B in Fig. 10.8 is visualised in detail in Fig. 10.10.
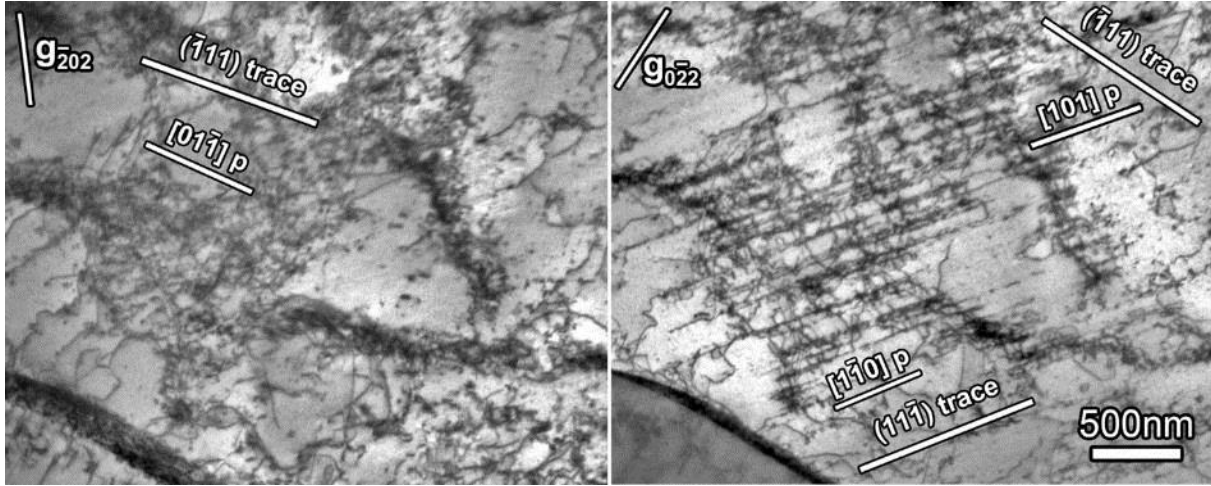
Figure 10.10: Detail of spatial dislocation structure reminiscent of vein-like arrangement from the place marked by symbol B in Fig. 10.8. In the image taken with $\mathbf{g}$ = [0$\bar{2}$2] dislocations from three different slip systems are distinguishable as they form vein-like dislocation structure.

On the right image under diffraction condition $\mathbf{g}$ = [0$\bar{2}$2], the structure of vein-like spatial arrangement is very well resolved. It is evident that the dislocations of primary slip system with $\mathbf{b}$ = 1/2[1$\bar{1}$0] form the base of the whole dislocation configuration. In comparison with area A showed in Fig. 10.9, the onset of alternation of areas rich and poor in dislocations is much more conspicuous. Primary dislocations 1/2[101] and secondary slip system dislocations 1/2[01$\bar{1}$] form spatial arrangement which highly resembles well known vein structure observed in conventional 316L steel [16–18], where the formation of these lower-stored-energy configuration is usually connected with the softening response of material.

Several studies performed on 316L [14, 16–18, 95, 96] showed that when the plastic strain amplitude is sufficiently high the rearrangement from planar to spatial structures starts due to the activation of cross-slip mechanisms. In the case of 316L some evidence of spatial rearrangement of dislocations is found almost in every grain. In our case the observations of vein-like and wall/channel structures were extremely rare even for high strained samples. Based on these facts, conclusion is made that the plastic strain amplitude ε_{ap} = $4.8{\times}10^{-3}$ reached in case of Sanicro 25 is near a transient value of saturated ε_{ap} which is needed for the start of the formation of low energy spatial dislocation arrangements and therefore for the change of the cyclic stress-strain response of the material leading to cyclic softening. It should be also noticed that no cellular structures were observed at room temperature for all strain amplitudes.

10.2 Microstructural changes as a result of cyclic loading at 700°C

10.2.1 Dislocation structure evolution

Cyclic loading leads to a significant change in the substructure of the alloy. First, the dislocation structure changes depending on the composition of the material, interstitial content, temperature, and the imposed plastic strain amplitude. At room temperature, surprisingly strong planarity of the dislocation slip prevails with significant plastic strain localization into thin deformation bands (Chapter 10.1 and [116, 129]).
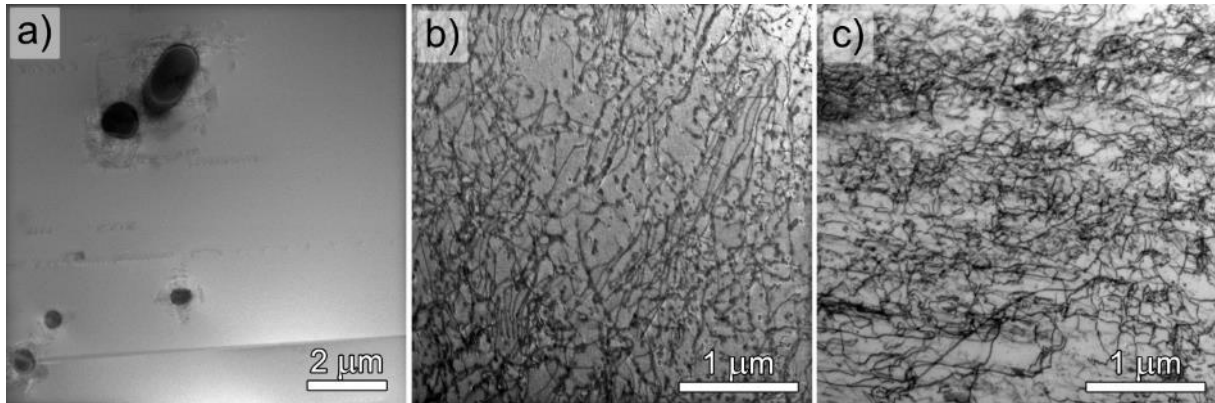
Figure 10.11: (a) BF-STEM image of the microstructure in the initial state taken close to [001] zone axis. As a result of annealing, dislocation density is low ($\sim 9 \times 10^{12}$ m^{-2}). The only precipitates present are Z-phase complex nitrides. BF-STEM-DCI images of typical dislocation structure observed after cyclic loading with total strain amplitudes (b) 0.2% and (c) 0.7%, respectively. Dislocation densities were estimated to (b) $\sim 9 \times 10^{13}$ m^{-2} and (c) $\sim 4.5 \times 10^{14}$ m^{-2}. Images were taken close to [112] zone axis with preferential use of <111> diffraction vector.

At high temperatures, the importance of thermally activated effects is significantly enhanced leading to completely different dislocation structures. Regardless of the imposed plastic strain during cyclic loading, all grains are filled with a high density of homogeneously distributed dislocations. In Figs. 10.11b and 10.11c, the dislocation structures observed *post mortem* in samples tested with total strain amplitudes of 0.2% and 0.7%, respectively, are shown. When compared to the initial state (see Fig. 10.11a), cyclic loading leads to a dramatic increase of the dislocation density. Knowing the thickness of the foil, the average dislocation density was roughly estimated as $\sim 9 \times 10^{13}$ m^{-2} and $\sim 4.5 \times 10^{14}$ m^{-2} for samples tested with total strain amplitudes 0.2% and 0.7%, respectively. That is by several magnitudes higher than dislocation density of 9×10^{12} m^{-2} measured for solution annealed initial state. Several different samples cut from specimens loaded at total strain amplitudes 0.35% and 0.50% were inspected in detail and results are presented as follows.

10.2.1.1 Low strain amplitudes ($\varepsilon_a = 3.5 \times 10^{-3}$)

Characteristic dislocation structures in the specimen cycled at 700°C with $\varepsilon_a = 3.5 \times 10^{-3}$ (saturated plastic strain amplitude $\varepsilon_{aps} = 1.0 \times 10^{-3}$) differ significantly from structures produced at room temperature. The striking feature is a very high dislocation density in all

grains. Typical and representative arrangements are shown in Fig. 10.12. In the foil cut perpendicular to the loading axis of specimen the grain oriented appropriately for double slip was analysed in detail. In Fig. 10.12a, the bands rich in dislocations are found. Observations in different diffraction conditions have shown that mainly dislocations from primary slip system $(111)[\bar{1}01]$ and secondary slip system $(11\bar{1})[011]$ with the two highest SFs 0.462 and 0.401, respectively, are present.
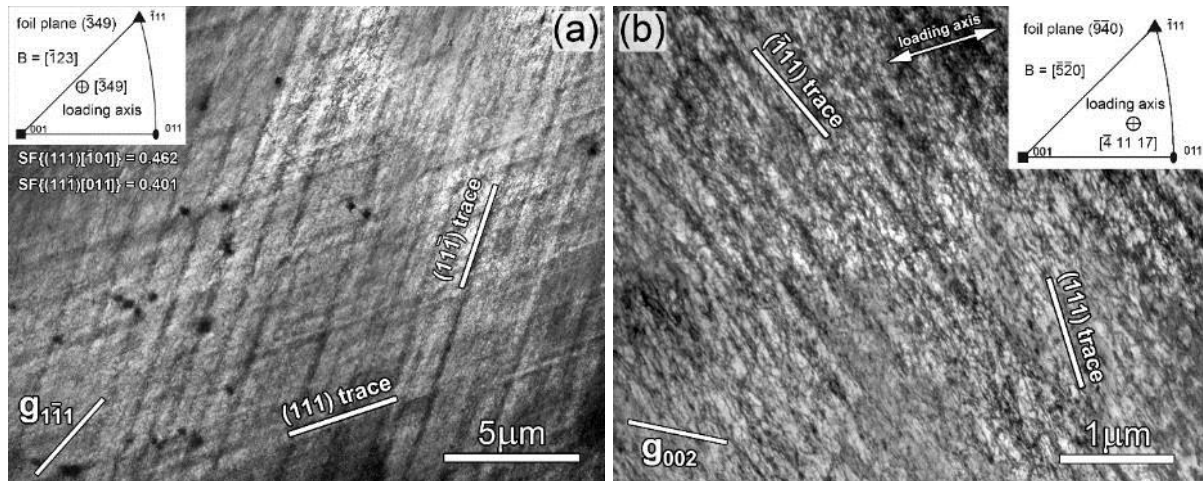
Figure 10.12: Characteristic dislocation structures observed at 700°C. (a) High dislocation density bands and areas with homogeneous high dislocation density distribution in grain oriented for double-slip. (b) Grain oriented for single slip. Dislocations from at least two slip systems are imaged.

The most significant and notable difference when compared to ambient temperature conditions is that the areas between the bands are filled with homogeneous high density distribution of dislocations. In these areas no significant localization was observed and dislocations were distributed homogeneously. Grain oriented for single slip investigated in the foil cut parallel with the loading axis is shown in Fig. 10.12b. Traces of primary and secondary slip planes are marked in the image as well as direction of loading axis. Inclination of (111) and $(\bar{1}11)$ planes to the beam direction was 49 and 19 degrees, respectively. Because of the different tilt of the slip planes with respect to the electron beam direction, the dislocations from secondary slip system appear to form the high dislocation density bands while the primary dislocations appear as homogeneously dispersed within observed volume of the material.

Detail of area between high dislocation density bands in the grain cut from a foil at the angle of 45 degrees relative to the loading axis is shown in Fig. 10.13. Using imaging in different diffraction conditions it was found that numerous dislocations lie on other slip planes than the primary one. This evidence supports the hypothesis that the cross-slip of the primary dislocations, as a thermally activated process [45, 130], substantially contributes to the production of high dislocation density in regions between bands, since the dislocations movement is no more fixed only to primary slip plane.
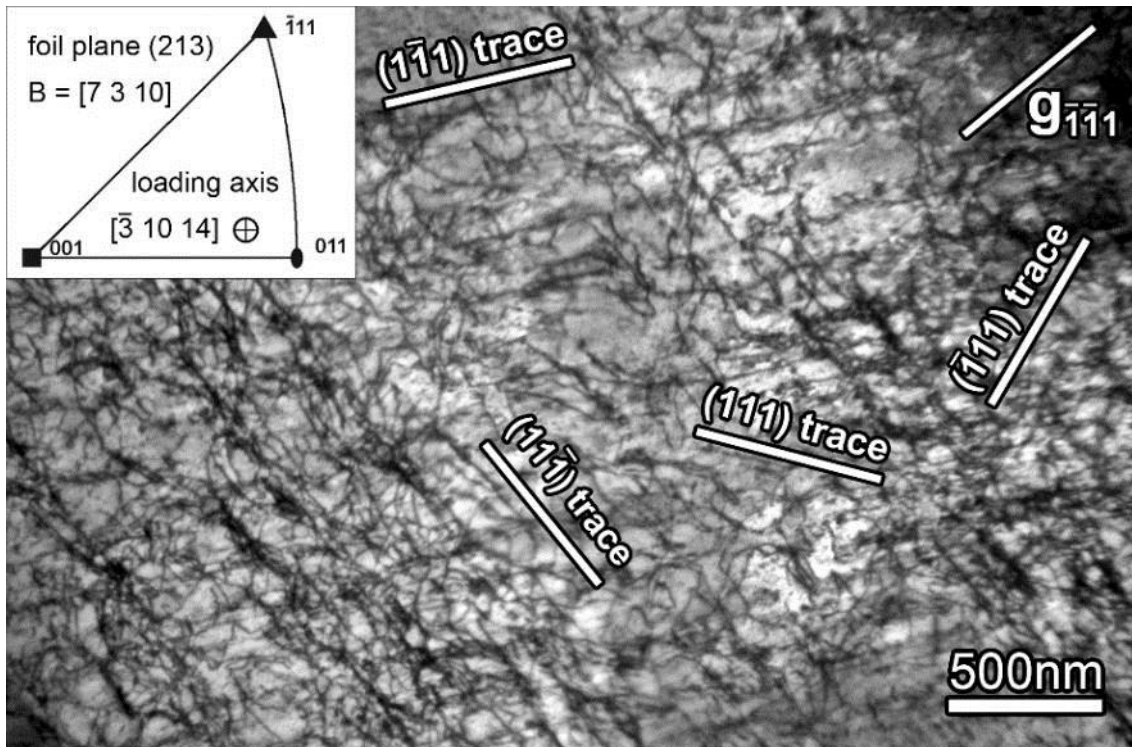
Figure 10.13: Detail of dislocation structure from the area between high dislocation density bands. Dislocations lying on several {111} slip planes were distinguished supporting hypothesis about high temperature enhanced cross-slip effect.

10.2.1.2 High strain amplitudes ($\varepsilon_a = 5 \times 10^{-3}$)

In case of cyclic loading with $\varepsilon_a = 5 \times 10^{-3}$ (saturated $\varepsilon_{ap} = 2.2 \times 10^{-3}$) character of deformation microstructure is almost the same as for lower strain amplitude. Typical dislocation structure observed for these loading conditions is shown in Fig. 10.14. In diffraction condition $\mathbf{g_1}$ = [111] dislocations from primary slip system are very well distinguished as parallel with the trace (111) since the beam direction is perpendicular to the normal vector of primary slip plane (111). Tilting of grain into other diffraction condition $\mathbf{g_2}$ = [200] reveals microstructure from different perspective where it could be seen that volume in between primary slip planes is homogeneously filled with dislocations from other slip systems. Additional TEM work then proved that dislocations which moved on all four possible slip planes {111} are present there.

Almost no signs of low energy spatial dislocation structures were found. Only in a few grains (<5% of all investigated grains), the onset of cellular structure formation close to grain boundaries was observed. Example of such a grain is shown in Fig. 10.16. In the central part of the grain, deformation microstructure is the same as in Fig. 10.14, i.e. the same as in the majority of grains. Mostly dislocations lying on primary (111) and dislocation activity on secondary (11$\bar{1}$) slip planes are observed. However in the areas near the grain boundary, where the influence of additional internal stresses of neighbour grains could be expected, arrangement of dislocations is different and onset of oriented cellular structure formation is found.
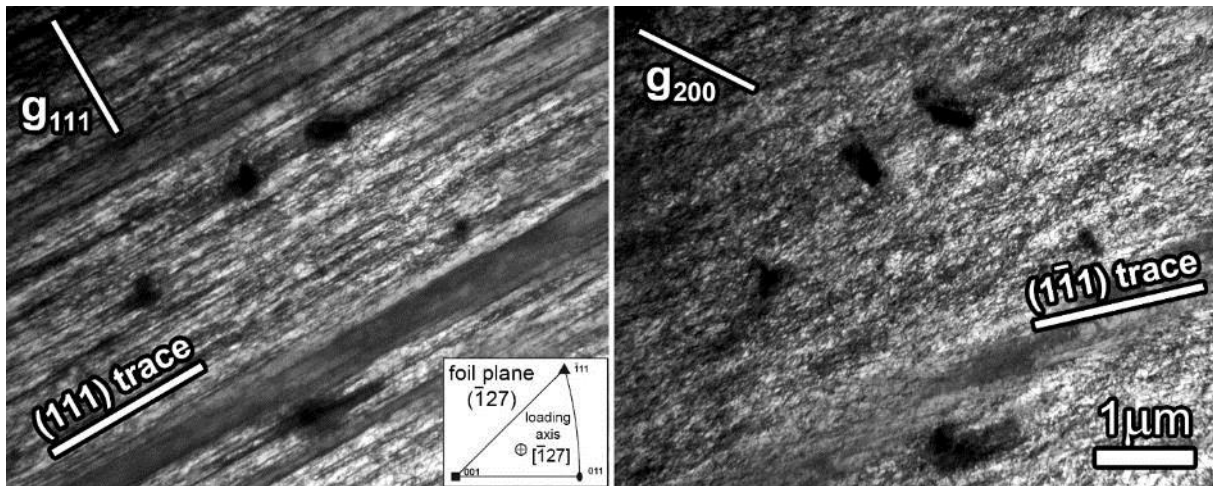
Figure 10.14: Typical dislocation structure observed at 700°C at $\varepsilon_a = 0.50\%$. TEM foil cut perpendicular to loading axis. On the left, image taken in $g_1 = [111]$, $B_1 = [\bar{5}\bar{2}7]$. On the right, image taken in $g_2 = [200]$, $B_2 = [025]$.
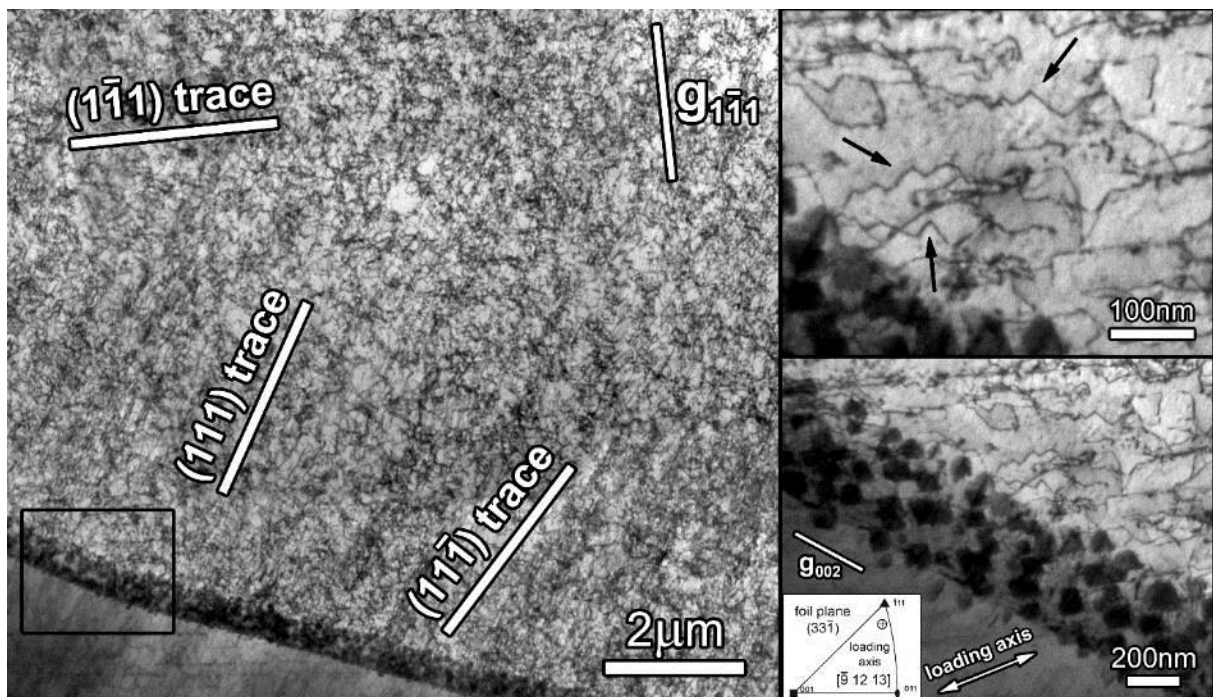
Figure 10.15: Dislocation structure in grain located in foil cut parallel with the loading axis (marked in the image). Homogeneously distributed dislocations lying on three different slip planes are present; $g_1 = [1\bar{1}1]$, $B_1 = [76\bar{1}]$. In inset, detail of low angle (4°) grain boundary shows arrangement of cuboidal secondary $M_{23}C_6$ chromium carbides of size about 80 nm; $g_2 = [002]$, $B_2 = [430]$. Indication of dislocations pinned by nanoparticles is marked by black arrows.

It has been reported previously for both simple metals (e.g. copper [131]) and complex structural alloys (e.g. 316L [132, 133]) that after a rapid initial increase the total dislocation density has a tendency to reach saturated equilibrium values in the very early stage of cyclic loading. After which, dislocations tend to form arrangements with lower stored internal energy. Sufficiently high temperature and external loads enhance diffusion of point defects

103

and facilitate dislocation climb and cross-slip. Mutual interaction of dislocation strain fields leads to dislocation annihilation or dipole formation and are important to the recovery processes. Initially tangled dislocations rearrange to cellular structures featuring boundaries that are made up of walls with a high density of dislocations with alternating signs. Upon further recovery, dislocations in the cell interiors are annihilated. The internal stored strain energy is significantly decreased usually leading to so called softening of the material response to external load.
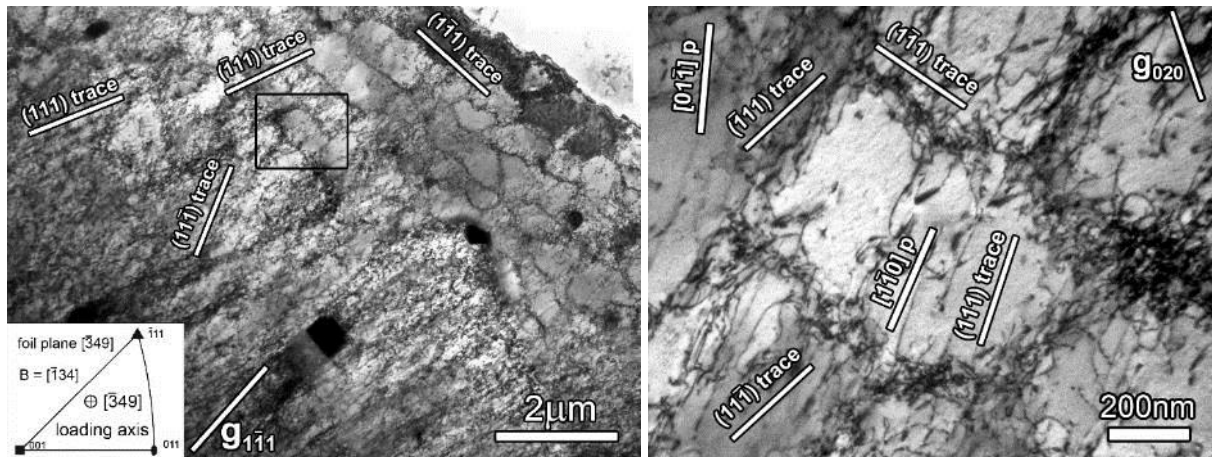
Figure 10.16: Grain oriented conveniently for double-slip. Within the bulk, homogeneous high dislocation density arrangement is observed. In the area near the grain boundary, oriented cellular structure could be observed. $\boldsymbol{g} = [1\bar{1}1]$, $\boldsymbol{B} = [\bar{1}34]$.

In Sanicro 25, despite the evidence of cross-slip, climb, and activation of various slip systems [129], no signs of recovery process leading to the formation of wall and cellular structures are observed. Tangled and homogeneous dislocation structures of high density prevail during the entire fatigue life, suggesting the presence of other microstructural features that dramatically affect the mobility of dislocations.

10.2.2 Precipitation of secondary phases

Along with the Z-phase present already in the initial state, the large number of alloying elements with high concentration in Sanicro 25 results in a significant precipitation of secondary phases.

The presence of interstitial carbon in steels with high Cr content is known to lead to rapid nucleation of numerous $M_{23}C_6$ Cr-rich carbides [123, 126]. At high temperatures, they nucleate very quickly and can be found even in stabilized steels after very short aging times (e.g. less than one hour at 750°C [126]). Preferential nucleation sites are grain boundaries, but they can be found partially also inside the grains at twin boundaries and dislocations or stacking faults. According to literature [126, 134], structure of $M_{23}C_6$ is cubic $Fm\bar{3}m$ (space group 225, Pearson symbol cF116). The term $M_{23}C_6$, where M means "metal", is a more general notation for $Cr_{23}C_6$, as also Ni, Mo, Fe or in small quantities Mn can be found to substitute partially for chromium. Lattice parameter is reported to vary between 10.57 and 10.68 Å, depending on the chemical content. Model of the $Cr_{23}C_6$ carbide created using parameters of Bowman et al. [134] in Crystal Maker software is shown in Fig. 10.17.
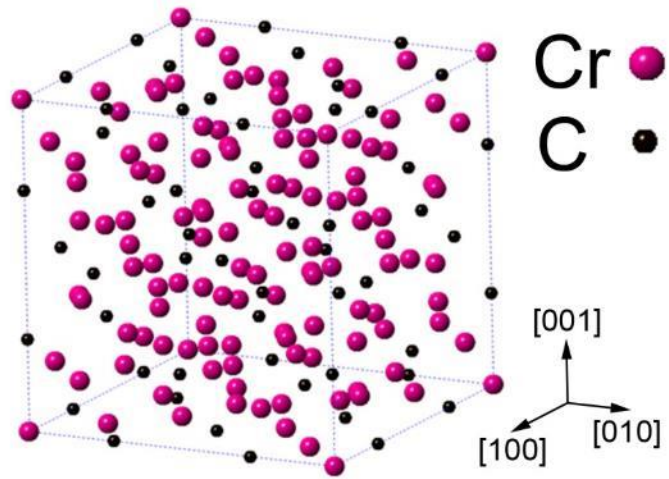
Figure 10.17: Model of Cr$_{23}$C$_6$ carbide. Unit cell is viewed along [$\bar{5}$11] direction.
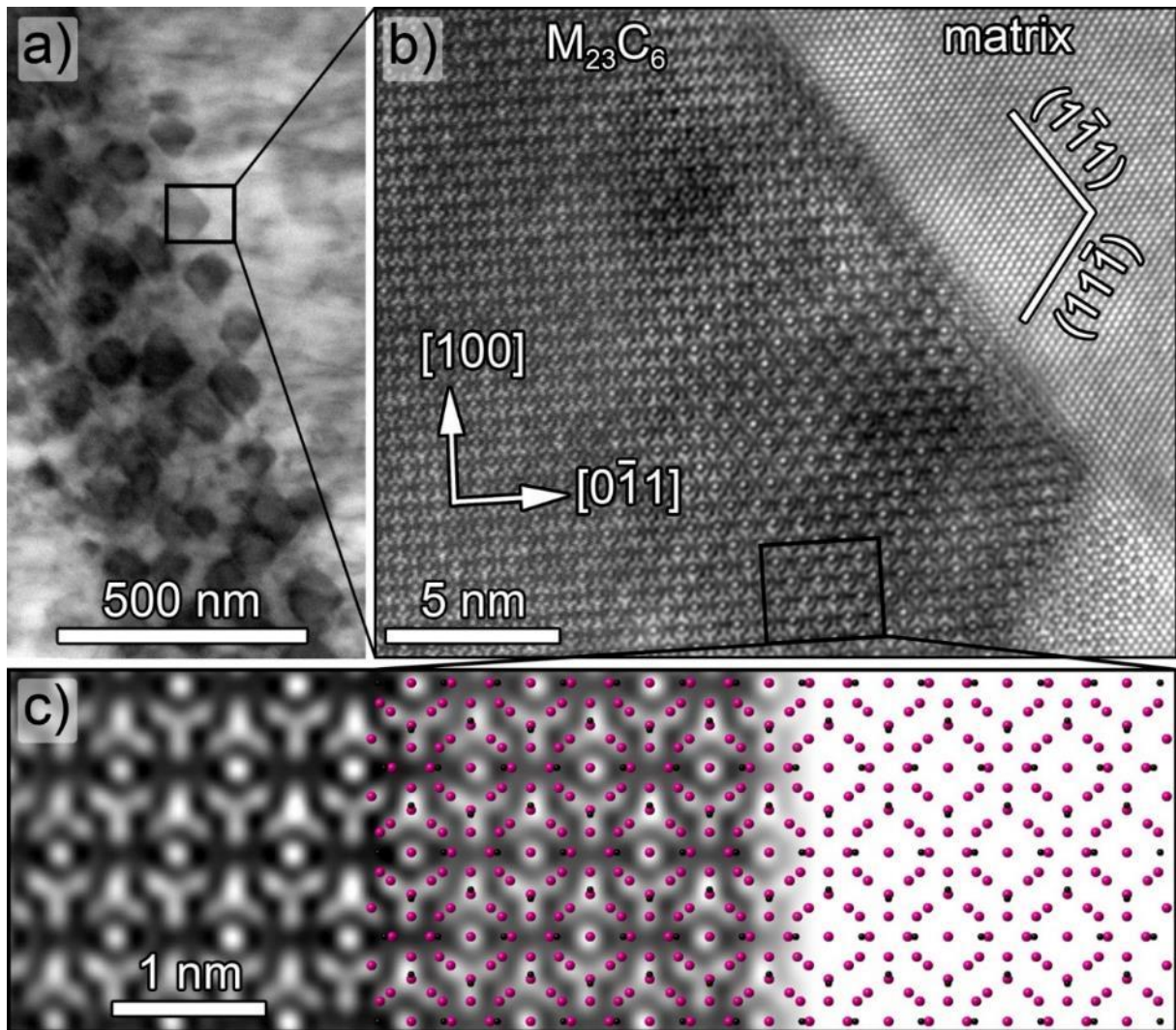
Figure 10.18: (a) An array of M$_{23}$C$_6$ Cr-rich carbides nucleated at the low angle grain boundary. (b) HAADF-STEM image showing atomic structure of carbide viewed along [011] zone axis. (c) Experimentally obtained and FFT filtered image of the carbide structure is compared with the model of structure made in Crystal Maker software.

An example of cuboidal $M_{23}C_6$ Cr-rich carbides nucleated at the low angle grain boundary (approx. 4°) during fatigue at 700°C is shown in Fig. 10.18a. The atomic resolution HAADF-STEM imaging then reveals structure of the particle viewed along the [011] zone axis. Fast Fourier transformation (FFT) filtering (frequencies corresponding to the noise were excluded) of the image was used to emphasize the carbide structure and also the (111)-type interface with the matrix. The FFT diffraction patterns determined from the matrix and $M_{23}C_6$ precipitate suggest a cube-on-cube orientation. In the reciprocal space, the shorter distance to the carbide diffraction spots (by a factor of 3) relative to that of the FCC matrix corresponds well to the reported lattice parameter of $M_{23}C_6$, which is approximately three times larger than the lattice parameter of the austenitic FCC matrix [126]. Small lattice misfit of carbide and austenitic matrix suggests the coherent, and later, when particle coarsens, semi-coherent interface with misfit dislocations accommodating lattice mismatch and relieving coherency strains. According to Howe [50] such an interface can have rather small energy ranging from 50 to 300 mJm^{-2}. In Fig. 10.18d, the experimentally obtained atomic structure was compared to a $Cr_{23}C_6$ model created in the Crystal Maker software. In the model, carbon atoms are colored in black and chromium atoms in pink.
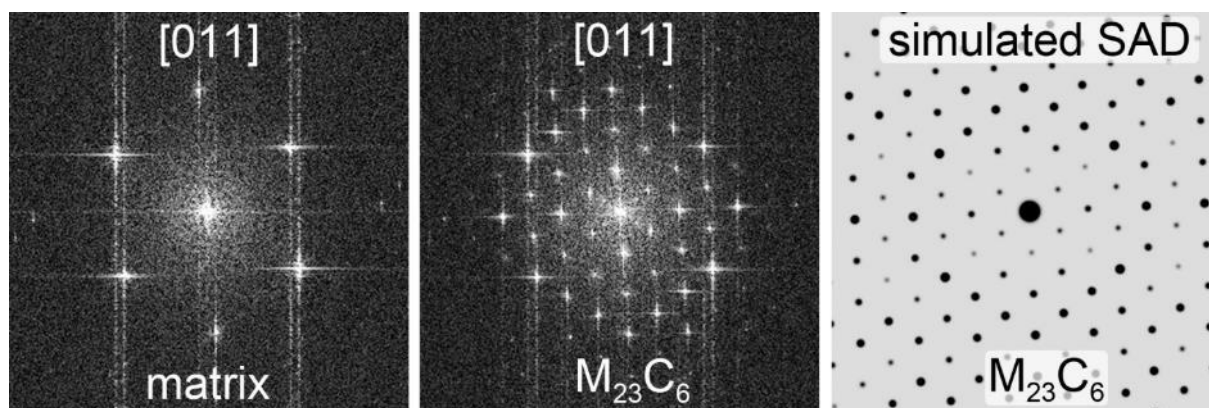
Figure 10.19: FFT diffraction patterns demonstrate cube-on-cube orientation of carbide relative to the FCC matrix. The shorter distance to the carbide diffraction spots by a factor of 3 relative to that of the matrix documents that the carbide has lattice parameter almost exactly three times bigger than that of austenitic matrix. On the right, FFT diffraction patterns are compared to the selected area electron diffraction (SAD/SAED) pattern of $Cr_{23}C_6$ simulated using Crystal Maker software.

Chemical content of the carbide and its surroundings was studied by high spatial resolution EDS-STEM analysis. In Fig. 10.20, HAADF-STEM Z-contrast image accompanied with elemental maps shows $M_{23}C_6$ Cr-rich carbides nucleated at the grain boundary. Sample was extracted from the grip of the specimen fatigued with total strain amplitude 0.2% at 700°C. The microstructure observed in the sample corresponds to the material aged for 153 hours at 700°C. It is clear that the carbides are rich in Cr, C and also Mn. In the vicinity of precipitates, matrix is significantly enriched in Ni at the expense of heavily depleted Cr.

In addition to Z-phase and $M_{23}C_6$ Cr-rich carbides, Zurek et al. [25] also observed Cr_2N, μ-phase of the type Fe_7W_6, and a small amount of W-rich Laves phase. However, these phases were detected only after aging of Sanicro 25 for several thousands of hours. Fatigued samples in this work were thermally exposed from 6 to 153 h. None of the latter phases were detectable by electron microscopy or neutron diffraction, suggesting that the time needed for

their nucleation and coarsening is significantly longer than reached during cyclic loading [135].
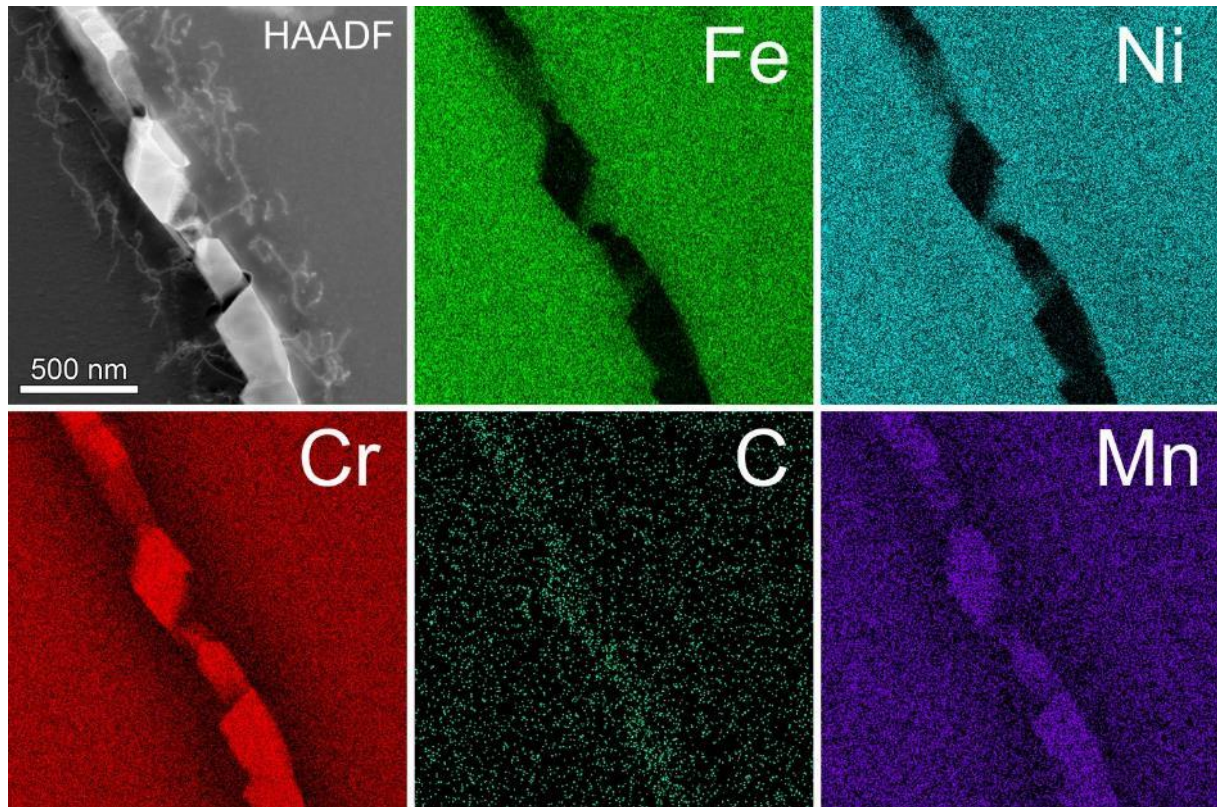
Figure 10.20: HAADF-STEM Z-contrast image shows $M_{23}C_6$ Cr-rich carbides nucleated at the grain boundary. Material was aged for 153 hours at 700°C. Carbides are rich in Cr, C and also Mn. In the vicinity of precipitates, Cr-depleted and Ni-enriched zones are found.

Thermodynamic calculations (ThermoCalc) reported by Chai et al. [9] indicate nucleation of two additional phases, one Cu-rich and one Nb-rich, that may be more directly relevant in terms of high temperature strengthening. To confirm their presence in fatigued samples, advanced scanning transmission electron microscopy characterization methods were used. Selected samples of specimens fatigued over a wide range of strain amplitudes at 700°C (further details in [129, 136, 137]) were analysed and the presence of strengthening nanoparticles was evaluated. The grips of the specimens were also studied in order to separate thermal from thermo-mechanical effects on microstructure.

High spatial resolution EDS mapping was performed on a TEM foil extracted from the sample cyclically loaded with the total strain amplitude $\varepsilon_a = 0.27\%$ (4482 cycles to fracture; i.e. 23 hours at 700°C). As apparent in Fig. 10.21, two different kinds of nanometer-sized particles embedded in the matrix were detected: copper-rich and niobium-rich. A detailed analysis of the structure of each of these particle types, and their role in high temperature strengthening will now be presented.
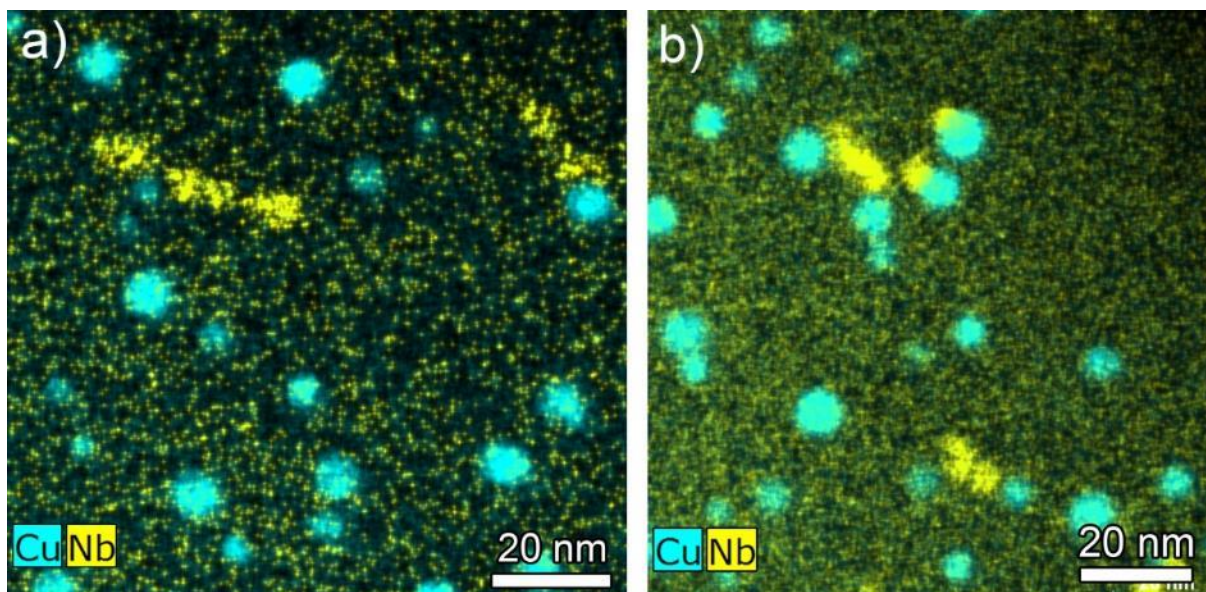
Figure 10.21: High spatial resolution EDS mapping of specimen loaded with ε_a = 0.27% (exposed for 23 hours at 700°C) obtained close to <112> zone axis. Spherical Cu-rich particles are densely and homogeneously dispersed while Nb-rich nanoprecipitates are less numerous and not uniformly located. In (a), few Nb-rich particles are arranged along a dislocation line. In (b) Nb-rich particles are distributed more as arrays of individual particles.

10.2.3 Cu-rich nanoparticles

Numerous, spherically-shaped copper-rich particles distributed homogeneously within the measured volume were reported in very similar alloys containing the same Cu levels [21, 129, 138, 139], as fine round objects with higher contrast than the austenitic matrix. In the present work, probe-corrected HAADF-STEM imaging together with high spatial resolution Super-X EDS mapping is utilized for complete characterization of these particles (see Fig. 10.22).

Two types of spherical objects were found, exhibiting either lower or higher contrast relative to the matrix (see Fig. 10.23a). Thorough analysis has shown that the lower contrast objects are truncated spherically-shaped holes in the matrix. As a result of sample preparation, Cu-rich particles located close to the TEM foil surface were polished out by the electrolyte, as confirmed by EDS, which indicates *no* copper in the dark features. The higher contrast objects of similar size scale are the Cu-rich nanoparticles remaining embedded in the matrix. In order to identify these objects, HAADF-STEM imaging was utilized using a low camera length of 73 mm, with an inner and outer angle cut off of approximately 55 mrad and 370 mrad, respectively, to enhance Z-contrast. Under these conditions, the intensity of atomic columns is approximately related to their mean square atomic number (Z^2). Since Cu has a higher atomic number (29) than Cr (24), Fe (26) and Ni (28), Cu-rich regions have slightly higher contrast than the matrix, enabling their visualization as exemplified in Figs. 10.22 and 10.23b.
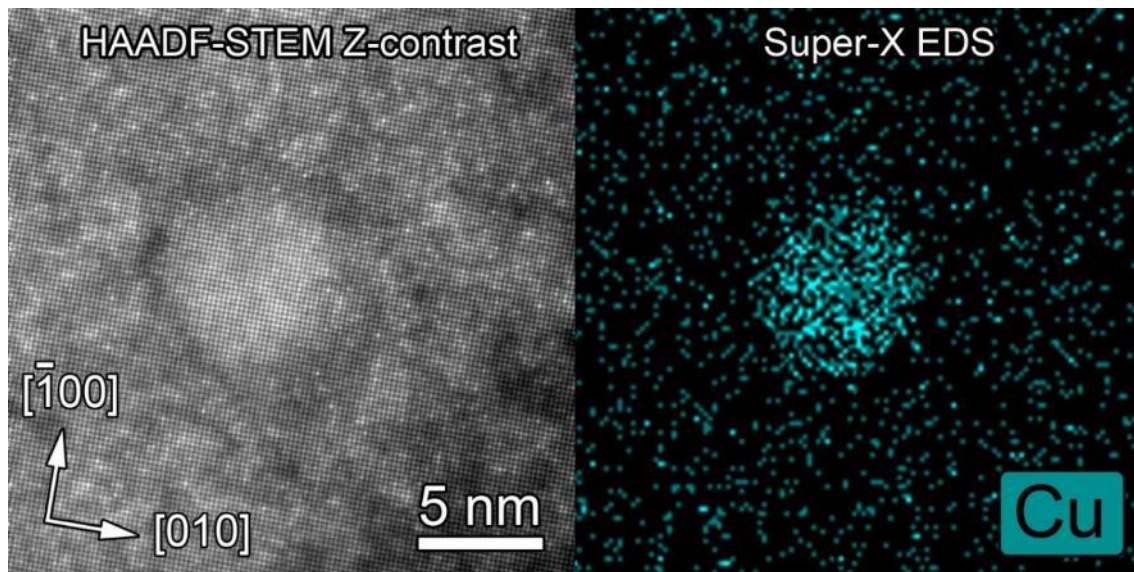
Figure 10.22: (a) HAADF-STEM Z-contrast image showing Cu-rich nanoparticle embedded in the austenitic matrix. The structure is viewed along [001] *zone axis. (b) The location of copper atoms is further confirmed by STEM-EDS scan performed on the same area.*
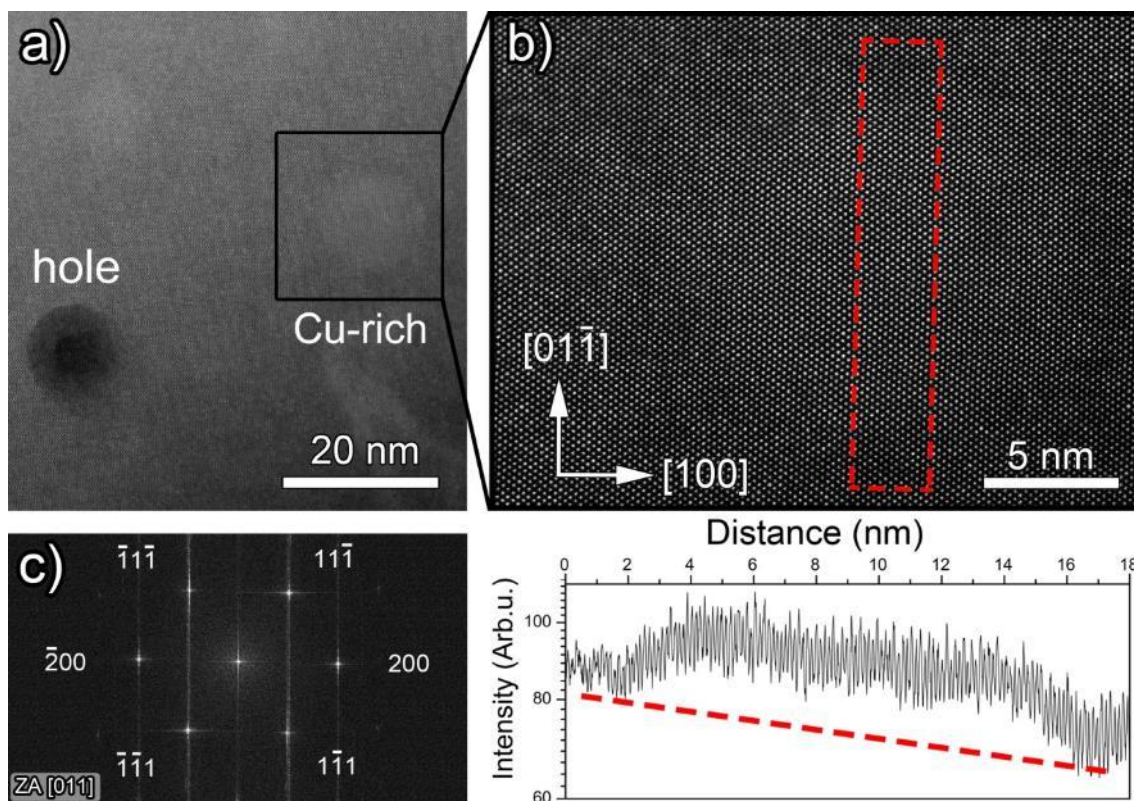
Figure 10.23: [011] *zone axis HAADF-STEM image showing (a) comparison of Cu-rich precipitate (higher contrast) and truncated spherically-shaped hole in the matrix from which a precipitate was polished out (lower contrast). (b) Detail of inset shows fully coherent Cu-rich nanoparticle embedded in the matrix. Since copper has a higher atomic number than matrix elements, Z-contrast enables imaging of precipitates. (c) FFT made from particle and matrix shows no extra superlattice spots. Inset illustrates increased atomic columns intensity*

in the Cu-rich region (area marked by red dashed rectangle in (b)). Dashed line in inset denotes decreasing signal variation with decreasing specimen thickness.

For specimen loaded with total strain amplitude 0.27% for 23 h, a surface areal density of 3.2×10^{14} m^{-2} was determined by counting only holes and dividing by two (accounting for holes at the top and at the bottom of the foil). In addition to latter specimen, two other samples were investigated, one loaded with total strain amplitude 0.5% (6 h at 700°C) and one loaded with 0.2% (153 h at 700°C). EELS enabled estimation of the average foil thickness t, based on the t/λ measurement. Taking the Sanicro 25 density and stoichiometry values, the electron inelastic mean free path λ was estimated to be 124 nm for Sanicro 25 by using the equation of Iakoubovskii et al. [140] revised by Egerton [141]. The thickness of the foil was then calculated to (100 ± 30) nm. For best interpretation of results, areas with similar thickness were selected at different samples. Knowing the distribution of precipitates from EDS mapping, the particle volume density was estimated as well as the mean size of the particles, a median, and a minimum and maximum size of the particles. Results are shown in Figs. 10.24 and 10.25. It is clear that average size of the particles increases with time, however, particles are very stable and do not coarsen significantly. Particle volume density seems to be decreasing slightly with time spent at 700°C. Nucleation and coarsening behavior of Cu-rich particles will be discussed later.
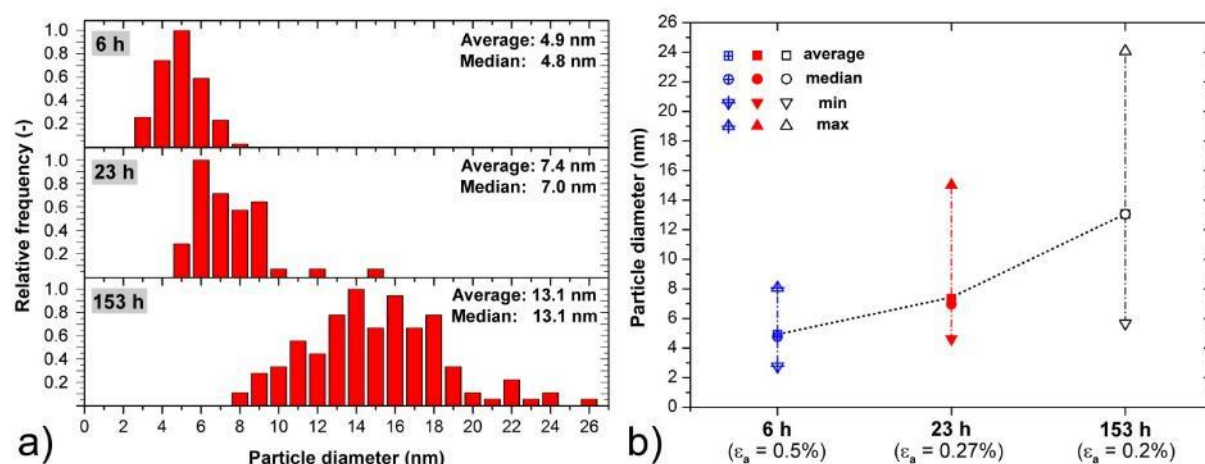
Figure 10.24: (a) Histograms showing size distribution of Cu-rich particles in specimens fatigued with different total strain amplitudes with different times of exposure to temperature of 700°C. Average and median diameter of the particles is noted. (b) Diagram showing evolution of the average, median, maximum and minimum diameter of Cu-rich particles determined for different samples.
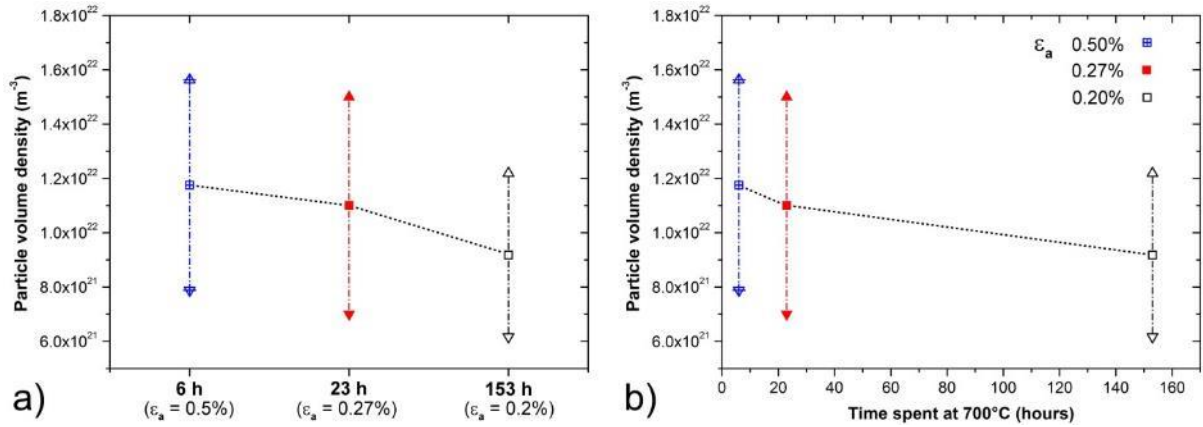
Figure 10.25: (a) Cu-rich particle volume densities determined for specimens loaded with different strain amplitudes. (b) Cu-rich particle volume densities as a function of time spent at a temperature of 700°C.

In earlier studies of conventional steels [139, 142], Cu-rich nanoparticles are reported to be semi-coherent with the matrix. However, in the present work, no misfit dislocations or discontinuities in atomic column spacing across the precipitate/matrix interface were observed. Pure copper has the same cubic $Fm\overline{3}m$ crystallographic structure as the austenitic matrix with the lattice parameter a_{Cu} = 3.615 Å (JCPDS 04-0836) [143]. As reported previously [135], neutron powder diffraction on the instrument MEREDIT@NPI was used to precisely measure the austenitic matrix lattice parameter of Sanicro 25 a_{γ} = 3.60692(8) Å, which is slightly larger when compared to conventional steels. Therefore, in Sanicro 25, pure copper would have a small positive lattice misfit of δ = 0.22%, smaller than that for Cu in conventional austenitic steels. The coherency between particles and matrix is consistent with fast Fourier transformation pattern analysis made from the HAADF-STEM image of the particle area as shown in Fig. 10.23c. Only spots corresponding to the matrix are observed in the FFT, indicating coherent lattice matching. Taking in account the coefficient of thermal expansion which is reported to be about 17×10^{-6} K^{-1} for both pure copper [144] and Sanicro 25 [9], small positive lattice misfit is suggested to prevail also at 700°C. Coherent Cu-rich nanoparticles are in perfect cube-on-cube orientation relationship with the matrix. The surprising conformity of crystal structures suggests a particularly low interfacial energy, as well as a potentially low nucleation barrier, as is discussed further below.

The composition of the initial state of the alloy was also analysed using STEM EDS. Raw data were extracted from the original spectral maps and quantified using the Bruker Esprit software and the Cliff-Lorimer k-factor fit. Standard k-factors calculated by Bruker Esprit software were used. No Cu-rich nanoparticles were found. Quantified maps showed a homogeneous Cu-enriched solid solution with an average of approximately 3.3 at.%. This result is fully in agreement with recent work of Chi et al. [142], who used 3D atom probe tomography (APT) to perform compositional analysis of Cu-phase precipitation. After solid solution treatment and cooling to room temperature, their APT results indicated that all Cu atoms dissolved in the austenitic matrix and formed a supersaturated solid solution.
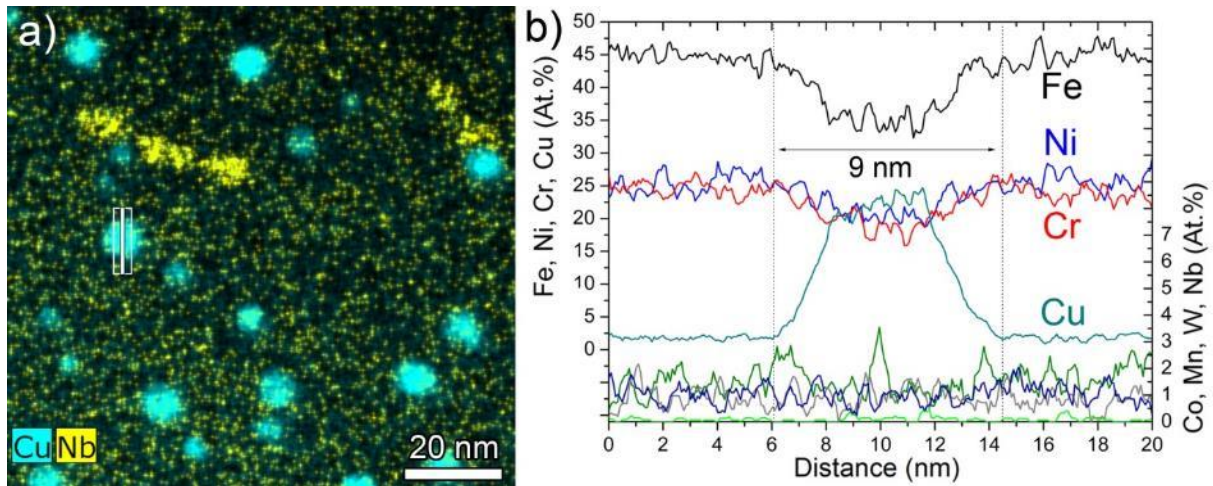
Figure 10.26: (a) EDS mapping of specimen loaded with $\varepsilon_a = 0.27\%$ obtained close to <112> zone axis. One particle was selected for detailed chemical content quantification. (b) Quantified EDS line scan across the Cu-rich particle demonstrates an increase of copper content and depletion of base matrix elements.

After 23 hours of exposure at 700°C and superimposed cycling of Sanicro 25, spherical regions rich in copper are formed. In Fig. 10.26b, the composition (in at.%) is plotted as a function of distance across such a region. Compared to the initial state, the copper content in the matrix decreased notably to about 1.9 at.%, while in the spherical Cu-rich regions it increased substantially, with the relative ratios of Fe, Ni, and Cr all decreasing. Using a particle thickness of 9 nm (the measured diameter of sphere) and foil thickness of 50 nm (from EELS t/λ measurement), the EDS data confirm a Cu content within the particle of at least 75 at.%, consistent with the APT results of Chi et al. [142]. Jiang et al. and Chi et al. [139, 142] also reported that the nucleation of the Cu-rich precipitates is a process with an incremental change in the chemical composition without crystallographic structure transformation. An increase of temperature to 700°C and an apparently high chemical driving force in the supersaturated solid solution induces rapid diffusion of copper atoms into cluster-type Cu-rich regions. As high temperature exposure continues, the Cu-rich nanoprecipitates are formed as the base matrix elements (Fe, Cr, Ni) diffuse away. Inspection of the foil from the specimen grips has not revealed any notable difference in nanoparticle distribution or average size, suggesting that mechanical loading does not have any significant effect on their nucleation.

10.2.4 Nb-rich nanoparticles

The Nb-rich particles not only have distinctly different structural characteristics, but their distribution is also non-uniform. In fatigued samples, these Nb-rich particles are usually found in three different configurations. Most frequent are accumulations of a few single particles (see Fig. 10.27a) gathered closely together into chain-like features in the matrix. In terms of the whole grain volume, these groups are dispersed very heterogeneously forming areas with a high density of particles separated by regions free of nanoparticles, as seen in the LAADF image of Fig. 10.27a, where Nb-rich particles have higher intensity than the matrix.
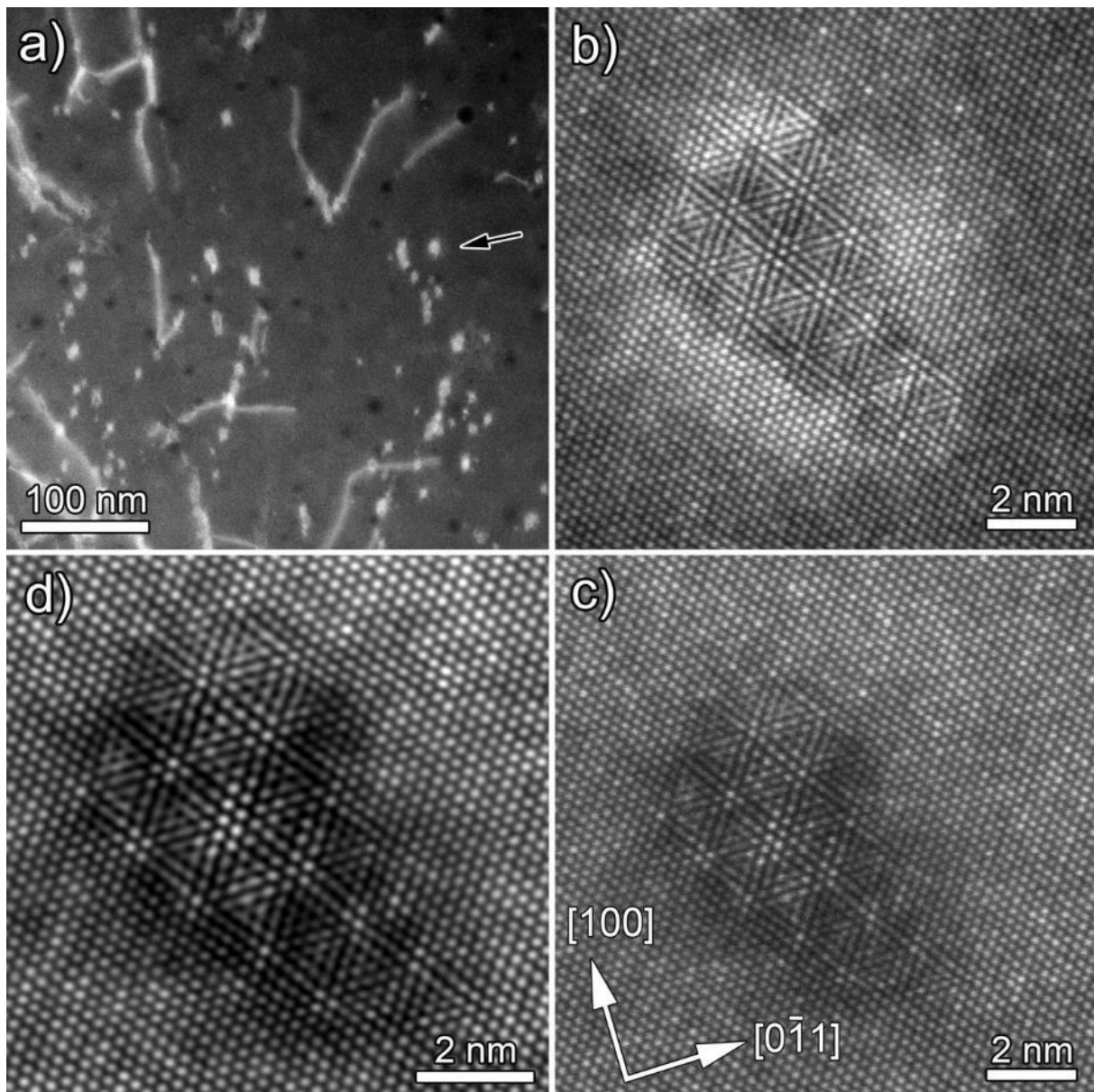
Figure 10.27: (a) LAADF-STEM [011] *zone axis image with enhanced strain contrast enabling visualisation of nanoprecipitates along with dislocations in a fatigued specimen. The particle volume density can differ significantly on a local basis. Example of group of NbC particles with high volume density is highlighted by black arrow. (b) HAADF-STEM* [011] *zone axis image of one of the NbC nanoprecipitates of size about 4 nm, long camera length of 230 mm is used to emphasize elastic strain field caused by precipitate in the matrix. (c) Same image visualised using Z-contrast using low camera length of 73 mm. (d) Magnified image was FFT filtered using a mask which included all fundamental and satellite intensities for central and diffracted beams.*

In the second mode of configuration, particles are arranged in high density along dislocation lines (see Figs. 10.28a, 10.28b and 10.30a). Finally particles can also be observed in more sparse, pinning interaction with dislocations, as will be discussed further below. Due to their highly inhomogeneous spatial distribution, the particle density differs locally. Using average

113

foil thickness (100±30 nm) determined by EELS the particle volume density was roughly estimated to vary from $(8.9\pm2.8)\times10^{20}$ m^{-3} to $(3.7\pm1.2)\times10^{21}$ m^{-3} as seen in Fig. 10.27a.
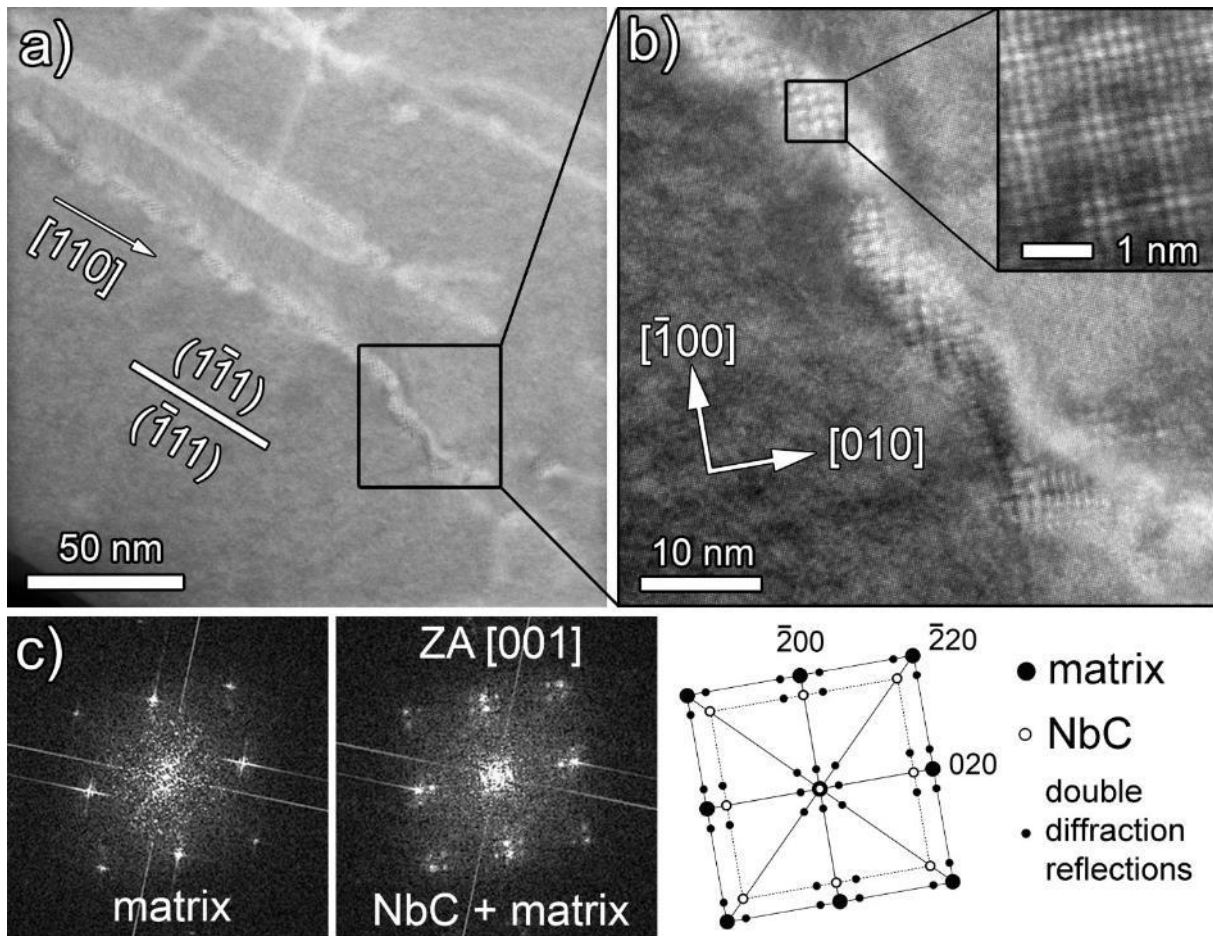
Figure 10.28: Specimen loaded with total strain amplitude 0.27% (exposed for 23 hours at 700°C). HAADF-STEM image showing (a) NbC particles nucleated on the dislocation viewed along [001] *zone axis. (b) Detail of Moiré-like pattern observed in locations where NbC particles are present and overlap with the matrix. (c) Comparison of an FFT pattern from NbC and matrix demonstrating cube-on-cube relationship. Schematic drawing explains which lattice each spot corresponds to.*

The average size of Nb-rich particles found in aggregated groups, their median, minimal and maximal size was determined for three different specimens cyclically loaded with total strain amplitudes 0.2%, 0.27% and 0.35% (exposed to temperature of 700°C for 153 h, 23 h and 10 h). Results are shown in Fig. 10.29. The shapes of the particles were found to be not well-defined or consistent in all investigated cases.

Probe-corrected HAADF-STEM imaging was used for atomic resolution structural analysis of areas where strong Nb content was detected by EDS. For both [001] and [011] zone axes, distinctive Moiré-like contrast was typically observed at nanoparticle locations, similar to the high resolution TEM images first reported in [129, 135].
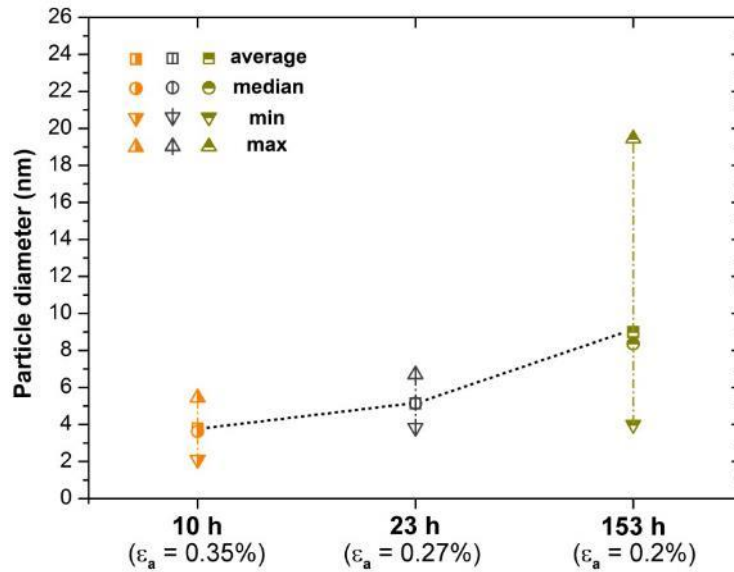
Figure 10.29: Statistics of Nb-rich particle diameter(median and average diameter, maximal and minimal size of particles) observed in three different samples cyclically loaded with total strain amplitudes 0.2%, 0.27% and 0.35% (exposed to temperature of 700°C for 153 h, 23 h and 10 h).

Translational Moiré fringes are parallel contrast lines formed in high resolution TEM imaging by the interference of diffracting crystal lattice planes that are overlapping, which might have different spacing and/or orientation [145, 146]. Definitive determination that the contrast exemplified in Figs. 10.27b, 10.28b and 10.30b is indeed due to a Moiré effect requires additional analysis. Unlike HRTEM, HAADF-STEM images are formed from incoherent inelastically scattered electrons. For this imaging mode, Moiré fringe contrast has not been rigorously simulated previously. Rather than adding wave function amplitudes as in HRTEM, the intensities from individual atoms, considered here as individual scatterers, must be summed in HAADF-STEM. Since the incoherent HAADF-STEM images are interpreted more directly in terms of atom types and positions, the term "Moiré-like contrast" is used below.

Particles observed in fatigued specimens are too small for thorough structural analysis. Therefore, samples after only thermal exposure were additionally inspected revealing that without the presence of mechanical loading, groups of aggregated small 4-6 nm sized nanoparticles are not present in the matrix. On the contrary, much larger precipitates of size 10-20 nm are found, but only at dislocations, as seen in Fig. 10.28b, 10.30a and 10.30b. As cyclic stress was not present, and dislocations were immobile, particles had more time to coarsen and grow as was reported previously by Poddar et al. [145].

The corresponding FFT pattern from the NbC particle region in Fig. 10.30b and FFT filtered image in Fig. 10.30c is shown in Fig. 10.30d. In addition to the intense spots of the austenite matrix, weaker satellite reflections belonging to a second lattice and several double-diffraction reflections are observed. Although not shown here for brevity, this interpretation of the FFT features has been validated by STEM nano-beam diffraction showing consistent results. Patterns obtained for [001] and [011] zone axis orientations indicate that the precipitates have a FCC crystal structure oriented in a cube-on-cube relationship with the austenite matrix.
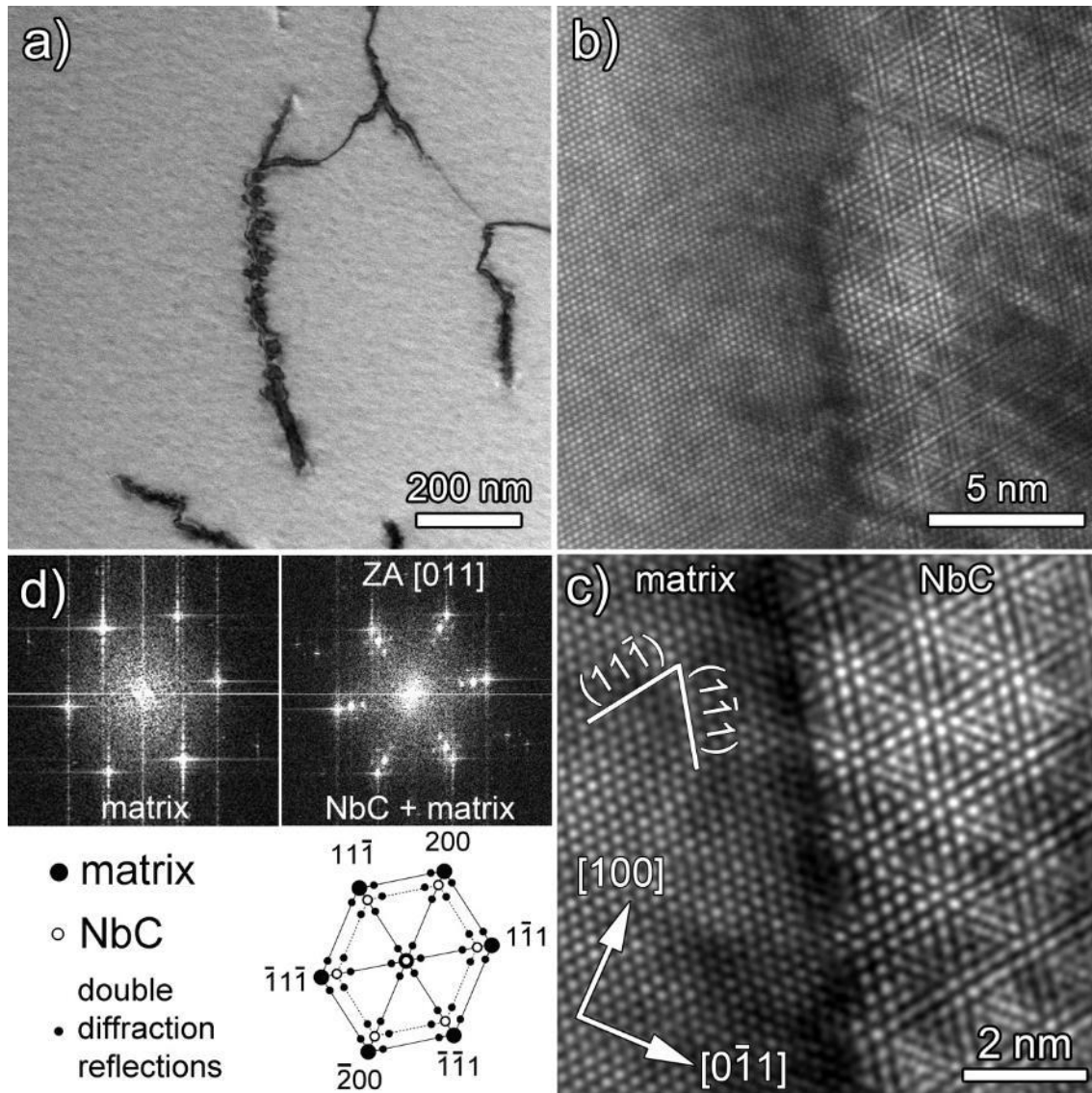
Figure 10.30: (a) BF STEM-DCI image showing array of NbC nanoparticles nucleated along a dislocation in the grip part of specimen after thermal exposure only (23 hours at 700°C). (b) Raw HAADF-STEM [011] zone axis image showing NbC precipitates of size about 13 nm arranged along a dislocation. (c) FFT filtered image showing detail of $(1\bar{1}1)$ interface between the matrix and NbC precipitate. The Moiré-like contrast indicates that the matrix is overlapping with the NbC precipitate. (d) Comparison of an FFT pattern from NbC and matrix demonstrating cube-on-cube relationship. Schematic drawing explains which lattice each spot corresponds to.

By measuring the distance from the central spot (000) to the diffracted spots (*hkl*) corresponding to matrix and precipitate cube directions in reciprocal space, it was determined that the precipitate has a *d*-spacing that is about 1.22 times larger than that of the FCC matrix, indicating positive lattice misfit of about 22%. Using both the lattice parameter of the austenitic matrix (from neutron diffraction measurements) and the matrix/precipitate misfit, the precipitate lattice constant is estimated to be approximately 4.41 Å, what is in good agreement with results previously obtained using TEM-based methods [129, 135].

The remarkable features of these precipitates – (a) Nb-rich, (b) observation of Moiré-like contrast and (c) corresponding FFT diffraction patterns indicating FCC structure with cube-on-cube orientation and large positive lattice misfit – are consistent with the results published earlier by Sourmail [126] and Haddrill et al. [147]. In the Fe-Ni-Cr based steels with high carbon and nitrogen content, they report a strong tendency for nucleation of NbX (X = C, N) precipitates due to the high affinity of Nb to form both carbides and nitrides. Possible phases have a $Fm\overline{3}m$ structure with lattice parameters of NbN and NbC a = 4.4 Å and a = 4.47 Å, respectively [126].

To identify which type of nanoparticles is present in Sanicro 25, EELS analysis was used for the detection of light elements. Only a carbon signal was found in the Nb-rich nanoprecipitates, whereas no nitrogen was detected, suggesting the presence of NbC. Nucleation of the NbN phase is presumably less probable since the coarse Z-phase (CrNbN) primary precipitates likely consumes most of the available N [129, 135]. It is important to note that despite the fact that only NbC variant of MX phase was experimentally confirmed in our measurements, Nb(C,N) variant cannot be completely excluded. Therefore, further within the text, if particular case in which composition was experimentally measured is not commented, more general designation Nb(C,N) will be used for correctness.

For further analysis of the contribution to the strengthening mechanisms, most important is to determine the nature of the interface between these NbC nanoparticles and the matrix. Several authors describe NbC precipitates as coherent or semi-coherent [145, 148–151]. Nevertheless, if both lattice misfit and particle size are taken in account, coherency with the matrix is very arguable. Howe [50] stated that the physical limit for misfit dislocation-based interface structures is approximately at misfits of 25%, where spacing of misfit dislocations is close to $4b$ and their cores start to overlap. If we consider lattice parameter of NbC to be 4.47 Å [126], according to Eq. (3.4) lattice misfit with matrix of Sanicro 25 will be 24% what is close to the Howe´s limit. Spacing between misfit dislocations (Eq. 3.5) lying on {111} planes would then be 16.83 Å, what is $4.7b$.

No clear experimental evidence of misfit dislocations presence at the particle-matrix interface, which might be able to accommodate significant lattice misfit, was obtained within the framework of this study. Fig. 10.27b shows a small single particle in the fatigued part of specimen without any clear observation of misfit dislocations. The same results were obtained in the case of an array of larger NbC precipitates nucleated along a dislocation in the grip part of the specimen as seen in Fig. 10.30b. Here, it is important to note that just the experimental observation of the structure of interface is not an easy task. Usual thickness of the TEM foil is about 50 to 100 nm. Particles were found to be from about 3 to 15 nm in size. That means in majority of cases there will be an overlap of precipitate structure with the structure of the matrix forming some level of Moiré effect thus preventing direct observations of the interface.

For closer inspection of the $(1\overline{1}1)$ NbC/matrix interface, the image was FFT filtered using a mask which included all fundamental and satellite intensities for central and diffracted beams (see Fig. 10.30c). It is evident that the two structures have cube-on-cube orientation. Detail of the interface in Fig. 10.31a reveals presence of coincidence lattice points where the two lattices are well aligned. However, as a result of significant lattice misfit, these alternate with areas several atomic planes thick where atomic columns of the two crystal structures do not align well with each other, as demonstrated by schematic structural model in the red dashed rectangle in Fig. 10.31a. Hypothetically, if the nature of the interface is incoherent (similarly

as schematically visualised in Fig. 3.8a), it would suggest a notable decrease of local atomic density in these "misaligned" regions, consistent with the significant decrease of relative atomic column intensities in HAADF-STEM Z-contrast images as illustrated by line scans plotted in Fig. 10.31b. However, if the interface is indeed semi-coherent, the decrease of relative intensity could be connected with the presence of misfit dislocations cores. Here it should be added that in reality, MX precipitates are three-dimensional objects of octahedral shape [151] and arrangement of possible misfit dislocations would then be very complicated thus preventing easy experimental characterization. Also, there is a possibility that at the onset of nucleation, nano-sized MX precipitates do not have perfectly stoichiometric structure what would also affect character of interface. Considering experimental evidence, nano-sized NbC precipitates exhibit characteristics of an incoherent, rather than semi-coherent, relationship with the austenitic matrix. However, other tools such as constitutive modelling and simulations along with further experimental work at atomic-scale have to be used to find definite answer and solution.
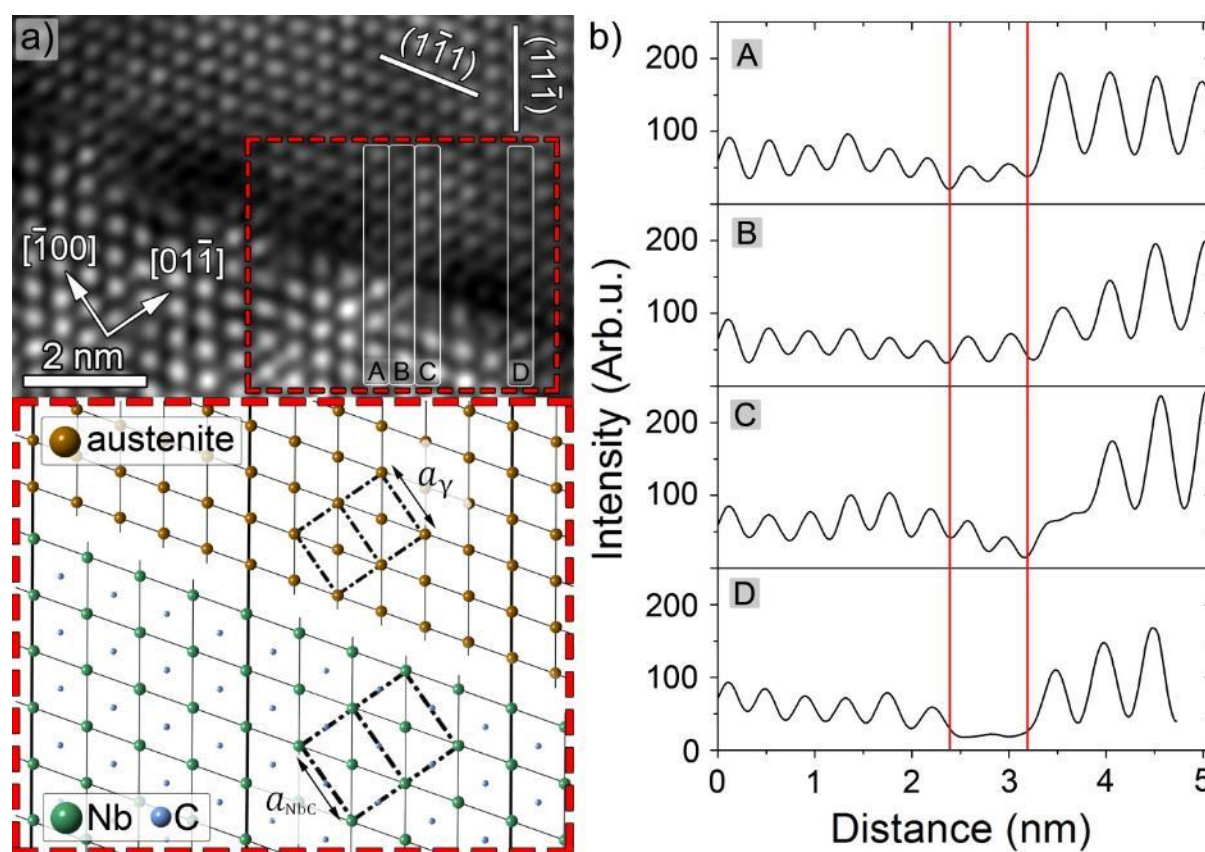
Figure 10.31: (a) FFT filtered HAADF-STEM image showing fully incoherent interface between NbC nanoparticle and matrix. Area of the interface marked by red dashed rectangle is visualized in inset as atomic structure model. Unit cells of two crystal structures are highlighted. Decrease of atomic density in the areas where atomic columns of two lattices do not fit each other leads to decrease of contrast in HAADF-STEM image. (b) Line scans across the interface showing relative intensity of atomic columns in the HAADF-STEM image as a function of distance. They demonstrate decrease of contrast where atomic density is diminished as a result of relatively poor lattice plane alignment across the interface.

10.2.4.1 HAADF-STEM simulation of Moiré-like contrast exhibited by NbC

In order to further validate the interpretation of the NbC nanoprecipitate structure observed experimentally with Moiré-like contrast, HAADF-STEM images were simulated using the µSTEM program, based on the quantum excitation of phonons (QEP) model [152].
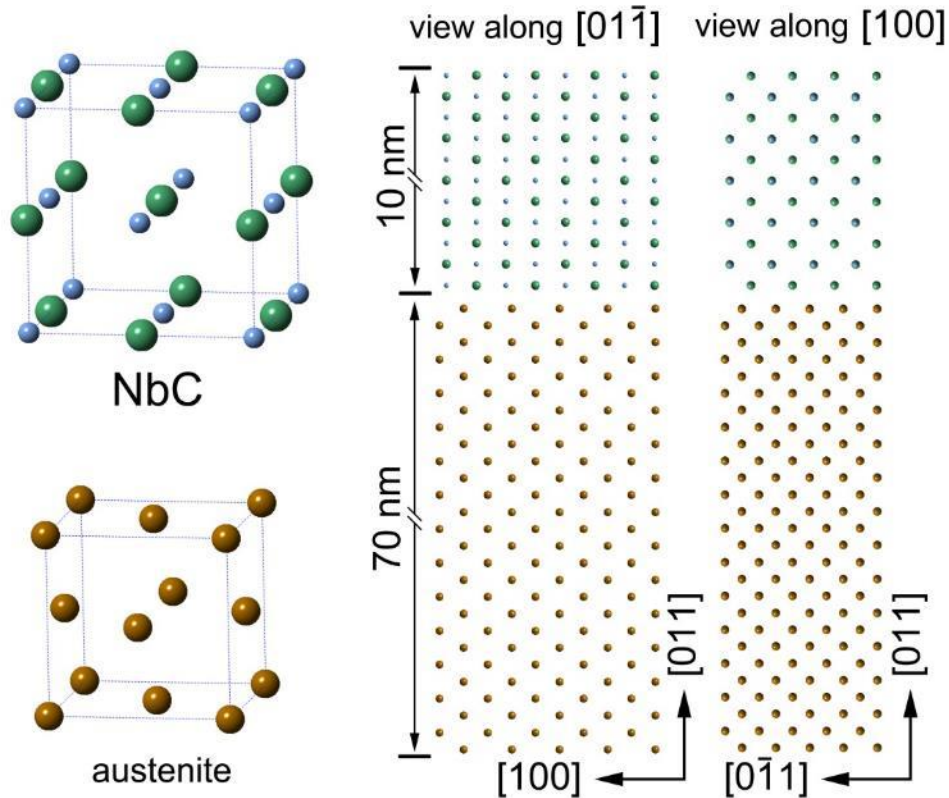
Figure 10.32: Schematic of the crystal structure used as input for the image simulation. Relaxed 10 nm thick incoherent NbC particle was placed on top of the austenite matrix with cube-on-cube orientation. Total thickness of the structure used in the model was 80 nm in the [011] *direction as based on the experimental sample shown in Fig. 10.29b.*

In the QEP model, a quantum mechanical approach is taken, whereby momentum and energy transfer are included through inelastic scattering, specifically through phonon excitation. The crystal structure used as input for the image simulation was a relaxed incoherent NbC particle on top of the austenite matrix with cube-on-cube orientation (see Fig. 10.32 and Table 10.1 summarizing structural information about two nano-scale phases studied in this work). The structure used in the model was 80 nm thick in the <011> direction, consisting of a 10 nm thick NbC particle and 70 nm austenite matrix. The foil thickness was determined to be around 85 nm thick in the region of interest by comparison between experimental and simulated position averaged convergent beam electron diffraction (PACBED) patterns [153]. The thickness of the particle was estimated to be about 10 nm based on the measurement of its diameter in the {011} plane. To ensure accurate representation of the experimental data in the simulations, the microscope conditions from the probe corrected FEI Titan[3] 80-300 S/TEM were used. Specifically, a convergence semi-angle of 12 mrad, C_s coefficient of 2 µm, and C_5 of 1 mm were used at a Scherzer defocus of -2.3 nm. Finally, a detection range from 55 to 370 mrad was used, which corresponds to HAADF image acquisition using a camera length of 73

mm on this microscope. Additionally, finite source size and detector noise were incorporated in the simulation as described by LeBeau et al. [154].
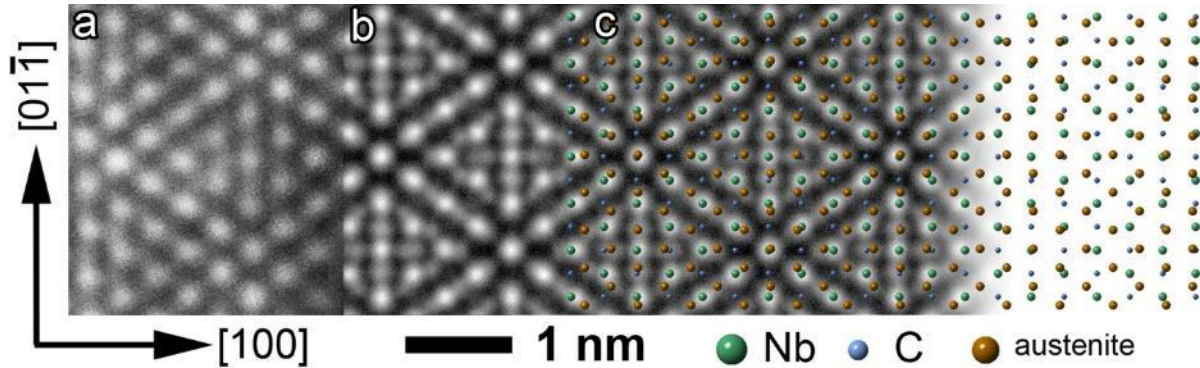
Figure 10.33: (a) Experimentally obtained HAADF-STEM image of NbC precipitate on the top of austenite matrix is compared to (b) simulated image along the [011] *zone axis (with reference to Figure 10.32) based on the atomic structure model (c). Fully incoherent nanoparticle overlaps with austenite matrix with cube-on-cube relationship forming Moiré-like contrast.*

In Fig. 10.33, results from experiment and simulation are compared. The experimental image of Fig. 10.33a was corrected for scan distortion using the method of Ophus et al. [155]. Fig. 10.33b shows the simulated image that clearly exhibits the distinctive Moiré-like contrast. Finally, in Fig. 10.33c, the simulated image is overlaid with the atomic model used in the simulations, with NbC carbide on top of the austenite matrix. The simulated structure shows good qualitative agreement between the experimental and simulated images, with increased contrast on columns that are coincident between the two overlapping crystals, supporting the assumed structure of NbC nanoprecipitates with cube-on-cube orientation relationship to the matrix and an incoherent nature of the interface.

Phase	Space Group	Structure	Wyckoff positions of atoms	Site occupancy	Lattice parameter (Å)
Austenite	Fm$\bar{3}$m (225)	-	4a (Fe, Ni, Cr)	Fe (0.472) Ni (0.262) Cr (0.262)	3.60692(8)*
Cu	Fm$\bar{3}$m (225)	A1/cF4	4a (Cu)	Cu (1)	3.615**
NbC	Fm$\bar{3}$m (225)	B1/cF8	4a (Nb);4b (C)	Nb (1) C (1)	4.47***
Notes: *neutron powder diffraction **taken from JCPDS 04-0836, [143] ***taken from T. Sourmail [126]					

Table 10.1: Overview summarizing the structural information of the austenitic matrix and two studied nano-scale phases used in this work.

As reported by [126, 145] the precipitation of fully incoherent Nb(C,N) particles in the defect-free austenite is extremely difficult due to the large positive misfit. However, the present results indicate that nucleation does occur at lattice defects, where part of the strain energy can be released by replacement of a dislocation segment with the precipitate nucleus, thereby

helping to overcome the nucleation barrier and enabling the existence of Nb(C,N) nanoprecipitates in the austenite matrix. In the presence of thermal exposure only, Nb(C,N) precipitates are found nucleated only on defects (Figs. 10.29a and 10.29b). It is surmised that the abundant nanoparticle arrays embedded in the matrix found only after high temperature cyclic loading (Figs. 10.28a and 10.28b) are remnant left behind after detachment from dislocations. A more quantitative investigation of this detachment phenomenon and subsequent interaction with dislocations under fatigue loading conditions will be described in discussion section.[135, 156]

11. Microstructural evolution – Manaurite XTM

Several specimens were selected for a *post-mortem* study of deformation microstructure which formed as a result of cyclic loading both at a room temperature and at a temperature of 700°C. Since overall microstructure of Manaurite XTM centrifugally casted alloy has heterogeneous characteristics in terms of large columnar dendritic grains, instead of traditional electrolytic polishing the focused ion beam nanofabrication was used to prepare site-specific TEM lamellae. Details of preparation of specimens with polished surface from which TEM foils were extracted are described in Experimental section IV. The foils were subsequently characterized using high-resolution STEM microscopy.

11.1 Room temperature cyclic loading

Two specimens were selected for analysis of microstructures formed at room temperature cyclic loading. Specimen loaded with total strain amplitude $\varepsilon_a = 3.5 \times 10^{-3}$ (saturated plastic strain amplitude $\varepsilon_{aps} = 1.4 \times 10^{-3}$) represents loading with lower strain amplitudes while the specimen loaded with $\varepsilon_a = 6.5 \times 10^{-3}$ (saturated plastic strain amplitude $\varepsilon_{aps} = 3.7 \times 10^{-3}$) is representative of loading with higher strain amplitudes. In Fig. 11.1, the two columnar dendritic grains with the serrated grain boundary are shown using secondary electrons mode in SEM. The site for the extraction of TEM foil was localized in the grain on the right hand side as shown in Fig. 11.1a. The goal was to avoid regions possibly affected by long-range stress fields such as serrated grain boundaries or interdendritic regions with primary precipitates. To obtain representative deformation microstructure of the face-centered cubic matrix, site was selected approximately in the middle of the central dendrite axis, as shown in Fig. 11.1b.
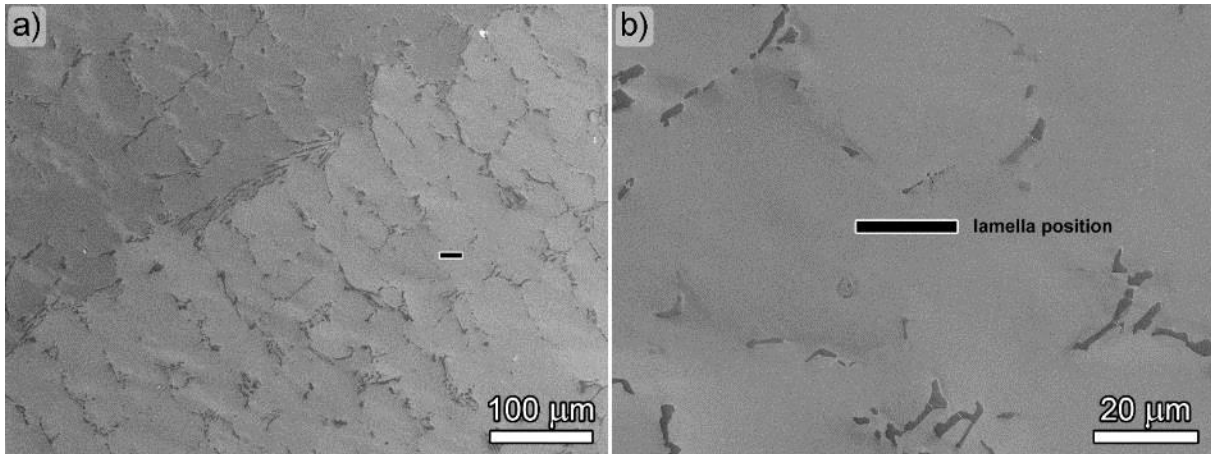
Figure 11.1: (a) SEM overview image of the polished area where the thin foil was extracted for subsequent analysis in TEM. Secondary electrons mode is showing serrated grain boundary of two dendritic grains. Foil was extracted approximately 120 microns from the grain boundary, in the middle of right hand side grain close to the central dendrite axis. (b) Extraction was done in such a way so the foil contains mostly face-centered cubic matrix.

After final thinning, TEM foil of approx. 150 nm in thickness was obtained and subsequently analyzed using high-resolution STEM. Overview of the whole lamella is shown in Fig. 11.2a and 11.2b using BF and annular dark field (ADF) detector, respectively.

Figure 11.2: (a) BF-STEM diffraction contrast image showing dislocation structure formed after cyclic loading with total strain amplitude 0.35% at room temperature. View direction is along the zone axis [$\bar{1}$11]. *Loading axis corresponds to vector* [110] *when taken with respect to the grain orientation. (b) ADF-STEM image.*

Extracted lamella contains region of two grains separated by low-angle grain boundary (misorientation is less than 2°). Two large primary eutectic M_7C_3 Cr-rich carbides are observed. View direction is parallel with the zone axis $[\bar{1}11]$ of the matrix. Individual dislocations and pile-ups are observed with no evidence of any significant localization, neither complex spatial dislocation structures formation. Grains orientation with respect to the loading axis of the cylindrical specimen was determined and is shown in stereographic triangle demarked by three vectors [010], [111] and [110]. For this notation, loading axis corresponds to vector L_D = [110]. Schmid factors of possible slip systems were determined revealing that for this particular orientation of grain only four of twelve possible slip systems have non-zero Schmid factors. These slip systems correspond to glide planes (111) and (11$\bar{1}$) and all have Schmid factors equal to 0.408.
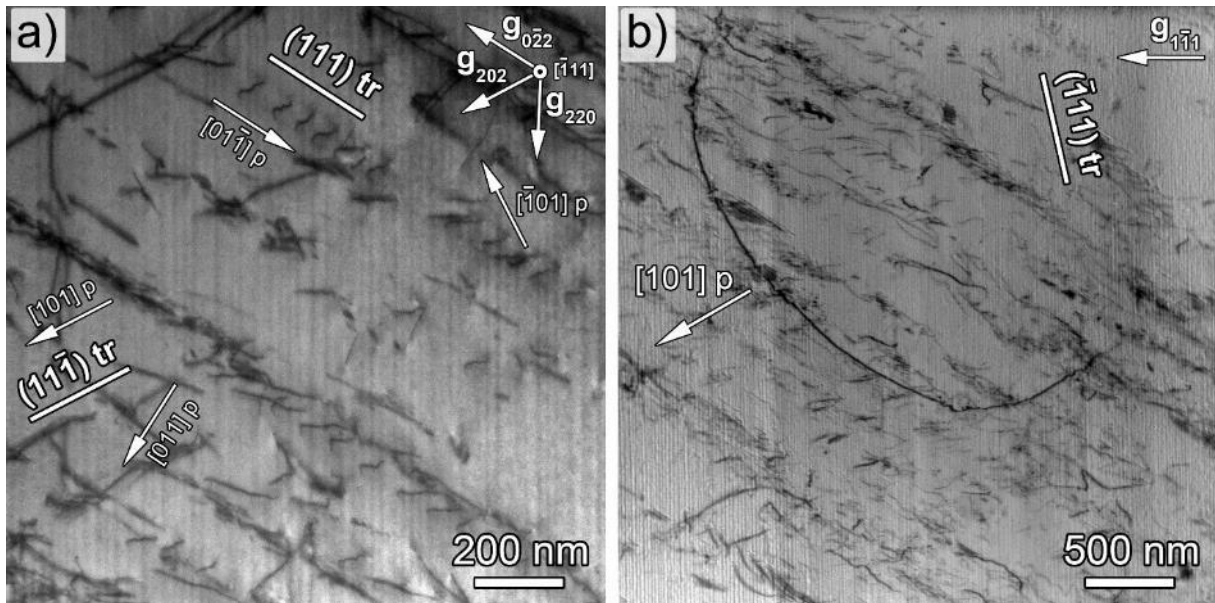
Figure 11.3: (a) Detail showing dislocations from four slip systems lying on two slip planes (111) and (11$\bar{1}$). View direction is along the zone axis $[\bar{1}11]$. (b) Detail showing dislocation with Burgers vector 1/2[101].

The grains were tilted out of the zone axis to obtain two-beam STEM diffraction contrast imaging with different excitation vectors corresponding to particular lattice vectors of <220> and <111> types. Dislocation structure was analysed and dislocations identified using g.b analysis of Burgers vector. Indeed, most of the dislocations observed are located on glide planes (111) and (11$\bar{1}$) corresponding to slip systems with high Schmid factors. Also a few dislocations were found located on (1$\bar{1}$1) plane. However, the trace of this set of planes is parallel with the direction of ion beam scanning during the foil thinning, so there is a chance that dislocation segments lying on (1$\bar{1}$1) plane are just artefacts related to the specimen preparation. Few individual dislocations lying also on the fourth possible plane, i.e. the plane ($\bar{1}$11) parallel with the plane of the image, were also observed as shown in Fig. 11.3b.
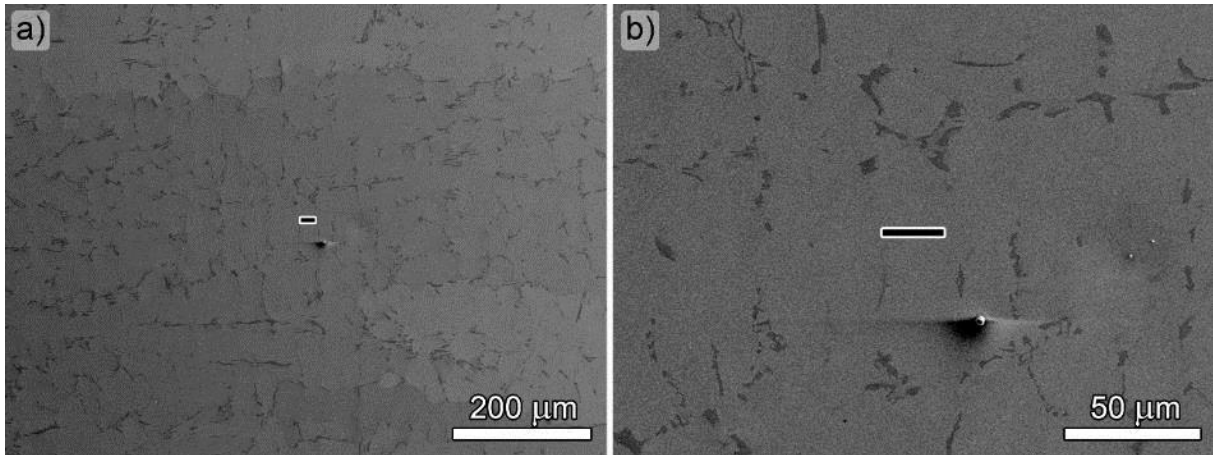
Figure 11.4: Specimen after cyclic loading with total strain amplitude 0.65% at room temperature. (a) SEM overview image of the polished area where the thin foil was extracted for subsequent analysis in TEM. (b) Extraction was done in such a way so the foil contains only face-centered cubic matrix and other phases are avoided.
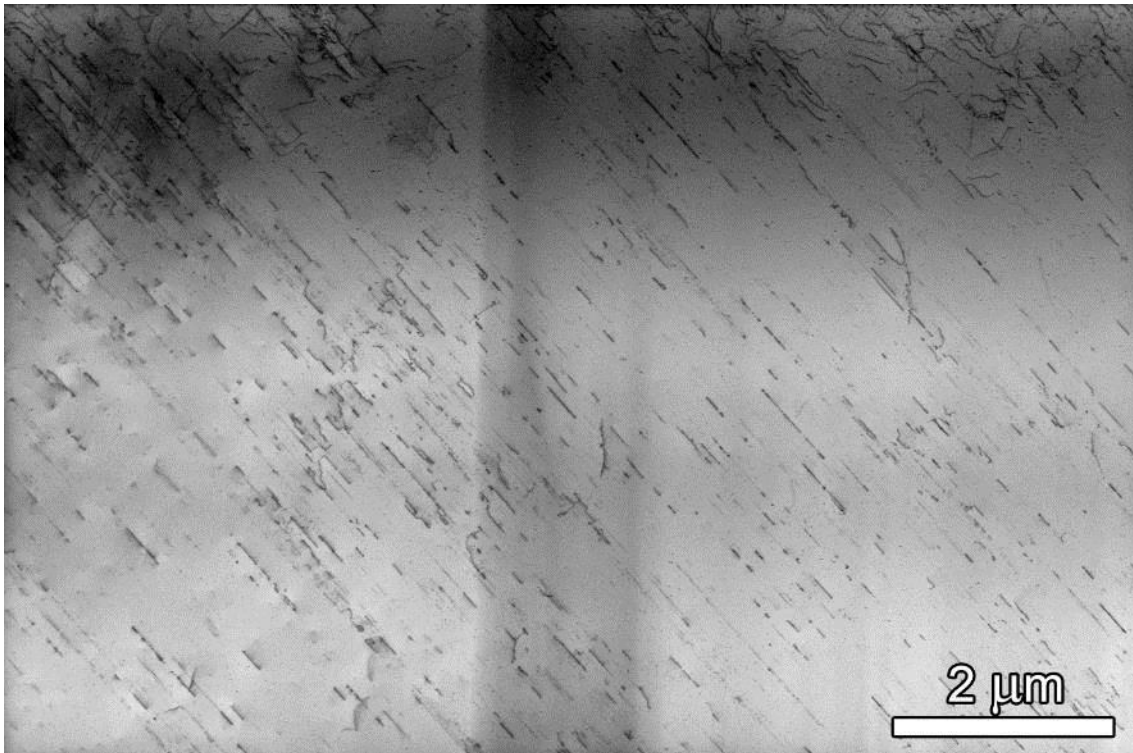
Figure 11.5: Dislocation structure observed in thin foil extracted from the specimen after loading with total strain amplitude 0.65% at room temperature. Image was obtained using BF-STEM detector in dual-beam system Helios. Individual dislocations are observed, mostly from one activated slip system. No evidence for cyclic slip localization and formation of spatial dislocation arrangements.

Analysis of dislocation structure reveals that there is a higher dislocation density around the grain boundary and especially in the vicinity of primary eutectic precipitates when compared to the areas of matrix far away from any primary phases. This can be result of locally different stress fields coming from the precipitates presence.

The most important observation is that the character of the deformation structure, i.e. dislocation arrangement, is significantly planar. When compared to Sanicro 25 alloy, there is no evidence for localization of cyclic slip into high dislocation bands, neither for formation of spatial dislocation structures. Also, at room temperatures, there are no small precipitates present in the matrix, only large primary eutectic Cr-rich carbides (M_7C_3 and $M_{23}C_6$) and occasionally smaller Nb-rich particles (MC).

In Fig. 11.4, area of the lamella extraction is shown for the specimen loaded with total strain amplitude 0.65% at room temperature. Again, lamella was prepared from the matrix region corresponding to the central dendritic axis. In Fig. 11.5, the whole lamella is shown after final polishing. Same as for the specimens tested with low strain amplitude, low dislocation density is observed. Only one slip system is activated with individual dislocations of pile-ups present. No evidence for localization of cyclic plastic behavior is found as shown in details in Fig. 11.6. Same structure was also observed in case of another lamella (not shown here) prepared from different area of this fatigued sample.
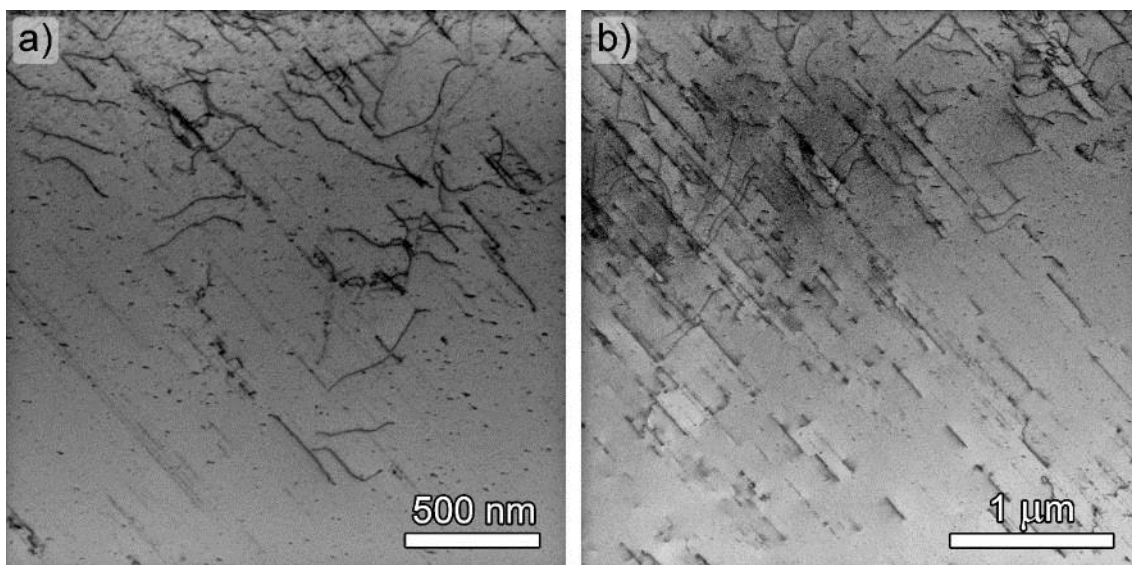
Figure 11.6: Details of dislocation structure observed in thin foil extracted from the specimen after loading with total strain amplitude 0.65% at room temperature. Individual dislocations are observed with no evidence for cyclic slip localization and formation of spatial dislocation arrangements.

11.2 Cyclic loading at a temperature of 700°C

At high temperature, first specimen loaded with total strain amplitude $\varepsilon_a = 3.5 \times 10^{-3}$ (saturated plastic strain amplitude $\varepsilon_{aps} = 1.3 \times 10^{-3}$) was selected for detailed microstructural analysis as a representative of testing with low strain amplitude. Specimen was cyclically loaded for 5 hours, so with 2 hours needed for stabilization, in total it spent about 7 hours at a temperature of 700°C. Area from which the thin foil for subsequent high resolution analysis was extracted is shown in Fig. 11.7. Place was selected in the austenitic matrix in such a way that the primary eutectic carbides were avoided.
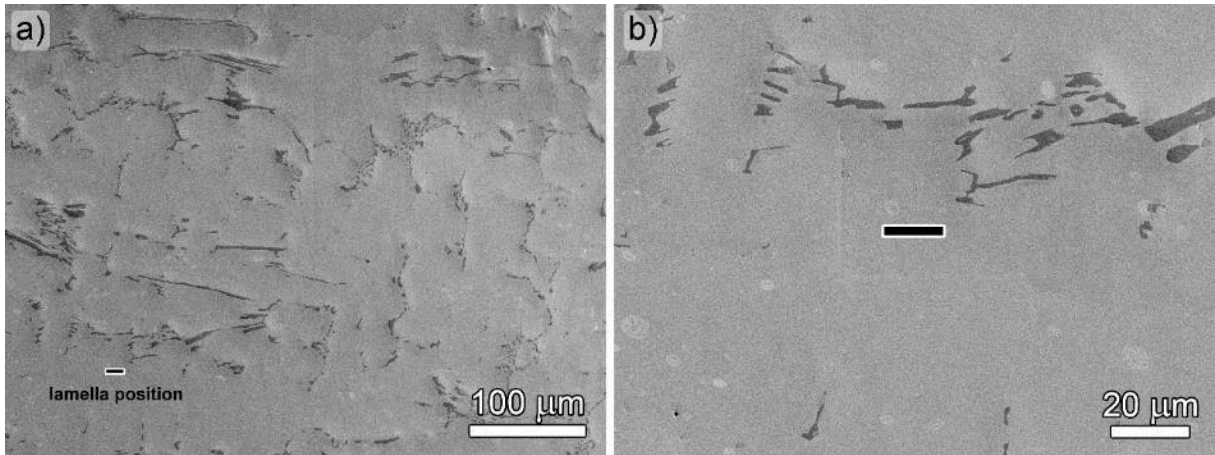
Figure 11.7: Specimen after cyclic loading with total strain amplitude 0.35% at temperature of 700°C. (a) SEM overview image of the polished area where the thin foil was extracted for subsequent analysis in TEM. Position is marked with black bar. (b) Detail of the extraction area. Foil was lifted out from the area of central dendritic axis. Primary eutectic precipitates were avoided.
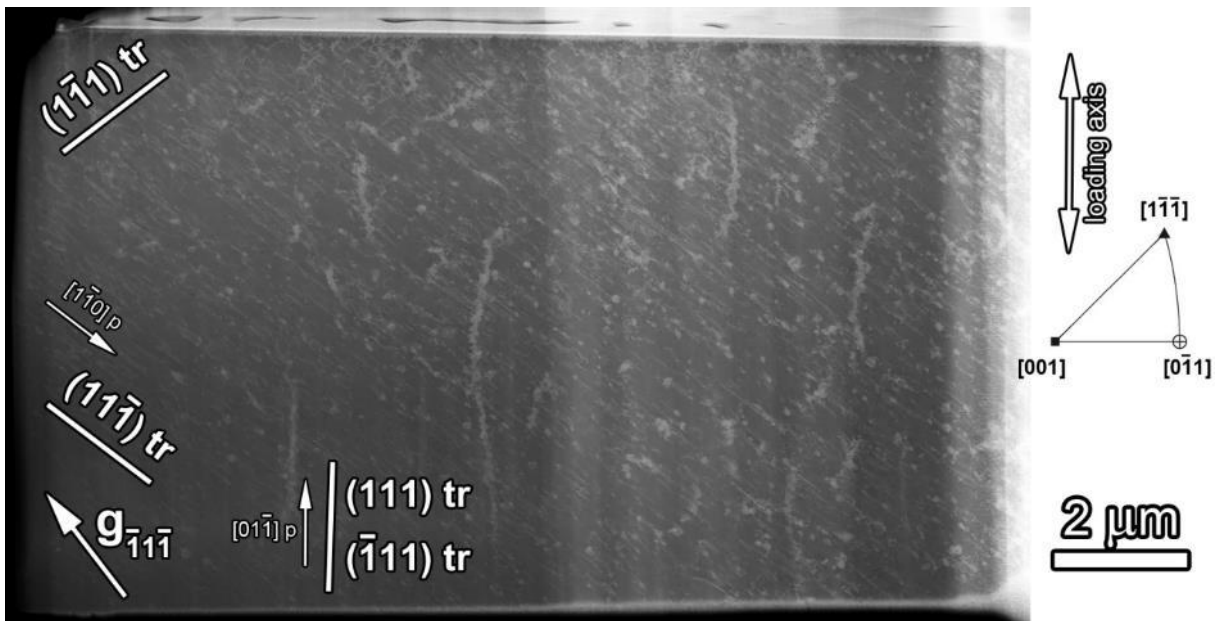
Figure 11.8: LAADF-STEM diffraction contrast image showing deformation structure formed after cyclic loading with total strain amplitude 0.35% at 700°C (spent 7 hours at high temperature). View direction is close to the zone axis [011], *however two beam condition is set only for diffraction vector* [$\bar{1}1\bar{1}$]. *Loading axis corresponds to vector* [$0\bar{1}1$] *when taken with respect to the grain orientation.*

Thin TEM lamella after final step of polishing with focused ion beam is shown in Fig. 11.8 using LAADF-STEM diffraction contrast imaging. View direction is close to the zone axis [011], however two beam condition is set only for the diffraction vector [$\bar{1}1\bar{1}$]. Grain orientation with respect to the loading axis of the cylindrical specimen was determined and is shown in stereographic triangle demarked by three vectors [001], [$1\bar{1}\bar{1}$] and [$0\bar{1}1$]. For this notation, loading axis corresponds to vector $\mathbf{L_D}$ = [$0\bar{1}1$]. Schmid factors of possible slip

127

systems were determined revealing that for this particular orientation of grain only four of twelve possible slip systems have non-zero Schmid factors. These slip systems correspond to glide planes (111) and (1$\bar{1}$1) and all have Schmid factors equal to 0.408. More detailed picture of the microstructure is shown in Fig. 11.9.

Contrast and crystallography analysis has revealed that the majority of the dislocations observed are screw segments with Burgers vector ½[1$\bar{1}$0] lying on (11$\bar{1}$) slip planes. Individual dislocation segments are observed with no evidence of cyclic slip localization or formation of complex spatial dislocation structures.
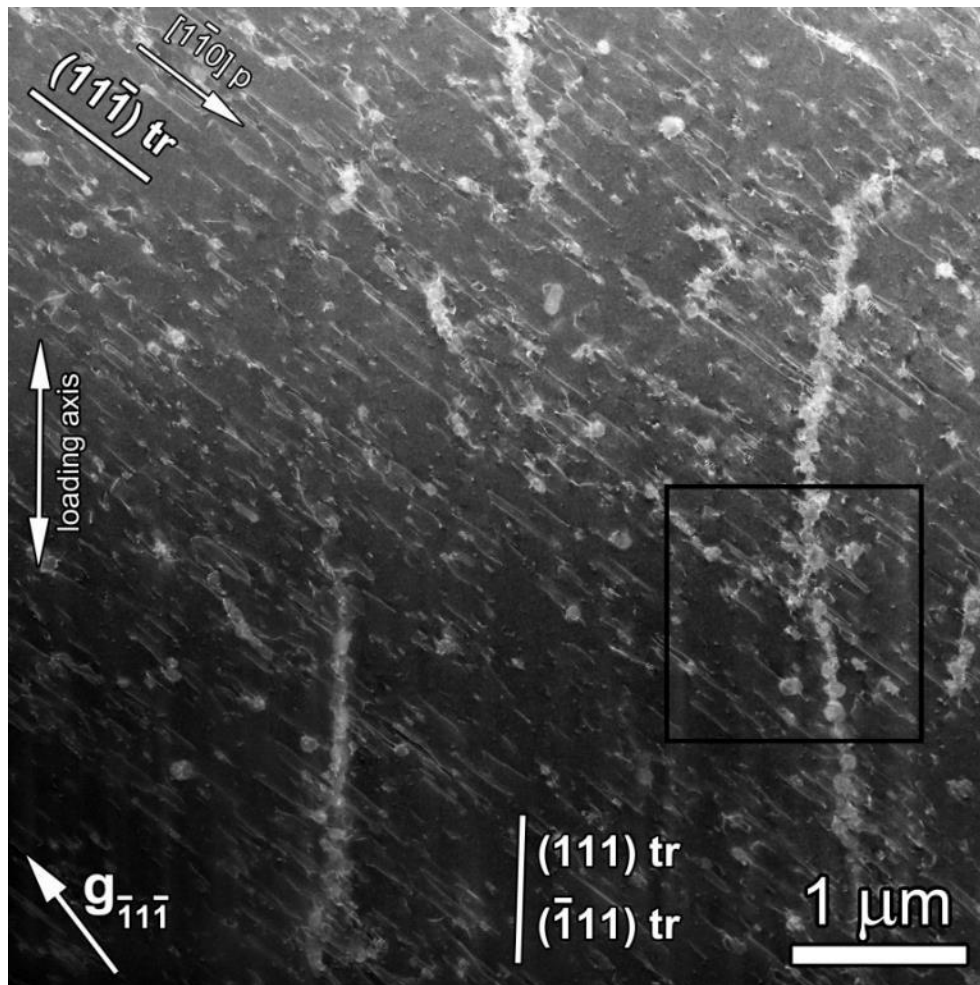
Figure 11.9: LAADF-STEM diffraction contrast image showing details of deformation microstructure. Dislocations with Burgers vector ½[1$\bar{1}$0] lying on (11$\bar{1}$) slip planes are observed as well as numerous secondary $M_{23}C_6$ carbides precipitated as a result of cyclic loading at a temperature of 700°C. Carbides are found in the matrix or nucleated along immobile ½[0$\bar{1}$1] dislocations. Black rectangle highlights area where EDS analysis was done.

Along with dislocations, also numerous secondary precipitates are found nucleated during cyclic loading at high temperature. Some of the precipitates are located in the free matrix and some particles are nucleated along the dislocations. These dislocations were found to be screw or mixed/almost screw segments with Burgers vector ½[0$\bar{1}$1] lying on (111) or ($\bar{1}$11) planes.

Since Schmid factors for these slip systems are zero, it is suggested that these dislocations were immobile during cyclic loading thus being nucleation site for particles precipitation.

High resolution EDS analysis was done in the area highlighted by black rectangle in Fig. 11.9. Results are shown in Fig. 11.10 plotted as EDS maps. It is clear that the precipitates are rich in Cr, C and also in Mn and Si. Owing to high carbon and chromium content, several different types of carbides can precipitate in Manaurite XTM at high temperatures as was noticed previously [29]. Chemical content and also relatively short ageing time would suggest $M_{23}C_6$ type of carbide, usually observed as first nucleated phase in alloys with high Cr and C content. To confirm what phase is present, specimen was tilted into zone axis [011] to conduct high-resolution HAADF-STEM Z-contrast imaging.
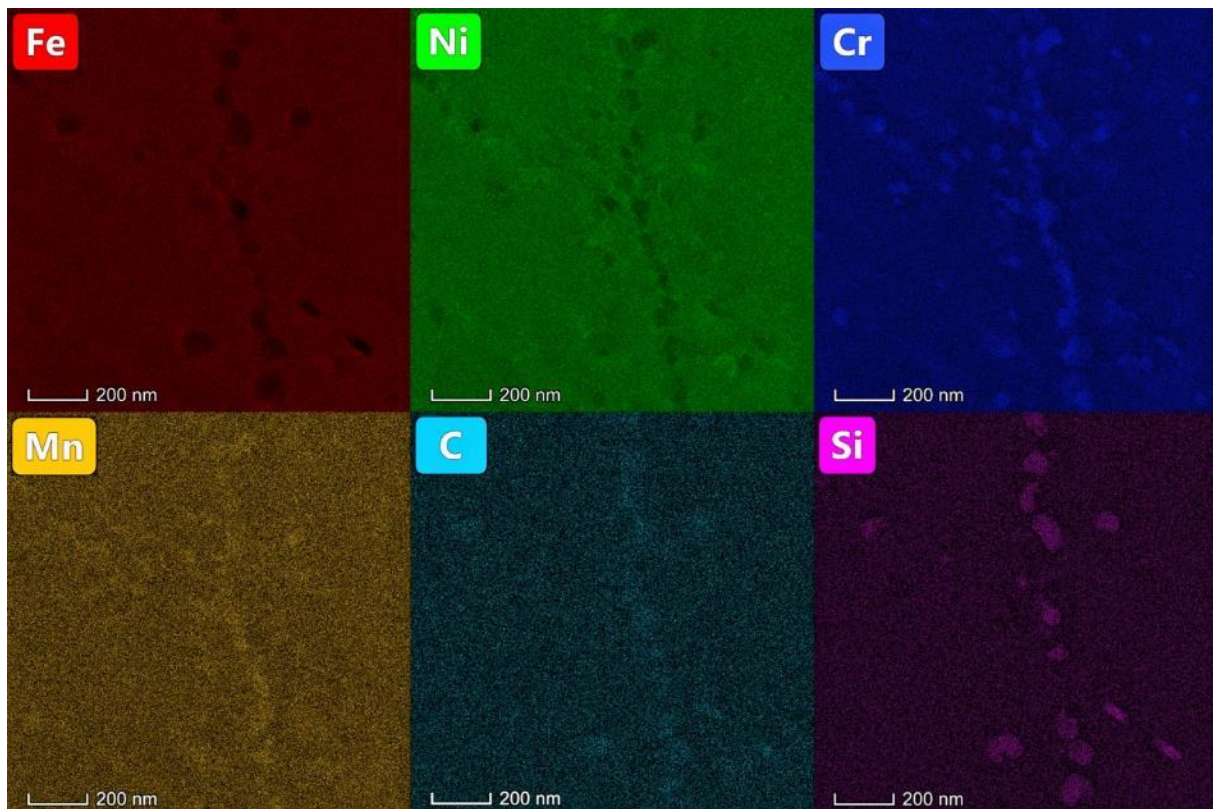
Figure 11.10: EDS map analysis from the region highlighted by black rectangle in Fig. 11.9. Precipitates are rich in Cr, C and also Mn and Si.

Comparison of LAADF-STEM two-beam diffraction contrast image and HAADF-STEM Z-contrast zone axis atomic-resolution image is shown in Fig. 11.11a and 11.11b, respectively. Several precipitates were analysed in detail. Example of detailed structure characterization of two precipitates highlighted by black rectangle in Fig. 11.11b is demonstrated in Fig. 11.12. Both particles have well distinguished octahedral shape with {111}-type of facets at the semi-coherent interface with the matrix. FFT pattern was obtained from the STEM image of the precipitate atomic structure and compared with simulated diffraction pattern corresponding to $Cr_{23}C_6$ carbide (see Fig. 11.12c). It demonstrates cube-on-cube orientation of the particle with the matrix. As a last step, the structure of carbide was confirmed by direct comparison of $Cr_{23}C_6$ structural model created using the Crystal Maker software and FFT filtered STEM

image of the atomic structure of the precipitate. Good agreement was obtained as is shown in Fig. 11.12d.

According to ThermoCalc analysis presented by Joubert et al. [29], several phases are possible to precipitate in alloy as Manaurite XTM at high temperatures, e.g. MC ((Nb,Ti)C), G-phase (NiNbSi) and also $M_{23}C_6$. However, our experimental results suggest that prevailing secondary phase nucleated in specimens cyclically loaded at a temperature of 700°C is semi-coherent carbide of $M_{23}C_6$-type rich in Cr, Si and Mn. Interestingly, no nano-scale MC precipitates were observed as in case of Sanicro 25.

As is shown in Fig. 11.12, carbides are of size in tens of nanometers, what can be considered as large from the perspective of the strengthening effect. Average diameter of $M_{23}C_6$ carbides was estimated to be 69 nm with particle sizes ranging from 35 to 110 nm. As was already mentioned, $M_{23}C_6$ Cr-rich carbide is usually first secondary phase to appear at high temperatures around 700°C in alloys rich in Cr and C. Taking into account elementary concepts of precipitation strengthening, it can be expected that in the early stages of their nucleation and growth, $M_{23}C_6$ Cr-rich carbides can present obstacle for dislocation movement, especially in cases where they nucleate at immobile dislocation cores, with pipe diffusion facilitating their growth. However, as they overcome the critical size and Orowan bowing becomes the governing mechanism of particle-dislocation interaction, their strengthening effect rapidly diminishes with further coarsening and growth.
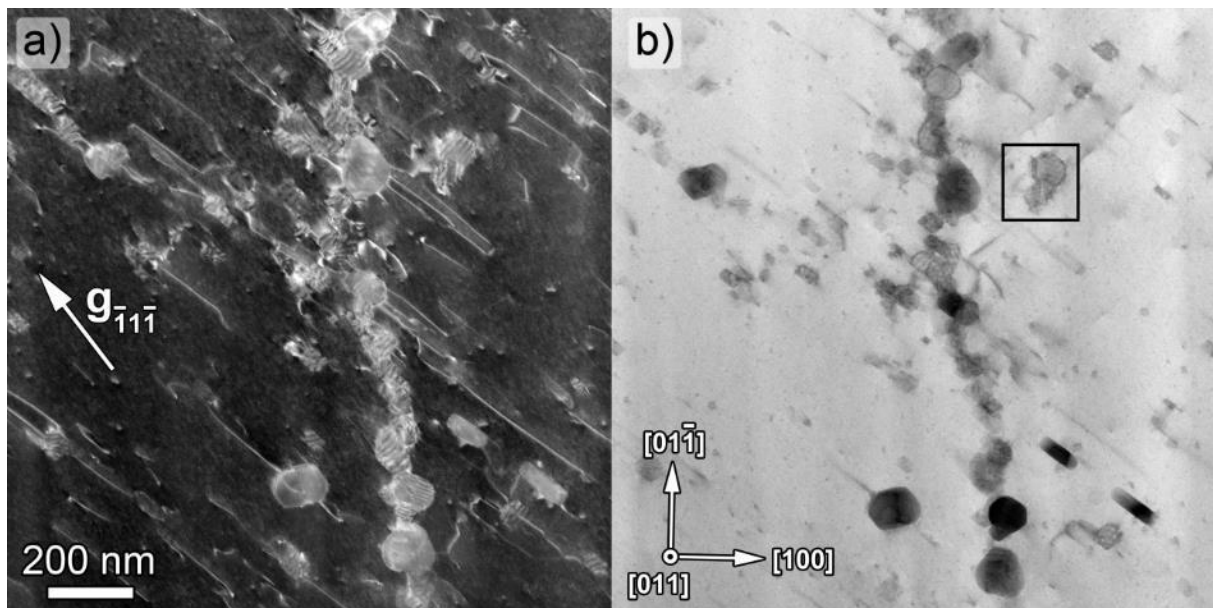
Figure 11.11: (a) LAADF-STEM diffraction contrast image showing array of $M_{23}C_6$ carbides precipitated along dislocation. Primary dislocations lying on $(11\bar{1})$ slip planes are visible as well. (b) Specimen was tilted so the view direction is along [011] zone axis. Several precipitates were analyzed to confirm the structure of $M_{23}C_6$ Cr-rich phase. Two precipitates highlighted by black rectangle are shown in detail in Fig. 11.12.
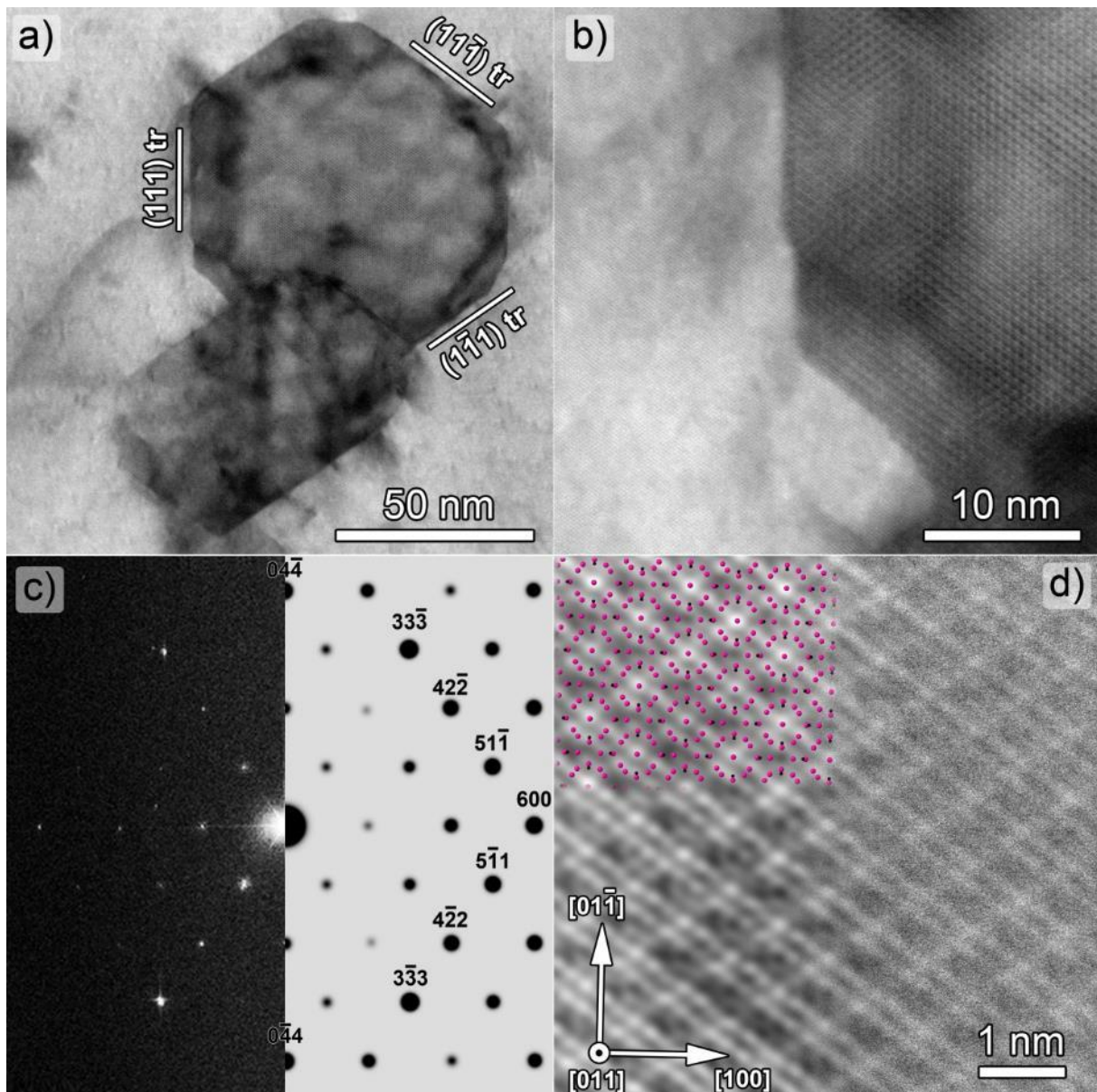
Figure 11.12: (a) HAADF-STEM Z-contrast image showing two $M_{23}C_6$ carbides rich in Cr, Si and Mn. They have facetted {111}-type of the interface with the matrix. (b) Atomic structure of the precipitate was analysed and FFT diffraction patterns obtained. (c) FFT pattern of the carbide is compared to the diffraction pattern simulated using crystal model of $Cr_{23}C_6$ structure. (d) Atomic structure of carbide is viewed along [011] zone axis. Experimentally obtained and FFT filtered image of the carbide structure is compared with the model of structure made in Crystal Maker software.

VI. DISCUSSION

In this section, basic mechanical properties as well as properties corresponding to cyclic loading are discussed in relation to microstructural characteristics of Sanicro 25 and Manaurite XTM. Both materials are also compared with other similar alloys used in same or similar industrial applications and in similar service conditions. List of the materials discussed in this section is shown in Tab. 12.1 along with their chemical composition.

As was already noted previously, austenitic stainless steel (AISI) 316L is typical representative of conventional alloy widely used in applications up to 600°C. On the other hand, Super304H, NF709 and HR3C as well as Sanicro 25 belong to the class of advanced heat-resistant alloys designed for construction of coil and pipe systems sustaining higher operation temperatures up to 700°C. The three other alloys, Manaurite XTM, Sandvik 353MA and Fe-45Ni-23Cr-7W alloy, were designed mainly as structural materials of coil and pipe systems in ethylene cracking furnaces. Notably higher content of Ni and Cr in the matrix is the main characteristic differentiating these three alloys from the conventional AISI 316L or advanced heat-resistant steels. Manaurite XTM is the only alloy from the list produced by centrifugal casting.

	Fe	Ni	Cr	W	Cu	Co	Nb	Mn	Si	N	C	Mo	
San25	Bal.	25.0	22.5	3.6	3.0	1.5	0.5	0.5	0.2	0.23	0.1	-	-
316 (L/H)	Bal.	10.0-14.0	16.0-18.0	-	-	-	-	2.0 max	1.0 max	0.1 max	0.03-0.1	2.0-3.0	+P,S, B
NF709	Bal.	23.0-27.0	19.0-22.0	-	-	-	0.1-0.4	1.5 max	0.75 max	0.1-0.2	-	1.0-2.0	+B, Ti,
HR3C	Bal.	17.0-23.0	24.0-26.0	-	-	-	0.2-0.6	2.0 max	0.75 max	0.15-0.3	0.04-0.1	-	-
Super 304H	Bal.	7.5-10.5	17.0-19.0	-	2.5-3.5	-	-	1.0 max	0.3 max	0.05-0.12	0.07-0.13	-	+B, Al
Man XTM	Bal.	43.0-48.0	35.0-37.0	-	0-0.25	-	0.5-1.0	0-1.5	1.20-2.00	.	0.40-0.45	0-0.5	+Ti, P, S
45Ni-23Cr-7W	Bal.	45.2	23.4	7.5	-	-	0.18	1.02	0.15	-	0.07	-	+Ti
Sand 353MA	Bal.	35	25	-	-	-	-	1.5	1.6	0.16	0.07	-	+P,S

Table 12.1: Comparison of chemical composition of different Fe-Ni-Cr based alloys used for construction of coils and pipes in high temperature applications (in wt.%).[9, 10, 24, 27, 157–161]

After discussion of basic tensile mechanical properties at room and elevated temperatures, general cyclic properties related to the fatigue life of materials are compared and discussed. Afterwards, attention is focused on the materials response under load, change of the cyclic stress within the fatigue life and differences between room and elevated temperature cyclic loading. In the last section, key mechanisms leading to extraordinary cyclic strengthening of Sanicro 25 alloy are identified, explained and discussed.

12. Basic mechanical properties – tensile tests

Tensile stress-strain curves of Sanicro 25 and Manaurite XTM (axial direction) are compared both at room and elevated temperature as shown in Fig. 12.1. Corresponding tensile parameters are noted in Tab. 12.2 along with tensile parameters of similar alloys listed in Table 12.1.
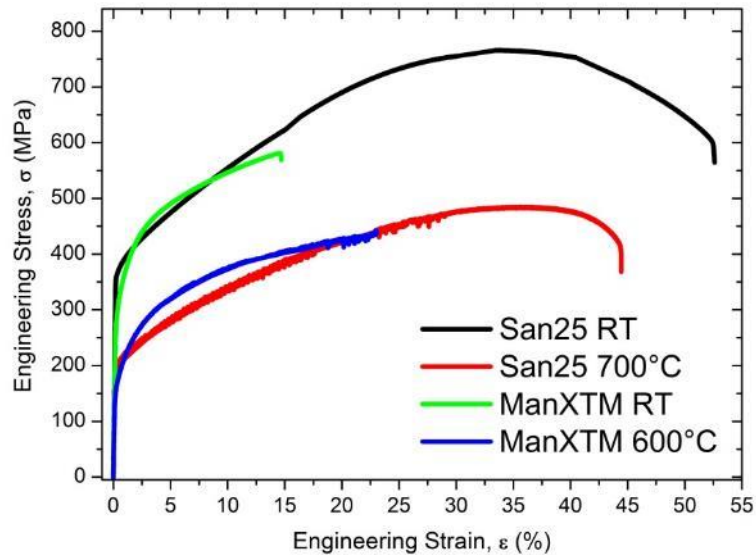
Figure 12.1: Tensile stress-strain curves of Sanicro 25 at room temperature and at 700°C compared with stress-strain curves of Manaurite XTM at room temperature and at 600°C. Corresponding parameters as modulus, yield strength, ultimate tensile strength and elongation are listed in Tab. 12.1. Plotted stress-strain curves of Manaurite XTM were obtained from testing of specimens produced as parallel with axis of centrifugally casted tube, i.e. perpendicular to the dendrites.

Sanicro 25 has higher ultimate tensile strength and yield strength both at room and elevated temperatures, when compared to Manaurite XTM. Striking difference is in a ductility of materials. While Sanicro 25 in solution annealed state has elongation at fracture about 52% at room temperature, Manaurite XTM reaches only about 15%. This prevails also at high temperature, where Sanicro 25 has elongation about 44% while Manaurite XTM only about 23%. This suggests that Manaurite XTM will have much lower workability than Sanicro 25.

In Fig. 12.2, ultimate tensile strength versus total elongation to fracture diagram is plotted. Sanicro 25 and Manaurite XTM are compared with similar alloys. Here it is important to note, that mechanical properties of alloys and austenitic steels can differ significantly depending on the thermo-mechanical treatment defining initial state in which the materials are delivered. For comparison in this work, selection of alloys was done in such a way that the list contains the similar types not only regarding composition, but also the thermo-mechanical treatment.

	E [GPa]	Y.S. at 0.2% [MPa]	U.T.S. [MPa]	Total fracture strain [%]
Sanicro 25				
Initial state, RT *(producer)*	197	≥310	≥680	≥40
Initial state, RT	198	368	765	52
Initial state, 700°C	150	198	485	44
Manaurite XTM				
RT *(producer)*	182	345	570	12
RT	172	302	581	14.5
600	122	224	442	>23
316L [159, 160]				
RT	193	290	579	50
600	153	140	452	44
700	143	131	345	43
NF709/Alloy 709 [161]				
RT(official datasheet)	193	≥270	≥640	≥30
RT	193	251	624	51
650	153	168	519	36
750	145	174	368	32
HR3C [149]				
RT	196	368	740	48
650	148	180	492	45
Super304H [162]				
RT	-	284	576	72
600	-	193	432	42
650	-	204	402	40
Sandvik 353 MA *(producer)*				
RT	190	≥300	≥650	≥40
600	155	≥138	≥422	-
Fe-45Ni-23Cr-7W alloy [157]				
RT	-	260	637	59
600	-	163	453	74
700	-	151	423	69

Table 12.2: Basic tensile properties of similar type of alloys used as structural materials for construction of pipes and coils in power generation industry are compared at room and elevated temperatures. Part of the tensile data sets of Sandvik Sanicro 25, Sandvik 353 MA and Manaurite XTM were obtained from hard copies of datasheets delivered with the material.
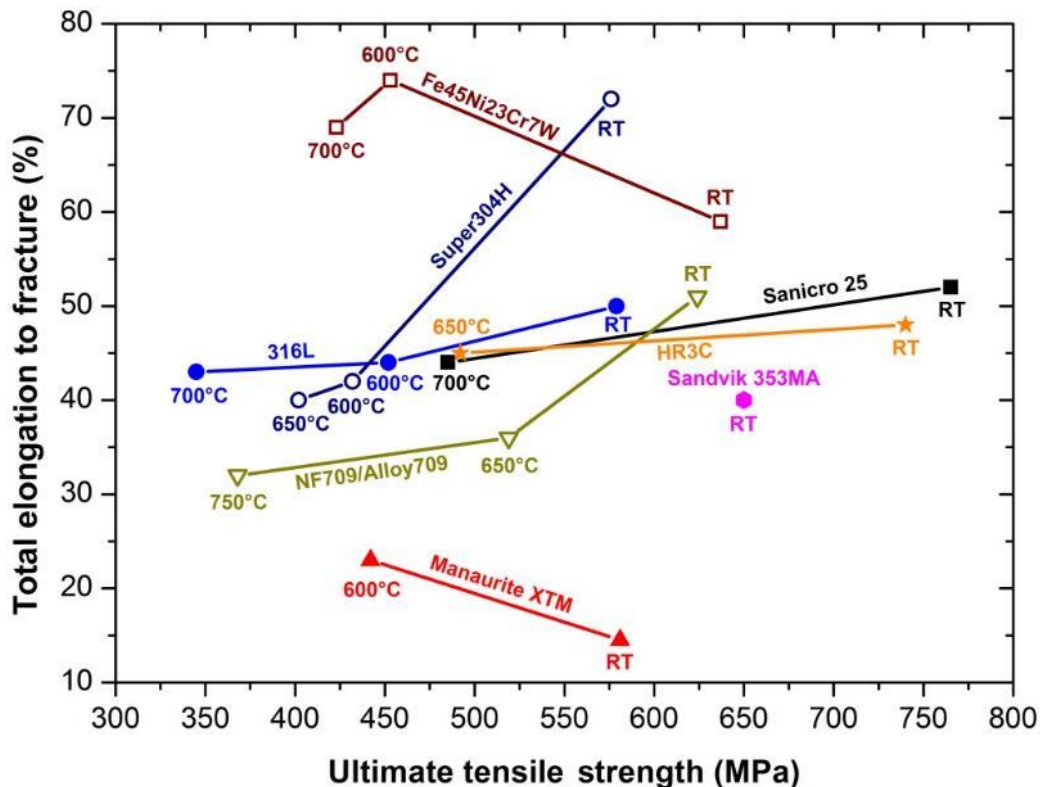
Figure 12.2: Ultimate tensile strength versus elongation diagram. Alloys of similar class used as structural materials for construction of pipes and coils in power generation industry are compared both at room temperature and at elevated service temperatures ranging from 600°C to 750°C.

It is clear that Sanicro 25 has the highest strength of all alloys both at room and high temperatures. The closest competitor, NF709, has the ultimate tensile strength by more than 100 MPa lower with ductility being similar. However, at high temperatures contrary to Sanicro 25, NF709´s elongation to fracture diminishes as well as total strength. Most comparable material to Sanicro 25 in the diagram is modified HR3C alloy as it has similar strength and ductility both at room and high temperature. On the other hand, conventional 316L austenitic steel has similar level of ductility, but is much weaker regarding strength. Interestingly, when in solution annealed state, the modified Super304H austenitic steel alloyed with copper has worse characteristics then conventional 316L steel.

When compared to other alloys, Manaurite XTM has very poor tensile characteristics, i.e. low ductility and low ultimate tensile strength. Opposite case is the Fe45Ni23Cr7W alloy which has the best values of total elongation to fracture of all materials in Fig. 12.2. Tensile test data for another alloy used in ethylene cracking furnaces, Sandvik 353MA, are available only for room temperature, thus the high temperature comparison was not done.

13. Fatigue properties

13.1 Comparison of fatigue life curves - Sanicro 25 versus Manaurite XTM

In this section, fatigue properties of both materials are discussed also in relation to other alloys from the Tab. 12.1. Coffin-Manson and Derived Wöhler fatigue life curves as well as cyclic stress-strain curves were plotted. Corresponding parameters obtained from the fatigue life curves are summarized in Tab. 13.1.

T [°C]	K' [MPa]	n'	ε_f'	c	σ_f' [MPa]	b [MPa]
Sanicro 25						
22	1006	0.186	0.700	-0.526	962	-0.100
700	1243	0.181	0.090	-0.539	797	-0.090
Manaurite XTM						
22	1084	0.173	0.138	-0.457	877	-0.095
700	802	0.167	0.085	-0.510	600	-0.106

Table 13.1: Comparison of low cycle fatigue parameters of both studied materials at two temperatures.

Fatigue life of both materials can be characterized by the Coffin-Manson law. In Fig. 13.1, plastic strain amplitude in half-life is plotted as a function of number of cycles to fracture for both materials at two temperatures. In case of Sanicro 25, the cycling at a temperature of 700°C results in more than 50 times reduction in fatigue life for equal saturated plastic strain amplitudes when compared to room temperature. The study of the surface relief evolution at both temperatures presented in [116, 123, 136, 163] revealed the principal sources of this difference in fatigue life.
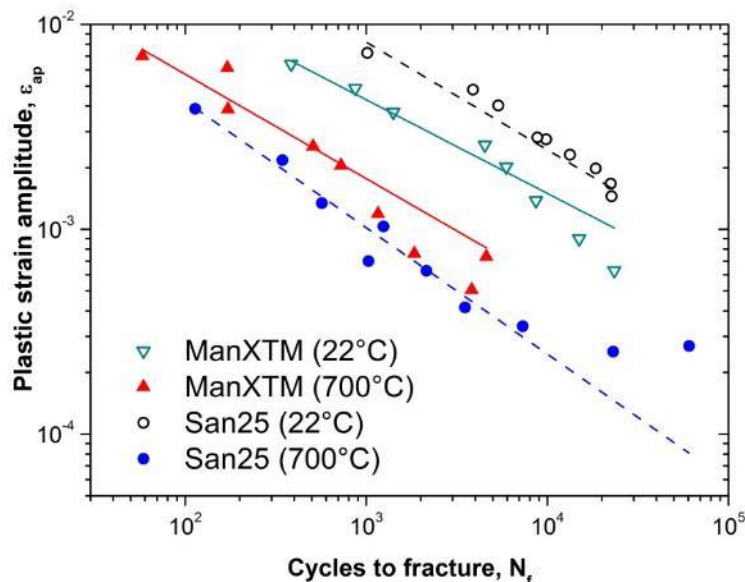
Figure 13.1: Comparison of Coffin-Manson fatigue life curves of Sanicro 25 and Manaurite XTM at two temperatures.

Fatigue crack initiation in room temperature cyclic loading is due to the pronounced localization of the cyclic plastic strain into PSBs and formation of the PSMs consisting of extrusions and intrusions, similarly to the case of conventional steels as thoroughly studied 316L steel. From the tips of intrusions stage I cracks develop in individual grains and start

growing and linking with other cracks until principal crack is formed. Despite the fact that cyclic slip localization starts early in fatigue life, crack initiation and early growth of short cracks leading to macrocrack formation is a slow process. Polák et al. [136] and Mazánová and Polák [116, 163] reported that the number of initiated cracks in low strain amplitude cyclic loading is low and linking of the cracks does not contribute to the short crack growth significantly. Since the fatigue life is determined preferentially by the growth rate of short cracks the fatigue life of Sanicro 25 in cycling at room temperature depends primarily on the plastic strain amplitude and for low plastic strain amplitudes is therefore long.

At high temperatures, the situation is completely different. As shown previously, cyclic slip localization during the cyclic loading of Sanicro 25 at 700°C is very weak and plays no role in fatigue crack initiation. It was reported by Mazánová et al. [123] that the fatigue crack initiation at high temperature is intergranular. The observations of the specimen surface already at the low number of loading cycles revealed that the majority of grain boundaries are oxidized and cracked, and the network of surface cracks is produced in the regions around grain boundaries. It is indicated that the cracking and the enhanced oxidation of grain boundaries is connected with the decrease of the chromium content in the matrix close to the grain boundaries and thus lower resistance to oxidation. Chromium content decreases as a result of rapid nucleation of Cr-rich $M_{23}C_6$ carbides at high temperatures. It is concluded that the presence of the dense network of surface cracks would promote their linkage during further cycling and substantially enhance the growth rate of short cracks leading to early formation of the principal crack. Both the early initiation of the cracks and the enhanced crack growth rate due to linkage of grain boundary cracks result in substantial reduction of the fatigue life of Sanicro 25 at high temperature in comparison with that at room temperature [123, 136].

Coffin-Manson fatigue life curves in Fig. 13.1 demonstrate that at room temperature Manaurite XTM has shorter fatigue life than Sanicro 25. This can be caused by the presence of high amount of brittle eutectic primary carbides within the cast dendritic microstructure of the alloy. Overview SEM image in Fig. 13.2a shows bulk microstructure after cyclic loading with total strain amplitude 0.35% at room temperature. Experimental observations reveal that majority of eutectic primary carbides are cracked (see details in Figs. 13.2b and 13.2c). It has been also found that several cracks initiated and propagated from the cracked carbide into the matrix. That is in contrast with Sanicro 25 where room temperature crack initiation is observed only on the surface. Taking into account weak localization of cyclic plastic slip in austenitic matrix, initiation, propagation and further connection of cracks from brittle eutectic primary carbides can be the main reason why fatigue resistance of Manaurite XTM at room temperature is worse than that of Sanicro 25.

At high temperatures, where the major role is played by surface oxidation, Manaurite XTM has higher fatigue life than Sanicro 25. Here, it is important to focus on chemical composition of both alloys. Mazánová et al. [123] reported that high Cr content leads to formation of thin oxide layer on the surface, which then acts as a barrier and prevents further penetration of oxygen into the matrix. While Sanicro 25 has chromium content of 22.5 wt%, Manaurite XTM can have up to 37 wt%. Moreover, it is alloyed also with Ti, which is another element known to contribute to the oxidation resistance. Having higher content of Cr, Ti and also Ni, Manaurite XTM has better oxidation resistance than Sanicro 25 what is the main factor standing behind its longer fatigue life at a temperature of 700°C.
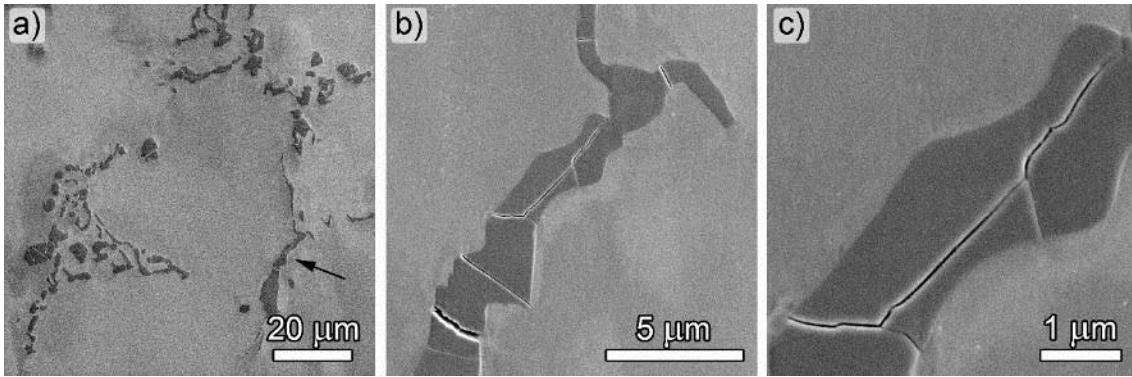
Figure 13.2: Manaurite XTM: (a) Overview of polished cross-section of the specimen after cyclic loading with total strain amplitude 0.35% at room temperature. Austenitic matrix contains high amount of eutectic primary carbides. Black arrow highlights place shown in detail in (b) and (c). Brittle primary eutectic carbides crack as a result of cyclic loading at room temperature. Interface between cracked carbides and matrix then acts as site for fatigue crack initiation and growth.

In Fig. 13.3, comparison of derived Wöhler fatigue life curves is plotted for both materials at room temperature and at 700°C. The curves show fatigue life dependence in case of constant stress amplitude loading. In this loading regime, Manaurite XTM has slightly longer fatigue life than Sanicro 25 at room temperature. That is probably connected with significant cyclic plastic localization behaviour exhibited by Sanicro 25. As will be explained in next chapter, it leads to cyclic softening behaviour. If constant stress amplitude loading is applied, plastic deformation produced during cycling will increase in Sanicro 25 subsequently leading to fatigue fracture earlier than Manaurite XTM.
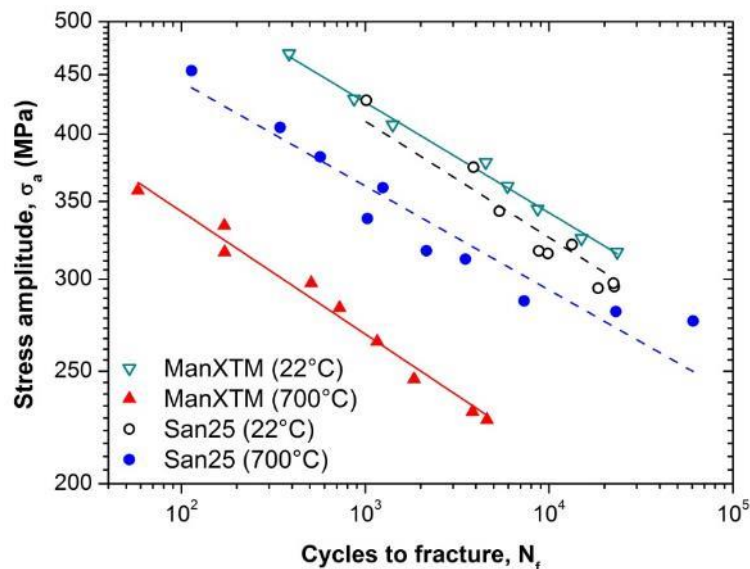
Figure 13.3: Comparison of Derived Wöhler fatigue life curves of Sanicro 25 and Manaurite XTM at two temperatures.

When tested at high temperature, fatigue life of both materials diminishes. As was discussed earlier in relation to chemical composition of both materials, Sanicro 25 seems to have worse oxidation resistance then Manaurite XTM. However, due to internal microstructural changes,

139

it also exhibits extraordinary cyclic strengthening. When cyclically loaded with constant stress amplitude, Sanicro 25 has much longer fatigue life than Manaurite XTM due to the cyclic increase of the strength.

In Fig. 13.4, comparison of cyclic stress-strain curves is done for Sanicro 25 and Manaurite XTM at two temperatures. At room temperature, to reach given plastic strain amplitude in half-life, much higher stress amplitude is needed in case of Manaurite XTM than for Sanicro 25. As will be discussed in relation to the curves of cyclic plastic response, this is connected to strong localization of cyclic slip observed in Sanicro 25 and not in case of large dendritic grains with high amount of eutectic primary carbides in Manaurite XTM.
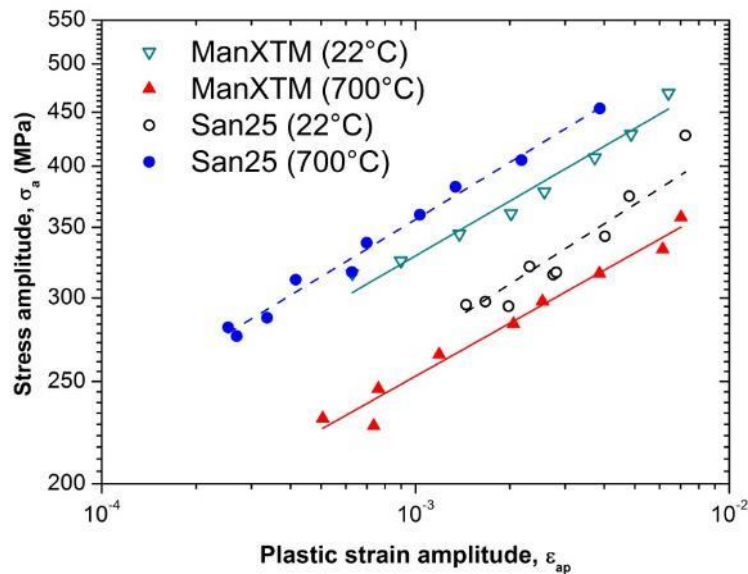
Figure 13.4: Comparison of cyclic stress-strain curves of Sanicro 25 and Manaurite XTM at two temperatures.

When cyclic loading of Manaurite XTM is done at high temperature, cyclic stress-strain curve is lying at much lower stresses. That is commonly seen high temperature behaviour for many austenitic steels and alloys, but not in case of Sanicro 25. At a temperature of 700°C, this alloy exhibits significant increase of cyclic stress, with cyclic stress-strain curve lying well above that at room temperature. This extraordinary behaviour will be explained in further sections.

13.2 Comparison of high temperature fatigue life curves with other alloys

In following graphs, comparison of fatigue life curves of Sanicro 25 and Manaurite XTM at high temperature is made with other similar alloys. Coffin-Manson fatigue life curves are compared in Fig. 13.5. In case of loading with constant plastic strain amplitude, the Sanicro 25 alloy would have the shortest fatigue life of all alloys, even shorter than Manaurite XTM and conventional 316L steel loaded at 600°C.

When cyclic loading is done with constant stress amplitude, Sanicro 25 again belongs to the alloys with the best fatigue performance. Derived Wöhler curves in Fig. 13.6 reveal that for stress amplitudes below 300 MPa, the Sanicro 25 has the longest fatigue life, while for

loading with stress amplitudes higher than 300 MPa, more cycles to failure are needed in case of Fe45Ni23Cr7W alloy. Again, the most comparable to Saniro 25 is HR3C alloy, which has just slightly shorter fatigue life. On the other hand, Manaurite XTM is the material with shortest fatigue life when loaded in stress controlled mode.

Figure 13.5: Comparison of Coffin-Manson fatigue life curves of Sanicro 25 and Manaurite XTM obtained at 700°C with other alloys tested at high temperatures. Data for HR3C, 316L and Fe45Ni23Cr7W are taken from [158], [164] *and* [157].
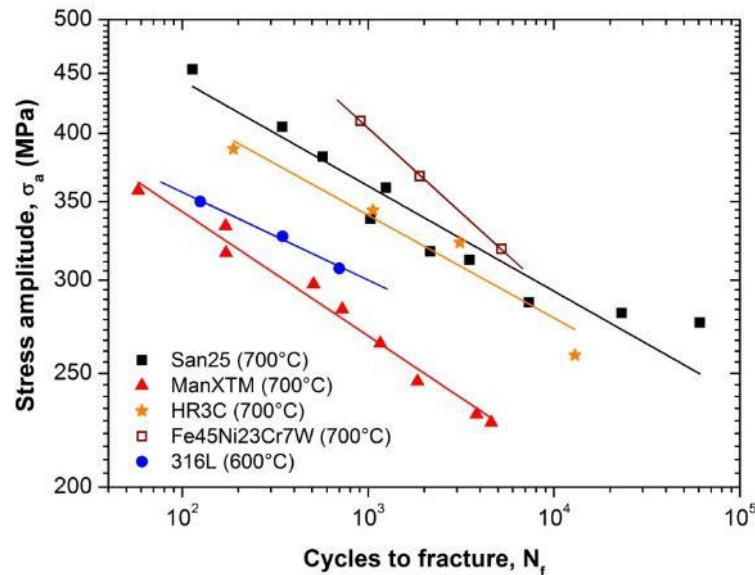
Figure 13.6: Comparison of Derived Wöhler fatigue life curves of Sanicro 25 and Manaurite XTM obtained at 700°C with other alloys tested at high temperatures. Data for HR3C, 316L and Fe45Ni23Cr7W are taken from [158], [164] *and* [157].

In Fig. 13.7, fatigue life curves of Sanicro 25, Manaurite XTM and other alloys cyclically loaded at high temperatures are plotted as total strain amplitude versus number of cycles to fracture. Interestingly, in this case the longest fatigue life is exhibited by HR3C alloy at 700°C.
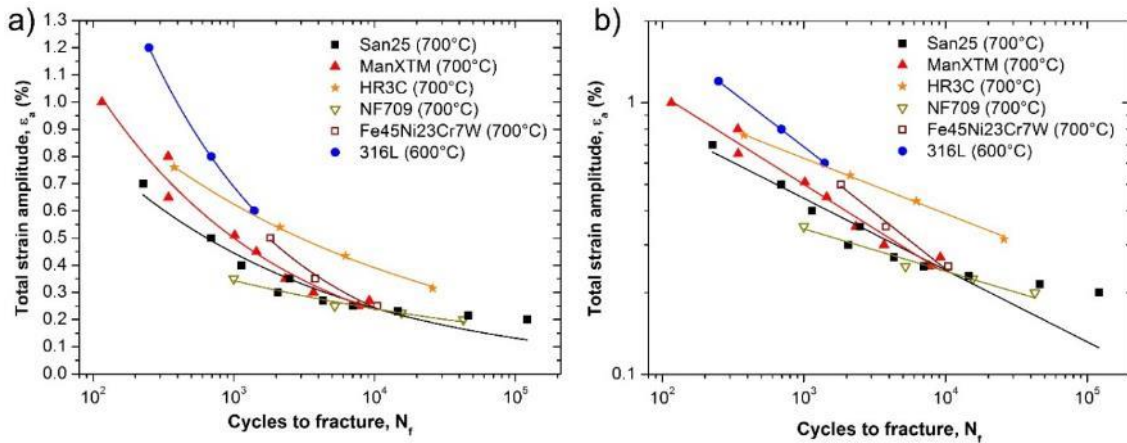
Figure 13.7: Comparison of fatigue life curves of Sanicro 25 and Manaurite XTM with other alloys. Total strain amplitude versus number of cycles to fracture is plotted as (a) logarithmic versus linear scale and as (b) logarithmic versus logarithmic scale micrographs. Data taken from [158], [164], [157], [24].

Cyclic stress-strain curves in Fig. 13.8 demonstrate significant cyclic strength of Sanicro 25 relative to other alloys. For given constant plastic strain amplitude, to cyclically load Sanicro 25 the highest stress amplitude is needed. Similar performance is exhibited by HR3C and Fe45Ni23Cr7W alloys. On contrary, cyclic stress-strain curve of Manaurite XTM is lying well below on the similar level as curve of conventional 316L steel loaded at 600°C.
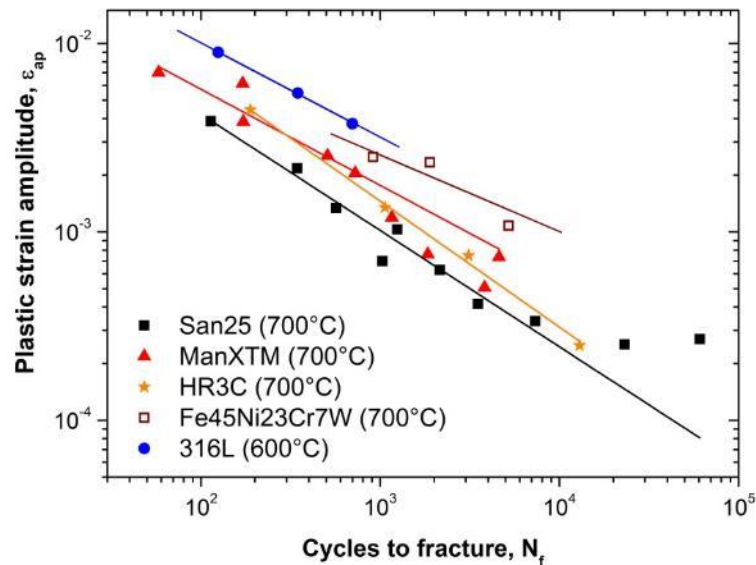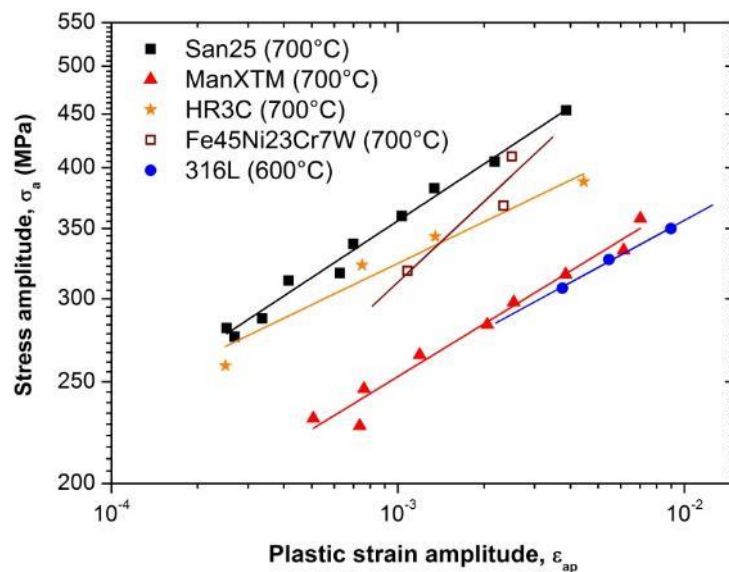

Figure 13.8: Comparison of cyclic stress-strain curves of Sanicro 25 and Manaurite XTM obtained at 700°C with other alloys tested at high temperatures. Data for HR3C, 316L and Fe45Ni23Cr7W are taken from [158], [164] and [157].

142

13.3 Cyclic response at room temperature

Cyclic hardening/softening curves of Sanicro 25 and Manaurite XTM loaded over a wide interval of total strain amplitudes at room temperature are compared in Fig. 13.9. Stress amplitude σ_a is plotted vs. number of cycles N. Same scales were used for x and y axes in both diagrams.
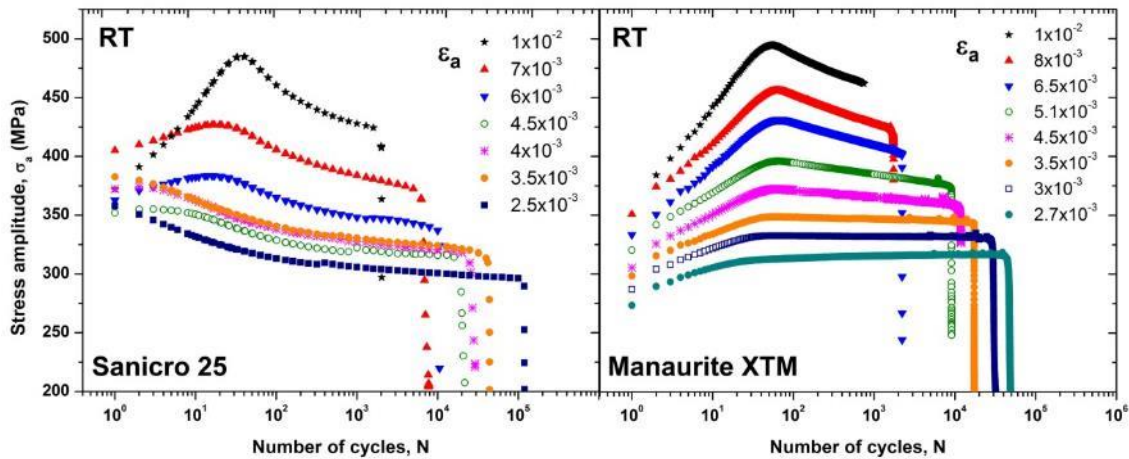
Figure 13.9: Cyclic hardening/softening curves of Sanicro 25 and Manaurite XTM at room temperature are compared. Stress amplitude σ_a is plotted vs. number of cycles N. Applied total strain amplitudes are given in the Figures.

Cyclic plastic behaviour of both alloys at room temperature is comparable, especially for high strain amplitudes. After initial hardening period which is more significant for high strain amplitudes, cyclic softening occurs with tendency to saturation into the stabilized cyclic response. It is clear that in case of Sanicro 25, the softening is more distinctive than for Manaurite XTM. Origin of the cyclic behaviour of both alloys is discussed as follows.

At room temperature, under cyclic loading with low strain amplitudes, the dislocation density increases significantly. In structural alloys, easy cross-slip of dislocations is restricted and their movement is limited to planar slip within one slip system only. As a result, dislocation interaction becomes more complicated and more tangled structures are formed. Characteristic initial hardening cyclic response of material occurs for both Sanicro 25 and Manaurite XTM. Such a behaviour was thoroughly documented for example in case of conventional 316L austenitic steel [16, 18]. Simple planar structures characteristic by pile-ups, stacking faults and dislocation tangles were observed in both studied materials (see Figs. 10.1 and 11.2). However, there are also some differences. In case of Sanicro 25, in the majority of grains localized dislocation structure developed. High dislocation density thin bands reminiscent of PSBs are separated by dislocation-free regions. These bands correspond well to PSMs observed on the surface. It is known that PSBs are the main structural features that can accommodate cyclic plastic deformation and they are usually observed in the form of ladder-like structures in copper [59, 80–83], nickel [84] and 316L steels [16, 17, 59].

Sanicro 25 is a complex structural material with high content of Ni and Cr in the matrix and alloyed with several other substitutional elements as W. When compared to simple metals, in majority of observed cases, PSBs in Sanicro 25 have dislocation configuration different from

the typical ladder-like structure. No distinctive walls or dislocation rich laths separated by channels are found. They have character of thin localized bands of high dislocation density where dislocation rich and dislocation poor areas could alternate randomly. Bands are substantially thinner than the typical ladder-like structure what suggests much stronger localization than in the case of simple metals. As noted in Section 2, the materials with high stacking fault energies, e.g. aluminium ($\approx$ 140 mJm^{-2}) or copper ($\approx$ 78 mJm^{-2}), exhibit more spatial dislocation arrangements then metals, e.g. silver ($\approx$ 20 mJm^{-2}) or structural alloys with low stacking fault energies.[36, 39, 41]

In the case of many austenitic stainless steels, the stacking fault energy was determined to be relatively low. For example, stacking fault energy of conventional 316L austenitic steel was reported to be even lower than 20 mJm^{-2} [23, 97, 165]) implying large dissociation distance between Shockley partial dislocations, thus preventing easy recombination and cross-gliding. High-purity austenitic stainless steels with high Ni and Cr content comparable to Sanicro 25 alloy were recently studied by Lu et al. [23]. Depending on elemental content, they have determined stacking fault energy to be about ~27 or ~35 mJm^{-2}. Bonny et al. [166] used interatomic potentials for tertiary system FeNiCr to model stable stacking fault energy for various combinations of Ni and Cr in the solid solution. For Ni/Cr ratio corresponding to Sanicro 25, the stacking fault energy determined from the model is about ~25 mJm^{-2} as shown in Fig. 13.10.
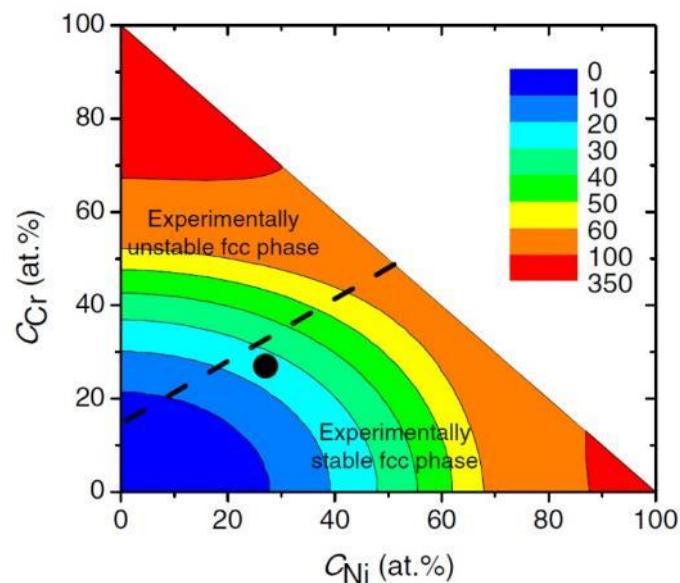
Figure 13.10: Stable stacking fault energy (mJm^{-2}) as a function of composition obtained from the interatomic potential. Assumed Sanicro 25 composition is marked by black dot. Taken from Bonny et al. [166].

For complex highly-alloyed steel, these are rather high values, not very different from conventional steel as mentioned 316-type. It is therefore suggested that the stacking fault energy is not the main factor causing strong planarity of dislocation slip in Sanicro 25. There are other important factors to be considered which can be playing a role in the slip modification in FCC metals, such as short range ordering (SRO) of nitrogen and chromium atoms, as was reported previously [132, 167, 168].

Both planar character of dislocation slip and strong localization are probably one of the reasons why dislocation configuration reminiscent of ladder-like structure is found only exceptionally. The onset of this arrangement was observed at high strain amplitude at fracture (see Fig. 10.7) or also at low strain amplitude (0.25%) in TEM lamellae prepared from the surface grains of samples cycled only to 10% of the fatigue life as shown in Fig. 13.11 [169, 170].

At high strain amplitudes, secondary slip systems are activated. In most of grains of Sanicro25, two or three slip systems are active what leads to significantly increased dislocation density in comparison with low strain amplitudes. Similarly to conventional 316L steel [18], this causes notable initial cyclic hardening (up to 20 or 30 cycles at the highest strain amplitude). In further cyclic loading, dislocations move and annihilate by interacting with opposite sign dislocations. As a consequence, the total dislocation density tends to reach its equilibrium state and remains almost constant after achieving a maximum. Subsequently, slip on the critical plane prevails leading to further localization on this plane. That is well documented by observations presented in [115, 169, 170]. In contrast with the matrix, there are no dislocations from the secondary slip systems present in PSBs, what suggests that at the beginning of the loading, all systems were active, but later only one slip system prevailed. This localization of plastic strain leads to so-called cyclic softening response of the material. In case of Manaurite XTM, no strong evidence of plastic deformation localization, neither formation of any complex dislocation structures, was found. That is the main reason, why Manaurite XTM does not exhibit so significant cyclic softening behaviour as Sanicro 25.
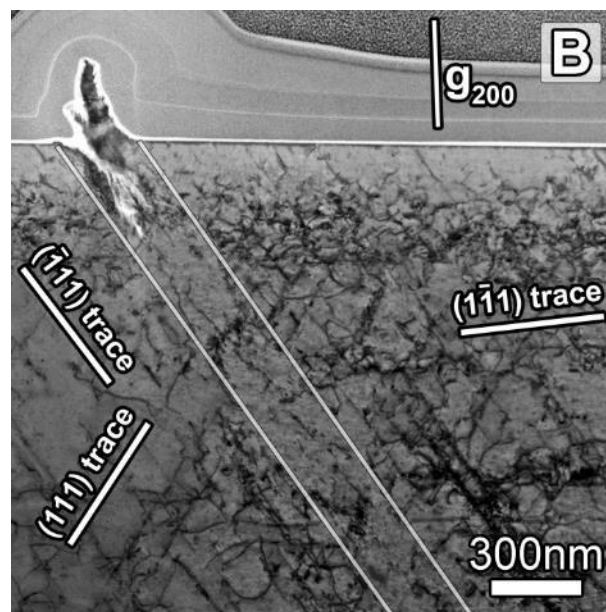
Figure 13.11: BF-STEM diffraction contrast image of the lamella extracted from the surface of fatigued Sanicro 25 alloy. Specimen cycled with constant total strain amplitude 0.25% to 10000 cycles (~1/10 N_f) Detailed image shows the persistent slip marking consisting of extrusion and intrusion and a crack starting from the tip of the intrusion. Dislocation arrangement in the underlying persistent slip band is ladder-like, i.e. multipole configurations of edge dislocations forming dislocation walls in PSB are separated by dislocation-free channels. Taken from [116].

Investigations of simple metals and then also structural materials as 316L steels [14, 16–18, 95, 96] showed that at sufficiently high plastic strain amplitudes the activation of secondary slip systems facilitate the interactions between dislocations. Dislocations can form multi-pole arrangements or they can annihilate. As a result of these reactions, the planar structures can rearrange into configurations where the overall internal energy of the system will be lowered. Such a low energy dislocation structures are veins, walls and channels and as a final stage of recovery, dislocation cells. However, these spatial low energy structures are observed very rarely in Sanicro 25, what is well in accordance with the overall strongly planar character of dislocation slip documented in this alloy. Usually they are not so well developed like in copper or 316L and even at high strain amplitudes they show distinctive planar character (see Fig. 10.8).

Fraction of grains containing the characteristic types of dislocation structures observed in Sanicro 25 is shown in Tab. 13.2. Our results are compared with 316L steel study made by Obrtlík et al. [16]. For a given saturated plastic strain amplitude low energy spatial structures are already formed in case of 316L steel while in Sanicro 25, planar arrangements still strongly prevail.

	316L		Sanicro 25	
ε_{ap} (%)	0.10	0.50	0.18	0.48
Low dislocation density	-	-	10%	-
Planar structures	5%	-	90%	90%
Imperfect vein structure	68%	-	-	5%
Wall/channel structures	27%	34%	-	5%
Equally oriented cells	-	35%	-	-
Disoriented cells	-	31%	-	-

Table 13.2: Fraction of grains containing the characteristic types of dislocation structures observed in Sanicro 25 compared with 316L steel study made by Obrtlik et al. [16].

It is worthy to note that the experimental results are also in a good agreement with work published by Polák and co-workers [137] who used a statistical-theory-based analysis of the hysteresis loop shape to study the evolution of the cyclic plastic response of Sanicro 25. The effective stress and the probability density function of the internal critical yield stresses of the microvolumes as a function of number of cycles was evaluated. At the beginning of cyclic loading, the early hysteresis loops were characterized by the presence of two peaks of approximately same height in the second derivative. First peak corresponded to the fictive stress 250 MPa and the other to 440 MPa in case of low strain amplitude and 630 MPa at high strain amplitude. With increasing number of cycles, in the domain where material exhibits saturation of cyclic stress, second peak diminished while the first peak increased and shifted to the smaller fictive stress. As the localization of cyclic slip is promoted into the PSBs, the first peak completely dominates. This statistical analysis documents that the microvolumes with smaller internal critical stresses become more active what exactly corresponds to the cyclic softening behavior of the alloy.

13.4 Cyclic response at high temperature

Cyclic hardening/softening curves of Sanicro 25 and Manaurite XTM loaded over a wide interval of total strain amplitudes at a temperature of 700°C are compared in Fig. 13.12. Stress amplitude σ_a is plotted vs. number of cycles N. Same scales were used for x and y axes in both diagrams.

It is evident that the behaviour of both alloys is significantly different from that at room temperature. At high temperature cyclic loading, they exhibit significant increase of cyclic stress, i.e. cyclic strengthening. In case of Manaurite XTM, most notable increase of strength is observed in the initial period of cycling, during first 20 to 100 cycles. Then there is a tendency to reach saturated level of stress. Sanicro 25 shows even better properties. For example, at the end of fatigue life the stress amplitude of 298 MPa needs to be applied to produce total strain of 0.51% in Manaurite XTM, while in case of Sanicro 25 it is the stress amplitude of almost 407 MPa. The cyclic strengthening of Sanicro 25 lasts for longer period and is much more significant than in case of other similar alloys as was discussed in relation to Figs. 13.5 and 13.7. In following chapters, the attention is focused on detailed explanation of cyclic strengthening behaviour of Sanicro 25 alloy. The key acting mechanisms are then discussed in relation to Manaurite XTM.
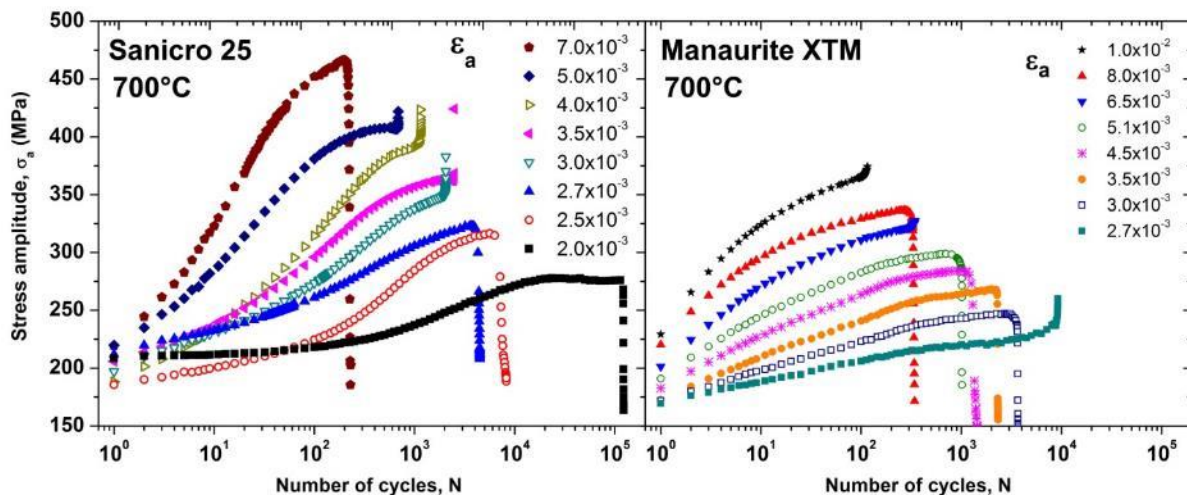
Figure 13.12: Cyclic hardening/softening curves of Sanicro 25 and Manaurite XTM at temperature 700°C are compared. Stress amplitude σ_a is plotted vs. number of cycles N. Applied total strain amplitudes are given in the Figures.

Evolution of the hysteresis loop shape in Fig. 13.13a for total strain amplitude 0.7% illustrates the significant increase of cyclic stress as a function of number of cycles. Cyclic strengthening is also demonstrated in Fig. 13.13b where the increase of cyclic stress in four different stages of fatigue life is plotted for all strain amplitudes. The increase of stress amplitude $\delta\sigma_a$ is defined as the difference between magnitudes of the stress amplitude in a particular cycle $N>1$ and the first cycle $N=1$. It is apparent that cyclic strengthening is present during the whole fatigue life in all tests of Sanicro 25 at 700°C. The higher the applied strain amplitude, the more significant the increase of the cyclic stress is observed during the initial period of cycling. With further cyclic loading, the tendency to reach saturation of the cyclic stress is noticed, especially in the case of lower strain amplitude tested samples, i.e. samples tested for

the highest number of cycles. Thermal exposure of specimens ranged from 153 to 6 hours for the lowest and highest strain amplitude, respectively.
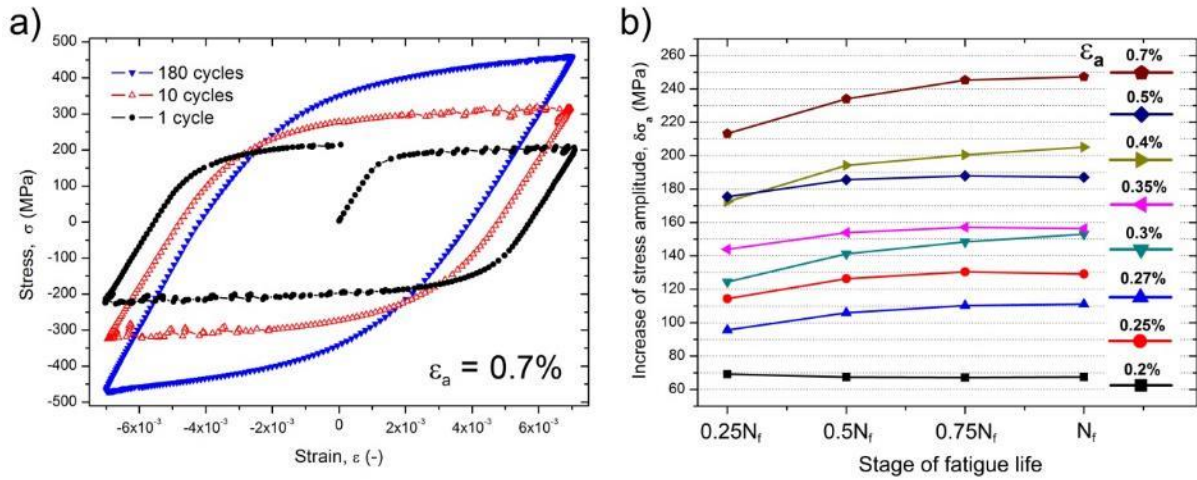
Figure 13.13: (a) Evolution of the hysteresis loop shape with cycling at total strain amplitude 0.7% at 700°C. (b) Increase of stress amplitude with respect to the cyclic stress in the first loading cycle in different stages of the fatigue life plotted for all strain amplitudes tested in case of Sanicro 25 at 700°C.

Sanicro 25 exhibits extraordinary cyclic strengthening not only in the isothermal symmetrical cyclic loading, but also in different modes of loading. In particular, it was observed during isothermal cycling with 10 min dwell periods at 700°C (see Fig. 13.14a), and then also during thermo-mechanical cyclic loading (TMF) in temperature interval of 250-700°C (see in-phase TMF in Fig. 13.14b, and out-of-phase in Fig. 13.14c) as reported in [171, 172].
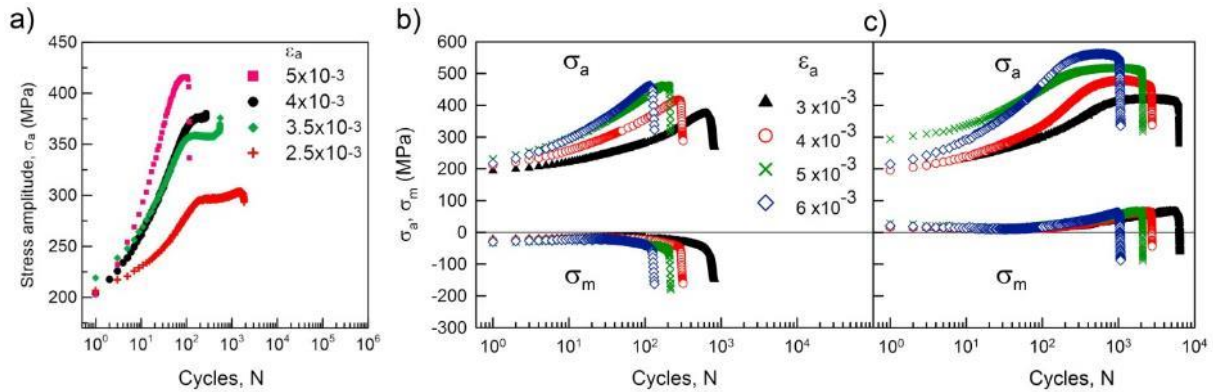
Figure 13.14: Cyclic hardening/softening curves of Sanicro 25. (a) Cyclic loading with 10 min dwell period in tension at temperature 700°C. Thermo-mechanical fatigue cyclic loading in range of temperatures from 250°C to 700°C. (b) In-phase loading. (c) Out-of-phase loading. Taken from [171, 172].

Cyclic plastic response of Sanicro 25 loaded in total strain amplitude control at 700°C was compared with conventional 316L austenitic steel loaded at 600°C (more details about the material and testing can be found in [164]). Hardening/softening curves are plotted in Fig. 13.15 as stress amplitude σ_a versus number of cycles N. All tests were conducted until failure, where the number of cycles at failure of the specimen is designated as N_f. In case of

conventional 316L steel, after short initial hardening, saturated cyclic response prevails until failure. On the contrary, Sanicro 25 exhibits an extraordinary increase of cyclic stress that persists for a much longer fraction of the total fatigue life.
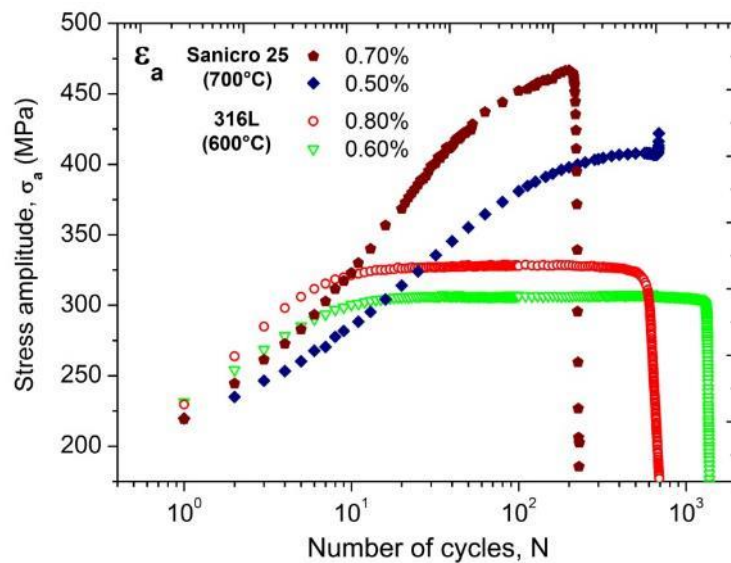
Figure 13.15: Selected cyclic hardening curves of Sanicro 25 loaded in constant total strain amplitude at temperature of 700°C compared with hardening/softening curves of conventional 316L austenitic steel tested at 600°C. Stress amplitude versus number of cycles is plotted.

Cyclic loading leads to significant change of the alloy microstructure. Thorough and detailed studies of cyclic response of 316L steel in relation to observed dislocation substructures were reported by Li et al. [95, 96], Obrtlík et al. [16], Kruml et al. [17] and Gerland et al. [133]. Fundamental work on the dislocation structure evolution was then accomplished by Pham et al. [132]. With initial cyclic loading, dislocation sources are activated leading subsequently to dramatic increase of dislocation density. At high temperatures, thermally activated and diffusion-assisted effects are facilitated, so dislocations can climb and cross-slip. Increased mutual dislocation-dislocation interactions suppress dislocation mobility and lead to initial cyclic hardening. However, shortly after a rapid initial increase the total dislocation density has a tendency to reach saturated equilibrium value in the very early stage of cyclic loading (a few tens of cycles as shown in case of 316L in Fig. 13.15) [132]. Both at room and elevated temperatures, dislocations tend to form arrangements with lower stored internal energy. Mutual interaction of dislocation strain fields leads to dislocation annihilation or dipole formation and are important for the recovery processes. Initially tangled dislocations transform into veins and walls and channels. With further cyclic loading, sub-grain-type cellular structures featuring boundaries that are made up of dislocation walls are formed. Upon further recovery, dislocations in the cell interiors are annihilated and the internal stored strain energy is significantly decreased leading to the softening of the material response to external load (see schematic visualisation in Fig. 13.16).
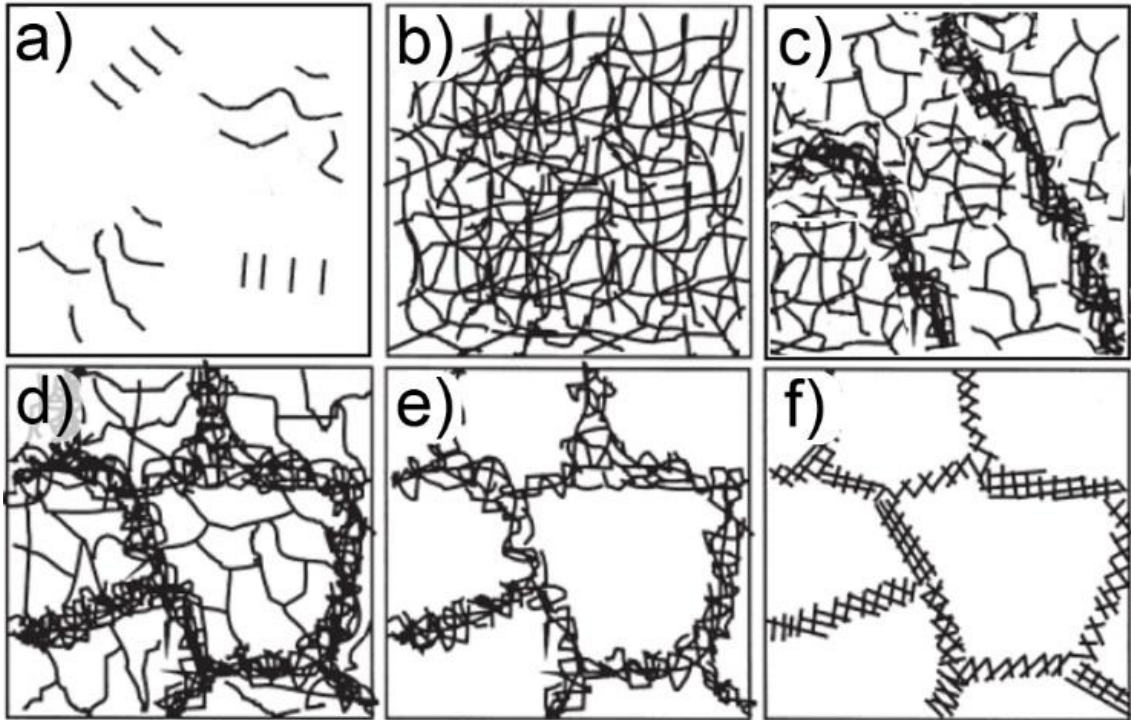
Figure 13.16: Schematic showing evolution of dislocation structure in conventional 316L austenitic steel as a result of cyclic loading at high temperature. (a) Individual dislocations and pile-ups are observed in initial state. (b) Dislocation tangles formed as a result of initial cyclic loading. (c) Onset of recovery process where veins and walls and channels are formed. (d) Cellular dislocation structure. (e) With further cyclic loading, dislocations in the cells interior are annihilated. (d) Well developed sub-grain-type of cellular structure at the end of recovery process. Image modified after T. Mayer [39]*.*
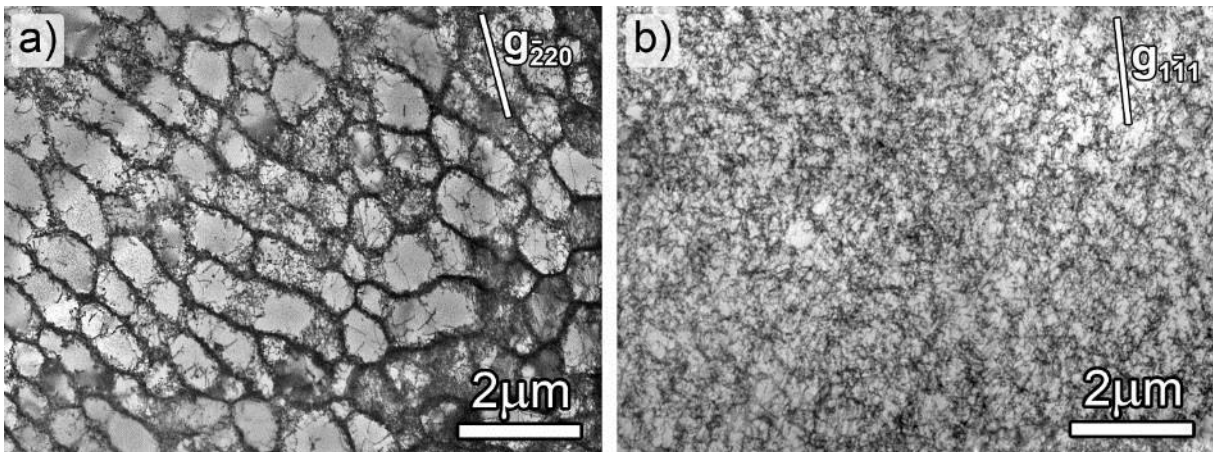
Figure 13.17: Comparison of dislocation structures. (a) Well developed oriented cells formed in conventional 316L steel after cyclic loading with total strain amplitude 0.6% at 600°C. (b) Microstructure characteristic by homogeneous dislocation distribution with high density observed in Sanicro 25 alloy after cyclic loading with total strain amplitude 0.5% at 700°C.

When oriented and disoriented cells are established, stabilized cyclic plastic response usually prevails until the fracture. Dislocation structure observed in 316L steel after cyclic loading with total strain amplitude of 0.6% at a temperature of 600°C (see Fig. 13.17a) is compared

with dislocation structure found in Sanicro 25 loaded with total strain amplitude 0.5% at 700°C. (corresponding hardening/softening curves are shown in Fig. 13.15). While in case of conventional 316L steel, well developed dislocation cells are observed as expected, in Sanicro 25 homogeneous dislocation structure with high density is found with no evidence of recovery. In following chapter, the nanostructure origins of the mechanisms possibly affecting mobility of dislocations in Sanicro 25 during cyclic loading so the recovery processes are suppressed are summarized and discussed.

14. Nanostructure origins of the extraordinary cyclic strengthening of Sanicro 25 at a temperature 700°C

Initial condition of the alloy, particularly the chemical composition and microstructural state, determines mechanisms of deformation and corresponding overall mechanical response of material under static and cyclic loading conditions. The present work has shown that a specific combination of a high number and content of alloying elements in Sanicro 25 leads to accelerated diffusion and precipitation effects resulting in the nucleation of two distinctive populations of nanoparticles embedded in the matrix - particles rich in copper and nano-sized NbC carbides. Both types of nanoprecipitates play essential roles in the unusual high temperature cyclic behaviour that is not observed in the case of conventional stainless steels (see Fig. 13.15).

14.1 Cu-rich particles

In the initial state, i.e. after annealing at 1200°C for 1 h and rapid cooling to room temperature in air, no Cu-rich precipitates are present. All copper atoms are dissolved and homogeneously dispersed in the austenitic matrix forming a supersaturated solid solution [135]. This state does not correspond to the minimum of the free enthalpy. Since the diffusion rate at room temperature is very low, the equilibrium arrangement cannot be achieved. However, when exposed to an elevated temperature of 700°C, the diffusion of copper atoms is high enough to facilitate nucleation of spherical Cu-rich cluster-type regions in the austenitic matrix thereby allowing reaching the minimum of the enthalpy. As copper atoms segregate, matrix elements diffuse away resulting in the formation of Cu-rich particles. In addition to the atom probe tomography work of Chi et al. [142], the precipitation and coarsening behaviour of Cu-rich nanoparticles was later studied by Bai et al. [21] and Ou et al. [22] in 18Cr-9Ni austenitic steel (Super304H) at 650°C. Both studies state that the growth and coarsening behaviour of the Cu-rich particles follows the diffusion-controlled Lifshitz-Slyozov-Wagner (LSW) theory of Ostwald ripening. Two main factors are reported to dominate the growth kinetics: (1) interfacial energy between the Cu-rich nanoparticles and the matrix and the (2) diffusion coefficient of solute atoms.

Bai et al. used the Lifshitz-Slyozov equation and measured data at 650°C to evaluate the interfacial energy. In the first approximation they used a diffusion factor and diffusion activation energy of Cu in a simple γ-Fe instead of that in the austenitic matrix and

determined the diffusion coefficient of Cu in γ-Fe as 1.961×10^{-17} cm^2/s and the interfacial energy equal to 86 mJ/m^2. In the second approximation, the austenitic matrix was considered as a complex solid solution Fe-18Cr-9Ni-3Cu. The diffusion coefficient of Cu in this solid solution was then calculated to 9.351×10^{-17} cm^2/s and the interfacial energy to 17 mJ/m^2. In other work, Ou et al. [22] measured the average particle diameter as a function of time and empirically determined the activation energy for the Cu-rich phase coarsening to be (212 ± 3) kJ/mol. This is close to the activation energy of 254 kJ/mol for volume diffusion of copper in the 18Ni-8Cr austenitic steel [22, 173], suggesting that the coarsening of Cu-rich precipitates is controlled mainly by the volume diffusion of copper atoms in the austenitic matrix.

In accordance with the latter, both works report very slow growth rate for Cu-rich precipitates in Super304H steel at 650°C. First, homogeneously dispersed small Cu-rich nanoparticles with very high volume density nucleate. Their size is only about 3 nm after 5 hours of aging at 650°C, as documented by Chi et al. [142] and Jiang et al. [139]. At higher temperature slightly larger particles can be observed, in good agreement with our results obtained for Sanicro 25. After 6 hours at 700%, precipitates have an average diameter 4.9 nm, then after 23 hours they have an average diameter 7.4 nm and an average volume density $(1.1\pm0.4) \times 10^{22}$ m^{-3}. As thermal exposure continues, Chi et al. reports that the volume density of particles reaches saturation (within approximately 100 hours) and then significantly decreases at the expense of their coarsening. That is also in a good agreement with our results as was shown in Figs. 10.24 and 10.25. After 153 hours at 700°C, the volume density of Cu particles decreased while their average diameter reached 13.1 nm. Once nucleated and stabilized, the growth rate is slow. Remarkably, the size of the copper particles is reported to be only about 35 nm even after 10,000 hours of aging at 650°C. Very small interfacial energy along with small coherency strains imply that the driving force for further coarsening is small as well.

14.2 Nb(C, N) particles

Sanicro 25 has a high content of Nb, along with interstitial C and N, relative to conventional stainless steels. As reported by Sourmail [126], owing to high affinity of Nb for both interstitial elements, having a sufficient amount of free Nb and C and/or N available in the solid solution is one of the key prerequisites for possible nucleation of Nb(C,N) phase in the austenitic steels at high temperatures. In Sanicro 25, no nitrogen was detected by EELS in precipitate locations suggesting that it is mostly consumed by coarse Z-phase and therefore the precipitated secondary nanoparticles are primarily NbC [135].

While there are no precipitates present in the initial state of the alloy, after aging at 700°C, numerous NbC carbides are nucleated on individual dislocations. Poddar et al. [145] reported, that because of large positive lattice misfit between the two crystal structures, the precipitation of the NbC phase in the defect-free austenite matrix is extremely difficult. According to Howe [50], two structures with mutually large lattice mismatch ($\delta \geq 0.25$) preventing good matching across the interface will have large interfacial energy significantly dominated by the structural contribution. Such an incoherent structure can have interfacial energy up to approximately 500-1000 mJ/m^2. However, a large nucleation barrier can be overcome by nucleation at lattice defects, where part of the strain energy can be released by replacement of the dislocation line length and strain field with the precipitate nucleus. As a

result, the mode of NbC precipitation is profoundly affected by plastic deformation. Depending on the deformation conditions, the overall characteristics of nanoprecipitates in terms of their size and distribution can differ significantly.
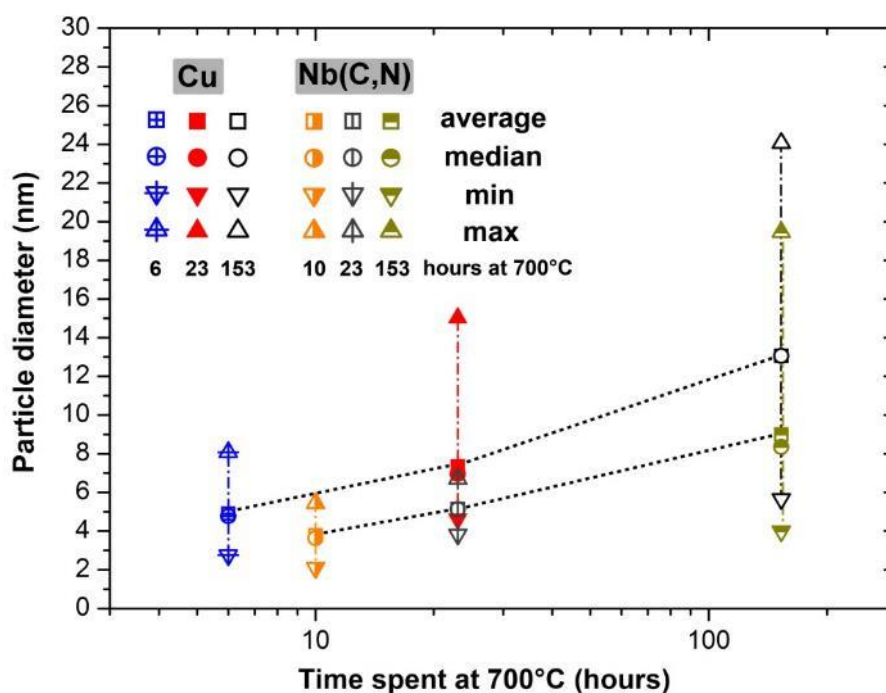
Figure 14.1: Evolution of average size of two populations of nanoparticles during cyclic loading. Both Cu and Nb(C,N) precipitates maintain nano-scale character even after more than 100 hours spent at 700°C.

The application of cyclic straining dramatically increases the dislocation density. With the aide of thermally-enhanced cross-slip and climb, dislocations develop a homogeneous distribution of tangled configurations, with very high density within all grains. During the tension-compression cycling, the stress-strain state in each individual grain changes. As cycling continues, subsets of the dislocation structure become mobilized and present potent NbC nucleation sites. Provided a sufficient source of free Nb and C in the solid solution, the time needed for the rapid nucleation of NbC is very short [145]. Carbon as a fast diffusion interstitial element can segregate around dislocation cores and form Cottrell atmospheres [174]. While ab-initio studies of Korzhavyi et al. [175] showed that C-based solute atmospheres have negligible effect on solid solution strengthening in Sanicro 25, they do significantly contribute to nucleation of NbC nanoprecipitates at dislocations by providing sufficiently high content of free C in the vicinity of dislocation cores.

Not all of the existing particles are decorating dislocations as shown in Fig. 10.27a. Arrays of NbC carbides approximately 5 nm in diameter are found heterogeneously dispersed with locally varying number and volume density. This indicates that it is possible for dislocations to break away from the NbC precipitates, leaving behind this non-uniform distribution of nanoparticles demarking the former positions of the dislocation lines (see Fig 10.27a). That is in agreement with work of Dutta et al. [176], who hypothesized that nucleation of Nb(C, N) precipitates on dislocation nodes only eliminates the core energy of the dislocation over the

length of the particle diameter and therefore the dislocations are not strongly pinned at the early stages of nucleation.
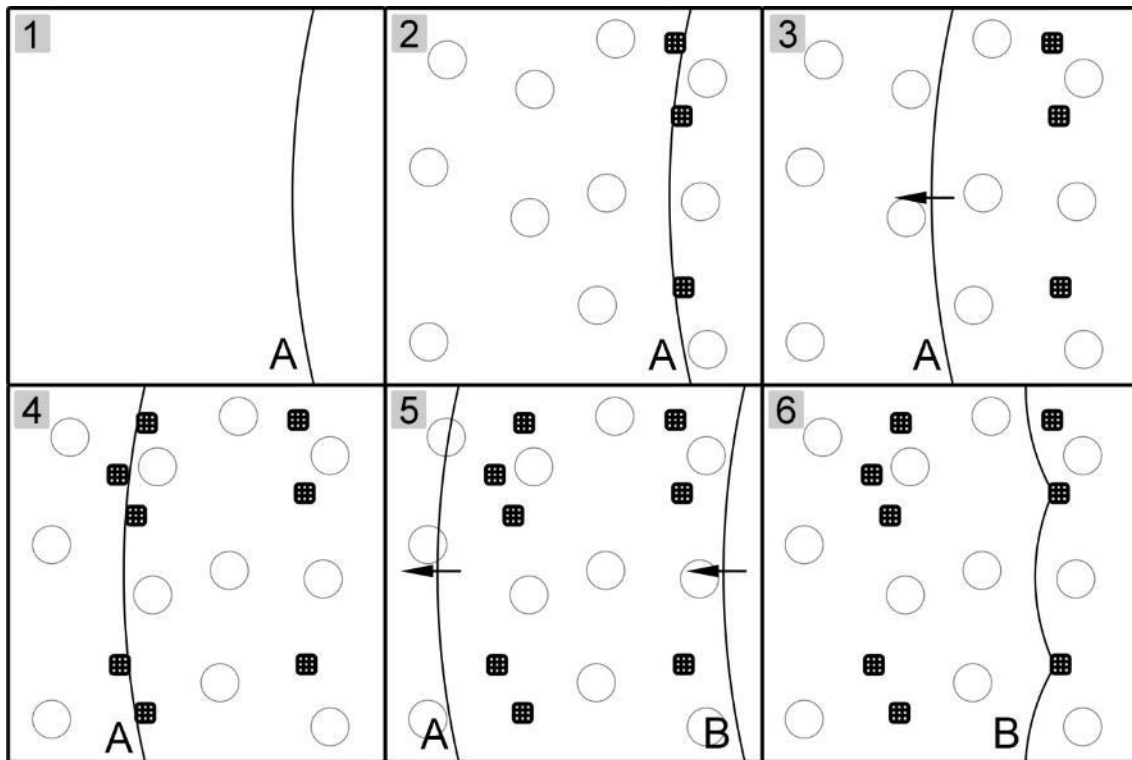
Figure 14.2: Schematic visualisation of heterogeneous nucleation of dispersoid-like NbC nanoprecipitates during cyclic loading and their effect on the cyclic strengthening behaviour. (1) In the initial state, there are no precipitates. Edge dislocation A is immobile. (2) Material is heated to the high temperature. Cu-rich nanoparticles (drawn as spheres in the image) nucleate homogeneously in the matrix while nano-scale NbC (drawn as black squares in the image) precipitate heterogeneously on the dislocation line. (3) Material is loaded cyclically, stress-strain state in the grain changes and as a result the dislocation A is detached leaving array of NbC particles behind. (4) As cyclic loading continues, stress-strain state in the grain can change rapidly and dislocation can become immobile again presenting nucleation site for another NbC to precipitate. In (5), the whole process repeats and the dislocation A is detached again moving away, while dislocation B is moving towards array of NbC precipitates nucleated in (2). In (6), dislocation B interacts with the array of precipitates, overcomes them by climb but is pinned by them at the exit side of the particles. Extra detachment stress is needed to mobilise dislocation B again.

Interestingly, the particles found in non-uniform distributions are notably smaller than precipitates decorating completely pinned dislocation lines suggesting that once detached from dislocations, they do not coarsen significantly, at least over the time-scales of the fatigue experiments. Dutta et al. [176] studied kinetics of heterogeneous nucleation of Nb(C, N) carbonitrides on dislocations in austenite and found out that the coarsening mechanism is governed by accelerated pipe diffusion of Nb atoms along the dislocation cores. At 700°C, volume diffusion rate of interstitial C through the lattice is high. However, to provide sufficient supply of Nb atoms to the location of nucleated precipitate to support further coarsening, dislocation cores are needed for accelerated pipe diffusion to be in operation. It

has been calculated by Dutta et al. [176] that the volume diffusion rate of Nb is approximately by one magnitude slower, than accelerated pipe diffusion through dislocation cores. So, if dislocation on which precipitate nucleates is detaches under cyclic stress, the precipitates do not grow significantly and dispersoid-like arrangement of nanoscale NbC particles is maintained for long period. That is demonstrated in Fig. 14.1 where evolution of size of the NbC precipitates with the time spent at 700°C during the cyclic loading is plotted along with the results obtained for Cu nanoparticles. NbC precipitates maintain nano-scale characteristics for long period of time.
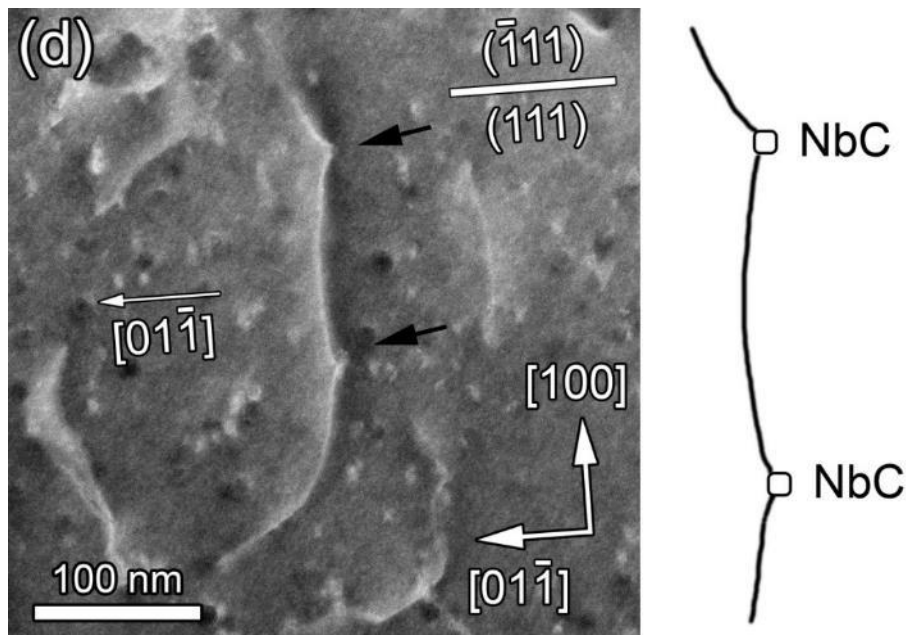
Figure 14.3: LAADF-STEM image obtained along [011] *zone axis with enhanced strain contrast (a large camera length 230 mm was used) showing two NbC particles (marked by black arrows) pinning* ½[01$\bar{1}$] *edge dislocation. A distinctive bowing of the dislocation line between the particles is noted.*

Once mobilized, the dislocations will nonetheless experience an increasingly dense array of precipitates that retards their motion and makes likely the subsequent arrest and additional heterogeneous nucleation of additional NbC particles along the dislocation lines. It is possible that this process could repeat numerous times, on an individual dislocation basis, and lead to continually increasing density of NbC obstacles in the microstructure as a function of cyclic loading. The whole mechanism is schematically visualised in Fig. 14.2. Experimental observation of ½[01$\bar{1}$] edge dislocation pinned by two NbC precipitates is shown in Fig. 14.3.

14.3 High temperature cyclic strengthening

In each cycle, the overall yield stress can be determined by several components. First, grain boundary strengthening should be considered. The average grain size of the Sanicro 25 is 60 µm. Since this grains size is relatively large, then, according to the Hall-Petch equation (3.47), grain effects can be considered as negligibly small. As next, the stress corresponding to the lattice friction should be considered. This contribution usually plays an important role at room

temperatures but should be negligible at a temperature of 700°C. On the other hand, the mutual interaction of solid solution and precipitation strengthening with forest dislocation hardening, appear to play a fundamental role in the high-temperature cyclic loading. While much more detailed quantitative description of the interaction of dislocations with both Cu- and Nb-rich nanoparticles is needed, the approximate approach is used here for the preliminary discussion of the alloy cyclic strengthening mechanism.

Korzhavyi and Sandstöm [175] used first-principles calculations for evaluation of the contribution of W, Nb, Cu and also C and N to the solid solution hardening. Their model, based on work from Hirth and Lothe [174], determined the effect of solute clouds created around dislocations and slowing down their motion. While the contribution of fast diffusion interstitials C and N is negligible at 700°C in Sanicro 25, substitutional W can lead to significant solid solution strengthening with an increase of the yield strength by up to 27 MPa [175]. Using the Taylor relationship [177] between uniaxial yield strength and the resolved shear stress in a polycrystal, $\Delta\sigma_y = T_f.\Delta\tau_s$ with Taylor factor $T_f = 3.06$ determined for FCC crystals [177], an increase of the flow stress as a result of solid solution strengthening by W, $\Delta\tau_{ssW}$ can be estimated and is approximately 9 MPa.

Cu-rich nanoparticles are small, coherent with cube-on-cube orientation relationship relative to the matrix, and finely-dispersed with high volume density. Gliding dislocations shear them rather than bypass them as reported previously by Ou et al. [22]. Fine and Isheim [178] documented that as a simplified first approximation, the precipitation strengthening can be related to the force F acting on the appropriate dislocation segment of length L needed to shear the precipitate by a distance of one Burgers vector b:, i.e. equation (3.11).

The applied stress is increased until shearing takes place. This determines $\Delta\tau$, the increase in flow stress due to the precipitates. The dislocation moves through the precipitate in steps of b, where each step has a different F value. The maximum value of F then determines the flow stress $\Delta\tau$. This approach is the basis for the general Friedel-Brown-Ham equation [53, 179] for weak precipitates that are sheared rather than bypassed:

$$\Delta\tau = \frac{2}{bL(T)^{3/2}}\left(\frac{F_m}{2}\right)^{3/2}, \qquad (14.1)$$

where F_m is again the maximum restraining force acting on the dislocation and T is the dislocation line tension usually approximated as ½ (Gb^2). As described by Fine and Isheim [178], the derivation of equation (14.1) starts with a force balance between the dislocation line tension and the force necessary to shear the precipitate F_m, when the angle of bend of the dislocation impinged on the precipitate is at its critical breaking value.

Ou et al. [22] reported that for Cu-particles in FCC matrix the shear stress increment due to the shearing process, $\Delta\tau$, comes from four main components: (I) Coherency strengthening as a result of the lattice misfit stresses, (II) chemical strengthening coming from the atomic bond switching when a dislocation shears a precipitate, (III) strengthening due to the difference in stacking fault energies in precipitate and matrix and (IV) strengthening as a result of the different shear modulus of the particle relative to the matrix. It is worthy of note that for Cu- particles in BCC matrix, the governing mechanism of strengthening is dislocation core– precipitate interaction as studied by Fine and Isheim [178]. In this work, only coherency strengthening is considered, as the contribution of other mechanisms to the shear yield stress increase was reported to be negligibly small [22]. Derived from the equation (14.1), the shear

yield stress due to coherency strain can be expressed by the equation (3.25), where $k = 3$ for edge dislocation. The modified Brown and Ham formula can be written as [53]:

$$\Delta\tau_{coh} = 4.1 G \varepsilon^{3/2} f^{1/2} \left(\frac{r}{b}\right)^{1/2}, \qquad (14.2)$$

where the coherency strain ε is given by equation (3.22) [22]. The bulk modulus B of the Cu-rich precipitate is 144.4 GPa [22], Young's modulus E of the austenitic matrix is 198 GPa, shear modulus G of the austenitic matrix is 76.7 GPa and Poisson´s ratio v is 0.29 [136]. The Burgers vector b of $a/2<110>$ dislocations is 0.255 nm. The lattice misfit δ of the Cu-rich particle and the matrix is 0.22%. Calculation is done with the particle parameters obtained for the sample tested with strain amplitude 0.27%. The volume fraction of the precipitates is calculated as $f = 2\pi r^2 N_s/3$, where N_s is the surface areal density of 3.2×10^{14} m^{-2}. When substituted into equation (14.2), the shear stress $\Delta\tau_{coh}$ for the coherent Cu-rich particles of diameter varying from 4.6 to 15 nm can be estimated to be in the range from 4 to 8 MPa.
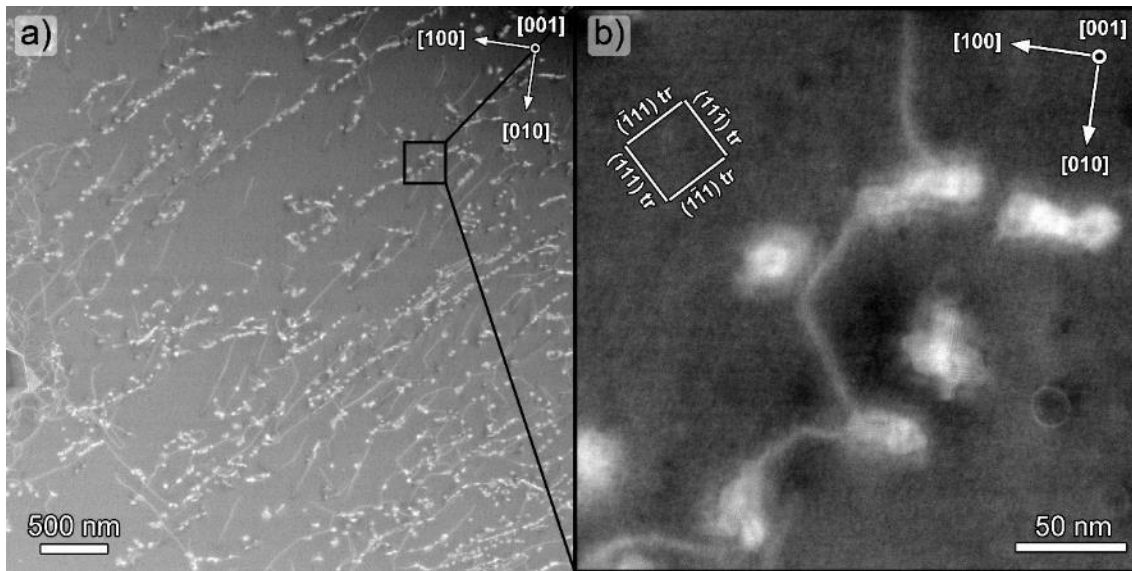
Figure 14.4: LAADF-STEM diffraction contrast image obtained along [001] zone axis with a large camera length 230 mm emphasizing strain contrast and showing deformation microstructure in specimen loaded with total strain amplitude 0.2% at 700°C. (a) Dispersion of numerous Nb(C,N) nano-precipitates is observed along with dislocations. (b) Detail is showing attractive pinning interaction of nano-precipitates with dislocation, which is attached at the exit side of the particles.

NbC nanoparticles are non-shearable. Moreover, being of large lattice misfit with semi-coherent character and in aggregated configurations, they are difficult to be overcome by dislocations even when climb by-pass is active at high temperature. It has been observed that the dislocations attach at the departure side of the particles (see Figs. 14.3 and 14.4b). In other words, a small length of dislocation line is trapped at the interface and unable to glide away. The dislocations also show some evidence of bowing, further suggesting that they are indeed attached to the "exit side" of NbC nanoparticles. This is similar to observations of dislocation interactions with incoherent dispersoids in oxide dispersion strengthened alloys [2, 3, 180]. As noted earlier, Rösler and Arzt [2, 3] developed a model based on the key idea that dislocations more commonly reside in attractive traps because the dislocation line reduces its energy by

lying at the interface between the matrix and an incoherent dispersoid. The attractive interaction causes a threshold stress τ_d, which must be exceeded in order to detach the dislocation from the particle after climb is completed (see Eq. (3.44) [2]). According to Arzt and Wilkinson [2], only a very modest attractive interaction between dislocations and particles is required in order for dislocation detachment to become the strength-controlling process. Considering an array of NbC particles as an incoherent dispersoid, Eq. (3.44) can be used to estimate the dislocation detachment threshold stress τ_d. Calculating for an average particle radius of 2.55 nm and the highest local estimated particle volume density of 4.9×10^{21} m^{-3}, the threshold stress τ_d can reach up to 20 MPa for minimum possible attractive interaction (expressed by $k = 0.94$ [2]) and up to 50 MPa for maximum attractive interaction ($k = 1$). As the detachment stress is function of $1/\lambda$, it can go even higher if the density of NbC nanoparticles is increased during cycling.
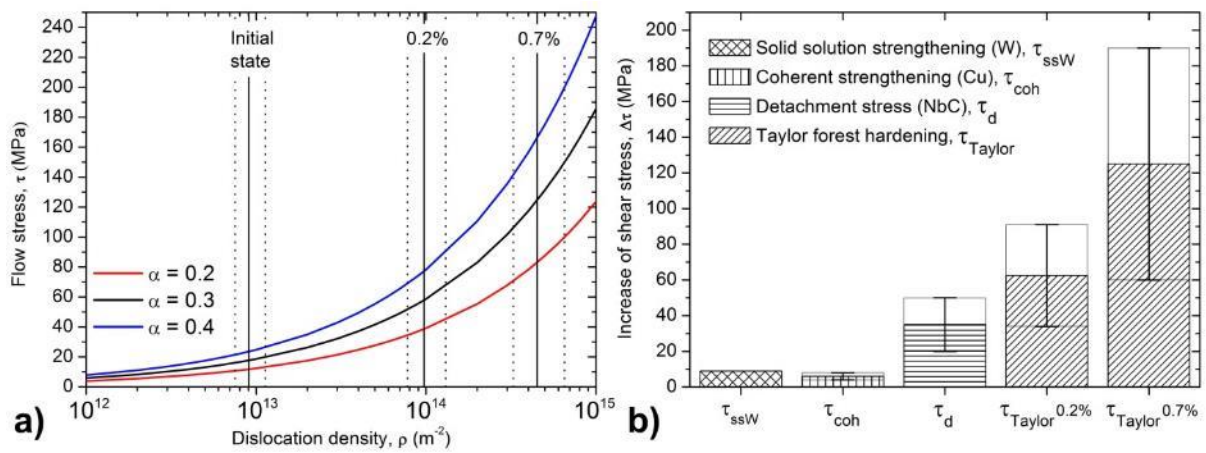
Figure 14.5: (a) Taylor dislocation forest strengthening. Flow stress τ_{Taylor} is plotted as a function of dislocation density ρ. Experimentally estimated dislocation densities in initial state and after loading with strain amplitudes 0.2 and 0.7% are marked in the graph (see Chapter 10.2.1). (b) Comparison of increase of shear stress due to different strengthening mechanisms present during cyclic loading.

In accord with experimental results, it can be assumed that the dislocations are completely randomly distributed within the grains. In this case, the interaction of glide and forest dislocations should be well-approximated by the Taylor work-hardening relationship between dislocation density ρ and flow stress τ_{Taylor} in a single crystal, i.e. by equation (3.46) [55]. In Fig. 14.5a, Eq. (3.46) is plotted and correlated to the experimentally obtained estimates of dislocation densities for strain amplitudes 0.2 and 0.7% (see Chapter 10.2.1). As shown in Fig. 14.5b, it is evident that the increase of flow stress as a result of dislocation forest strengthening is much more significant than is the increase of shear stress caused by other strengthening mechanisms. However, the precipitates and the solutes retard dislocation motion sufficiently so that the normal recovery processes and cell substructure development are suppressed. As a result, the microstructural state is characterized by enhanced dislocation-dislocation interactions leading subsequently to extraordinary cyclic strength at high temperature.

It is worthy to note that these experimental results are fully in accord with previous work from Polák and co-workers [137] who used a statistical-theory-based analysis of the hysteresis loop

shape to study the evolution of the cyclic plastic response of Sanicro 25 at high temperature. They evaluated the effective stress and the probability density function of the internal critical yield stresses of the microvolumes as a function of number of cycles. With increasing number of cycles, the effective stress almost doubled relative to the initial state suggesting the obstacles which can be overcome by thermal activation, e.g. precipitates, became present in the bulk. Moreover, the probability density function peak diminished, became wider, and shifted to much higher critical internal yield stresses. This is in a very good correlation with microstructural observations, where homogeneous dislocation arrangement with high density, combined with a dispersion of pinning nanoparticles, represents the microvolume with heavily retarded dislocation mobility.

15. High temperature cyclic strength – Sanicro 25 versus Manaurite XTM

Novel alloy with trade name Sandvik Sanicro 25 is one of the most recent representatives of heat-resistant materials based on face-centered cubic solid solution matrix designed for high temperature applications. It has been shown that when compared with other alloys within the class, Sanicro 25 exhibits the best strengthening properties at high temperatures. This work described, that during cyclic loading at a temperature of 700°C, the strength of this material is determined by nucleation of two populations of nanoparticles subsequently heavily affecting dislocations mobility thus leading to notable suppression of usual recovery processes. Identification of precipitation strengthening as the key mechanism suggests that from the perspective of alloy design, absolutely essential is sensitive and properly set alloying leading to precipitation of high density dispersion of nanoparticles which are small and stable for long time with further exposure at high temperatures. On the other hand, precipitation of other detrimental phases has to be suppressed. Current study of high temperature performance of Sanicro 25 proofs that the alloy based on Fe-25Ni-22.5Cr matrix alloyed with 0.5 wt% of Nb, 3 wt% of Cu, 0.23 wt% of N and up to 0.1 wt% of C can provide desired properties.

Manaurite XTM is a commercial centrifugally casted alloy designed as a construction material in ethylene cracking furnaces. While it was designed mainly to resist creep or creep-fatigue damage at temperatures close to 1000°C, in this work it served as a comparison material for study and discussion of mechanisms governing high temperature cyclic strengthening. When compared to Sanicro 25, austenitic matrix of Manaurite XTM contains much higher levels of Ni and Cr, added presumably for improvement of oxidation and carburization resistance. Also, it has four times higher content of interstitial carbon, but no nitrogen. Similarly to Sanicro 25, also Manaurite XTM is alloyed with Nb with content ranging from 0.5 to 1.0 wt%. While it can be alloyed also with copper, it is only up to 0.25 wt%, what are, according to literature [22, 142], too low levels to cause Cu-rich nanoparticles nucleation in austenitic matrix. These slight differences in alloying and overall design of the alloy lead to dramatically different high temperature performance connected with different microstructural changes. While in Sanicro 25, major secondary precipitates nucleated are dispersions of Cu-rich and Nb(C,N) nanoparticles, in Manaurite XTM none of these phases are observed. Experimental work has revealed that the main secondary precipitate is $M_{23}C_6$

type of carbide rich in Cr, Si and Mn. This phase is observed also in Sanicro 25, but is found mostly at the grain boundaries. If they are eventually nucleated within the bulk of the grain, they are much smaller than in case of Manaurite XTM, even for much longer thermal exposure times. It seems that high chromium content combined with high content of interstitial carbon substantially facilitates preferential nucleation of $M_{23}C_6$ phase, at the expense of other possible phases, including MX. According to Sourmail [126], $M_{23}C_6$ carbides are reported to have much higher coarsening and growth rate than other phases in austenite. Therefore, in the early stages of the nucleation and growth, $M_{23}C_6$ carbides can contribute to some high temperature cyclic strengthening of Manaurite XTM. However, as they overcome the critical size and the Orowan bowing becomes the governing mechanism of particle-dislocation interaction, their strengthening effect rapidly diminishes with further coarsening and growth.

To conclude, at high temperature the initial increase of dislocation density along with rapid nucleation of $M_{23}C_6$ carbides presenting effective obstacles to dislocation motion leads to some level of cyclic strengthening of Manaurite XTM during first few cycles. However, soon the equilibrium dislocation density is reached in the grains and with further coarsening of particles, their contribution to the overall flow stress diminishes. The cyclic plastic response saturates at much lower levels that in case of Sanicro 25.

VII. CONCLUSIONS

Experimental study of low cycle behavior of two advanced alloys based on Fe-Ni-Cr matrix tested both at room temperature and at a temperature of 700°C led to the following conclusions:

SANICRO 25

- After solution annealing, i.e. in the initial state of material, the only observed primary precipitates are the particles of Z-phase rich in Nb, Cr and N. Precipitates of about 100 nm in diameter found within grain interior and also at grain boundaries are the most frequent. No other phases were found.

- In room temperature cycling, cyclic plastic deformation is localized into the dislocation rich bands corresponding to PSMs observed on the surface. In most cases, the bands have irregular dislocation arrangement different from the typical ladder-like structure. No distinctive wall and channel arrangements are usually found, but they have character of alternating dislocation rich and dislocation poor areas. Character of dislocation slip is strongly planar. At low strain amplitudes, plastic strain localization leads to initial cyclic softening subsequently followed by saturation. At high strain amplitudes, before cyclic softening, also notable initial cyclic hardening is present due to secondary slip systems activation.

- Spatial low energy dislocation structures like veins, ladders or walls alternating with channels were observed very rarely even at very high strain amplitudes. Planar character of slip prevails also in these dislocation arrangements. No cellular structures were found at all at room temperature cycling.

- Coffin-Manson and also derived Wöhler curves at 700°C are substantially shifted to lower fatigue lives relative to those at room temperature. On the other hand, cyclic stress-strain curve at 700°C lies well above that at room temperature. This is related to an extraordinary cyclic strengthening of the alloy at high temperatures.

- Cu-rich nanoparticles precipitate homogeneously with high number density in the matrix as a result of elevated temperature. They have face-centered cubic crystal structure and are coherent with the austenitic matrix with a positive lattice misfit of only 0.22%.

- Supported by sufficient content of Nb and interstitial C available in solid solution, elevated temperature along with the high dislocation density facilitates the rapid nucleation of nano-scale NbC carbides only on dislocations. Larger particles are found along dislocation lines, smaller precipitates in aggregated groups from which dislocations have apparently detached as a result of cyclic stress.

- Under concurrent cyclic loading, the NbC nanoparticles can become liberated from dislocations - it is possible that this process could repeat numerous times, on an individual dislocation basis, and lead to continually increasing density of NbC obstacles in the microstructure as a function of cyclic loading.

- Experimentally obtained and simulated Moiré-like contrast under HAADF-STEM conditions confirms cube-on-cube orientation and the incoherent or semi-coherent nature of the NbC nanoparticles relative to the austenite matrix.

- Enhanced at high temperature, cross-slip and climb lead to a remarkably homogeneous dislocation structure with high dislocation density. A dense volume dispersion of coherent Cu-rich nanoparticles, and rising number of incoherent/semi-coherent NbC carbides, supported also by presence of W in solid solution, result in significant retardation of dislocation motion. Since dislocation mobility is affected, no low-energy dislocation structures are formed, supressing normal recovery processes. This microstructural state is characterized by significant dislocation-dislocation interactions as described by the Taylor equation for forest strengthening. As a consequence, Sanicro 25 exhibits extraordinary cyclic hardening leading to the remarkably high saturated cyclic stress at 700°C.

MANAURITE XTM

- In the as-cast state, the Manaurite XTM has dendritic structure composed of austenitic matrix and interdendritic regions containing eutectic primary carbides of M_7C_3 and $M_{23}C_6$ type rich in Cr and MC type rich in Nb. Grains are columnar and have size up to several milimeters.

- In room temperature cycling, mostly simple planar slip of individual dislocations is observed in the austenitic matrix. Dislocation density is higher in the vicinity of primary eutectic carbides or at the grain boundaries at 700°C lies. No signs of cyclic slip localization are observed, neither evidence of low energy dislocation structures formation. After initial increase of dislocation density leading to work hardening, cyclic plastic behavior of Manaurite XTM at room temperature is characterized by saturated response.

- Coffin-Manson and also derived Wöhler curves at 700°C are shifted to lower fatigue lives relative to those at room temperature. This is same also in case of cyclic stress-strain curve, which lies well below that at room temperature.

- Owing to very high Cr content combined with high amount of C, major secondary precipitate to rapidly nucleate in Manaurite XTM during cyclic loading at 700°C is $M_{23}C_6$ carbide rich in Cr, Si and Mn. Even after very short aging times, they are already relatively large. In contrast to Sanicro 25, they are found in numerous aggregated configurations in the bulk of the grains or nucleated at immobile dislocations. On the other hand, no stable nano-scale precipitates are found in the matrix.

- At the onset of nucleation, $M_{23}C_6$ carbides can present obstacle to dislocation movement thus contributing to the increase of high temperature strength within a few first cycles as observed on hardening/softening curves. However, with their rapid coarsening, as they become too large with large average distance between them, their strengthening role diminishes and cyclic plastic response has tendency to saturation.

VIII. REFERENCES

[1]   POLLOCK, Tresa M. and Sammy TIN. Nickel-Based Superalloys for Advanced Turbine Engines: Chemistry, Microstructure and Properties. *Journal of Propulsion and Power*. 2006, **22**(2), 361–374. ISSN 0748-4658, 1533-3876. Doi: 10.2514/1.18239

[2]   ARZT, E. and D.S. WILKINSON. Threshold stresses for dislocation climb over hard particles: The effect of an attractive interaction. *Acta Metallurgica*. 1986, **34**(10), 1893–1898. ISSN 00016160. Doi: 10.1016/0001-6160(86)90247-6

[3]   RÖSLER, J. and E. ARZT. A new model-based creep equation for dispersion strengthened materials. *Acta Metallurgica et Materialia*. 1990, **38**(4), 671–683. ISSN 09567151. Doi: 10.1016/0956-7151(90)90223-4

[4]   YEH, J.-W., S.-K. CHEN, S.-J. LIN, J.-Y. GAN, T.-S. CHIN, T.-T. SHUN, C.-H. TSAU and S.-Y. CHANG. Nanostructured High-Entropy Alloys with Multiple Principal Elements: Novel Alloy Design Concepts and Outcomes. *Advanced Engineering Materials*. 2004, **6**(5), 299–303. ISSN 1438-1656, 1527-2648. Doi: 10.1002/adem.200300567

[5]   CANTOR, B., I.T.H. CHANG, P. KNIGHT and A.J.B. VINCENT. Microstructural development in equiatomic multicomponent alloys. *Materials Science and Engineering: A*. 2004, **375**–**377**, 213–218. ISSN 09215093. Doi: 10.1016/j.msea.2003.10.257

[6]   SINGH, S., N. WANDERKA, B.S. MURTY, U. GLATZEL and J. BANHART. Decomposition in multi-component AlCoCrCuFeNi high-entropy alloy. *Acta Materialia*. 2011, **59**(1), 182–190. ISSN 13596454. Doi: 10.1016/j.actamat.2010.09.023

[7]   OTTO, F., Y. YANG, H. BEI and E.P. GEORGE. Relative effects of enthalpy and entropy on the phase stability of equiatomic high-entropy alloys. *Acta Materialia*. 2013, **61**(7), 2628–2638. ISSN 13596454. Doi: 10.1016/j.actamat.2013.01.042

[8]   OTTO, F., A. DLOUHÝ, Ch. SOMSEN, H. BEI, G. EGGELER and E.P. GEORGE. The influences of temperature and microstructure on the tensile properties of a CoCrFeMnNi high-entropy alloy. *Acta Materialia*. 2013, **61**(15), 5743–5755. ISSN 13596454. Doi: 10.1016/j.actamat.2013.06.018

[9]   CHAI, G. and U. FORSBERG. Sanicro 25. In: *Materials for Ultra-Supercritical and Advanced Ultra-Supercritical Power Plants*. B.m.: Elsevier, 2017, p. 391–421. ISBN 978-0-08-100552-1. Doi: 10.1016/B978-0-08-100552-1.00012-9

[10]   BARNARD, P. Austenitic steel grades for boilers in ultra-supercritical power plants. In: *Materials for Ultra-Supercritical and Advanced Ultra-Supercritical Power Plants*. Elsevier, 2017, p. 99–119. ISBN 978-0-08-100552-1.

[11] MATHEW, M.D., G. SASIKALA, K. BHANU SANKARA RAO and S.L. MANNAN. Influence of carbon and nitrogen on the creep properties of type 316 stainless steel at 873 K. *Materials Science and Engineering: A*. 1991, **148**(2), 253–260. ISSN 09215093. Doi: 10.1016/0921-5093(91)90827-A

[12] KIM, Dae Whan, Jong-Hwa CHANG and Woo-Seog RYU. Evaluation of the creep–fatigue damage mechanism of Type 316L and Type 316LN stainless steel. *International Journal of Pressure Vessels and Piping*. 2008, **85**(6), 378–384. ISSN 03080161. Doi: 10.1016/j.ijpvp.2007.11.013

[13] VODÁREK, Vlastimil. Creep behaviour and microstructural evolution in AISI 316LN+Nb steels at 650°C. *Materials Science and Engineering: A*. 2011, **528**(12), 4232–4238. ISSN 09215093. Doi: 10.1016/j.msea.2011.02.025

[14] GERLAND, M., R. ALAIN, B. AIT SAADI and J. MENDEZ. Low cycle fatigue behaviour in vacuum of a 316L-type austenitic stainless steel between 20 and 600°C—Part II: Dislocation structure evolution and correlation with cyclic behaviour. *Materials Science and Engineering: A*. 1997, **229**(1–2), 68–86. ISSN 09215093. Doi: 10.1016/S0921-5093(96)10560-8

[15] ALAIN, R., P. VIOLAN and J. MENDEZ. Low cycle fatigue behavior in vacuum of a 316L type austenitic stainless steel between 20 and 600°C Part I: Fatigue resistance and cyclic behavior. *Materials Science and Engineering: A*. 1997, **229**(1–2), 87–94. ISSN 09215093. Doi: 10.1016/S0921-5093(96)10558-X

[16] OBRTLÍK, Karel, Tomáš KRUML and Jaroslav POLÁK. Dislocation structures in 316L stainless steel cycled with plastic strain amplitudes over a wide interval. *Materials Science and Engineering: A*. 1994, **187**(1), 1–9. ISSN 09215093. Doi: 10.1016/0921-5093(94)90325-5

[17] KRUML, T., J. POLÁK, K. OBRTLÍK and S. DEGALLAIX. Dislocation structures in the bands of localised cyclic plastic strain in austenitic 316L and austenitic-ferritic duplex stainless steels. *Acta Materialia*. 1997, **45**(12), 5145–5151. ISSN 13596454. Doi: 10.1016/S1359-6454(97)00178-X

[18] PHAM, M.S., C. SOLENTHALER, K.G.F. JANSSENS and S.R. HOLDSWORTH. Dislocation structure evolution and its effects on cyclic deformation response of AISI 316L stainless steel. *Materials Science and Engineering: A*. 2011, **528**(7–8), 3261–3269. ISSN 09215093. Doi: 10.1016/j.msea.2011.01.015

[19] YAN, Xiao-Li, Xian-Cheng ZHANG, Shan-Tung TU, Sardari-Lal MANNAN, Fu-Zhen XUAN and Yong-Cheng LIN. Review of creep–fatigue endurance and life prediction of 316 stainless steels. *International Journal of Pressure Vessels and Piping*. 2015, **126**–**127**, 17–28. ISSN 03080161. Doi: 10.1016/j.ijpvp.2014.12.002

[20] BUSS, T. M. and C. J. HYDE. Cyclic thermomechanical testing of 316 stainless steel. *Materials at High Temperatures*. 2015, **32**(3), 276–279. ISSN 0960-3409, 1878-6413. Doi:10.1179/0960340914Z.00000000068

[21] BAI, J.W., P.P. LIU, Y.M. ZHU, X.M. LI, C.Y. CHI, H.Y. YU, X.S. XIE and Q. ZHAN. Coherent precipitation of copper in Super304H austenite steel. *Materials*

Science and Engineering: A. 2013, **584**, 57–62. ISSN 09215093. Doi: 10.1016/j.msea.2013.06.082

[22] OU, Ping, Hui XING, Xuanli WANG, Jian SUN, Zhengqiang CUI and Changshun YANG. Coarsening and Hardening Behaviors of Cu-Rich Precipitates in Super304H Austenitic Steel. *Metallurgical and Materials Transactions A*. 2015, **46**(9), 3909–3916. ISSN 1073-5623, 1543-1940. Doi: 10.1007/s11661-015-3004-3

[23] LU, Jun, Lars HULTMAN, Erik HOLMSTRÖM, Karin H. ANTONSSON, Mikael GREHK, Wei LI, Levente VITOS and Ardeshir GOLPAYEGANI. Stacking fault energies in austenitic stainless steels. *Acta Materialia*. 2016, **111**, 39–46. ISSN 13596454. Doi: 10.1016/j.actamat.2016.03.042

[24] CHAI, Guocai, Magnus BOSTRÖM, Magnus OLAISON and Urban FORSBERG. Creep and LCF Behaviors of Newly Developed Advanced Heat Resistant Austenitic Stainless Steel for A-USC. *Procedia Engineering*. 2013, **55**, 232–239. ISSN 18777058. Doi: 10.1016/j.proeng.2013.03.248

[25] ZUREK, J., S.-M. YANG, D.-Y. LIN, T. HÜTTEL, L. SINGHEISER and W. J. QUADAKKERS. Microstructural stability and oxidation behavior of Sanicro 25 during long-term steam exposure in the temperature range 600-750 °C: Microstructural stability and oxidation behavior of Sanicro 25. *Materials and Corrosion*. 2015, **66**(4), 315–327. ISSN 09475117. Doi: 10.1002/maco.201407901

[26] RUTKOWSKI, Bogdan, Aleksander GIL and Aleksandra CZYRSKA-FILEMONOWICZ. Microstructure and chemical composition of the oxide scale formed on the sanicro 25 steel tubes after fireside corrosion. *Corrosion Science*. 2016, **102**, 373–383. ISSN 0010938X. Doi: 10.1016/j.corsci.2015.10.030

[27] DI GIANFRANCESCO, A. The fossil fuel power plants technology. In: *Materials for Ultra-Supercritical and Advanced Ultra-Supercritical Power Plants*. B.m.: Elsevier, 2017, p. 1–49. ISBN 978-0-08-100552-1.

[28] ALVINO, Antonello, Daniela LEGA, Francesco GIACOBBE, Vittorio MAZZOCCHI and Antonio RINALDI. Damage characterization in two reformer heater tubes after nearly 10 years of service at different operative and maintenance conditions. *Engineering Failure Analysis*. 2010, **17**(7–8), 1526–1541. ISSN 13506307. Doi: 10.1016/j.engfailanal.2010.06.003

[29] JOUBERT, Jean-Marc, Wisline ST-FLEUR, Julia SARTHOU, Antonin STECKMEYER and Benjamin FOURNIER. Equilibrium characterization and thermodynamic calculations on highly alloyed refractory steels. *Calphad*. 2014, **46**, 55–61. ISSN 03645916. Doi: 10.1016/j.calphad.2014.02.002

[30] ALLAHKARAM, Saeed Reza, Sadegh BORJALI and Hamed KHOSRAVI. Investigation of weldability and property changes of high pressure heat-resistant cast stainless steel tubes used in pyrolysis furnaces after a five-year service. *Materials & Design*. 2012, **33**, 476–484. ISSN 02613069. Doi: 10.1016/j.matdes.2011.04.052

[31] DE ALMEIDA, Luiz Henrique, André Freitas RIBEIRO a Iain LE MAY. Microstructural characterization of modified 25Cr–35Ni centrifugally cast steel furnace

tubes. *Materials Characterization*. 2002, **49**(3), 219–229. ISSN 10445803. Doi: 10.1016/S1044-5803(03)00013-5

[32] NUNES, F.C., L.H. DE ALMEIDA, J. DILLE, J.-L. DELPLANCKE and I. LE MAY. Microstructural changes caused by yttrium addition to NbTi-modified centrifugally cast HP-type stainless steels. *Materials Characterization*. 2007, **58**(2), 132–142. ISSN 10445803. Doi: 10.1016/j.matchar.2006.04.007

[33] KENIK, E. Structure and phase stability in a cast modified-HP austenite after long-term ageing. *Scripta Materialia*. 2003, **49**(2), 117–122. ISSN 13596462. Doi: 10.1016/S1359-6462(03)00238-0

[34] FROMENT, Gilbert F., Juray DE WILDE and Kenneth B. BISCHOFF. *Chemical reactor analysis and design*. 3rd ed. Hoboken, N.J: Wiley, 2011. ISBN 978-0-470-56541-4.

[35] ALBRIGHT, Lyle F. and James C. MAREK. Coke formation during pyrolysis: roles of residence time, reactor geometry, and time of operation. *Industrial & Engineering Chemistry Research*. 1988, **27**(5), 743–751. ISSN 0888-5885, 1520-5045. Doi: 10.1021/ie00077a004

[36] HULL, Derek and David J. BACON. *Introduction to dislocations*. 5. ed. Amsterdam: Elsevier/Butterworth-Heinemann, 2011. ISBN 978-0-08-096672-4.

[37] DE GRAEF, Marc and Michael E. MCHENRY. *Structure of materials: an introduction to crystallography, diffraction, and symmetry*. Second edition, fully revised and updated. New York: Cambridge University Press, 2012. ISBN 978-1-107-00587-7.

[38] WEST, Anthony R. *Basic solid state chemistry*. 2nd ed. New York: John Wiley & Sons, 1999. ISBN 978-0-471-98755-0.

[39] MAYER, Thomas. *Characterisation and modelling of the microstructural and mechanical evolution of a steam turbine rotor steel*. B.m., 2012. ETH Zurich. Available from: http://hdl.handle.net/20.500.11850/61912

[40] KRUML, Tomáš. *Scriptum: Introduction to dislocations*. Brno University of Technology, 2017.

[41] KRUML, Tomáš. *Scriptum: Basics of plastic deformation of solids*. Brno University of Technology, 2017.

[42] HASSON, G.C. and C. GOUX. Interfacial energies of tilt boundaries in aluminium. Experimental and theoretical determination. *Scripta Metallurgica*. 1971, **5**(10), 889–894. ISSN 00369748. Doi: 10.1016/0036-9748(71)90064-0

[43] PREMYSL BERAN, MILAN HECZKO, TOMAS KRUML, TOBIAS PANZNER and STEVEN VAN PETEGEM. Complex investigation of deformation twinning in γ-TiAl by TEM and neutron diffraction. *Journal of the Mechanics and Physics of Solids*. 2016. ISSN 00225096. Doi: 10.1016/j.jmps.2016.05.004

[44] SMALLMAN, R. E., A. H. W. NGAN and R. E. SMALLMAN. *Physical metallurgy and advanced materials*. 7th ed. Amsterdam ; Boston: Butterworth Heinemann, 2007. ISBN 978-0-7506-6906-1.

[45] CAILLARD, Daniel and Jean-Luc MARTIN. *Thermally activated mechanisms in crystal plasticity*. Amsterdam ; Boston, Mass: Pergamon, 2003. Pergamon materials series, 8. ISBN 978-0-08-042703-4.

[46] SEEGER, A., J. DIEHL, S. MADER and H. REBSTOCK. Work-hardening and work-softening of face-centred cubic metal crystals. *Philosophical Magazine*. 1957, **2**(15), 323–350. ISSN 0031-8086. Doi: 10.1080/14786435708243823

[47] KRUML, T., O. CODDET and J.L. MARTIN. About the determination of the thermal and athermal stress components from stress-relaxation experiments. *Acta Materialia*. 2008, **56**(3), 333–340. ISSN 13596454. Doi: 10.1016/j.actamat.2007.09.027

[48] SPÄTIG, P., J. BONNEVILLE and J.-L. MARTIN. A new method for activation volume measurements: application to Ni3(Al,Hf). *Materials Science and Engineering: A*. 1993, **167**(1–2), 73–79. ISSN 09215093. Doi: 10.1016/0921-5093(93)90339-G

[49] ANDERSON, Peter M., John Price HIRTH and Jens LOTHE. *Theory of dislocations*. 2017 edition. Cambridge: Cambridge University Press, 2017. ISBN 978-0-521-86436-7.

[50] HOWE, James M. *Interfaces in materials: atomic structure, thermodynamics and kinetics of solid-vapor, solid-liquid and solid-solid interfaces*. New York, NY: Wiley, 1997. ISBN 978-0-471-13830-3.

[51] LLOYD, D.J. Precipitation Hardening. In: *Strength of Metals and Alloys (ICSMA 7)*. Elsevier, 1986, p. 1745–1778. ISBN 978-0-08-031640-6. Available from: https://linkinghub.elsevier.com/retrieve/pii/B9780080316406500128

[52] FRIEDEL, J. *Dislocations*. Burlington: Elsevier Science : Pergamon Press, 1964. ISBN 978-1-4831-3592-2.

[53] BROWN, L. M. and R.K. HAM. Dislocation-particle interactions. In: A KELLY a Robin NICHOLSON, ed. *Strengthening methods in crystals*. New York: Halstead Press Division, Wiley, 1972. ISBN 978-0-470-46800-5.

[54] GEROLD, V. and H. HABERKORN. On the Critical Resolved Shear Stress of Solid Solutions Containing Coherent Precipitates. *physica status solidi (b)*. 1966, **16**(2), 675–684. ISSN 03701972, 15213951. Doi:10.1002/pssb.19660160234

[55] TAYLOR, G. I. The Mechanism of Plastic Deformation of Crystals. Part I. Theoretical. *Proceedings of the Royal Society A: Mathematical, Physical and Engineering Sciences*. 1934, **145**(855), 362–387. ISSN 1364-5021, 1471-2946. Doi: 10.1098/rspa.1934.0106

[56] SEVILLANO, Javier Gil. Flow Stress and Work Hardening. In: R. W. CAHN, P. HAASEN and E. J. KRAMER, ed. *Materials Science and Technology*. Weinheim, Germany: Wiley-VCH Verlag GmbH & Co. KGaA, 2006. ISBN 978-3-527-60397-8. Doi: 10.1002/9783527603978.mst0049

[57] MUGHRABI, H. Dislocation wall and cell structures and long-range internal stresses in deformed metal crystals. *Acta Metallurgica*. 1983, **31**(9), 1367–1379. ISSN 00016160. Doi: 10.1016/0001-6160(83)90007-X

[58] MUGHRABI, H. The long-range internal stress field in the dislocation wall structure of persistent slip bands. *Physica Status Solidi (a)*. 1987, **104**(1), 107–120. ISSN 00318965, 1521396X. Doi:10.1002/pssa.2211040108

[59] LAIRD, Campbell, Philip CHARSLEY and Haël MUGHRABI. Low energy dislocation structures produced by cyclic deformation. *Materials Science and Engineering*. 1986, **81**, 433–450. ISSN 00255416. Doi: 10.1016/0025-5416(86)90281-8

[60] MUGHRABI, H. and T. UNGÁR. Chapter 60 Long-Range internal stresses in deformed single-phase materials: The composite model and its consequences. In: *Dislocations in Solids*. Elsevier, 2002, p. 343–411. ISBN 978-0-444-50966-6. Available from: http://linkinghub.elsevier.com/retrieve/pii/S1572485902800110

[61] ASHBY, M. F. The deformation of plastically non-homogeneous materials. *The Philosophical Magazine: A Journal of Theoretical Experimental and Applied Physics*. 1970, **21**(170), 399–424. ISSN 0031-8086. Doi: 10.1080/14786437008238426

[62] MUGHRABI, H. On the role of strain gradients and long-range internal stresses in the composite model of crystal plasticity. *Materials Science and Engineering: A*. 2001, **317**(1–2), 171–180. ISSN 09215093. Doi: 10.1016/S0921-5093(01)01173-X

[63] HALL, E O. The Deformation and Ageing of Mild Steel: III Discussion of Results. *Proceedings of the Physical Society. Section B*. 1951, **64**(9), 747–753. ISSN 0370-1301. Doi: 10.1088/0370-1301/64/9/303

[64] PETCH, N. J. The Cleavage Strength of Polycrystals. *Journal of the Iron and Steel Institute*. 1953, (174), 25–28.

[65] PTÁČEK, Luděk. *Nauka o materiálu I.* Brno: CERM, 2003. ISBN 978-80-7204-283-8.

[66] FOREMAN, A. J. E. and M. J. MAKIN. Dislocation movement through random arrays of obstacles. *Philosophical Magazine*. 1966, **14**(131), 911–924. ISSN 0031-8086. Doi: 10.1080/14786436608244762

[67] FOREMAN, A. J. E. and M. J. MAKIN. DISLOCATION MOVEMENT THROUGH RANDOM ARRAYS OF OBSTACLES. *Canadian Journal of Physics*. 1967, **45**(2), 511–517. ISSN 0008-4204, 1208-6045. Doi: 10.1139/p67-044

[68] ARGON, Ali S. *Strengthening mechanisms in crystal plasticity*. Oxford ; New York: Oxford University Press, 2008. Oxford series on materials modelling, 4. ISBN 978-0-19-851600-2.

[69] GRÖGER, R., A.G. BAILEY and V. VITEK. Multiscale modeling of plastic deformation of molybdenum and tungsten: I. Atomistic studies of the core structure and glide of 1/2 ⟨111⟩ screw dislocations at 0K. *Acta Materialia*. 2008, **56**(19), 5401–5411. ISSN 13596454. Doi: 10.1016/j.actamat.2008.07.018

[70] GRÖGER, R., V. RACHERLA, J.L. BASSANI and V. VITEK. Multiscale modeling of plastic deformation of molybdenum and tungsten: II. Yield criterion for single crystals based on atomistic studies of glide of 1/2 〈111〉 screw dislocations. *Acta Materialia*. 2008, **56**(19), 5412–5425. ISSN 13596454. Doi: 10.1016/j.actamat.2008.07.037

[71] GRÖGER, R. and V. VITEK. Multiscale modeling of plastic deformation of molybdenum and tungsten. III. Effects of temperature and plastic strain rate. *Acta Materialia*. 2008, **56**(19), 5426–5439. ISSN 13596454. Doi: 10.1016/j.actamat.2008.07.027

[72] GHONIEM†, Nasr M., Esteban P. BUSSO, Nicholas KIOUSSIS and Hanchen HUANG. Multiscale modelling of nanomechanics and micromechanics: an overview. *Philosophical Magazine*. 2003, **83**(31–34), 3475–3528. ISSN 1478-6435, 1478-6443. Doi: 10.1080/14786430310001607388

[73] SMITH, T. M., B. D. ESSER, N. ANTOLIN, A. CARLSSON, R. E. A. WILLIAMS, A. WESSMAN, T. HANLON, H. L. FRASER, W. WINDL, D. W. MCCOMB and M. J. MILLS. Phase transformation strengthening of high-temperature superalloys. *Nature Communications*. 2016, **7**, 13434. ISSN 2041-1723. Doi: 10.1038/ncomms13434

[74] KLESNIL, Mirko a Petr LUKÁŠ. *Fatigue of metallic materials*. 2nd rev. ed. Amsterdam ; New York: Elsevier, 1992. Materials science monographs, 71. ISBN 978-0-444-98723-5.

[75] POLÁK, Jaroslav. *Cyclic plasticity and low cycle fatigue life of metals*. Prag: Academia, 1991. ISBN 978-80-200-0008-8.

[76] POLÁK, J. Cyclic Deformation, Crack Initiation, and Low-cycle Fatigue. In: *Comprehensive Structural Integrity*. Elsevier, 2003, p. 1–39. ISBN 978-0-08-043749-1. Available from: http://linkinghub.elsevier.com/retrieve/pii/B008043749404060X

[77] LUKÁŠ, P., M. KLESNIL, J. KREJČÍ and P. RYŠ. Substructure of Persistent Slip Bands in Cyclically Deformed Copper. *Physica status solidi (b)*. 1966, **15**(1), 71–82. ISSN 03701972, 15213951. Doi: 10.1002/pssb.19660150105

[78] FELTNER, C.E and C LAIRD. Cyclic stress-strain response of F.C.C. metals and alloys—I Phenomenological experiments. *Acta Metallurgica*. 1967, **15**(10), 1621–1632. ISSN 00016160. Doi: 10.1016/0001-6160(67)90137-X

[79] LUKÁŠ, P and M KLESNIL. Cyclic stress-strain response and fatigue life of metals in low amplitude region. *Materials Science and Engineering*. 1973, **11**(6), 345–356. ISSN 00255416. Doi: 10.1016/0025-5416(73)90125-0

[80] WINTER, A.T., O.R. PEDERSEN and K.V. RASMUSSEN. Dislocation microstructures in fatigued copper polycrystals. *Acta Metallurgica*. 1981, **29**(5), 735–748. ISSN 00016160. Doi: 10.1016/0001-6160(81)90117-6

[81] ACKERMANN, F, L.P KUBIN, J LEPINOUX and H MUGHRABI. The dependence of dislocation microstructure on plastic strain amplitude in cyclically strained copper single crystals. *Acta Metallurgica*. 1984, **32**(5), 715–725. ISSN 00016160. Doi: 10.1016/0001-6160(84)90145-7

[82] POLÁK, J. and M. KLESNIL. Cyclic stress-strain response and dislocation structures in polycrystalline copper. *Materials Science and Engineering*. 1984, **63**(2), 189–196. ISSN 00255416. Doi: 10.1016/0025-5416(84)90120-4

[83] POLÁK, Jaroslav, Karel OBRTLÍK and Jan HELEŠIC. Cyclic strain localization in polycrystalline copper at room temperature and low temperatures. *Materials Science and Engineering: A*. 1991, **132**, 67–76. ISSN 09215093. Doi: 10.1016/0921-5093(91)90362-Q

[84] BUQUE, C. Persistent slip bands in cyclically deformed nickel polycrystals. *International Journal of Fatigue*. 2001, **23**(6), 459–466. ISSN 01421123. Doi: 10.1016/S0142-1123(01)00013-5

[85] CHARSLEY, P. and D. KUHLMANN-WILSDORF. Configurations of {100} dislocation walls formed during fatigue. *Philosophical Magazine A*. 1981, **44**(6), 1351–1361. ISSN 0141-8610, 1460-6992. Doi: 10.1080/01418618108235814

[86] CHARSLEY, P. Dislocation arrangements in polycrystalline copper alloys fatigued to saturation. *Materials Science and Engineering*. 1981, **47**(3), 181–185. ISSN 00255416. Doi: 10.1016/0025-5416(81)90044-6

[87] BOUTIN, J., N. MARCHAND, J.-P. BAÏLON and J.I. DICKSON. An intermediate plateau in the cyclic stress-strain curve of α brass. *Materials Science and Engineering*. 1984, **67**(2), L23–L27. ISSN 00255416. Doi: 10.1016/0025-5416(84)90062-4

[88] DRIVER, J.H. and P. RIEUX. The cyclic stress-strain behavior of polycrystalline Al-5wt.%Mg. *Materials Science and Engineering*. 1984, **68**(1), 35–43. ISSN 00255416. Doi: 10.1016/0025-5416(84)90241-6

[89] CHARSLEY, P. and L.J. HARRIS. Condensed dislocation structures in polycrystalline aluminium fatigued at 77K. *Scripta Metallurgica*. 1987, **21**(3), 341–344. ISSN 00369748. Doi: 10.1016/0036-9748(87)90225-0

[90] BLOCHWITZ, C., K. MECKE and R. STEPHAN. Der Einfluß der Stapelfehlerenergie und der Atomgröße-Schubmodul-Differenzen auf Versetzungsstruktur und ZSD ermüdeter kfz-Metallegierungen. *Kristall und Technik*. 1978, **13**(7), 851–861. ISSN 00234753, 15214079. Doi: 10.1002/crat.19780130720

[91] NAHM, H., J. MOTEFF and D.R. DIERCKS. Substructural development during low cycle fatigue of AISI 304 stainless steel at 649°C. *Acta Metallurgica*. 1977, **25**(2), 107–116. ISSN 00016160. Doi: 10.1016/0001-6160(77)90114-6

[92] BOULANGER L., BISSON A. and TAVASSOLI A. A. Labyrinth structure and persistent slip bands in fatigued 316 stainless steel. *Philosophical magazine. A. Physics of condensed matter. Defects and mechanical properties*. 1985, **51**, L5. ISSN 0141-8610.

[93] L'ESPERANCE, G., J.B. VOGT and J.I. DICKSON. The identification of labyrinth wall orientations in cyclically deformed AISI-SAE 316 stainless steel. *Materials Science and Engineering*. 1986, **79**(2), 141–147. ISSN 00255416. Doi: 10.1016/0025-5416(86)90397-6

[94] GERLAND, M. and P. VIOLAN. Secondary cyclic hardening and dislocation structures in type 316 stainless steel at 600°C. *Materials Science and Engineering*. 1986, **84**, 23–33. ISSN 00255416. Doi: 10.1016/0025-5416(86)90219-3

[95] LI, Yuanfeng and Campbell LAIRD. Cyclic response and dislocation structures of AISI 316L stainless steel. Part 1: single crystals fatigued at intermediate strain amplitude. *Materials Science and Engineering: A*. 1994, **186**(1–2), 65–86. ISSN 09215093. Doi: 10.1016/0921-5093(94)90306-9

[96] LI, Yuanfeng and Campbell LAIRD. Cyclic response and dislocation structures of AISI 316L stainless steel. Part 2: polycrystals fatigued at intermediate strain amplitude. *Materials Science and Engineering: A*. 1994, **186**(1–2), 87–103. ISSN 09215093. Doi: 10.1016/0921-5093(94)90307-7

[97] HONG, Sun Ig and C. LAIRD. Mechanisms of slip mode modification in F.C.C. solid solutions. *Acta Metallurgica et Materialia*. 1990, **38**(8), 1581–1594. ISSN 09567151. Doi: 10.1016/0956-7151(90)90126-2

[98] POLÁK, J., V. MAZÁNOVÁ, M. HECZKO, R. PETRÁŠ, I. KUBĚNA, L. CASALENA and J. MAN. The role of extrusions and intrusions in fatigue crack initiation. *Engineering Fracture Mechanics*. 2017, **185**, 46–60. ISSN 00137944. Doi: 10.1016/j.engfracmech.2017.03.006

[99] ESSMANN, U. and H. MUGHRABI. Annihilation of dislocations during tensile and cyclic deformation and limits of dislocation densities. *Philosophical Magazine A*. 1979, **40**(6), 731–756. ISSN 0141-8610, 1460-6992. Doi: 10.1080/01418617908234871

[100] POLÁK, Jaroslav and Jiří MAN. Experimental evidence and physical models of fatigue crack initiation. *International Journal of Fatigue*. 2016. ISSN 01421123. Doi: 10.1016/j.ijfatigue.2016.02.021

[101] ESSMANN, U., U. GÖSELE and H. MUGHRABI. A model of extrusions and intrusions in fatigued metals I. Point-defect production and the growth of extrusions. *Philosophical Magazine A*. 1981, **44**(2), 405–426. ISSN 0141-8610, 1460-6992. Doi: 10.1080/01418618108239541

[102] MUGHRABI, H. Microstructural mechanisms of cyclic deformation, fatigue crack initiation and early crack growth. *Philosophical Transactions of the Royal Society A: Mathematical, Physical and Engineering Sciences*. 2015, **373**(2038), 20140132–20140132. ISSN 1364-503X, 1471-2962. Doi: 10.1098/rsta.2014.0132

[103] TANAKA, K. and T. MURA. A Dislocation Model for Fatigue Crack Initiation. *Journal of Applied Mechanics*. 1981, **48**(1), 97. ISSN 00218936. Doi: 10.1115/1.3157599

[104] SANGID, Michael D. The physics of fatigue crack initiation. *International Journal of Fatigue*. 2013, **57**, 58–72. ISSN 01421123. Doi: 10.1016/j.ijfatigue.2012.10.009

[105] SAUZAY, Maxime and Mohamed Ould MOUSSA. Prediction of grain boundary stress fields and microcrack initiation induced by slip band impingement. *International Journal of Fracture*. 2013, **184**(1–2), 215–240. ISSN 0376-9429, 1573-2673. Doi: 10.1007/s10704-013-9878-4

[106] SAUZAY, Maxime and Kokleang VOR. Influence of plastic slip localization on grain boundary stress fields and microcrack nucleation. *Engineering Fracture Mechanics* . 2013, **110**, 330–349. ISSN 00137944. Doi: 10.1016/j.engfracmech.2013.04.019

[107] POLÁK, J. On the role of point defects in fatigue crack initiation. *Materials Science and Engineering*. 1987, **92**, 71–80. ISSN 00255416. Doi: 10.1016/0025-5416(87)90157-1

[108] POLÁK, J. Electrical resistivity of cyclically deformed copper. *Czechoslovak Journal of Physics*. 1969, **19**(3), 315–322. ISSN 0011-4626, 1572-9486. Doi: 10.1007/BF01712868

[109] BASINSKI, Z.S. and S.J. BASINSKI. Electrical resistivity of fatigued copper crystals. *Acta Metallurgica*. 1989, **37**(12), 3275–3281. ISSN 00016160. Doi: 10.1016/0001-6160(89)90200-9

[110] POLÁK, J. Resistivity of fatigued copper single crystals. *Materials Science and Engineering*. 1987, **89**, 35–43. ISSN 00255416. Doi: 10.1016/0025-5416(87)90247-3

[111] POLÁK, Jaroslav and Maxime SAUZAY. Growth of extrusions in localized cyclic plastic straining. *Materials Science and Engineering: A*. 2009, **500**(1–2), 122–129. ISSN 09215093. Doi: 10.1016/j.msea.2008.09.022

[112] POLÁK, J. and J. MAN. Mechanisms of extrusion and intrusion formation in fatigued crystalline materials. *Materials Science and Engineering: A*. 2014, **596**, 15–24. ISSN 09215093. Doi: 10.1016/j.msea.2013.12.005

[113] POLÁK, Jaroslav and Jiří MAN. Fatigue crack initiation – The role of point defects. *International Journal of Fatigue*. 2014, **65**, 18–27. ISSN 01421123. Doi: 10.1016/j.ijfatigue.2013.10.016

[114] MAN, J., M. VALTR, M. PETRENEC, J. DLUHOŠ, I. KUBĚNA, K. OBRTLÍK and J. POLÁK. AFM and SEM-FEG study on fundamental mechanisms leading to fatigue crack initiation. *International Journal of Fatigue*. 2015, **76**, 11–18. ISSN 01421123. Doi: 10.1016/j.ijfatigue.2014.09.019

[115] POLÁK, Jaroslav, Veronika MAZÁNOVÁ, Ivo KUBĚNA, Milan HECZKO and Jiří MAN. Surface Relief and Internal Structure in Fatigued Stainless Sanicro 25 Steel. *Metallurgical and Materials Transactions A*. 2016, **47**(5), 1907–1911. ISSN 1073-5623, 1543-1940. Doi: 10.1007/s11661-016-3374-1

[116] POLÁK, J, V MAZÁNOVÁ, M HECZKO, I KUBĚNA and J MAN. Profiles of persistent slip markings and internal structure of underlying persistent slip bands: Profiles of PSMs and structure of PSBs. *Fatigue & Fracture of Engineering Materials & Structures*. 2017, **40**(7), 1101–1116. ISSN 8756758X. Doi: 10.1111/ffe.12567

[117] MAN, J., P. KLAPETEK, O. MAN, A. WEIDNER†, K. OBRTLÍK and J. POLÁK. Extrusions and intrusions in fatigued metals. Part 2. AFM and EBSD study of the early growth of extrusions and intrusions in 316L steel fatigued at room temperature. *Philosophical Magazine*. 2009, **89**(16), 1337–1372. ISSN 1478-6435, 1478-6443. Doi: 10.1080/14786430902917624

[118] MAZÁNOVÁ, V., V. ŠKORÍK, T. KRUML and J. POLÁK. Cyclic response and early damage evolution in multiaxial cyclic loading of 316L austenitic steel. *International Journal of Fatigue*. 2017, **100**, 466–476. ISSN 01421123. Doi: 10.1016/j.ijfatigue.2016.11.018

[119] SURESH, S. *Fatigue of Materials*. 2. vyd. Cambridge: Cambridge University Press, 1998. ISBN 978-0-511-80657-5.

[120] MARSHALL, P. *Austenitic stainless steels*. London: Elsevier Applied Science Publ, 1984. ISBN 978-0-85334-277-9.

[121] PINEAU, A. and S. D. ANTOLOVICH. High temperature fatigue: behaviour of three typical classes of structural materials. *Materials at High Temperatures*. 2015, **32**(3), 298–317. ISSN 0960-3409, 1878-6413. Doi: 10.1179/0960340914Z.00000000072

[122] PAVINICH, W. and R. RAJ. Fracture at elevated temperature. *Metallurgical Transactions A*. 1977, **8**(12), 1917–1933. ISSN 0360-2133, 1543-1940. Doi: 10.1007/BF02646566

[123] MAZÁNOVÁ, V., M. HECZKO and J. POLÁK. Fatigue crack initiation and growth in 43Fe-25Ni-22.5Cr austenitic steel at a temperature of 700 °C. *International Journal of Fatigue*. 2018, **114**, 11–21. ISSN 01421123. Doi: 10.1016/j.ijfatigue.2018.04.033

[124] COFFIN, L. F. The effect of frequency on the cyclic strain and fatigue behavior of cast rené at 1600° F. *Metallurgical Transactions*. 1974, **5**(5), 1053–1060. ISSN 0360-2133, 1543-1916. Doi: 10.1007/BF02644317

[125] MCMAHON, C. J. and L. F. COFFIN. Mechanisms of damage and fracture in high-temperature, low-cycle fatigue of a cast nickel-based superalloy. *Metallurgical Transactions*. 1970, **1970**(1(12)), 3443–3450. ISSN 10735615. Doi: 10.1007/BF03037877

[126] SOURMAIL, T. Precipitation in creep resistant austenitic stainless steels. *Materials Science and Technology*. 2001, **17**(1), 1–14. ISSN 0267-0836, 1743-2847. Doi: 10.1179/026708301101508972

[127] DANIELSEN, Hilmar K., John HALD, Flemming B. GRUMSEN and Marcel A. J. SOMERS. On the crystal structure of Z-phase Cr(V,Nb)N. *Metallurgical and Materials Transactions A*. 2006, **37**(9), 2633–2640. ISSN 1073-5623, 1543-1940. Doi: 10.1007/BF02586098

[128] GEROLD, V. and H.P. KARNTHALER. On the origin of planar slip in f.c.c. alloys. *Acta Metallurgica*. 1989, **37**(8), 2177–2183. ISSN 00016160. Doi: 10.1016/0001-6160(89)90143-0

[129] HECZKO, M., J. POLÁK and T. KRUML. Microstructure and dislocation arrangements in Sanicro 25 steel fatigued at ambient and elevated temperatures. *Materials Science and Engineering: A*. 2017, **680**, 168–181. ISSN 09215093. Doi: 10.1016/j.msea.2016.10.076

[130] PÜSCHL, W. Models for dislocation cross-slip in close-packed crystal structures: a critical review. *Progress in Materials Science*. 2002, **47**(4), 415–461. ISSN 00796425. Doi: 10.1016/S0079-6425(01)00003-2

[131] LAIRD, Campbell, Philip CHARSLEY and Haël MUGHRABI. Low energy dislocation structures produced by cyclic deformation. *Materials Science and Engineering*. 1986, **81**, 433–450. ISSN 00255416. Doi: 10.1016/0025-5416(86)90281-8

[132] PHAM, M.S., C. SOLENTHALER, K.G.F. JANSSENS and S.R. HOLDSWORTH. Dislocation structure evolution and its effects on cyclic deformation response of AISI 316L stainless steel. *Materials Science and Engineering: A*. 2011, **528**(7–8), 3261–3269. ISSN 09215093. Doi: 10.1016/j.msea.2011.01.015

[133] GERLAND, M., R. ALAIN, B. AIT SAADI and J. MENDEZ. Low cycle fatigue behaviour in vacuum of a 316L-type austenitic stainless steel between 20 and 600°C—Part II: Dislocation structure evolution and correlation with cyclic behaviour. *Materials Science and Engineering: A*. 1997, **229**(1–2), 68–86. ISSN 09215093. Doi: 10.1016/S0921-5093(96)10560-8

[134] BOWMAN, A. L., G. P. ARNOLD, E. K. STORMS and N. G. NERESON. The crystal structure of Cr23C6. *Acta Crystallographica Section B Structural Crystallography and Crystal Chemistry*. 1972, **28**(10), 3102–3103. ISSN 05677408. Doi: 10.1107/S0567740872007526

[135] HECZKO, Milan, Bryan D. ESSER, Timothy M. SMITH, Přemysl BERAN, Veronika MAZÁNOVÁ, Tomáš KRUML, Jaroslav POLÁK and Michael J. MILLS. On the origin of extraordinary cyclic strengthening of the austenitic stainless steel Sanicro 25 during fatigue at 700 °C. *Journal of Materials Research*. 2017, **32**(23), 4342–4353. ISSN 0884-2914, 2044-5326. Doi: 10.1557/jmr.2017.311

[136] POLÁK, Jaroslav, Roman PETRÁŠ, Milan HECZKO, Ivo KUBĚNA, Tomáš KRUML and Guocai CHAI. Low cycle fatigue behavior of Sanicro25 steel at room and at elevated temperature. *Materials Science and Engineering: A*. 2014, **615**, 175–182. ISSN 09215093. Doi: 10.1016/j.msea.2014.07.075

[137] POLÁK, Jaroslav, Roman PETRÁŠ, Milan HECZKO, Tomáš KRUML and Guocai CHAI. Evolution of the cyclic plastic response of Sanicro 25 steel cycled at ambient and elevated temperatures. *International Journal of Fatigue*. 2016, **83**, 75–83. ISSN 01421123. Doi: 10.1016/j.ijfatigue.2015.03.015

[138] TOHYAMA, A. and Y. MINAMI. Development of the High Temperature Materials for Ultra Super Critical Boilers. In: *Advanced Heat Resistant Steel for Power Generation*. London, UK: The Institute of Materials, 1999, p. 494–506.

[139] JIANG, Jun and Lihui ZHU. Strengthening mechanisms of precipitates in S30432 heat-resistant steel during short-term aging. *Materials Science and Engineering: A*. 2012, **539**, 170–176. ISSN 09215093. Doi: 10.1016/j.msea.2012.01.076

[140] IAKOUBOVSKII, K., K. MITSUISHI, Y. NAKAYAMA and K. FURUYA. Thickness measurements with electron energy loss spectroscopy. *Microscopy Research and*

Technique. 2008, **71**(8), 626–631. ISSN 1059910X, 10970029. Doi: 10.1002/jemt.20597

[141] EGERTON, R.F. *Electron Energy-Loss Spectroscopy in the Electron Microscope*. Boston, MA: Springer US, 2011. ISBN 978-1-4419-9582-7. Doi: 10.1007/978-1-4419-9583-4

[142] CHI, Cheng-yu, Hong-yao YU, Jian-xin DONG, Wen-qing LIU, Shi-chang CHENG, Zheng-dong LIU and Xi-shan XIE. The precipitation strengthening behavior of Cu-rich phase in Nb contained advanced Fe–Cr–Ni type austenitic heat resistant steel for USC power plant application. *Progress in Natural Science: Materials International*. 2012, **22**(3), 175–185. ISSN 10020071. Doi: 10.1016/j.pnsc.2012.05.002

[143] AMERICAN INSTITUTE OF PHYSICS and Dwight E. GRAY, ed. *American Institute of Physics handbook: Section editors: Bruce H. Billings [and others] Coordinating editor: Dwight E. Gray*. 3d ed. New York: McGraw-Hill, 1972. ISBN 978-0-07-001485-5.

[144] TPRC, Yeram S. TOULOUKIAN and THERMOPHYSICAL PROPERTIES RESEARCH CENTER, ed. *Thermophysical properties of matter: the TPRC data series; a comprehensive compilation of data by the Thermophysical Properties Research Center (TPRC), Purdue Univ. 12 12: Thermal expansion Metallic elements and alloys*. 2. print. New York: IFI, 1977. Thermophysical properties of matter, 12. ISBN 978-0-306-67032-9.

[145] PODDAR, Debasis, Pavel CIZEK, Hossein BELADI and Peter D. HODGSON. Evolution of strain-induced precipitates in a model austenitic Fe-30Ni-Nb steel and their effect on the flow behaviour. *Acta Materialia*. 2014, **80**, 1–15. ISSN 13596454. Doi: 10.1016/j.actamat.2014.07.035

[146] WILLIAMS, David B. and C. Barry CARTER. *Transmission Electron Microscopy*. Boston, MA: Springer US, 2009. ISBN 978-0-387-76500-6. Doi: 10.1007/978-0-387-76501-3

[147] HADDRILL, D.M., R.N. YOUNGERAND and R.G. BAKER. Precipitation of niobium carbide on dislocations in austenite. *Acta Metallurgica*. 1961, **9**, 982.

[148] CARROLL, M.C. and L.J. CARROLL. Fatigue and creep-fatigue deformation of an ultra-fine precipitate strengthened advanced austenitic alloy. *Materials Science and Engineering: A*. 2012, **556**, 864–877. ISSN 09215093. Doi: 10.1016/j.msea.2012.07.082

[149] ZHANG, Zhen, Zhengfei HU, Haoyun TU, Siegfried SCHMAUDER and Gaoxiang WU. Microstructure evolution in HR3C austenitic steel during long-term creep at 650C. *Materials Science and Engineering: A*. 2017, **681**, 74–84. ISSN 09215093. Doi: 10.1016/j.msea.2016.10.077

[150] SOLENTHALER, Christian, Mageshwaran RAMESH, Peter J. UGGOWITZER and Ralph SPOLENAK. Precipitation strengthening of Nb-stabilized TP347 austenitic steel by a dispersion of secondary Nb(C,N) formed upon a short-term hardening heat treatment. *Materials Science and Engineering: A*. 2015, **647**, 294–302. ISSN 09215093. Doi: 10.1016/j.msea.2015.09.028

[151] CAUTAERTS, N., R. DELVILLE, E. STERGAR, D. SCHRYVERS and M. VERWERFT. Characterization of (Ti,Mo,Cr)C nanoprecipitates in an austenitic stainless steel on the atomic scale. *Acta Materialia*. 2019, **164**, 90–98. ISSN 13596454. Doi: 10.1016/j.actamat.2018.10.018

[152] ALLEN, L.J., A.J. D ALFONSO and S.D. FINDLAY. Modelling the inelastic scattering of fast electrons. *Ultramicroscopy*. 2015, **151**, 11–22. ISSN 03043991. Doi: 10.1016/j.ultramic.2014.10.011

[153] LEBEAU, James M., Scott D. FINDLAY, Leslie J. ALLEN and Susanne STEMMER. Position averaged convergent beam electron diffraction: Theory and applications. *Ultramicroscopy*. 2010, **110**(2), 118–125. ISSN 03043991. Doi: 10.1016/j.ultramic.2009.10.001

[154] LEBEAU, James M., Scott D. FINDLAY, Leslie J. ALLEN and Susanne STEMMER. Quantitative Atomic Resolution Scanning Transmission Electron Microscopy. *Physical Review Letters*. 2008, **100**(20). ISSN 0031-9007, 1079-7114. Doi: 10.1103/PhysRevLett.100.206101

[155] OPHUS, Colin, Jim CISTON and Chris T. NELSON. Correcting nonlinear drift distortion of scanning probe and scanning transmission electron microscopies from image pairs with orthogonal scan directions. *Ultramicroscopy*. 2016, **162**, 1–9. ISSN 03043991. Doi: 10.1016/j.ultramic.2015.12.002

[156] HECZKO, M., B.D. ESSER, T.M. SMITH, P. BERAN, V. MAZÁNOVÁ, D.W. MCCOMB, T. KRUML, J. POLÁK and M.J. MILLS. Atomic resolution characterization of strengthening nanoparticles in a new high-temperature-capable 43Fe-25Ni-22.5Cr austenitic stainless steel. *Materials Science and Engineering: A*. 2018, **719**, 49–60. ISSN 09215093. Doi: 10.1016/j.msea.2018.02.004

[157] NOGUCHI, Y., H. OKADA, H. HIRATA and F. MINAMI. Effect of aging on high temperature fatigue properties of Ni-23Cr-7W alloy for boiler pipes and tubes. *International Journal of Pressure Vessels and Piping*. 2018, **165**, 81–89. ISSN 03080161. Doi: 10.1016/j.ijpvp.2018.06.007

[158] HE, Junjing, Rolf SANDSTRÖM and Stojan VUJIC. Creep, low cycle fatigue and creep-fatigue properties of and modified HR3C. *Procedia Structural Integrity*. 2016, **2**, 871–878. ISSN 24523216. Doi: 10.1016/j.prostr.2016.06.112

[159] HONG, S. The tensile and low-cycle fatigue behavior of cold worked 316L stainless steel: influence of dynamic strain aging. *International Journal of Fatigue*. 2004, **26**(8), 899–910. ISSN 01421123. Doi: 10.1016/j.ijfatigue.2003.12.002

[160] KOSMAČ, Alenka. *Stainless steels at high temperatures*. Brussels: Euro Inox, 2012. Materials and applications series, 18. ISBN 978-2-87997-064-6.

[161] UPADHAYAY, Swathi, Hangyue LI, Paul BOWEN and Afsaneh RABIEI. A study on tensile properties of Alloy 709 at various temperatures. *Materials Science and Engineering: A*. 2018, **733**, 338–349. ISSN 09215093. Doi: 10.1016/j.msea.2018.06.089

[162] VINOTH KUMAR, M., V. BALASUBRAMANIAN and A. GOURAV RAO. Hot tensile properties and strain hardening behaviour of Super 304HCu stainless steel. *Journal of Materials Research and Technology*. 2017, **6**(2), 116–122. ISSN 22387854. Doi: 10.1016/j.jmrt.2016.05.004

[163] MAZÁNOVÁ, V. and J. POLÁK. Initiation and growth of short fatigue cracks in austenitic Sanicro 25 steel. *Fatigue & Fracture of Engineering Materials & Structures*. 2018, **41**(7), 1529–1545. ISSN 8756758X. Doi: 10.1111/ffe.12794

[164] ŠKORÍK, Viktor, Ivo ŠULÁK, Karel OBRTLÍK and Jaroslav POLÁK. Thermo-mechanical and isothermal fatigue behavior of austenitic stainless steel AISI 316L. In: *Metal 2015: 24th International Conference on Metallurgy and Materials*: *Metal 2015: 24th International Conference on Metallurgy and Materials*. Brno: Tanger Ltd., 2015, p. 1–7. ISBN 978-80-87294-58-1.

[165] OBRTLÍK, Karel, Tomásš KRUML and Jaroslav POLÁK. Dislocation structures in 316L stainless steel cycled with plastic strain amplitudes over a wide interval. *Materials Science and Engineering: A*. 1994, **187**(1), 1–9. ISSN 09215093. Doi: 10.1016/0921-5093(94)90325-5

[166] BONNY, G, N CASTIN and D TERENTYEV. Interatomic potential for studying ageing under irradiation in stainless steels: the FeNiCr model alloy. *Modelling and Simulation in Materials Science and Engineering*. 2013, **21**(8), 85004. ISSN 0965-0393, 1361-651X. Doi: 10.1088/0965-0393/21/8/085004

[167] BYRNES, M.L.G., M. GRUJICIC and W.S. OWEN. Nitrogen strengthening of a stable austenitic stainless steel. *Acta Metallurgica*. 1987, **35**(7), 1853–1862. ISSN 00016160. Doi: 10.1016/0001-6160(87)90131-3

[168] VOGT, J.-B. Fatigue properties of high nitrogen steels. *Journal of Materials Processing Technology*. 2001, **117**(3), 364–369. ISSN 09240136. Doi: 10.1016/S0924-0136(01)00799-3

[169] POLÁK, Jaroslav, Veronika MAZÁNOVÁ, Milan HECZKO, Ivo KUBĚNA and Jiří MAN. Profiles of persistent slip markings and internal structure of underlying persistent slip bands. *Fatigue & Fracture of Engineering Materials & Structures*. 2017, **40**(7), 1101–1116. ISSN 1460-2695. Doi: 10.1111/ffe.12567

[170] MAZÁNOVÁ, Veronika, Milan HECZKO, Ivo KUBĚNA and Jaroslav POLÁK. Surface Relief Formation in Relation to the Underlying Dislocation Arrangement. *Key Engineering Materials*. 2017. ISSN 1662-9795.

[171] PETRÁŠ, R., V. ŠKORÍK and J. POLÁK. Thermomechanical fatigue and damage mechanisms in Sanicro 25 steel. *Materials Science and Engineering: A*. 2016, **650**, 52–62. ISSN 09215093. Doi: 10.1016/j.msea.2015.10.030

[172] PETRÁŠ, Roman and Jaroslav POLÁK. Damage mechanism in austenitic steel during high temperature cyclic loading with dwells. *International Journal of Fatigue*. 2018, **113**, 335–344. ISSN 01421123. Doi: 10.1016/j.ijfatigue.2018.02.017

[173] SUZUKI, S., K. SUZUKI, F. KUROSAWA and H. KOBAYASHI. Application of glow discharge optical emission spectroscopy to diffusion measurement of copper in

ferritic and austenitic iron and steels. *Surface and Interface Analysis*. 1992, **19**(1–12), 638–642. ISSN 0142-2421, 1096-9918. Doi: 10.1002/sia.7401901119

[174] HIRTH, John Price and Jens LOTHE. *Theory of dislocations*. 2. ed., reprint. Malabar, Fla: Krieger Publishing Company, 1992. ISBN 978-0-89464-617-1.

[175] KORZHAVYI, P.A. and R. SANDSTRÖM. First-principles evaluation of the effect of alloying elements on the lattice parameter of a 23Cr25NiWCuCo austenitic stainless steel to model solid solution hardening contribution to the creep strength. *Materials Science and Engineering: A*. 2015, **626**, 213–219. ISSN 09215093. Doi: 10.1016/j.msea.2014.12.057

[176] DUTTA, B., E. VALDES and C.M. SELLARS. Mechanism and kinetics of strain induced precipitation of Nb(C,N) in austenite. *Acta Metallurgica et Materialia*. 1992, **40**(4), 653–662. ISSN 09567151. Doi: 10.1016/0956-7151(92)90006-Z

[177] TAYLOR, G.I. Dislocations and Plasticity. In: Richard GRAMMEL, ed. *Deformation and Flow of Solids: Colloquium Madrid September 26-30, 1955*. Berlin, Heidelberg: Springer-Verlag, 1956, p. 3–12. ISBN 978-3-642-48236-6.

[178] FINE, M.E. and D. ISHEIM. Origin of copper precipitation strengthening in steel revisited. *Scripta Materialia*. 2005, **53**(1), 115–118. ISSN 13596462. Doi: 10.1016/j.scriptamat.2005.02.034

[179] FRIEDEL, J, N KURTI and R SMOLUCHOWSKI. *Dislocations*. London, UK: Pergamon Press, 1964. ISBN 978-0-08-013523-6.

[180] BRANDES, M.C., L. KOVARIK, M.K. MILLER, G.S. DAEHN and M.J. MILLS. Creep behavior and deformation mechanisms in a nanocluster strengthened ferritic steel. *Acta Materialia*. 2012, **60**(4), 1827–1839. ISSN 13596454. Doi: 10.1016/j.actamat.2011.11.057

IX. LIST OF ABBREVIATIONS / SYMBOLS

Abbreviations

ADF – annular dark field

APB – anti-phase boundary

APT – atom-probe tomography

A-USC – advanced ultra-super critical

BCC – body-centered cubic

BF – bright field

CRSS – critical resolved shear stress

CSL – coincidence site lattice

CSSC – cyclic stress-strain curve

CTEM – conventional transmission electron microscopy

DCFI – drift correction frame integration

DCI – diffraction contrast imaging

EBSD – electron backscatter diffraction

EDS – energy dispersion X-ray spectroscopy

EELS – electron energy-loss spectroscopy

FCC – face-centered cubic

FEG – field emission gun

FFT – fast Fourier transformation

FIB – focused ion beam

HAADF – high-angle annular dark-field

HAGB – high-angle grain boundary

HCP – hexagonal close-packed

HEA – high-entropy alloy

HRTEM – high resolution transmission electron microscopy

LAADF – low-angle annular dark-field

LAGB – low-angle grain boundary

LCF – low cycle fatigue

ODS – oxide dispersion strengthened

PACBED – position averaged convergent beam electron diffraction

PSB – persistent slip band

PSM – persistent slip marking

QEP – quantum excitation of photons

SAD/SAED – selected area electron diffraction

SC – super-critical

SEM – scanning electron microscopy

SF – Schmid factor

SFE – stacking fault energy

STEM – scanning transmission electron microscopy

TEM – transmission electron microscopy

TMF – thermo-mechanical fatigue

Symbols

t – translation vector

a, b, c – non-complanar vectors (primitive vectors)

u, v, w – integers

$a, b, c, \alpha, \beta, \gamma$ – lattice parameters

g – reciprocal lattice vector

a^*, b^*, c^* – basic vectors in reciprocal space

$h\,k\,l$ – Miller indices

d_{hkl} – interplanar spacing

τ – shear stress

G – shear modulus

b – spacing between atoms in the direction of the shear stress

a – spacing of the rows of atoms

x – shear translation of the two rows away from the low-energy position of stable equilibrium

τ_{th} – theoretical critical shear stress

l – dislocation line vector

b – Burgers vector

ρ – dislocation density

V – volume

l – line length

E – strain energy

r_0 – dislocation core radius

R – crystal radius

ϑ – misorientation angle

h – distance between boundary dislocations

Σ – degree of fit between the structures of two crystallites

T – temperature

T_m – melting temperature

σ – tensile stress

F – applied force

A – area

A_0 – cross sectional area

λ – angle between F and slip direction **b**

n – normal vector to the slip plane

ϕ – angle between F and **n**

F_c – tensile force required to start slip of the dislocation

τ_c – critical resolved shear stress

m – Schmid factor

γ_{SEF} – stacking fault energy

d_{SFE} – equilibrium distance between two partial dislocations

$\tau *$ – applied resolved shear stress

K – resisting force

$\Delta F *$ – Helmholtz free energy change

$V *$ – activation volume

$\Delta G *$ – Gibbs free energy change

k – Boltzmann factor

δ – lattice parameter misfit

D – spacing of misfit dislocations

T – dislocation line tension force

L – obstacle spacing

E – Young modulus of elasticity

f – volume fraction of the particles

σ_y – yield stress

k_y – strengthening coefficient

ε_a – total tensile strain amplitude

ε_{ap} – plastic tensile strain amplitude

σ_a – tensile stress amplitude

V_H – hysteresis loop shape parameter

W – hysteresis loop area, specific energy dissipated in a material within one cycle

ΔK – range of stress intensity factor

N – number of cycles

N_f – number of cycles to fracture

K' – fatigue hardening coefficient

n' – fatigue hardening exponent

ε'_f – fatigue ductility coefficient

c – fatigue ductility exponent

σ'_f – fatigue strength coefficient

b – fatigue strength exponent

$R_{p0.2}$, $R_{p0.02}$ – yield stress defined at engineering strain equal to 0.2% and 0.02% respectively

σ_f – ultimate tensile strength

ε_f – total fracture strain

$\boldsymbol{B}$ – beam vector direction

λ – electron mean free path

T_f – Taylor factor

B – bulk modulus of elasticity

X. Curriculum Vitae

Milan Heczko

(* December 8, 1988)

heczko@ipm.cz

ORCID ID: 0000-0002-8049-4527

SCOPUS Author ID: 55887299700

ResearcherID: A-9917-2017

EDUCATION

Brno University of Technology, Faculty of Mechanical Engineering   **Brno, Czech Republic**
& Institute of Physics of Materials AS CR
     PhD Physical and Materials Engineering   Sep 2013 – 2018 (*expected*)

The Ohio State University, Department of Materials Science & Engineering   **Columbus, Ohio, USA**
     Fulbright Visiting Research Scholar   Aug 2016 – Jun 2017

Masaryk University, Faculty of Science   **Brno, Czech Republic**
     MS Condensed Matter Physics (Mgr.)   Sep 2011 – Jun 2013
     BS Physics (Bc.)   Sep 2008 – Jun 2011

RESEARCH EXPERIENCE

Institute of Physics of Materials ASCR   **Brno, Czech Republic**
     PhD Student   Aug 2011 - present
         Advisors: Prof. Tomáš Kruml, Prof. Jaroslav Polák

The Ohio State University, Center for Electron Microscopy and Analysis   **Columbus, Ohio, USA**
     Fulbright Visiting Research Scholar   Aug 2016 – Jun 2017
         Advisor: Prof. Michael J. Mills

Paul Scherrer Institut, Laboratory for Nuclear Materials   **Villigen, Switzerland**
     Visiting Researcher   Sep 2015 – Dec 2015
         Advisor: Prof. Philippe Spätig

Masaryk University, Faculty of Science   **Brno, Czech Republic**
     MS Student   Aug 2011 – Jun 2013
         Advisor: Mgr. Ondřej Caha, Ph.D

AWARDS

The J. William Fulbright Scholarship for Graduate Study & Research 2016/2017   May 2016
The Thermo Fisher Scientific & Czechoslovak Microscopy Society Fellowship   August 2018

TEACHING EXPERIENCE

Presenter and lecturer   **Brno University of Technology**
Introduction to Materials Science and Engineering   Feb 2014 – Jun 2016
Structure and Properties of Materials   Feb 2014 – Jun 2016

CONFERENCE SPEAKING ENGAGEMENTS

ICSMA-18   Columbus, OH, USA, 2018
28th Colloquium on Fatigue Mechanisms   Erlangen, Germany, 2017
Fulbright Meeting & Orientation 2017   Salt Lake City, UT, USA, 2017
Microscopy & Microanalysis 2016   Columbus, OH, USA, 2016
MSMF-8   Brno, Czech Republic, 2016
27th Colloquium on Fatigue Mechanisms   Vienna, Austria, 2016
ICSMA-17   Brno, Czech Republic, 2015
Junior EUROMAT 2014   Lausanne, Switzerland, 2014

XI. Milan Heczko – List of publications

[1] HECZKO, M., B.D. ESSER, T.M. SMITH, P. BERAN, V. MAZÁNOVÁ, D.W. MCCOMB, T. KRUML, J. POLÁK and M.J. MILLS: Atomic resolution characterization of strengthening nanoparticles in a new high-temperature-capable 43Fe-25Ni-22.5Cr austenitic stainless steel, *Materials Science & Engineering A*. 2018, **719**, 49-60.

[2] MAZÁNOVÁ, V., M. HECZKO and J. POLÁK: Fatigue crack initiation and growth in 43Fe-25Ni-22.5Cr austenitic stainless steel at a temperature of 700°C, *International Journal of Fatigue*. 2018, **114**, 11-21.

[3] POLÁK, J., V. MAZÁNOVÁ, R. PETRÁŠ and M. HECZKO: Early damage and fatigue crack initiation at ambient and elevated temperatures in heat resistant austenitic steel, *MATEC Web of Conferences*. 2018, **165**, 04008.

[4] SPÄTIG, P., M. HECZKO, T. KRUML and H.-P. SEIFERT: Influence of mean stress and light water reactor environment on fatigue life and dislocation microstructures of 316L austenitic steel, *Journal of Nuclear Materials*. 2018, **509**, 15-28.

[5] HECZKO, M., B.D. ESSER, T.M. SMITH, P. BERAN, V. MAZÁNOVÁ, T. KRUML, J. POLÁK and M.J. MILLS: On the origin of extraordinary cyclic strengthening of the austenitic stainless steel Sanicro 25 during fatigue at 700°C, *Journal of Materials Research*. 2017, **32**(23), 4342-4353.

[6] POLÁK, J., V. MAZÁNOVÁ, M. HECZKO, R. PETRÁŠ, I. KUBĚNA, L. CASALENA and J. MAN: The role of extrusions and intrusions in fatigue crack initiation, *Engineering Fracture Mechanics*. 2017, **185**, 46-60.

[7] POLÁK, J., V. MAZÁNOVÁ, M. HECZKO, I. KUBĚNA and J. MAN: Profiles of persistent slip markings and internal structure of underlying persistent slip bands, *Fatigue & Fracture of Engineering Materials & Structures*. 2017, **40**(7), 1101-1116.

[8] HECZKO, M., P. SPÄTIG, H.-P. SEIFERT and T. KRUML: Correlation between dislocation structures and mechanical fatigue response of 316L austenitic steel loaded with and without mean stress at high temperature in air and water environment, *Solid State Phenomena*. 2017, **258**, 534-537.

[9] MAZÁNOVÁ, V., M. HECZKO, I. KUBĚNA and J. POLÁK: Surface Relief Formation in Relation to the Underlying Dislocation Arrangement, *Solid State Phenomena*. 2017, **258**, 526-529.

[10] CHLUPOVÁ, A., M. HECZKO, K. OBRTLÍK, P. BERAN and T. KRUML: Effect of alloying and thermal processing on mechanical properties of TiAl alloys, *Solid State Phenomena*. 2017, **258**, 501-505.

[11] HECZKO, M., J. POLÁK and T. KRUML: Microstructure and dislocation arrangements in Sanicro 25 steel fatigued at ambient and elevated temperatures, *Materials Science & Engineering A*. 2017, **680**, 168-181.

[12] BERAN, P., M. HECZKO, T. KRUML, T. PANZNER and S. VAN PETEGEM: Complex investigation of deformation twinning in gamma-TiAl by TEM and neutron diffraction, *Journal of the Mechanics and Physics of Solids*. 2016, **95**, 647-662.

[13] CHLUPOVÁ, A., M. HECZKO, K. OBRTLÍK, J. POLÁK, P. ROUPCOVÁ, P. BERAN and T. KRUML: Mechanical properties of high niobium TiAl alloys doped with Mo and C, *Materials and Design*. 2016, **99**, 284-292.

[14] POLÁK, J., V. MAZÁNOVÁ, I. KUBĚNA, M. HECZKO and J. MAN: Surface relief and internal structure in fatigued stainless Sanicro 25 steel, *Metallurgical and Materials Transactions A*. 2016, **47**(5), 1907-1911.

[15] POLÁK, J., R. PETRÁŠ, M. HECZKO, T. KRUML and G. CHAI: Evolution of the cyclic plastic response of Sanicro 25 steel cycled at ambient and elevated temperatures, *International Journal of Fatigue*. 2016, **83**(I), 75-83.

[16] CHLUPOVÁ, A., T. KRUML, P. ROUPCOVÁ, M. HECZKO, K. OBRTLÍK and P. BERAN: The effect of Mo and/or C addition on microstructure and properties of TiAl alloys, In METAL (24th International Conference on Metallurgy and Materials) 2015 Conference Proceedings, p. 1300-1305, 03.- 05. June 2015, Brno, Czech Republic

[17] POLÁK, J., R. PETRÁŠ, M. HECZKO, I. KUBĚNA, T. KRUML and G. CHAI: Low cycle fatigue behavior of Sanicro 25 steel at room and at elevated temperature, *Materials Science & Engineering A*. 2014, **615**, 175-182.

[18] POLÁK, J., R. PETRÁŠ, M. HECZKO and G. CHAI: Analysis of Cyclic Plastic Response of Heat Resistant Sanicro 25 Steel at Ambient and Elevated Temperatures, *Procedia Engineering*. 2014, **74**, 68-73.

[19] CHLUPOVÁ, A., K. OBRTLÍK, P. BERAN, M. HECZKO, J. POLÁK and T. KRUML: Monotic and cyclic properties of TiAl alloys doped with Nb, Mo and C, *Procedia Engineering*. 2014, **74**, 405-408.

[20] BERAN, P., M. PETRENEC, M. HECZKO, B. SMETANA, M. ŽALUDOVÁ, M. ŠMÍD, T. KRUML and L. KELLER: In-situ neutron diffraction study of thermal phase stability in a γ-TiAl based alloy doped with Mo and/or C, *Intermetallics*. 2014, **54**, 28–38.

[21] PETRENEC, M., E. VRASPÍROVÁ, K. NĚMEC and M. HECZKO: Effect of cyclic heat treatment on cast structure of TiAl alloy, *Key Eng. Mater*. 2014, **586**, 222–225.

[22] PETRENEC, M., P. STRUNZ, U. GASSER, M. HECZKO, J. ZÁLEŠÁK and J. POLÁK: Nanostructure characterization of IN738LC superalloy fatigued at high temperature, *In Nanocon 2013 Conference Proceedings*, p. 712-717, 16.-18. October 2013, Brno, Czech Republic, art. no. 2001.

XII. Appendix – Fulbright program completion certificate